

The Validity of Using High Resolution Digital Image Correlation to Investigate the Influence of Stacking Fault Energies on Deformation Mechanics

Suzanne Cheney

November 2022

A thesis submitted to the School of Engineering and Innovation of The
Open University for the Degree of Doctor of Philosophy

I. Abstract

When placing metallic components in safety-critical environments, such as nuclear reactors, it is important to be able to accurately predict their service lifetime. For these predictions to be reliable in safety-critical environments they need to accommodate behaviour at the microscale as well as the macroscale. Micro-scale strain development can be measured during mechanical loading and then used to help predict failure within such components.

In this thesis, neutron diffraction (ND) was used to measure bulk-scale lattice strains for grains with orientations that correlate to the diffraction peaks. However, ND is expensive and only available at several national facilities. Therefore, high-resolution digital image correlation (HR-DIC) has been proposed as a cheaper and more accessible alternative. This project therefore compares the strain data collected from both ND and HR-DIC to evaluate the effectiveness of using HR-DIC as a bulk grain-scale technique.

To evaluate the effectiveness of HR-DIC as a bulk strain measurement technique, the effect of stacking fault energy (SFE) on deformation mechanics was selected as a comparable phenomenon. The materials were selected to represent a range of stacking fault energy, stainless steel 316 (SS316), INVAR and pure nickel. The samples were prepared to be tested in both *in situ* neutron diffraction tensile tests and *in situ* HR-DIC tensile tests, with post-mortem EBSD analysis performed on the neutron diffraction samples to investigate EBSD metrics.

For the SS316 sample, the HR-DIC showed three distinct orientation peaks, showing that the technique was able to accurately distinguish and divide the data into the orientation subsets. The 111-, 220-, and 200-orientation subsets show a broader range of strain behaviour in the low SFE materials (SS316 and INVAR) compared to the high SFE material (nickel). This was in good agreement with the results of the neutron diffraction tests and the EBSD metric analysis.

II. Acknowledgements

Firstly, I would like to thank my supervisors, Dr Alex Forsey, Dr Richard Moat and Dr Salih Gungor, for their endless support throughout my PhD. I couldn't have asked for a better supervisory team, and I feel very lucky to have worked with all of them. Without their vast knowledge, genuine kindness, and light-hearted spirits, I could not have completed this work.

I would also like to thank Damien Flack and Peter Ledgard for their help with specimen machining, Dr Zeeshan Mughal and Dr Giulia Degli-Alessandrini for their SEM work, and Dr Ellies Muyupa, Dr Yvonne Sutton, Stan Hiller and Gordon Imlach for their help in the experimental and laboratory work. Furthermore, it is gratefully acknowledged the encouragement and technical advice provided by EDF Energy staff Sarah Spindler, Mike Spindler and David Dean.

I am grateful to the Engineering and Physical Sciences Research Council for the financial support and to the ICO CDT for accepting me onto this project. I am also thankful to Rutherford Appleton Laboratory for allowing me to use ENGIN-X for my neutron diffraction tests and to Dr Joe Kelleher for his help with these tests. I would also like to thank Dr Carlos Tomé for access and advice on using the elastic-plastic self-consistent model.

I would like to thank all my colleagues in the materials department at the OU, they are an excellent group of people who have been a pleasure to work with. I would particularly like to thank Dr Yadu Das and Ehsan Afshin for their help with sample preparation.

Finally, I would like to thank my family and friends for their continued support and encouragement.

III. Preface

This thesis is submitted for the degree of Doctor of Philosophy at The Open University. The research described herein was conducted in the School of Engineering & Innovation, Faculty of Science, Technology, Engineering and Mathematics between September 2018 and November 2022 under the supervision of Dr Alex Forsey, Dr Richard Moat and Dr Salih Gungor. This work is original to the best of my knowledge, except where reference is made to the work of others. This work has not been submitted in whole or part for any other degree at any other university.

IV. Table of contents

I. Abstract.....	ii
II. Acknowledgements.....	iii
III. Preface	iv
IV. Table of contents	v
V. List of Figures	viii
VI. List of Tables	xvi
VII. List of Abbreviations	xvii
1. Introduction	1
1.1. Motivation.....	1
1.2. Aim and Objectives	3
1.3. Outline of the Thesis	3
2. Literature Review	5
2.1. Overview	5
2.2. Crystallographic Structure	5
2.2.1. Defects	6
2.3. Deformation in FCC Metals	9
2.3.1. Single-Crystal Deformation Mechanics.....	9
2.3.2. Polycrystalline Deformation Mechanics	12
2.3.3. Summary	13
2.4. Microstructural Features Analysis	13
2.4.1. EBSD Working Principles	14
2.5. Modelling polycrystalline deformation.....	18
2.5.1. Crystal Plasticity Finite Element Method	19
2.5.2. Self-Consistent Modelling	21
2.5.3. Summary	28
2.6. Microscale Strain Measurement.....	29
2.6.1. Microscope techniques	30
2.6.2. Diffraction techniques.....	35
2.6.3. Neutron Diffraction.....	35
2.6.4. Diffraction Peak Profile Analysis	37
2.6.5. Limitations of Diffraction Techniques	37
2.6.6. Digital Image Correlation	38
2.7. Summary	46
3. Research Questions	47

4.	Investigating the Influence SFE on Deformation Mechanics using in situ Neutron Diffraction ...	48
4.1.	Overview	48
4.2.	Methodology.....	48
4.2.1.	Materials	48
4.2.2.	<i>In situ</i> Tensile Testing at ENGIn-X.....	50
4.3.	Texture Analysis using EBSD	54
4.3.1.	Grain Size Measurements	56
4.4.	Elastic Modulus Measurements.....	57
4.4.1.	Sample Preparation for Elastic Modulus Tests	57
4.5.	EPSC modelling.....	58
4.5.1.	Optimisation.....	58
4.6.	Results.....	59
4.6.1.	EBSD Analysis	59
4.6.2.	Dynamic Elastic Modulus	61
4.6.3.	In situ Tensile tests.....	61
4.6.4.	Validation using the EPSC model	68
4.6.5.	Post-Mortem EBSD Analysis.....	74
4.7.	Discussion.....	77
4.8.	Summary	81
5.	Using EBSD metrics to quantify plastic strain accumulation	82
5.1.	Overview	82
5.2.	Methodology.....	82
5.2.1.	EBSD Analysis	82
5.2.2.	EBSD Metrics	82
5.3.	Results.....	83
5.3.1.	EBSD Raw Data.....	83
5.3.2.	Extracting EBSD Metrics.....	88
5.3.3.	Segmenting EBSD data	98
5.3.4.	Histograms plots of EBSD Metrics.....	106
5.3.5.	Segmented KAM Spatial Maps.....	125
5.4.	Discussion.....	129
5.5.	Summary	133
6.	Using HR-DIC as a method to measure strain.....	135
6.1.	Overview	135
6.2.	Methodology.....	135
6.2.1.	Sample Preparation.....	136

6.2.2.	EBSD Preparation	136
6.2.3.	Hardness Indents	137
6.2.4.	EBSD Mapping and Analysis	137
6.2.5.	Etching.....	139
6.2.6.	Mechanical Testing	141
6.2.7.	Sample Geometry	142
6.2.8.	Telecentric Lens	144
6.2.9.	Analysing DIC data	144
6.3.	Results.....	145
6.3.1.	EBSD Analysis	145
6.3.2.	HR-DIC.....	149
6.3.3.	Segmented EBSD Maps.....	165
6.3.4.	Histogram plots.....	171
6.3.5.	Regional Strain Plots	177
6.4.	Discussion.....	187
7.	Overall Discussion and Conclusions	192
7.1.	Introduction	192
7.2.	Discussion.....	192
7.3.	Conclusions	200
7.4.	Limitations Imposed on this Work.....	201
7.5.	Future work.....	202
8.	References	203

V. List of Figures

Figure 2.1: Schematic of some of the common unit cells for metallic crystalline structure (a) face-centred cubic (FCC), (b) body-centred cubic (BCC), and (c) hexagonal close-packed (HCP).	6
Figure 2.2: Two- dimensional schematic of an edge dislocation and its effect on the neighbouring atoms.	6
Figure 2.3: Diagram showing (a) a perfect FCC crystal without a stacking fault and (b) a crystal which contains a stacking fault.	7
Figure 2.4: (a) Stress-strain curve for 0 (low SFE) and 2 (high SFE) wt.% Al TWIP steels and (b) Lattice strains of the (111) and (222) diffractions (The error bar is smaller than the symbol size) (31).	8
Figure 2.5: Schematic illustrating the formulation of Schmid's law (diagram modified from reference (37)).	11
Figure 2.6: A Schematic of a randomly orientated polycrystalline microstructure which highlights the localised variations in micro strains at different length scales (on the macroscale (σI), intergranularly (σII) and intragranularly (σIII)) (41).	13
Figure 2.7: Schematic diagram showing Bragg's Law of Diffraction	14
Figure 2.8: Backscatter Kikuchi pattern of Type 316H austenitic stainless steel at 20keV (49).	15
Figure 2.9: Schematic of principal components of electron backscatter diffraction observation (48).	16
Figure 2.10 A crystal lattice which has been strained to 11% uniaxially in the horizontal direction and a schematic overlay of the patterns with strain (red) and without (black) (51).	17
Figure 2.11: EBSD pattern from (a) a well-prepared surface and from (b) a poorly prepared surface of zirconium (51).	18
Figure 2.12 Diagram showing the effect of two opposing edge dislocations on the crystal lattice leading to a degraded lattice pattern (51).	18
Figure 2.13: Mean ($h\ k\ l$) family lattice strain evolution in the loading direction for steel specimens with a grain size of 80 μm (left) and 350 μm (right), here the CPFEM modelled data is shown as lines (63).	20
Figure 2.14 Schematic illustration of an ellipsoidal, stiff anisotropic inclusion in a homogenous equivalent medium. Where stiffnesses are denoted E and strains ϵ . The strain field in the inclusion is constant, and regions of additional compressive (C) and tensile (T) are shown. The strain at infinity in the medium, ϵ_∞ , is equal to the average over all grains. (41)	21
Figure 2.15: Lattice strain data for 316H stainless steel showing the 111, 311 and 200 grain orientation subsets in the loading direction where the points show the experimental data based on single peak fit and the lines show the results of the EPSC model at (a) room temperature, (b) 425 °C and (c) 650 °C (9).	24
Figure 2.16: The measured and modelled elastic lattice strain in the (200) and (220) γ grain and γ' precipitation families for the fine γ' microstructure. Modelled results are presented as lines, while experimental data are presented as points. The horizontal dashed line indicates the onset of plastic deformation (72).	25
Figure 2.17: The measured and modelled elastic lattice strain in the (200) and (220) γ grain and γ' precipitation families for the (a) medium γ' microstructure and (b) coarse γ' microstructure. Modelled results are presented as lines, while experimental data are presented as points. The horizontal dashed line indicates the onset of plastic deformation (72).	26
Figure 2.18: Graph showing a range of different internal stress measurement techniques (3). With added reference to what constitutes micro-strain measurement in this thesis	29
Figure 2.19: Schematic calculation of GOS (49).	31
Figure 2.20: Schematic illustration of calculation by KAM (49).	32

Figure 2.21: A comparison between the True plastic strain and KAM of three SS316 samples. Sample A is subjected to a strain rate (s^{-1}) 2.0×10^{-4} and a grain size of 98 ± 8 , Sample B has a strain rate (s^{-1}) of 2.0×10^{-4} and a grain size of 93 ± 12 , Sample C has a strain rate (s^{-1}) of 1.5×10^{-3} and a grain size of 35 ± 1 . By comparing Sample A and Sample B, with the same strain, it shows that is an increase in KAM values with the increasing KAM (91).	33
Figure 2.22: ‘Comparison of IQ, KAM, GOS, and GAM maps for (A) deformed (B) partially recrystallised and (C) fully recrystallized samples. The misorientation spread $> 1.1^\circ$ is marked as white and indicated with the blue arrows’ (90).	34
Figure 2.23: (a) Reference Image, with an imposed grid to divide the surface into subsets, (b) diagram showing the subset tracking procedure (108).	39
Figure 2.24: Schematic illustration showing a reference subset before deformation and the deformed subset following deformation (113).	40
Figure 2.25: A schematic of the possible changes in shape that a subset may experience during deformation. Translation stretch, shear and distortion are shown here (55,114).	40
Figure 2.26: The HRDIC effective strain (ϵ_{eff}) map at macroscopic $\epsilon_{xx} \sim 0.02$, field of view 1×0.5 mm, spatial resolution 0.117 nm. G1-G5 highlight grains with different slip character and the effect of this on HRDIC ϵ_{eff} and EBSD lattice misorientation (grain reference orientation distribution mean) (21).	43
Figure 2.27: Low magnification strain maps overlaid with EBSD grain boundary maps, showing the heterogenous nature of strain accommodation within individual grains. Panels (a) and (b) show ϵ_{xx} at 5% and 10% applied strain respectively. (c) Histogram plot of ϵ_{xx} for individual grains at 5% and 10% macroscopic global strain. (d) Map of the average strain in the loading direction (ϵ_{xx}), averaged over each grain at 10% global strain used for producing (c) (15).	44
Figure 2.28: Mechanisms for martensitic phase transformation in fully austenitic grains. Grain 1 (top) and grain 2 (bottom) are shown with the corresponding DIC strain maps, made at various strain increments represented by red dots on the stress-strain curve (15).	44
Figure 2.29: Meso-scale DIC results (a-f), a) an example image used for analysis with insert showing pixel definition, b) spatially resolved map of loading direction strain (ϵ_{xx}) difference to global value at 0.075 strain, c) spatially resolved map of principal strain angle with respect to the loading direction at the same strain value, d) variation of elastic modulus along the length of sample gauge and e) variation of 0.2% proof stress along the length of sample gauge, f) Tensile curve to 0.01 strain of meso-scale sample, with curves from the red and blue regions highlighted in d) and e). Micro-scale DIC results (g-j), g) an example image used for analysis with insert showing pixel definition, h) Inverse pole figure EBSD orientation map of area tested using DIC i) spatially resolved map of difference in loading direction strain (ϵ_{xx}) to sample average (of 0.075 strain) and j) spatially resolved map of principal strain angle with respect to the loading direction (14).	45
Figure 4.1: A Schaeffler diagram showing the microstructure expected by the weighted percentages of chromium and nickel in stainless steels. Here the black lines are for castings and the blue is for welds (128). Using the chemical composition for SS316 from Table 4.1, the expected microstructure can be seen.	49
Figure 4.2: A schematic showing the tension test specimen design for the in situ neutron diffraction tests. Measurements are in mm.	50
Figure 4.3: A typical diffraction spectrum for a stainless steel specimen measured at ENGIN-X (97).	51
Figure 4.4: Schematic showing the neutron beam path and relative positions of the specimen and the detectors, which are used to record the longitudinal and transverse strains, in the ENGIN-X diffractometer.	52
Figure 4.5: An image showing the angle of the tensile testing machine and the source of the neutrons at ENGIN-X.	53
Figure 4.6 Set-up of the in-situ mechanical testing stress rig at ENGIN-X beamline.	54

Figure 4.7 Flow chart of parameter optimisation routine utilizing built-in MATLAB least-squares optimization capability.	59
Figure 4.8: EBSD maps with ipf colouring of the undeformed region used to provide the initial texture files for the EPSC model for (a) SS316, (b) INVAR and (c) pure nickel.	60
Figure 4.9: Macro stress-strain curves obtained during the in situ neutron diffraction tensile tests for the SS316, INVAR, and pure nickel specimens.	62
Figure 4.10: Plot showing the lattice strain for SS316 in the grain subsets: 111, 220 and 200. These are seen in both the transverse and longitudinal directions.	63
Figure 4.11: Plot showing the lattice strain for INVAR in the grain orientation subsets: 111, 200 and 200, in the transverse and longitudinal directions. Here (a) is the best fit scale to highlight the behaviours of the different orientation subset and (b) shows the comparative scale (same y-axis) to the SS316 specimen in Figure 4.10....	64
Figure 4.12: Plot showing the lattice strain for pure nickel in the grain subsets: 111, 200 and 200, for the transverse and longitudinal directions. Here (a) is the best fit scale to highlight the behaviours of the different orientation subset and (b) shows the comparative scale (same y-axis) to the SS316 specimen in Figure 4.10....	65
Figure 4.13: Plot of the FWHM compared to stress values for the in situ neutron diffraction tensile tests for the selected subsets of grains with crystallographic orientations within 7.5 degrees of the 111, 200 and 220 for SS316.	66
Figure 4.14: Plot of the FWHM compared to stress values for in situ neutron diffraction tensile tests for the selected subsets of grains with crystallographic orientations within 7.5 degrees of the 111, 200 and 220 for INVAR.	67
Figure 4.15: Plot of the FWHM compared to stress values for in situ neutron diffraction tensile tests for the selected subsets of grains with crystallographic orientations within 7.5 degrees of the 111, 200 and 220 for pure nickel.	68
Figure 4.16: Macro stress-strain graphs for SS316, showing the comparison between the experimental in situ neutron diffraction tensile tests (markers) and the EPSC model results (line).	69
Figure 4.17: Macro stress-strain graphs for INVAR, showing the comparison between the experimental in situ neutron diffraction tensile tests (markers) and the EPSC model results (line).	70
Figure 4.18: Macro stress-strain graphs for pure nickel, showing the comparison between the experimental in situ neutron diffraction tensile tests (markers) and the EPSC model results (line).	71
Figure 4.19: Graphs comparing the lattice strain obtained through in situ neutron diffraction tensile tests (markers) to that predicted by the EPSC model for SS316 for the grain families with orientations within 7.5 degrees of the 111, 220 and 200 orientations. The lattice strain values parallel (long) and perpendicular (trans) to the loading direction are shown in this figure.	72
Figure 4.20: Graphs comparing the lattice strain obtained through in situ neutron diffraction tensile tests (markers) to that predicted by the EPSC model for INVAR for the grain families with orientations within 7.5 degrees of the 111, 220 and 200 orientations. The lattice strain values parallel (long) and perpendicular (trans) to the loading direction are shown in this figure.	73
Figure 4.21: Graphs comparing the lattice strain obtained through in situ neutron diffraction tensile tests (markers) to that predicted by the EPSC model for pure nickel for the grain families with orientations within 7.5 degrees of the 111, 220 and 200 orientations. The lattice strain values parallel (long) and perpendicular (trans) to the loading direction are shown in this figure.	74
Figure 4.22: EBSD analysis of tensile test specimens (3% strain) after in situ neutron diffraction tensile testing for materials: (a) SS316, (b) INVAR and (c) pure nickel.	75
Figure 4.23: Pole figures for (a) undeformed and (b) deformed regions of the SS316 specimen.	76
Figure 4.24: Pole figures for (a) undeformed and (b) deformed regions of the INVAR specimen.	76

Figure 4.25: Pole figures for (a) undeformed and (b) deformed regions of the pure nickel specimen.....	77
Figure 5.1: Number of surrounding pixels for KAM calculations	83
Figure 5.2: Map plots of the EBSD data for the undeformed and deformed regions for (a) SS316, (b) INVAR and (c) pure nickel.....	84
Figure 5.3: Map plots of the Schmid factor values calculated from the EBSD data are shown for (a) SS316, (b) INVAR and (c) pure nickel	86
Figure 5.4: EBSD maps for Taylor factor values calculated from EBSD data from the deformed and undeformed regions cut from the samples (a) SS315, (b) INVAR and (c) pure nickel.....	87
Figure 5.5: EBSD maps for GOS calculated from EBSD data from the deformed and undeformed regions cut from the samples (a) SS315, (b) INVAR and (c) pure nickel.	89
Figure 5.6: EBSD maps for GAM calculated from EBSD data from the deformed and undeformed regions cut from the samples (a) SS315, (b) INVAR and (c) pure nickel.	91
Figure 5.7: EBSD maps for KAM in radians calculated from EBSD data from the deformed and undeformed regions cut from the samples (a) SS315, (b) INVAR and (c) pure nickel. The white regions on the figures are unindexed points.....	93
Figure 5.8: A comparison between the deformed and undeformed regions of the INVAR sample using a refined scale to highlight the change between samples for the EBSD metrics (a) GOS, (b) GAM and (c) KAM.	95
Figure 5.9: A comparison between the deformed and undeformed regions of the pure nickel sample using a refined scale to highlight the change between samples for the EBSD metrics (a) GOS, (b) GAM and (c) KAM.	97
Figure 5.10: The grains selected by the MATLAB code for undeformed SS316 showing the subsets of grains within 7.5 degrees of the (a) 111, (b) 220 and (c) 200 orientations.	99
Figure 5.11: The grains selected by the MATLAB code for deformed SS316 at 3% strain showing the subsets of grains within 7.5 degrees of the (a) 111, (b) 220 and (c) 200 orientations.	99
Figure 5.12: The grains selected by the MATLAB code for undeformed INVAR showing the subsets of grains within 7.5 degrees of the (a) 111, (b) 220 and (c) 200 orientations.	101
Figure 5.13: The grains selected by the MATLAB code for deformed INVAR showing the subsets of grains within 7.5 degrees of the (a) 111, (b) 220 and (c) 200 orientations.	102
Figure 5.14: The grains selected by the MATLAB code for undeformed pure nickel showing the subsets of grains within 7.5 degrees of the (a) 111, (b) 220 and (c) 200 orientations.	104
Figure 5.15: The grains selected by the MATLAB code for deformed pure nickel showing the subsets of grains within 7.5 degrees of the (a) 111, (b) 220 and (c) 200 orientations.	104
Figure 5.16: Histogram showing the number of counts (N) for each Schmid Factor for all grains, and for the subsets of grains within 7.5 degrees of crystallographic orientations 111, 220 and 200 for SS316 for the (a) undeformed and (b) deformed regions.....	107
Figure 5.17: Histogram showing the number of counts (N) for each Schmid Factor for all grains, and for the subsets of grains within 7.5 degrees of crystallographic orientations 111, 220 and 200 for INVAR for the (a) undeformed and (b) deformed regions.....	108
Figure 5.18: Histogram showing the number of counts (N) for each Schmid Factor for all grains, and for the subsets of grains within 7.5 degrees of crystallographic orientations 111, 220 and 200 for pure nickel for the (a) undeformed and (b) deformed regions.....	109
Figure 5.19: Histogram plot showing the Taylor Factor values for the total and the subsets of grains within 7.5 degrees of the 111, 220 and 200 orientations for deformed SS316	110

Figure 5.20: Histogram plot showing the Taylor Factor values for the total and the subsets of grains within 7.5 degrees of the 111, 220 and 200 orientations for undeformed and deformed INVAR.	111
Figure 5.21: Histogram plot showing the Taylor Factor values for the total and the subsets of grains within 7.5 degrees of the 111, 220 and 200 orientations for an undeformed and deformed nickel.	112
Figure 5.22: Histogram plots showing the GOS values for the grain subsets which are within 7.5 degrees of the 111, 220 and 200 orientations for the SS316 specimen for the (a) undeformed region and (b) deformed region.	113
Figure 5.23: Histogram plots showing the GOS values in degrees for the grain subsets which are within 7.5 degrees of the 111, 220 and 200 orientations for the INVAR specimen for the (a) undeformed region and (b) deformed region.	114
Figure 5.24: Histogram plots showing the GOS values in degrees for the grain subsets which are within 7.5 degrees of the 111, 220 and 200 orientations of pure nickel for the (a) undeformed region and (b) deformed region.	115
Figure 5.25: GAM histogram for SS316 (a) undeformed region and (b) deformed region, where the subsets of grains are defined as being within 7.5 degrees of the 111, 220 and 200 orientations.	116
Figure 5.26: GAM histogram for INVAR (a) undeformed region and (b) deformed region, where the subsets of grains are defined as being within 7.5 degrees of the 111, 220 and 200 orientations.	117
Figure 5.27: GAM histogram for nickel (a) undeformed region and (b) deformed region, where the subsets of grains are defined as being within 7.5 degrees of the 111, 220 and 200 orientations.	118
Figure 5.28: KAM histogram plot for SS316 where (a) undeformed region with the x-axis from 0 to 5 degrees and (a)(i) has an axis from 0 to 3 degrees, (b) deformed region with the x-axis from 0 to 5 degrees and (b)(i) has an axis from 0 to 3 degrees and (c) shows the difference between the two KAM values in radians, where the subsets of grains are defined as being within 7.5 degrees of the 111, 220 and 200 orientations.	120
Figure 5.29: KAM histogram plot for INVAR where (a) undeformed region with the x-axis from 0 to 5 degrees and (a)(i) has an axis from 0 to 1 degrees, (b) deformed region with the x-axis from 0 to 5 degrees and (b)(i) has an axis from 0 to 3 degrees and (c) shows the difference between the two KAM values, where the subsets of grains are defined as being within 7.5 degrees of the 111, 220 and 200 orientations.	122
Figure 5.30: KAM histogram plot for pure nickel where (a) undeformed region with the x-axis from 0 to 5 degrees and (a)(i) has an axis from 0 to 1.5 degrees, (b) deformed region with the x-axis from 0 to 5 degrees and (b)(i) has an axis from 0 to 1.5 degrees and (c) shows the difference between the two KAM values, where the subsets of grains are defined as being within 7.5 degrees of the 111, 220 and 200 orientations.	124
Figure 5.31: KAM spatial maps for SS316, which are segmented into the three orientation subsets (a) 111, (b) 220 and (c) 200 for both the undeformed and deformed regions, where the scale is KAM in degrees.	126
Figure 5.32: KAM spatial maps for INVAR, which are segmented into the three orientation subsets (a) 111, (b) 220 and (c) 200 for both the undeformed and deformed regions.	127
Figure 5.33: KAM spatial maps for pure nickel, which are segmented into the three orientation subsets (a) 111, (b) 220 and (c) 200 for both the undeformed and deformed regions.	128
Figure 5.34: Segmented Taylor factor maps for deformed SS316 for the grain subsets (a) 111, (b) 220 and (c) 200.	130
Figure 6.1: Flow chart showing the preparation steps for aligning the HR-DIC data to EBSD maps.	136
Figure 6.2: SEM image showing the hardness indents on an etched large-grain IN718 sample used as a test specimen to ensure the fiducial marker could be found.	137
Figure 6.3: SEM images showing the ROI of the EBSD maps to the hardness indents for (a) SS316, (b) INVAR and (c) pure nickel.	138

Figure 6.4 Schematic showing the procedure used to create a texture on the surface of the tensile specimens for HR-DIC analysis.	140
Figure 6.5: Photo of the etched surface for the SS316 sample.	140
Figure 6.6: Photo of the etched surface for the INVAR sample.	140
Figure 6.7: Photo of the etched surface for the pure nickel sample.	141
Figure 6.8: An image showing the set-up of the micro-tensile tester with the control computer, it also shows the set-up used for performing HR-DIC on a tensile sample.	142
Figure 6.9: The 4.5 kN ADMET mini-tensile testing machine used for the HR-DIC tensile tests.....	142
Figure 6.10: The approximate dimensions of the HR-DIC tensile test specimens.	143
Figure 6.11: Grip re-design with annotations, here (a) new grip design EDM and (b) original grip design.....	144
Figure 6.12: A 2 mm x 2 mm EBSD map for SS316 used in the segmentation of the HR-DIC data. The location of the hardness indent used as a fiducial marker is shown on the map.	146
Figure 6.13: A 2 mm x 2 mm EBSD map for INVAR used in the segmentation of the HR-DIC data. The location of the hardness indent used as a fiducial marker is shown on the map.	147
Figure 6.14: A 2 mm x 2 mm EBSD map for pure nickel used in the segmentation of the HR-DIC data. The location of the hardness indent used as a fiducial marker is shown on the map.	148
Figure 6.15: (a) DIC area for SS316 with the EBSD map region superimposed, showing how the region is segmented using the EBSD data. (b) shows a close-up image of one of the hardness indents.	150
Figure 6.16: Strain maps collected through DIC for SS316 at 3% global strain showing (a) the total area showing the maximum nominal strain and (b) showing the maximum principal strain for the area within the EBSD analysis.	152
Figure 6.17: Strain map for SS316 in the loading direction (E_{xx}) at 3% global strain where (a) shows the entire region captured by the telecentric lens and (b) the segmented region calculated by imposing EBSD analysts on the DIC analysis.....	153
Figure 6.18: Strain map for SS316 perpendicular to the loading direction (E_{yy}) at 3% strain where (a) shows the entire region captured by the telecentric lens and (b) the segmented region calculated by imposing EBSD analysts on the DIC analysis.	154
Figure 6.19: (a) Initial image collected for the DIC analysis for the tensile tests of INVAR with the EBSD map region superimposed. The hardness indents seen between 2000 and 4500 were used to align the EBSD map with the initial image to segment the strain results. (b) Shows a close-up image of one of the hardness indents.	155
Figure 6.20: Strain maps collected through DIC for INVAR at 3% global strain, showing the (a) total area maximum nominal strain and (b) the maximum principal strain for the area within the EBSD analysis.	157
Figure 6.21: Strain map for INVAR in the loading direction (E_{xx}) at 3% global strain where (a) shows the entire region captured by the telecentric lens and (b) the segmented region calculated by imposing EBSD analysts on the DIC analysis.....	158
Figure 6.22: Strain map for INVAR perpendicular to the loading direction (E_{yy}) at 3% global strain where (a) shows the entire region captured by the telecentric lens and (b) the segmented region calculated by imposing EBSD analysts on the DIC analysis.	159
Figure 6.23: Initial image collected for the DIC analysis for the tensile tests of pure nickel with the EBSD map region superimposed. The hardness indent used to align the EBSD map to the DIC data is seen at (2000,1000). (b) Shows a close-up image of one of the hardness indents.	160

Figure 6.24: Strain maps collected through DIC for pure nickel at 3% global strain showing the (a) total area maximum nominal strain and (b) the maximum principal strain for the area within the EBSD analysis.	162
Figure 6.25: Strain map for pure nickel in the loading direction (E_{xx}) at 3% global strain where (a) shows the entire region captured by the telecentric lens and (b) the segmented region calculated by imposing EBSD analysts on the DIC analysis.	163
Figure 6.26: Strain map for pure nickel perpendicular to the loading direction (E_{yy}) at 3% strain where (a) shows the entire region captured by the telecentric lens and (b) the segmented region calculated by imposing EBSD analysts on the DIC analysis.	164
Figure 6.27: EBSD map showing only grains within 7.5 degrees of the 111 crystallographic orientation for the SS316 specimen. Here the loading direction is parallel to the x-axis.	165
Figure 6.28: EBSD map showing only grains within 7.5 degrees of the 220 crystallographic orientation for the SS316 specimen. Here the loading direction is parallel to the x-axis.	166
Figure 6.29: EBSD map showing only grains within 7.5 degrees of the 200 crystallographic orientation for the SS316 specimen. Here the loading direction is parallel to the x-axis.	166
Figure 6.30: EBSD map showing only grains within 7.5 degrees of the 111 crystallographic orientation for the INVAR specimen. Here the loading direction is parallel to the x-axis.	167
Figure 6.31: EBSD map showing only grains within 7.5 degrees of the 220 crystallographic orientation for the INVAR specimen. Here the loading direction is parallel to the x-axis.	168
Figure 6.32: EBSD map showing only grains within 7.5 degrees of the 200 crystallographic orientation for the INVAR specimen. Here the loading direction is parallel to the x-axis.	168
Figure 6.33: EBSD map showing only grains within 7.5 degrees of the 111 crystallographic orientation for the pure nickel specimen. Here the loading direction is parallel to the x-axis.	169
Figure 6.34: EBSD map showing only grains within 7.5 degrees of the 220 crystallographic orientation for the pure nickel specimen. Here the loading direction is parallel to the x-axis.	170
Figure 6.35: EBSD map showing only grains within 7.5 degrees of the 200 crystallographic orientation for the pure nickel specimen. Here the loading direction is parallel to the x-axis.	171
Figure 6.36: Histogram plot for the E_{xx} strain values recorded for SS316 at 3% global strain for the 111, 220 and 200 subsets of grains.	172
Figure 6.37: Histogram plot for the E_{yy} strain direction values recorded for SS316 at 3% global strain for the 111,220 and 200 subsets of grains.	172
Figure 6.38: Histogram plot for the maximum principal strain values recorded for SS316 at 3% global strain for the 111, 220 and 200 subsets of grains.	173
Figure 6.39: Histogram plot for the E_{xx} strain values recorded for INVAR at 3% global strain for the 111,220 and 200 subsets of grains.	174
Figure 6.40: Histogram plot for the E_{yy} strain values recorded for INVAR at 3% global strain for the 111, 220 and 200 subsets of grains.	174
Figure 6.41: Histogram plot for the maximum principal strain values recorded for INVAR at 3% global strain for the 111,220 and 200 subsets of grains.	175
Figure 6.42: Histogram plot for the E_{xx} strain direction values recorded for pure nickel at 3% global strain for the 111,220 and 200 subsets of grains.	175
Figure 6.43: Histogram plot for the E_{yy} strain direction values recorded for pure nickel at 3% global strain for the 111,220 and 200 subsets of grains.	176

Figure 6.44: Histogram plot for the maximum principal strain values recorded for pure nickel at 3% global strain for the 111, 220 and 200 subsets of grains.	176
Figure 6.45: The SS316 Exx strain for regions with a high concentration of grains with the 111, 220 and 200 orientations from the start of the test to 3% strain, where (a) best fit scale and (b) is the relative scale.	179
Figure 6.46: The SS316 Eyy strain for regions with a high concentration of grains with the 111, 220 and 200 orientations from the start of the test to 3% strain, where (a) best fit scale and (b) is the relative scale.	180
Figure 6.47: The INVAR Exx strain for regions with a high concentration of grains with the 111, 220 and 200 orientations from the start of the test to 3% strain where (a) best fit scale and (b) is the relative scale.	182
Figure 6.48: The INVAR Eyy strain for regions with a high concentration of grains with the 111, 220 and 200 orientations from the start of the test to 3% strain where (a) best fit scale and (b) is the relative scale.	183
Figure 6.49: The pure nickel Exx strain plot for regions with a high concentration of grains with the 111, 220 and 200 orientations from the start of the test to 3% strain where (a) best fit scale and (b) is the relative scale.	185
Figure 6.50: The pure nickel Eyy strain plot for regions with a high concentration of grains with the 111, 220 and 200 orientations from the start of the test to 3% strain.	186
Figure 7.1: Strain data results collected for SS316 for the 111, 220 and 200 crystallographic orientation subsets. (a) Lattice strain data collected through in situ neutron diffraction for the longitudinal and transverse direction, (b) Difference in KAM values between the deformed and undeformed regions of the SS316 specimen, (c) and (d) the transverse and longitudinal (respectively) in situ HR-DIC strain data.	195
Figure 7.2: Strain data results collected for pure nickel for the 111, 220 and 200 crystallographic orientation subsets. (a) Lattice strain data collected through in situ neutron diffraction for the longitudinal and transverse direction, (b) Difference in KAM values between the deformed and undeformed regions of the pure nickel specimen, (c) and (d) the transverse and longitudinal (respectively) in situ HR-DIC strain data.	196
Figure 7.3: Strain data results collected for INVAR for the 111, 220 and 200 crystallographic orientation subsets. (a) Lattice strain data collected through in situ neutron diffraction for the longitudinal and transverse direction, (b) Difference in KAM values between the deformed and undeformed regions of the INVAR specimen, (c) and (d) the transverse and longitudinal (respectively) in situ HR-DIC strain data.	198

VI. List of Tables

<i>Table 2.1: Examples of SFE values for FCC metals.</i>	<i>9</i>
<i>Table 4.1: The chemical composition of the SS316 samples used in this test.</i>	<i>49</i>
<i>Table 4.2: The chemical composition of the INVAR samples used in this test.</i>	<i>50</i>
<i>Table 4.3 Specimen grinding guidelines used in the preparation of the specimen for EBSD analysis</i>	<i>56</i>
<i>Table 4.4: Specimen polishing guidelines used in the preparation of the specimen for EBSD analysis</i>	<i>56</i>
<i>Table 4.5: Shows the EBSD measurement parameters used.</i>	<i>56</i>
<i>Table 4.6: Specimen dimensions (an average taken from 8 measurements) for the dynamic elastic modulus. ..</i>	<i>58</i>
<i>Table 4.7: The grain size measurements for the SS316, INVAR and pure nickel samples.</i>	<i>61</i>
<i>Table 4.8: The dynamic elastic modulus results for the SS316, INVAR and pure nickel.</i>	<i>61</i>
<i>Table 4.9 The fitting parameters used in obtaining the best fit between the EPSC model and the experimental data.</i>	<i>68</i>
<i>Table 5.1 This table shows the number of grains identified by the MATLAB for the specified crystallographic orientations</i>	<i>98</i>
<i>Table 5.2: Pole figures for the undeformed and deformed regions of the SS316 specimen, where the grain subsets are defined to be within 7.5 degrees of the (a) 111, (b) 220, and (c) 200 orientations. The out of plane direction is the loading direction.</i>	<i>100</i>
<i>Table 5.3: Pole figures for the undeformed and deformed regions of the INVAR specimen, where the grain subsets are defined to be within 7.5 degrees of the (a) 111, (b) 220, and (c) 200 orientations. The out of plane direction is the loading direction.</i>	<i>103</i>
<i>Table 5.4: Pole figures for the undeformed and deformed regions of the pure nickel specimen, where the grain subsets are defined to be within 7.5 degrees of the (a) 111, (b) 220, and (c) 200 orientations. The out of plane direction is the loading direction.</i>	<i>105</i>
<i>Table 6.1: Duration of in situ HR-DIC tensile tests.</i>	<i>142</i>
<i>Table 6.2: Grain sizes for the materials used in the HR-DIC analysis.</i>	<i>148</i>
<i>Table 6.3: The image number where each sample reached 3% global strain.</i>	<i>149</i>
<i>Table 6.4: Regions selected from EBSD data for SS316 which contain the largest concentration of either 111, 220 or 200 orientation subsets.</i>	<i>177</i>
<i>Table 6.5: Regions selected from EBSD data for INVAR which contain the largest concentration of either 111, 220 or 200 orientation subsets.</i>	<i>181</i>
<i>Table 6.6: Regions selected from EBSD data for pure nickel which contain the largest concentration of either 111, 220 or 200 orientation subsets.</i>	<i>184</i>

VII. List of Abbreviations

BCC	Body Centred Cubic
CPFEM	Crystal Plasticity Finite Element Model
CRSS	Critically Resolved Shear Stress
DIC	Digital Image Correlation
EBSD	Electron Backscatter Diffraction
EDM	Electric Discharge Machining
EPSC	Elastic-Plastic Self-Consistent
FCC	Face Centred Cubic
FWHM	Full Width at the Half Maximum
GND	Geometrically Necessary Dislocations
HCP	Hexagonal Close Packed
HR-DIC	High Resolution Digital Image Correlation
ND	Neutron Diffraction
SEM	Scanning Electron Microscopy
SFE	Stacking Fault Energy
SS316	316 Stainless Steel
TEM	Transmission Electron Microscopy
TOF	Time of Flight

1. Introduction

1.1. Motivation

Finding clean and sustainable energy sources is essential in fighting climate change. Nuclear energy will play a vital role in supplying reliable, carbon-neutral energy to the UK. However, to ensure reliability it is essential to determine the service lifetime of nuclear reactors. The lifetime of a nuclear power plant is largely influenced by the capacity of the materials in its constituent components to withstand degradation (1–4). To build nuclear plants and have confidence that they will last, it is important to understand the materials used within them. Throughout a nuclear reactor's life, its constituent components are subjected to high stresses in high-pressure and temperature environments. The effects of these harsh conditions can be seen within the microstructure of a material. Therefore, when predicting material failure, it is important to thoroughly understand deformation at the microstructural level (5).

Nuclear power plants use metallic alloys throughout all areas of the process, this is due to their high-temperature mechanical properties and corrosion resistance. For example, the polycrystalline stainless steel 316 (SS316) is found in the boiler sections of Advanced Gas Cooled Nuclear Reactors (6). Polycrystals consist of multiple grains; within each of these grains the crystallographic orientation is uniform. Compared to a single crystal, which has highly anisotropic mechanical properties which are dependent on the orientation, a polycrystalline structure can be isotropic on the large-scale if all grains are randomly orientated. However, at the micro-scale, anisotropic deformation occurs with polycrystalline structures due to a mismatch in deformation rates caused by neighbouring grains containing different crystallographic orientations. Therefore, when the load approaches the yield stress of the material, some grains may begin to deform plastically, while others are still deforming elastically (7), this can lead to residual stresses left within the metal once the load is removed (8). Intergranular stresses forming between grains will affect the damage development within the material (9,10). Therefore, it is important to understand the influence that anisotropic deformation has on both microscopic and macroscopic scales, to assess, understand and potentially improve the material's mechanical properties (11).

In recent years, non-destructive *in situ* neutron diffraction has extensively been used to evaluate the stress-strain response for polycrystalline materials (3,9,12,13). Neutron diffraction utilises Bragg's law of diffraction by diffracting a beam of neutrons off the crystal lattice. For a fixed wavelength, only the grains orientated to satisfy Bragg's law will diffract, therefore only a subset of grains will contribute to the diffraction signal. Due to the penetration depth that uncharged neutrons can reach

within a metallic specimen, strain data can be collected from within the bulk of a material, sampling a large number of grains. However, neutron diffraction does not provide information on the influence of spatial strain effects caused by anisotropic deformation between neighbouring grains of different orientations. Additionally, neutron diffraction is only available at a limited number of national facilities, which limits the availability of this technique.

Digital image correlation (DIC) is an optical strain measurement technique that compares deformed images to an original, reference image to produce strain data throughout loading. DIC can be used on a range of different length scales, for example, by using scanning electron microscope (SEM) images, microscale strain data can be recorded. Typically, when DIC is used to measure microscale strain, it is referred to as high-resolution digital image correlation (HR-DIC). Previous works have used this to relate microscale features to local strain concentrations (14–18). This can be achieved by imposing HR-DIC strain data directly onto electron backscatter diffraction (EBSD) maps, the strain data can then be segmented into specific grains and related to spatial features of the material. Yet, the statical aggregate of the data collected through HR-DIC has not been investigated thoroughly.

An alternative to experimental measurement techniques is modelling material deformation. This can be advantageous, particularly for modelling specific environments components will experience in their lifetime. However, this can be a difficult and time-consuming process, especially for alloys with complex chemical compositions with multiple phases. Therefore, a method of simplifying material modelling is replacing a complex alloy with another alloy with a simplistic chemical composition yet still behaves in the same way during loading. Collaborators have suggested a good material analogy for SS316 is pure nickel, due to the high nickel content in SS316 and both materials having FCC crystallographic structures. However, SS316 has a low stacking fault energy (SFE), whereas nickel has a high SFE, these are intrinsic properties of the material that influences the mechanisms of deformation (19). Thus, this project proposes an alternative, the binary alloy INVAR (FeNi36), which has both a low SFE and an FCC microstructure without compromising on simplicity as it only consists of two elements.

This project investigates the effect of SFE on the deformation mechanics of three materials: SS316, INVAR and pure nickel. The influence of SFE was used as a method of comparing the strain measurement capabilities of aggregate HR-DIC to neutron diffraction. Historically, HR-DIC has been used to relate strain data to specific microstructural components, whereas neutron diffraction is a well-researched technique for providing bulk strain data for distinct grain orientations within a specimen. To extend the HR-DIC technique to investigate the aggregate strain data, 2 mm by 2 mm EBSD maps were superimposed on DIC data. To compare these results to neutron diffraction, the

EBSD maps were segmented into the same orientation subsets recorded by the neutron diffraction experiments. As neutron diffraction records elastic strain, whereas DIC records both elastic and plastic strain, post-mortem EBSD misorientation analysis was used to determine plastic strains within the neutron diffraction specimens. Further verification of these techniques came from the elastic-plastic self-consistent (EPSC) model which models elastic and plastic deformation.

1.2. Aim and Objectives

When testing alloys in safety-critical environment it is essential to predict failure. Failure can originate from strains at all length scales, therefore grain-scale strain measurements are important to yield an accurate prediction. Neutron diffraction is a well-established technique in measuring grain-scale strains on a bulk scale. However, this technique is only available at a limited number of national facilities and can be costly to perform. HR-DIC is another grain-scale strain measurement technique that in previous studies (15,20–22) has been used to relate strain concentrations to microstructural features of a material's surface, but relating these strains to the bulk of the material has not been explored. This project aims to collect aggregate strain data using HR-DIC and to assess to what extent the results are comparative to neutron diffraction. To achieve this, the following steps were implemented:

- Directly compare stress-strain data collected through HR-DIC to that of neutron diffraction for three samples with different SFE.
- Compare the EPSC model to both neutron data and HR-DIC as a method of corroborating the experimental data.
- Study EBSD metrics to determine whether the onset of plastic deformation can be determined and whether this aligns with the onset of plastic deformation in the *in situ* neutron diffraction results.
- HR-DIC is used to investigate the influence of SFE on deformation mechanics as it is a well-verified fundamental phenomenon.

1.3. Outline of the Thesis

This thesis will begin by discussing the relevant literature to this project. This includes the mechanisms of deformation that occur in single crystals which are used as a vehicle for describing polycrystalline deformation. In addition, this project utilises the phenomenon of the influence of stacking fault energy on deformation, therefore, this will be covered within this section. The literature review also includes a discussion of different deformation models as the elastoplastic self-consistent model (EPSC) is used in this project as a method of corroborating the experimental data.

Strain measurement techniques play a significant role in this project and therefore will be covered in detail within this section. Three original results chapters follow, which include the methodology, results and discussion which are relevant to the techniques used in each section. The first results chapter shows the results of the *in situ* neutron diffraction tensile test experiments with the complimentary EPSC model results presenting the influence of SFE on deformation behaviour. The second chapter presents the EBSD metrics performed on the spent neutron diffraction tensile test specimens, showing the accumulation of plastic strain. The third chapter presents the results of the *in situ* HR-DIC tensile tests for the SFE tests. The dissertation ends with a synoptic discussion and conclusions chapter where the key findings of the PhD project are reiterated, this is followed by a future work chapter which includes notes on how future projects could further investigate aggregate HR-DIC data.

2. Literature Review

2.1. Overview

The primary aim of this thesis is to investigate and evaluate the aggregate strain data collected using HRDIC on a large area of the surface of a material. This literature review will therefore first cover the fundamentals of deformation mechanics for both single-crystal and polycrystalline metals. It will also include an explanation of the primary fundamental phenomena used in this thesis (the influence of stacking fault energy on deformation mechanics) as a method of testing HR-DIC's effectiveness. Following this, the theory behind EBSD will be discussed in addition to how it is used to characterise the crystallographic structure of metals and alloys. Then, techniques for modelling polycrystalline deformation are discussed and compared. Finally, this chapter will review the experimental methods used for measuring strain in polycrystals.

2.2. Crystallographic Structure

In 1912, Max Laue presented the first observation, which was produced by his colleagues Walter Friedrich and Paul Knipping (23), of the diffraction of X-rays by a crystal (24) – the mineral zinc sulphide (ZnS). Laue and his colleagues had taken the ZnS X-ray pattern and assumed that the X-ray source was polychromatic (comprising of six or seven distinct wavelengths) and that structure consisted of a three-dimensional structure of tiny cubes, with zinc and sulphur occupying alternate corners (24). Later that year, Lawrence Bragg made two important proposals about Laue's work which explained the ellipsoidal shape of some of the diffraction spots and how some spots had different intensities (25). Firstly, Bragg suggested that Laue's results arose from the reflection of a continuous range of X-rays wavelengths by planes of atoms within the crystal, this interpretation led to Bragg's law of diffraction (further discussion can be found in section 2.4.1). Secondly, Laue's diffraction patterns of ZnS were characteristic of structures where atoms are present in the centre of the faces of each cube and not only at the edges – a face-centred lattice (24).

Solid crystalline material is one in which the atoms are situated in a repeating or periodic array over large atomic distances (26). Some of the properties of crystalline solids depend on the crystal structure of the material and therefore are influenced by the way atoms, ions and molecules are spatially arranged (26). Thus, the crystalline structure of the material influences the fundamental mechanical properties of the material. In metallic crystal structures, the unit cell is the smallest repeating unit within the crystal which has the full symmetry of the entire crystal structure (27). These unit cells repeat throughout the structure and form the building blocks of the crystallographic

structure. Examples of common metallic unit cells are the face-centred cubic (FCC), the body-centred cubic (BCC) and the hexagonal close-packed (HCP) which can be seen in Figure 2.1. The lengths of the principal axes, or edges, and the angles between them are defined as the cell parameters.

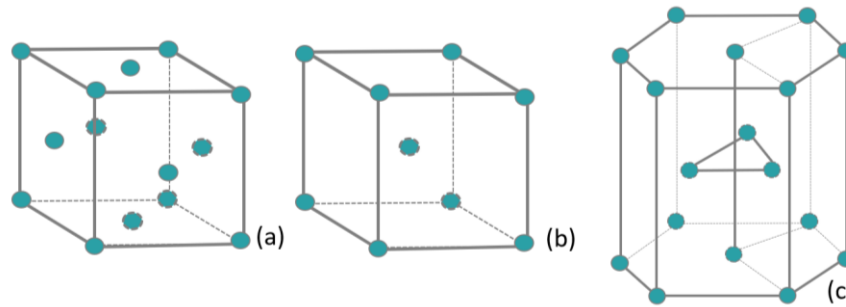


Figure 2.1: Schematic of some of the common unit cells for metallic crystalline structure (a) face-centred cubic (FCC), (b) body-centred cubic (BCC), and (c) hexagonal close-packed (HCP).

2.2.1. Defects

All crystal structures contain large numbers of various defects or imperfections (26). Defects can locally disrupt the regular arrangement of the atoms (28). They come in the form of point, line, planar, or volume defects, and these significantly modify the properties of crystalline solids.

2.2.1.1. Dislocations

Dislocations are line defects and are an important class of defects that impact the mechanical properties of crystalline solids. A dislocation is defined as a linear crystallographic defect within a crystal structure which contains an abrupt change in the arrangement of atoms (26). Dislocations can be of edge type, screw type or a mixture of these types (28). A schematic of an edge dislocation can be found in Figure 2.2. Once an external shear load is applied, edge dislocations will move parallel to the direction of the shear stress while screw dislocations will move in a direction that is perpendicular to it.

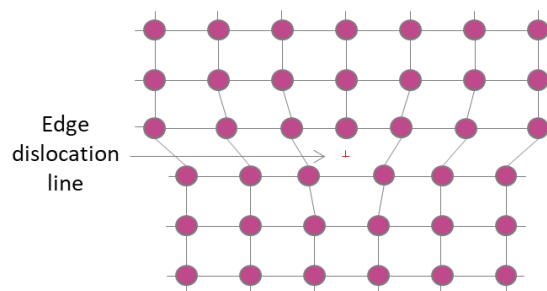


Figure 2.2: Two-dimensional schematic of an edge dislocation and its effect on the neighbouring atoms.

At stress levels significantly lower than the stress required to break a bond, dislocations can move to allow atoms to slide over each other, known as slip. The crystalline order is restored on either side of the dislocation but the atoms on one side have moved by one position. A partial dislocation forms when the crystalline order is not fully restored, this leaves behind a stacking fault in the crystalline structure.

2.2.1.2. Stacking Faults

Stacking faults are planar defects that occur in crystalline materials (26). As crystalline materials consist of repeating patterns of layers of atoms, errors can occur in the sequencing of these layers and are known as stacking faults. The most common stacking fault examples are found in close-packed crystal structures, such as face-centred cubic (FCC) with a stacking order ABCABCABC and a hexagonal close-packed (HCP) structure with the stacking order ABABABAB. Both FCC and HCP have the same beginning pattern of AB but there are two close-packed positions for the third row, this is either A again or C. Therefore, a stacking fault can reflect a local deviation from one of the close-packed stacking sequences to the other one. This is shown in Figure 2.3, with a perfect FCC crystal (a) with a sequence ABCABCABC and a stacking fault (b), which has the sequence ABCABABCA. Usually, only one- two- or three-layer interruptions in the stacking sequence are referred to as stacking faults. Stacking faults are in a higher energy state than the regular arrangement of atoms and can be quantified by the formation enthalpy per unit area called stacking fault energy.

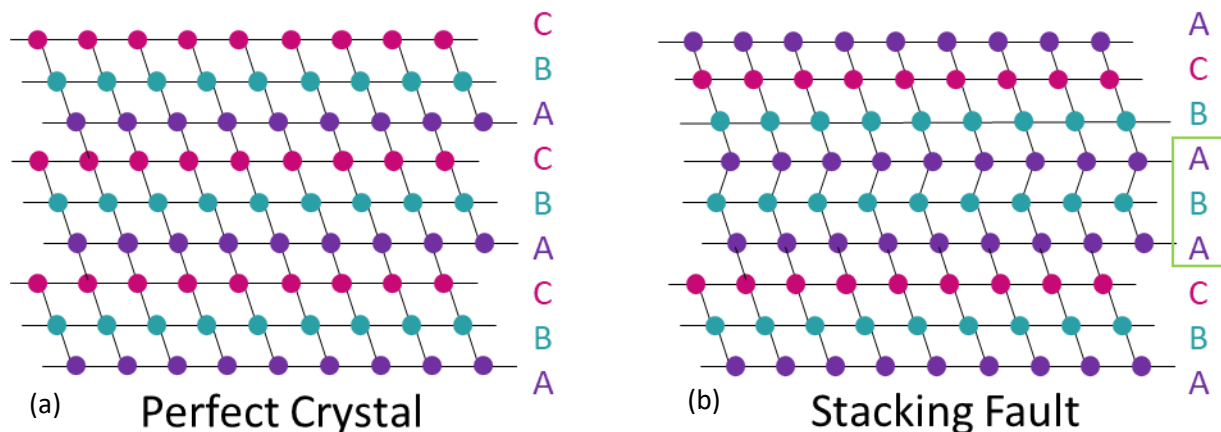


Figure 2.3: Diagram showing (a) a perfect FCC crystal without a stacking fault and (b) a crystal which contains a stacking fault.

The width of a stacking fault is determined by the balance between the repulsive force between two partial dislocations and the attractive force due to surface tension. The equilibrium width of a stacking fault is determined by the stacking fault energy (SFE). The SFE is an intrinsic mechanical

property which influences the mechanisms of deformation (19). When the SFE of a metal or alloy is high, the dissociation of a perfect dislocation into two partial dislocations is unlikely, therefore they deform by dislocation glide or cross-slip. Whereas, for low SFE materials are more likely to twin and create partial dislocations (29), this is because low SFE materials have wider stacking faults making it more difficult for the material to cross-slip. Additionally, due to the difference in deformation mechanics, materials with a low SFE also tend to experience work hardening following yield, whereas high SFE materials do not experience this (30). Kang et al. (31) studied the influence of adding Al in high-manganese twinning-induced plasticity (TWIP) steels, here it was seen that, by increasing Al from 0 wt.% to 2 wt.%, the SFE increased from 17 mJ/m² to 37 mJ/m². Figure 2.4 shows the influence that this increase in SFE had on the deformation behaviour, from the stress-strain curves the 2% Al specimen shows lower tensile strength and work hardening with no serration compared to the 0% Al specimen. Furthermore, the 0% Al specimen shows there to be more twin formation than the 2% Al specimen, which is to be expected of materials with low SFE. Austenitic stainless steels, such as stainless steel 316, typically have low-to-moderate SFE values (32), whereas pure metals such as nickel have a high SFE, examples of SFE values can be found in Table 2.1 (33).

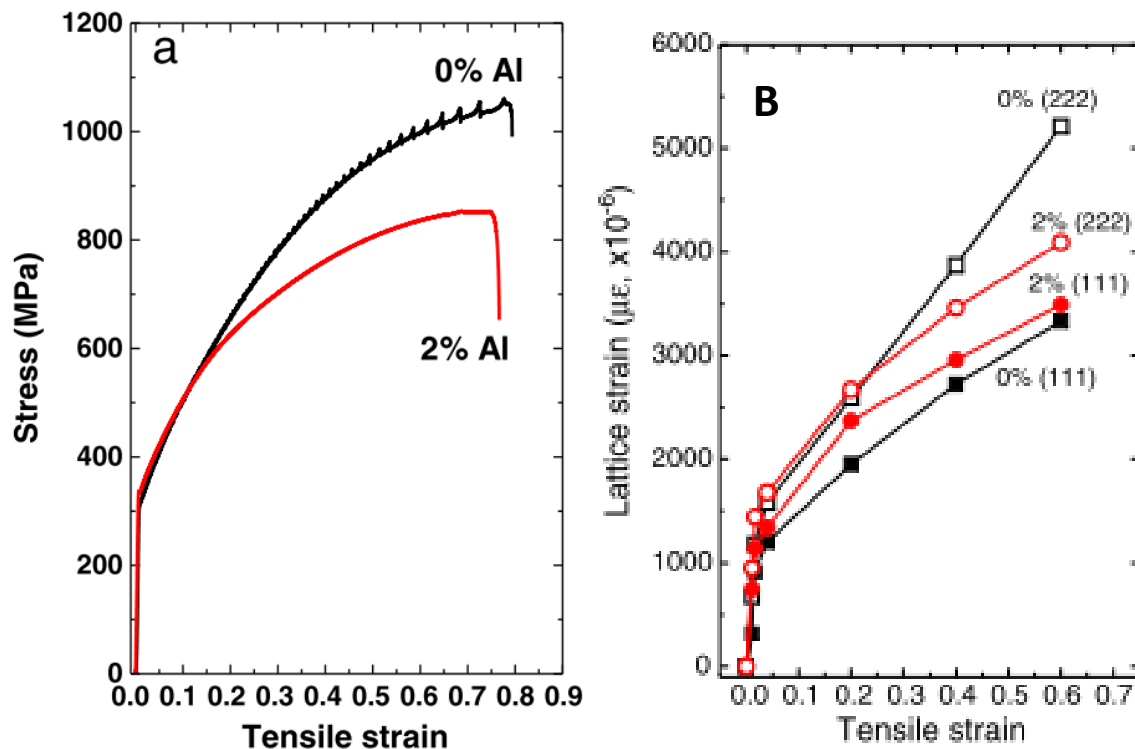


Figure 2.4: (a) Stress-strain curve for 0 (low SFE) and 2 (high SFE) wt.% Al TWIP steels and (b) Lattice strains of the (111) and (222) diffractions (The error bar is smaller than the symbol size) (31).

Table 2.1: Examples of SFE values for FCC metals.

Metal	Stacking Fault Energy (mJ/m ²)
Brass	<10 (33)
Stainless Steel	<10 (33)
Fe-Ni alloys (e.g., INVAR)	~15 to 60 (34)
Cu	~90 (33)
Ni	~200 (33)
Al	~250 (33)

2.3. Deformation in FCC Metals

Deformation of a material refers to the modification of the shape of a body due to the application of an external load. Upon application of increasing uniaxial load, polycrystalline materials undergo elastic deformation followed by plastic deformation. If material is deformed within the elastic region, the atoms in the crystalline structure will return to their original positions once the load is removed. However, plastic deformation causes the bonds between atoms to stretch and the lattice planes to shear. For lattice planes to shear, dislocation movement is needed which requires the breaking and joining of atomic bonds. Therefore, once the load is removed, the material cannot go back to its original shape.

Although this project looks solely at polycrystalline metals and alloys, to understand the influence of deformation on these materials, it is first important to understand single-crystal mechanical behaviour. This is because polycrystalline deformation behaviour is a complex combination of all individual grain behaviours, and at the grain scale, this is essentially a series of constrained single crystals.

2.3.1. Single-Crystal Deformation Mechanics

When an external load is applied to a metal, the spacings between lattice planes within the crystalline structure get stretched or compressed and elastic deformation occurs. When the load surpasses the stress needed to permit parallel lattice planes to slip over one another, causing permanent plastic deformation, the yield point has been reached. If the stress required to cause slip is high, twinning might occur as a mechanism that facilitates straining. Twinning is essentially another type of plastic deformation; this is often seen in FCC materials with low stacking fault energies where slip is less favourable.

Slip occurs by the movement of dislocations in the crystalline structure, this can only happen when the shear stress in the slip direction exceeds the critical resolved shear stress (CRSS). The CRSS, τ_C , is the stress above which dislocations can move within the slip plane and this can be determined by

using Schmid's law (35). Figure 2.5 shows a schematic diagram of plastic deformation caused by slip, this diagram shows two sets of orthogonal axes X (1, 2 and 3) and X' ($1'$, $2'$ and $3'$). The X set of orthogonal axes gives the external reference frame in which the components of stress σ_{ij} are specified, whereas X' is chosen so the $1'$ is parallel to the slip direction \mathbf{b} and $3'$ is parallel to the slip plane normal, \mathbf{n} . This means slip will occur when

$$\sigma'_{13} = \tau_c \quad (2-1)$$

where σ'_{ij} is the stress tensor in the X' reference frame. Following the tensor transformation law (36),

$$\sigma'_{13} = \alpha_{1i}\alpha_{3j}\sigma_{ij}, \quad (2-2)$$

where α_{ij} is the direction cosine between the i' and j' axes. To express the unit vectors \mathbf{b} and \mathbf{n} in the X system you get,

$$b_i = \alpha_{1i}, \quad n_j = \alpha_{3j}, \quad (2-3)$$

So, Schmid's Law is written as

$$b_i n_j \sigma_{ij} = \tau_c \quad (2-4)$$

Using the symmetry of the stress tensor, this can also be written as

$$\begin{aligned} \tau_c &= b_i n_j \sigma_{ij} \\ &= \frac{1}{2} (b_i n_j + b_j n_i) \sigma_{ij} \\ &\equiv \alpha_{ij} \sigma_{ij} \end{aligned} \quad (2-5)$$

where the symmetric tensor α_{ij} is called the Schmid tensor.

For a uniaxial load along the 3-axis, only the σ_{33} component of stress is non-zero. In this case, Schmid's law can be written as,

$$\tau_c = \sigma_{33} \cos \phi \cos \lambda \equiv m \sigma_{33} \quad (2-6)$$

where $\cos \phi$ and $\cos \lambda$ are the direction cosines between the tensile axis and the slip direction and the slip plane normal respectively. The slip system which initiates at the lowest tensile yield stress is that with the highest Schmid factor, m .

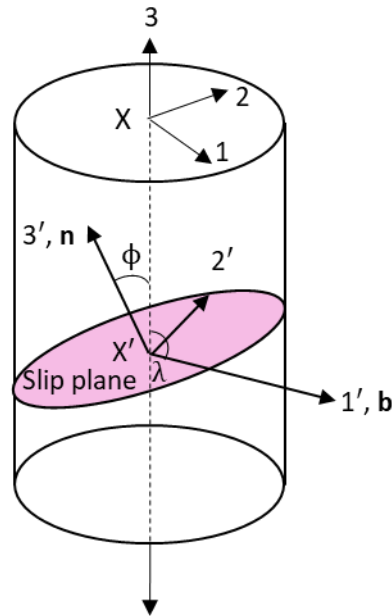


Figure 2.5: Schematic illustrating the formulation of Schmid's law (diagram modified from reference (37)).

The shear stress required to move a dislocation decreases as the spacing between lattice planes increases. (38). Therefore, slip occurs within the closest packed planes as they have the highest inter-planar spacing (37). This means the crystal planes in which slip occurs are parallel to each other and well-defined; the direction of slip within these planes is also consistent. The combination of the slip plane and the slip direction gives the slip system. For FCC crystals, the close-packed direction within the unit cell is found along the diagonals of each face, meaning the preferred slip systems are the twelve $\{111\} \langle 110 \rangle$ systems. When applying an external load to a single crystal of FCC structured material, the shear stress will increase in each of the available slip systems, until the CRSS is reached in one of the systems. The system with the highest Schmid factor will activate first. This is the first system for slip to occur, but if the load is increased further other slip systems may activate.

2.3.2. Polycrystalline Deformation Mechanics

Polycrystalline materials are essentially an aggregate of single crystals with various crystallographic orientations. Polycrystals are made up of grains, within which the orientation of the crystallographic texture is relatively constant; the interface that separates adjoining grains of different crystallographic orientations is known as the grain boundary (26). Due to the presence of grains, polycrystals have the intrinsic property known as texture (39). This is determined by the percentage of grains which are aligned within a given orientation. For a polycrystal where all grains are perfectly random, the texture will be zero, but if the material has a preferred orientation a weak, moderate, or strong texture could be present.

In addition to slip (discussed in section 2.3.1), polycrystalline FCC materials can deform by twinning. However, unlike dislocation slip-controlled plasticity which is understood in great detail, twinning is understood to a lesser extent, particularly its impact on work hardening (40) and as a result is the focus of much research in recent years. Twins occur when there are not enough slip systems to accommodate deformation or when the material has a low SFE due to dislocation mobility decreasing as SFE decreases. When a material undergoes twinning during deformation, localised stress concentrations can form.

As with Elastic deformation in single crystals, deformation is highly dependent on the orientation of the crystalline structure concerning its loading axis, this can be seen by considering Schmid's law (Figure 2.5). Hence, for polycrystalline structures, elastic deformation is likely to be occurring at different rates dependent on the individual grain's crystallographic orientation. Grains do not usually come apart or open up even when subjected to an external load, therefore, they are strongly constrained to the shape assumed by their neighbours (26). With an increasing external applied load, plastic deformation mechanisms, such as slip or twinning, may begin to occur in grains which are orientated favourably whereas others may continue to deform elastically. Figure 2.6 shows a schematic of the localised variations in strain caused by the loading of a randomly orientated polycrystalline microstructure (41), even as the overall macroscale stress (σ_I) remain constant throughout the material, fluctuations occur on the microscale due to the variations in the intergranular (σ_{II}) and intragranular (σ_{III}) stresses. This anisotropy in deformation can lead to intergranular strains resulting in residual stresses (41), which can potentially lead to failure occurring prematurely (2).

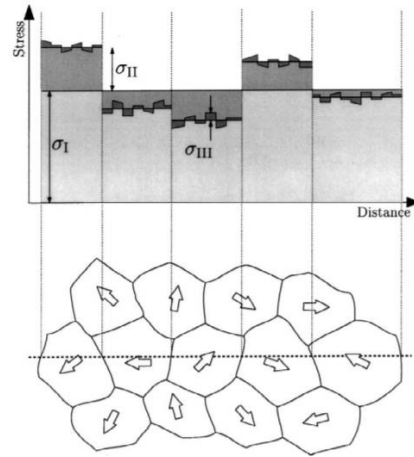


Figure 2.6: A Schematic of a randomly orientated polycrystalline microstructure which highlights the localised variations in micro strains at different length scales (on the macroscale (σ_I), intergranularly (σ_{II}) and intragranularly (σ_{III})) (41).

Like the Schmid factor for single crystals, the Taylor factor can be used to predict deformation in polycrystalline materials. The Taylor factor differs from the Schmid factor as it uses an isostrain assumption (strain assumed to be constant throughout), whereas the Schmid factor is based on the isostress assumption (stress assumed to be constant throughout) (42). The Taylor factor of a grain is a prediction of the amount of work required to deform that grain. As all grains are assumed to be under the same strain, a higher Taylor factor indicates that a greater amount of work should be necessary to deform that grain (21,43,44).

2.3.3. Summary

The complexity of polycrystalline deformation arises from the microstructure essentially consisting of many constrained single crystals, this results in several governing factors leading to the stress state of a given grain within the polycrystalline structure. The factors include the elastic strain of the grain, the Schmid factor of the grain, and the elastic and plastic anisotropy between the grain in question and its neighbours.

2.4. Microstructural Features Analysis

A key part of understanding a crystalline material, and how it will respond to an applied load, is determining its microstructure. Various techniques can be used to characterise the microstructure including x-ray diffraction (XRD) (45), neutron diffraction and/or electron diffraction in a transmission electron microscope (TEM) (46), spatially resolved acoustic spectroscopy (SRAS) (47) and electron backscatter diffraction (EBSD) (15,48) in a scanning electron microscope (SEM). The choice of which technique to choose depends on numerous factors, including spatial resolution, area/volume analysed, and whether the measurements are static or dynamic.

This project will use EBSD, which is a technique that can be used to analyse crystalline microstructures. EBSD can provide information about the structure, crystal orientation, phase, or strain in the material. Metallurgists have widely adopted EBSD due to the accessibility of SEMs, the speed of data acquisition, the ease of sample preparation and its ability to produce complementary information about the microstructure on a submicron scale (48,49). An SEM uses a focused electron beam which scatters off the surface of a specimen producing four different types of electrons; x-rays, secondary electrons, backscattered electrons and auger electrons (1). Generally, secondary electrons are used for imaging the surface of a specimen whereas backscattered electrons are used for analysing the crystallographic structure (1).

2.4.1. EBSD Working Principles

This section will briefly discuss the basic working principles of EBSD, more detail can be found in the following literature (48,50–52). EBSD analysis uses Bragg's law of diffraction, which is shown in Equation (2-7). When an incident electron beam interacts with an array of atoms in a crystallographic material, scattering happens in all directions forming wave fields. These wave fields interfere causing constructive interference when Bragg's law is satisfied.

$$\lambda = 2d_{hkl} \sin \theta_{hkl} \quad (2-7)$$

Where λ is the wavelength of the incident beam, d_{hkl} is the inter-planar spacing between lattice planes and θ_{hkl} is the angle of incidence of the beam (see Figure 2.7).

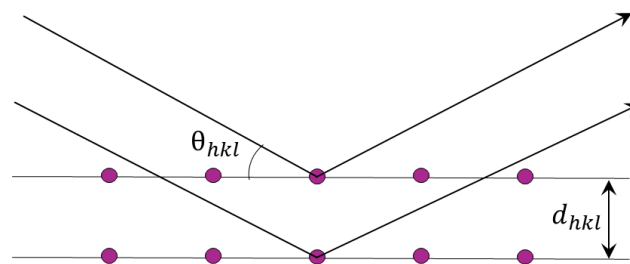


Figure 2.7: Schematic diagram showing Bragg's Law of Diffraction

EBSD analysis utilises Bragg's law of diffraction to produce EBSD patterns. These patterns are known as Kikuchi patterns (53) and are generated by backscatter diffraction of a stationary beam of high-energy electrons. The Kikuchi patterns are directly related to the orientations of the reflecting lattice. When an electron beam enters a crystalline solid, the electrons are scattered in all directions meaning that some of the electrons will arrive at each lattice plane at Bragg's angle (50). The electrons which arrive at Bragg's angle produce a strong, reinforced beam which yields the Kikuchi

bands. The patterns appear as a regular arrangement of parallel bands or lines on a continuous background, which can be seen in Figure 2.8 (49).

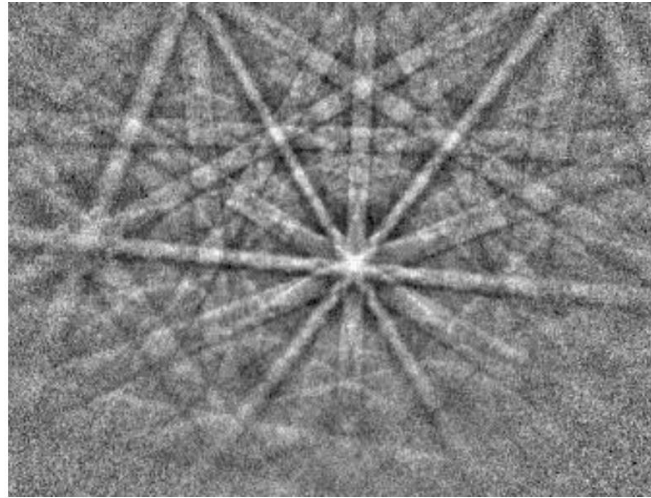


Figure 2.8: Backscatter Kikuchi pattern of Type 316H austenitic stainless steel at 20keV (49).

EBSD detectors use a phosphor screen to capture Kikuchi patterns which are located within the vacuum chamber of an SEM (54). The phosphor screen then transmits the Kikuchi pattern to a camera (52), which typically uses a charge-couple device (CCD) as a sensor. To analyse the output patterns, a computer and dedicated software are used (52). Typically, samples are mounted at a 70° angle to the electron beam inside the SEM chamber, which optimises both the contrast in the diffracted pattern and the percentage of electrons which are scattered from the sample. A schematic of the principal units required for electron backscatter diffraction can be found in Figure 2.9. The process uses an electron beam to scan the surface of the material, taking point-by-point measurements, and producing Kikuchi patterns at each point. A database is used to preselect the material and unit cell structure before the acquisition, the diffraction patterns collected at each point are compared to the diffraction pattern data in the database, and from this the orientation can be determined at each point.

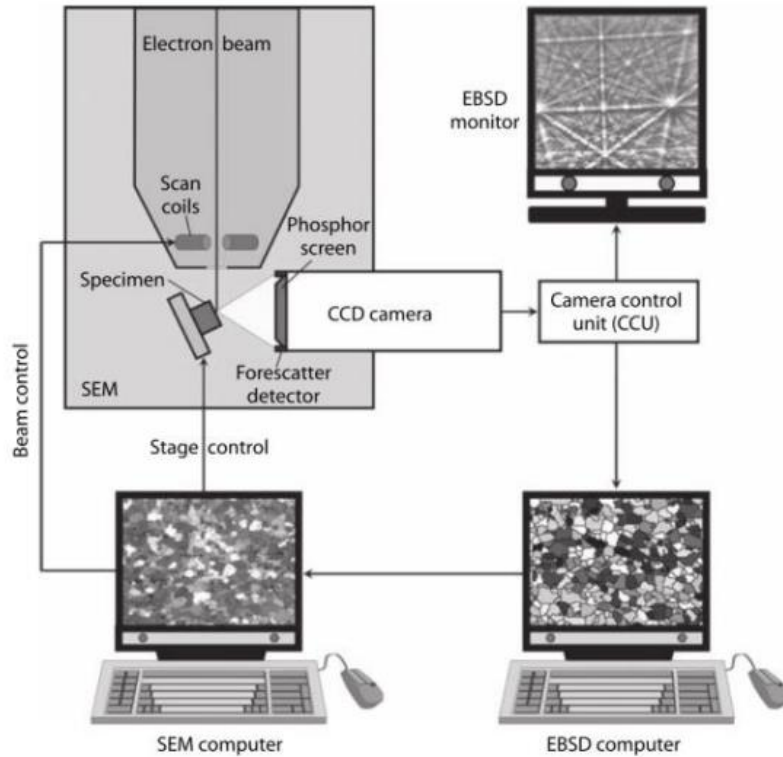


Figure 2.9: Schematic of principal components of electron backscatter diffraction observation (48).

EBSD maps of lattice orientation can be produced by scanning the surface of a material and collecting EBSD patterns at defined intervals, these are then interpreted by the EBSD software to identify the distinct change in crystallographic orientation which indicates a grain boundary, for example, a difference greater than 15 degrees. These EBSD maps can show the size and orientation of the individual surface grains. The resolution of the EBSD map produced is dependent on the spacing between each point measurement made in a square or hexagonal grid (55), this is known as the step size. Fractionally smaller changes in the crystallographic orientation are typically equated to fluctuations in plasticity within the grain.

2.4.1.1. Effect of strain on EBSD patterns

Grains are typically described as a region in which the orientation is constant, however in reality the orientation can vary in a continuous or discontinuous manner. This variation of orientation within a grain is known as orientation perturbation, spread or gradient. When these perturbations occur close to interfaces and deformed structures, they can echo the distribution of strain (50). These regions of strain cause local stress concentrations which affect EBSD patterns (48,51). The impact of these changes can be used to determine the strain, this method will be discussed in section 2.6.1.1.

Elastic strain

The uniaxial elastic strain of a single crystal can cause a change in one of the cell parameters which results in a shift in the pattern in one of the zone axis directions along with a change in the separation of the diffraction lines (see Figure 2.10) (51). However, recorded elastic strain in most real materials is very small, equivalent to a shift of only one or two pixels in the zone axis positions in the diffraction patterns. Additionally, if the crystal bends during elastic deformation, the pattern quality will further degrade (51). This makes it difficult to measure elastic strain using EBSD as the changes in the diffraction pattern are substantially small.

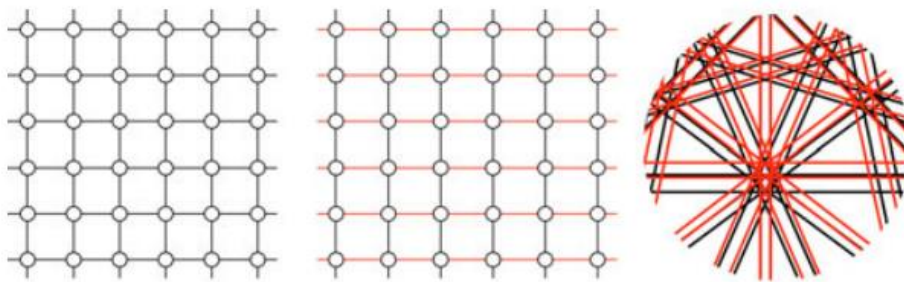


Figure 2.10 A crystal lattice which has been strained to 11% uniaxially in the horizontal direction and a schematic overlay of the patterns with strain (red) and without (black) (51).

Plastic Strain

Plastic strain can degrade the quality of diffraction patterns, this is why it is crucial to prepare the sample surfaces correctly to produce accurate EBSD data (51,56). An example of the effect of plastic deformation on the diffraction patterns can be found in Figure 2.11 (51). During plastic deformation, the distortions in the crystal lattice are relieved by the formation of dislocations and twins. Dislocations can be categorised into two groups (48). The first is statistically stored dislocations, where there is a region within the material which has a high dislocation density but a net Burgers vector of zero. The diffraction patterns from this region are degraded due to the local perturbations of the diffracting lattice planes leading to incoherent scattering (see Figure 2.12). The second is geometrically necessary dislocations (GNDs), which have a non-zero Burgers vector sum representing the excess dislocations stored within a Burger's circuit and contribute to a change in the crystallographic orientation i.e., lattice curvature. The quality of patterns generated from this region of the sample is degraded as they are a superposition of many patterns due to lattice bending. As GNDs result in lattice curvature, local misorientations can be recorded using EBSD analysis, these misorientations correlate to plastic strain. Whereas statistically stored dislocations cannot be measured using EBSD as they will not result in a misorientation of the lattice.

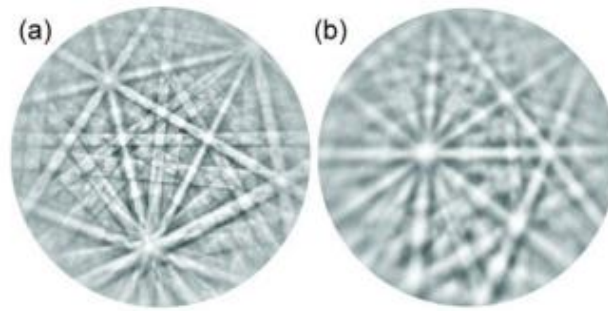


Figure 2.11: EBSD pattern from (a) a well-prepared surface and from (b) a poorly prepared surface of zirconium (51).

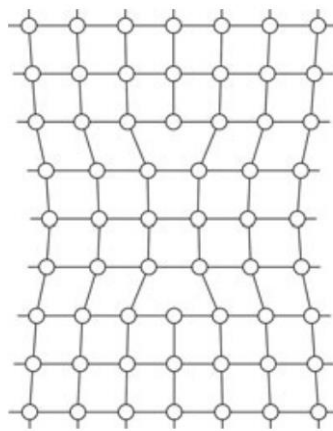


Figure 2.12 Diagram showing the effect of two opposing edge dislocations on the crystal lattice leading to a degraded lattice pattern (51).

2.5. Modelling polycrystalline deformation

As discussed in section 2.3.2, polycrystalline deformation is far more complex than single-crystal deformation and so has been difficult to quantify deformation on the microscale using experimental techniques. Therefore, historically modelling methods have been utilised to predict mechanical failure in polycrystals. Simplistic models such as Sachs (57), Taylor (43) and Bishop-Hill (58–60) are not able to consider elastic anisotropy (10). However, more complex models such as self-consistent and crystal plasticity finite element method (CPFEM) models can consider the anisotropy of elastic deformation.

The earliest model proposed for polycrystal plasticity was by Sachs (57), who proposed that the tensile yield stress of the polycrystal is the average of the constituent single-crystal yield stresses. Therefore, an averaging equation was used to produce the yield stress, σ_y , (Equation (2-8)).

$$\sigma_y = \langle 1/m \rangle \tau_c \quad (2-8)$$

Where m refers to the highest Schmid factor in each grain and τ_c is the critically resolved shear stress (CRSS) and is assumed the same in all systems. The Sachs model acts under the assumption that stress is partitioned among grains in proportion to their yield stress (37). The equation also implicitly assumes that slip occurs only in one slip system, which leads to incompatibility between grains.

In 1938 Taylor (43) proposed a model which would satisfy the compatibility requirement between grains (37). This was achieved by assuming the plastic strain, in contrast to the stress used in the Sachs model, was the same in all grains. The Sachs model can be used to produce a lower bound for the yield stress and the Taylor model can provide an upper bound (37). Bishop and Hill used a different method but reached similar outcomes to that of the Taylor model.

As this project studies polycrystalline deformation, it is important to select a model which considers anisotropic deformation. As the Schmid, Taylor, and Bishop and Hill do not consider anisotropic deformation, these have not been used in this project. Two models which do consider anisotropic deformation are the crystal plasticity finite element method (CPFEM) and self-consistent models, therefore, these models will be discussed in greater detail in the following sections.

2.5.1. Crystal Plasticity Finite Element Method

The CPFEM is a method of modelling polycrystalline deformation. The finite element (FE) method divides a complicated body with imposed constraints into smaller elements which are more readily evaluated. The size and number of these elements can be selected to model a polycrystalline microstructure. For CPFEM, each grain is presented as a 'brick' with the same crystallographic orientation throughout. CPFEM can simulate the strain information for near neighbour interactions by modelling the effect of different neighbouring environments on a specific grain with a given crystallographic orientation or size.

Dawson et al. (61) compared CPFEM predictions of the formation of intergranular strain in HY100, a polycrystalline low alloy steel, to the experimental measurements collected by using ex situ neutron diffraction tensile testing. The model used in this paper assumed each grain to be a 3D cubic shape with eight nodes and six neighbours. The CPFEM simulations were in reasonable agreement with the experimental results and captured the main trends of the average lattice strain, however, typically the models over-predicted the lattice strain in the transverse direction. This was thought to be caused by the model lacking single-crystal grain deformation anisotropy. Dawson et al. (62) also used

the CPFEM to compare the strain formation within an aluminium-magnesium alloy (AA-5182) where the results were used to show that the single crystal anisotropy within the AA-5182 was higher than that in aluminium. Dawson showed that by increasing the number of mesh elements, better statistical averages of lattice strains were achieved. However, the run time of the simulation was drastically increased with the greater number of elements. Da Fonseca et al. (63) used CPFEM to model two specimens of steel, one with a grain size of 80 μm and the other 350 μm . The results of the CPFEM models for the loading direction lattice strains are shown in Figure 2.13, this shows that the model usually captures the general trend of the lattice strains, however, in both samples it over-predicts the 110- orientation response. It was also found that the grain size did not have a significant impact on the development of intergranular stresses in the steel specimens. Guan et al. (22) compared HR-DIC data to CPFEM analysis to study slip activation and strain location in single and oligo-crystal Ni alloys under fatigue load. The CPFEM model showed to be in reasonable agreement with the HR-DIC data for the accumulated effect of plastic strain, however above nine load cycles the model and experimental HR-DIC data deviated. This was thought to occur because there are large amounts of deformation following this number of load cycles and the model is not able to consider cross-slip and latent hardening because each grain is modelled as a distinct region (22). This implies the model is more successful in the case of modelling uniaxial load as opposed to cyclic loading.

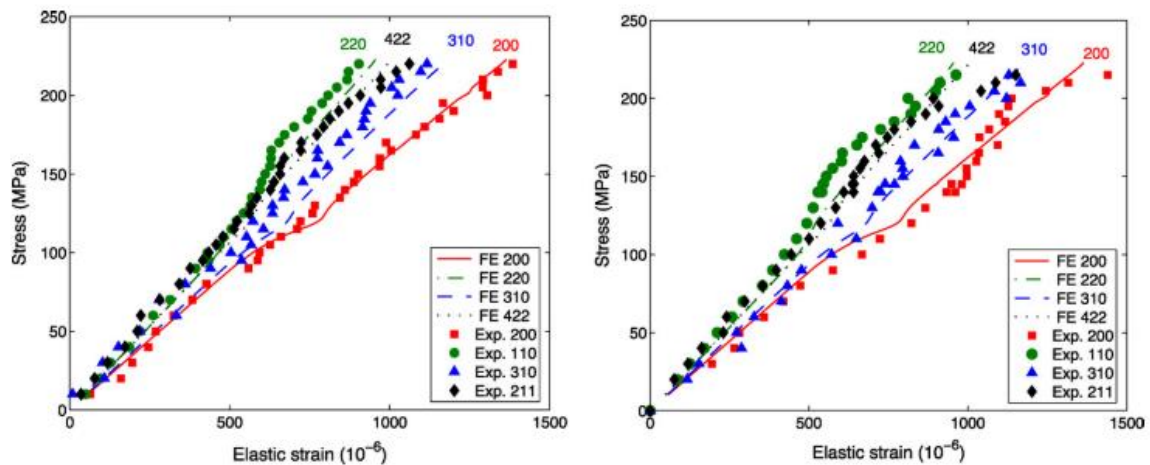


Figure 2.13: Mean $(h\ k\ l)$ family lattice strain evolution in the loading direction for steel specimens with a grain size of 80 μm (left) and 350 μm (right), here the CPFEM modelled data is shown as lines (63).

2.5.2. Self-Consistent Modelling

Self-consistent models of polycrystals use the Eshelby approach (64) which involves treating each “grain” as an ellipsoidal inclusion within a homogenous medium, a schematic illustration can be found in Figure 2.14. Assuming the grain is an ellipsoidal shape, allows the stress to be uniform within the grain, the details of this can be found in Eshelby’s paper (64). The homogenous medium encasing the inclusion is used to reflect the average stress-strain behaviour of the material. The size and shape of the ellipsoidal inclusion can be altered to reflect the dimensions of the grains within the polycrystalline material. This can be achieved by inputting an initial texture file into the code, which can be obtained by performing EBSD analysis on a sample of the material being modelled.

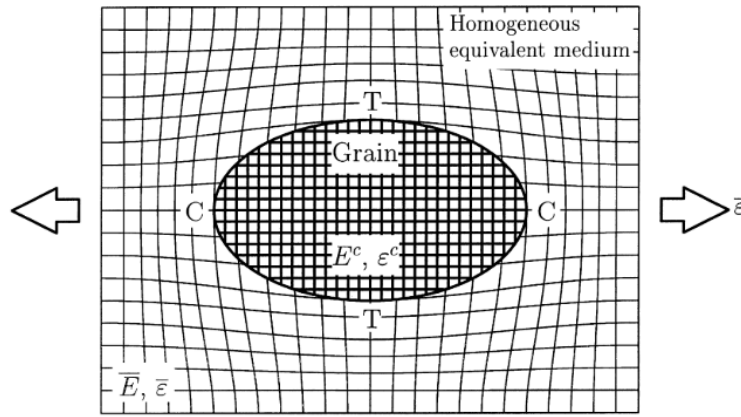


Figure 2.14 Schematic illustration of an ellipsoidal, stiff anisotropic inclusion in a homogenous equivalent medium. Where stiffnesses are denoted E and strains ϵ . The strain field in the inclusion is constant, and regions of additional compressive (C) and tensile (T) are shown. The strain at infinity in the medium, $\bar{\epsilon}$, is equal to the average over all grains. (41)

2.5.2.1. The Voce Hardening Function

The Voce hardening function used by both the self-consistent modelling approaches is shown in Equation (2-9) (9). The hardening model predicts the evolution of stress due to accumulated shear strain within each grain.

$$\tau = \tau_0 + (\tau_1 + \theta_1 G) \left(1 - \exp \left[\frac{\theta_0 G}{\tau_1} \right] \right) \quad (2-9)$$

where G is the accumulated shear strain in the grain, τ_0 is initial critically resolved shear stress (CRSS), θ_0 is the initial hardening rate, θ_1 is the asymptotic hardening rate, $(\tau_0 + \tau_1)$ is the back extrapolated CRSS. This equation finds the crystallographic shear flow stress τ . This equation essentially finds the resistance to activation that the deformation modes experience, where the

threshold value is given by τ_0 , this usually increases with deformation due to strain hardening, this follows the modified Voce law.

2.5.2.2. Elasto-Plastic Self-Consistent Model

The elastic-plastic self-consistent (EPSC) model is a computer code written in FORTRAN-77, which simulates the thermo-mechanical deformation of polycrystalline aggregates (65). Elasto-plastic is the mechanical regime addressed and self-consistent refers to the approach used. The formalism is based on the work of Hill (66,67) and Hutchinson (68) who studied the elastic stresses and strains which develop within the grains that form the polycrystalline aggregate to compensate for the elastic and plastic deformation. This section will discuss the basic methods used in the model, however, further detail can be found in the EPSC user manual (65).

The EPSC uses the Eshelby equivalent inclusion formalism, which solves the elastic problem of the stress and strain within an ellipsoidal inclusion that is embedded within an infinite homogenous medium which has different elastic constants, during the application of uniform stress (65). Although the Eshelby equivalent inclusion formalism is an elastic problem it can be extended to the plastic regime by expressing the solution in incremental (or rate) form and introducing the concept of instantaneous modulus which is related to the stress rate $\dot{\sigma}$ to the total (elastic + plastic) strain rate $\dot{\epsilon}$ (65), this can be found in equation (2-10).

$$\dot{\sigma} = \mathbf{L} \dot{\epsilon} \quad (2-10)$$

Where \mathbf{L} is the overall instantaneous elasto-plastic stiffness tensor. Similarly, for any given grain, the constitutive relation can be written as

$$\dot{\sigma}^C = L^C \dot{\epsilon}^C \quad (2-11)$$

Where the superscript denotes that a tensor refers to the grain with index C. The grain modulus L^C is dependent on the orientation of the grain, the single crystal elastic constants, and the level of deformation within the grain. To relate the individual grain to the bulk average the following equation can be used

$$(\dot{\sigma}^C - \dot{\sigma}) = -L^*: (\dot{\epsilon}^C - \dot{\epsilon}) \quad (2-12)$$

Where \mathbf{L}^* is the effective stiffness and is given by

$$\mathbf{L}^* = \mathbf{L} : (\mathbf{S}^{-1} - \mathbf{I}) \quad (2-13)$$

\mathbf{S} is the elasto-plastic Eshelby tensor, and \mathbf{I} is the fourth-order identity tensor. By combining equations (2-10), (2-11) and (2-12) a localisation tensor, \mathbf{A}^C , is defined as

$$\mathbf{A}^C = (\mathbf{L}^C + \mathbf{L}^*)^{-1} : (\mathbf{L} + \mathbf{L}^*) \quad (2-14)$$

with the property,

$$\dot{\epsilon}^C = \mathbf{A}^C : \dot{\epsilon} \quad (2-15)$$

If all grains are assumed to have the same ellipsoidal shape and orientation, then \mathbf{S} is the same for all grains and, therefore, \mathbf{L}^* is the same for all grains. The conditions of self-consistency require that the weighted averages, $\langle \rangle$, of stress rate and strain rate equal the macroscopic magnitudes of the stress and strain rate of the aggregate, meaning

$$\dot{\epsilon} = \langle \dot{\epsilon}^C \rangle \text{ and } \dot{\sigma} = \langle \dot{\sigma}^C \rangle \quad (2-16)$$

This leads to the expression for the macroscopic elasto-plastic stiffness, L ,

$$L = \langle (\mathbf{L}^C + \mathbf{L}^*)^{-1} \rangle^{-1} \langle (\mathbf{L}^C + \mathbf{L}^*)^{-1} \mathbf{L}^C \rangle \quad (2-17)$$

The EPSC model has been used in literature to simulate neutron diffraction tests. Daymond and Bouchard (9) compared neutron diffraction data to EPSC models for 316H stainless steel at a range of temperatures to examine changes in intergranular plastic strain behaviour as a function of temperature. The results of the room temperature, 425 °C, and 650 °C neutron diffraction lattice strain data and the EPSC model in the loading direction can be found in Figure 2.15. The model was found to be in reasonable agreement up to a temperature of 425 °C, however, at higher temperatures, there was seen to be greater strain recorded experimentally than the EPSC model predicted. The difference between the model and the experimental data at the higher temperature is suggested to be caused by the non-diffracting parts i.e., the grain boundaries relaxing and forcing additional tensile load onto the crystalline parts or to nonequilibrium effects.

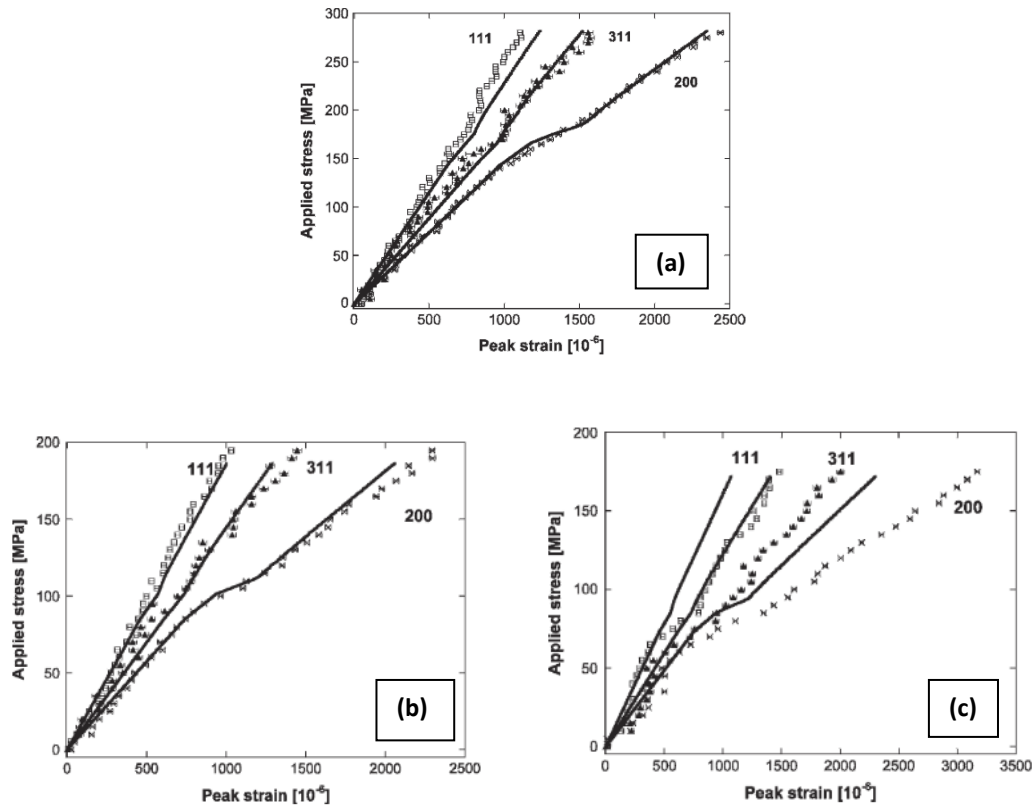


Figure 2.15: Lattice strain data for 316H stainless steel showing the 111, 311 and 200 grain orientation subsets in the loading direction where the points show the experimental data based on single peak fit and the lines show the results of the EPSC model at (a) room temperature, (b) 425 °C and (c) 650 °C (9).

Pang et al. (69) used the EPSC model to simulate neutron diffraction to study the generation of intergranular strains in 309H stainless steel under uniaxial loading. It was found that the model tended to overestimate the intergranular strains in the transverse direction to the tensile axis. Pang et al. (70) used the EPSC model to study the parallel and transverse intergranular strains of the Al7050 alloy. The model agreed with the experimental neutron diffraction, however, was also seen to overestimate the magnitude of intergranular strains. Korsunsky et al. (71) used the EPSC model and neutron diffraction measurements to assess polycrystalline fatigue. The cyclic response of both the 111 and the 200-orientation subsets of grains recorded by the neutron diffraction measurements was accurately reflected in the EPSC predictions. Neil et al. (13) used the EPSC model and neutron diffraction to study the lattice strains in both copper and stainless steel, the model accurately predicted the behaviour of the longitudinal lattice strains but was found to be less satisfactory at predicting the behaviour of the transverse lattice strains.

Francis et al. (72) used the addition of post-mortem STEM analysis to the EPSC model and neutron diffraction analysis as a method of verifying the results of the tests for a polycrystalline nickel-based

superalloy, Waspaloy. The fine microstructure showed that the crystalline structure and the precipitate deformed jointly (Figure 2.16), whereas for the medium and course microstructures a load transfer occurred between γ and γ' (Figure 2.17). STEM analysis confirmed this by showing the same slip system is active for both the γ and γ' in the fine structure, however, in the medium and course γ' microstructure stacking faults are restricted to the γ' phase.

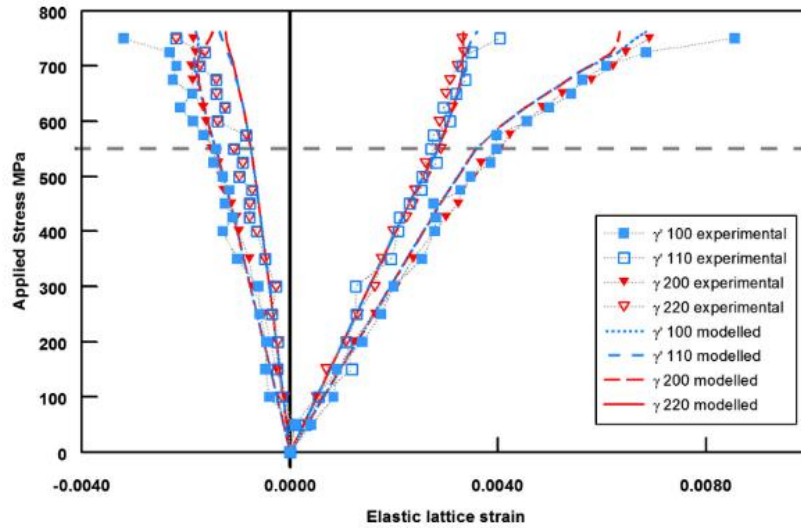


Figure 2.16: The measured and modelled elastic lattice strain in the (200) and (220) γ grain and γ' precipitation families for the fine γ' microstructure. Modelled results are presented as lines, while experimental data are presented as points. The horizontal dashed line indicates the onset of plastic deformation (72).

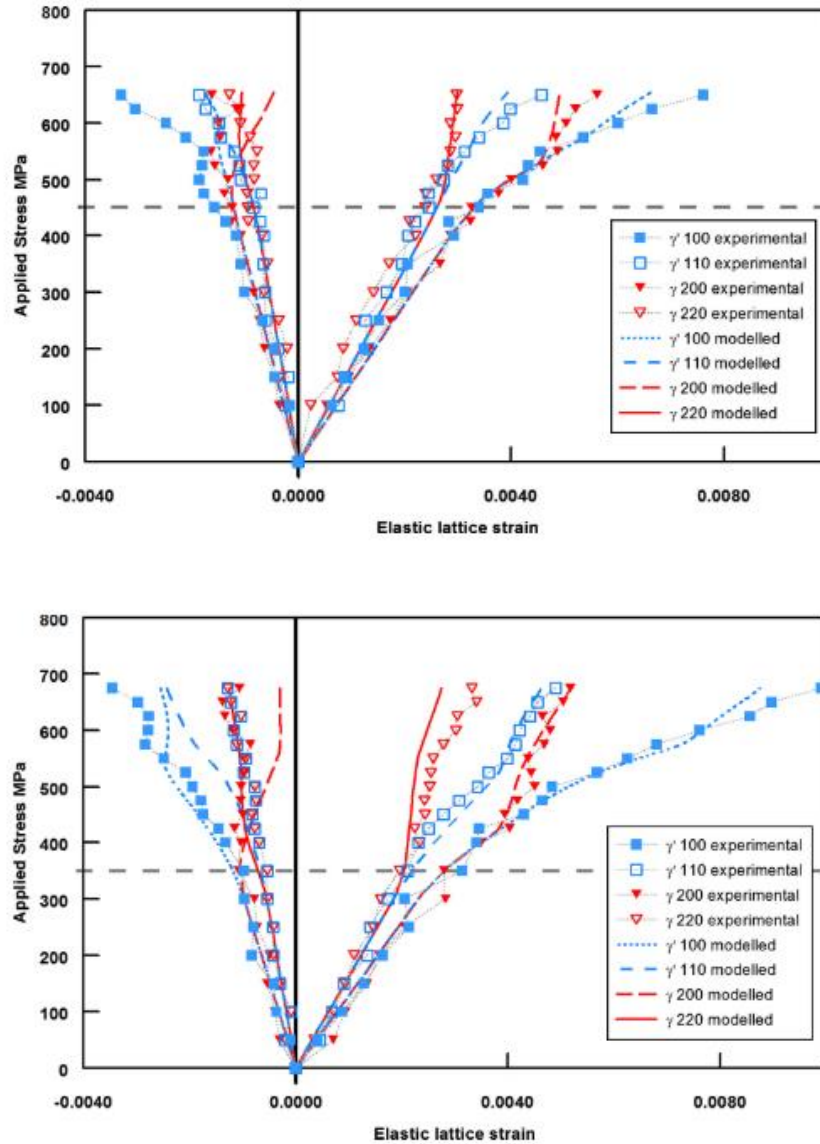


Figure 2.17: The measured and modelled elastic lattice strain in the (200) and (220) γ grain and γ' precipitation families for the (a) medium γ' microstructure and (b) coarse γ' microstructure. Modelled results are presented as lines, while experimental data are presented as points. The horizontal dashed line indicates the onset of plastic deformation (72).

One limitation of the EPSC model is that it is unable to sufficiently account for grain size dependency on yield stress (37). The Hall-Petch relationship states that the yield stress is linearly related to the inverse square root of the grain size. This is caused by dislocation pile-ups caused by deformation. For large grains, the dislocation pile-ups are longer and cause greater stress concentrations which can cause yield to occur at a lower applied stress. As the EPSC is independent of scale it cannot account for this. Hutchinson (68) states that this is navigated by interpreting the CRSS as that *in situ* rather than what is expected for an unconstrained single crystal, however, the model uses the properties of individual crystallites so this cannot be fully accepted.

2.5.2.3. Visco-Plastic Self-Consistent Model

At high strains, plastic deformation dominates over elastic deformation in which case the EPSC model would not be useful as this model assumes plastic deformation only as a change in the rate of strain, which is far more simplistic than what occurs during plastic deformation. The EPSC model works for low strain values as these are dominated by elastic deformation, but once plastic deformation dominates other methods need to be used. The visco-plastic self-consistent (VPSC) model uses the same fundamentals as the EPSC model but instead simulates plastic deformation within polycrystalline materials. The VPSC model represents the polycrystal microstructure as weighted orientations, here the orientations represent the grains and the weights represent the volume fractions of each of the orientations (73). The volume fractions are chosen to reproduce the initial texture of the material. Just like the EPSC model, the VPSC model uses the Eshelby inclusion approach. The effective medium represents the average environment that each grain would experience. VPSC simulates the plastic deformation of aggregates subjected to external strains and stresses. The model is based on the physical shear mechanisms of slip and twinning and also accounts for grain interaction effects (73). In addition to simulating the macroscopic stress-strain response, it also accounts for the hardening, reorientation, and shape change of individual grains; this means VPSC can be used to predict the evolution of hardening and texture associated with plastic deformation.

The VPSC model was extended to include elastic deformation as well as plastic by Wang et al. (7) this is the elastic-viscoplastic self-consistent (EVPSC) model. For monotonic loading it was found there was minimal difference between the VPSC and EVPSC, however, for unloading and strain path changes it was found that the EVPSC model produced a smooth elastic-plastic transition whereas the VPSC model produced a discontinuous response. Anglin et al. (74) used the VPSC model as a method to reduce the development time for the high-resolution visco-plastic model based on the fast Fourier transform (FFT). This is due to the computational speed available through using VPSC; the optimisation parameters found through VPSC were used as a starting point to run the FFT model. In this study, copper was selected as a fitting exercise and showed that for simple microstructures the VPSC model produced parameters which could be directly used for the VP-FFT model. For pearlitic, biphasic steel the VPSC model greatly reduced the computational time needed for VP-FFT as they showed a well-informed initial guess for the parameters. Therefore, showing that VPSC is not limited to single-phase materials. Many versions of the VPSC model have been developed, the VPSC+ model was developed by Jeong and Tomé (75) to account for the elastic contribution without losing the numerical efficiency of the visco-plastic approach. This approach was validated using experimental data for 316 L and Mg AZ31, as well as comparing it to the EVPSC, EPSC and VPSC models. The VPSC+

model showed improved numerical stability when imposing relatively large strain increments, although its computational advantage was decreased when twin orientation needed to be accounted for.

2.5.3. Summary

Modelling deformation can provide a useful tool in predicting the lifetime of metals. Constitutive models have proven to be useful tools for examining the microscale deformation in polycrystals (76). Models such as Sachs (57), Taylor (43) and the Bishop-Hill model (58–60) do not typically provide adequate results for polycrystalline deformation as anisotropy is not considered (10). The self-consistent elastic elastoplastic formulation was proposed by Hill (66) and Hutchinson (68) and was developed into the EPSC model by Turner and Tome (77). The self-consistent model uses the Eshelby approach (64) which has the main assumption that each grain is an ellipsoidal inclusion embedded within a homogenous aggregate which mimics the overall response of the polycrystal (77). The other approach of modelling polycrystalline structures is using the CPFEM model. This model can present either a 2D or 3D aggregate where each element represents a grain with independent yield stresses. Both EPSC and CPFEM have proven to yield accurate predictions when compared to neutron diffraction data. However, there is substantially less research comparing these models to HR-DIC data. This will be discussed further in the following sections.

CPFEM can sample a comparative number of grains to EPSC modelling, however, this can take a far greater computational time. The EPSC model assumes that the environment around each grain is homogenous, yet the CPFEM work indicates that the effect of neighbouring grains is significant, with the spread in elastic strains being of the order of half the axial strain at the yield point (61). For simplicity, the brick model typically used in CPFEM only allocates six neighbours per grain, where each grain is assumed to be a cubic 8 nodal shape, although real materials would typically have many more (61,62,78). Increasing the number of nodes and the number of neighbours increases the computational time of the model. In addition, representing a grain as a single element and simplifying its shape restricts its ability to deform differently from its neighbours, meaning the effect could be overestimated. It has been suggested that increasing the number of elements to 8 or 27 per grain would capture the intragranular strain caused by plastic deformation better (79).

Although the CPFEM model has the advantage of modelling the interaction of neighbouring grains, this requires a large amount of computational power, whereas the EPSC can be performed quicker and is able to accurately predict neutron diffraction data. Additionally, due to CPFEM treating each grain as an enclosed unit, it is not able to model cross-slip (discussed in section 2.5.1). As this project looks at the effect of SFE on deformation mechanics, not considering cross-slip could potentially

impact the results of the model as high SFE materials deform via dislocation glide or cross-slip. Hence, the EPSC model has been selected over the CPFEM model for this project.

2.6. Microscale Strain Measurement

Plastic deformation causes strains within a material; therefore, strain measurement techniques are important to understanding a material's behaviour. Strain can arise at different length scales within a material, including at the micro-scale. Strain at any length-scale within a material can contribute to macro-scale failure, therefore it is important to quantify strains at all length scales. Dependent on the length scale of strains within a material, there are a number of strain measurement methods which can be used, examples of such can be found in Figure 2.18. This project focuses on studying microscale strains over a bulk area; therefore, this section will discuss the techniques most suitable for these measurements.

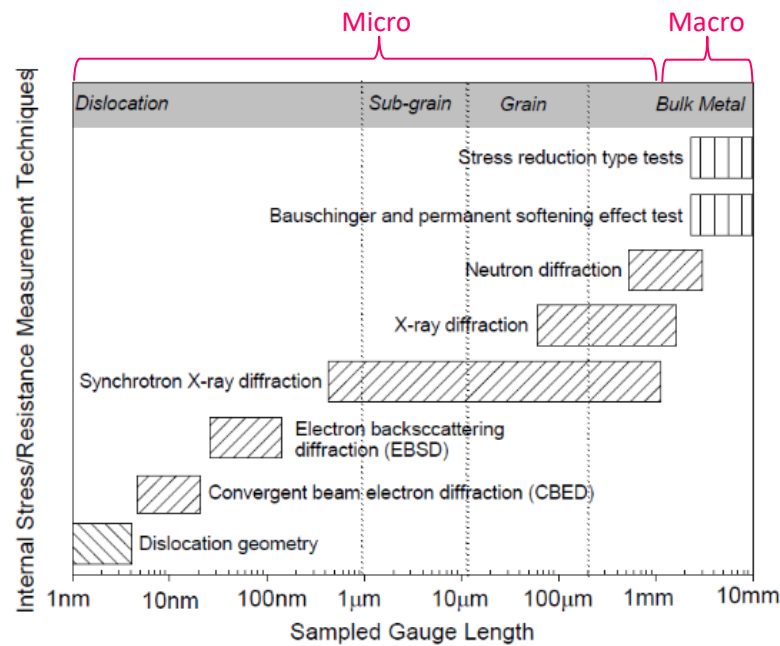


Figure 2.18: Graph showing a range of different internal stress measurement techniques (3). With added reference to what constitutes micro-strain measurement in this thesis

2.6.1. Microscope techniques

Microscopic techniques can detect abnormalities in the crystalline lattice caused by dislocations, therefore, utilise the geometry of dislocations to measure the strain within a material. In Figure 2.18, microscope techniques are the techniques able to measure strain at the dislocation level and require microscopic equipment to measure them, examples include EBSD and convergent beam electron diffraction (CBED) (80,81). EBSD is performed within an SEM, whilst CBED uses a scanning transmission electron microscope (STEM). Additionally, to measure dislocation geometry a transmission electron microscope (TEM) (82,83) can be used, which offers a higher resolution than an SEM. As EBSD is used within this project, previous studies which have utilised EBSD metrics, and the method of strain measurement will be discussed in further detail below.

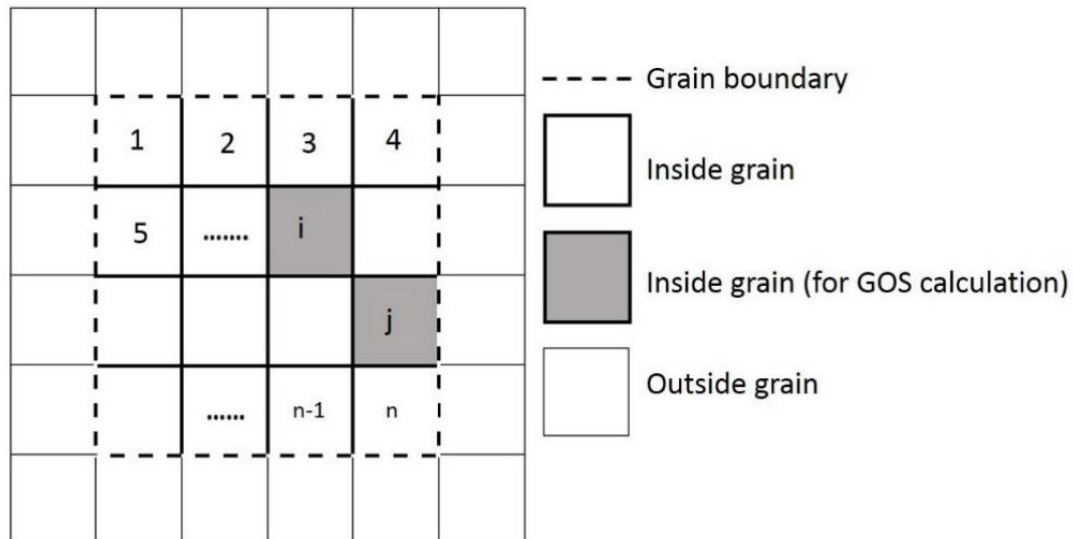
2.6.1.1. EBSD

Section 2.4.1.1 discusses how strain affects the resolution of EBSD analysis. This leads to the assumption that large concentrations of defects can be equated to plastic strain. However, not all defects are the result of plastic strain within the crystallographic lattice so instead of studying local defect concentrations researchers often use misorientation data from EBSD as a proxy for local strain (21). Through measuring lattice misorientation, EBSD analysis can be used to quantify local lattice distortions (51,84).

EBSD has been used to interpret the accumulation of plastic strains by determining local orientation change, local misorientation change (this is defined as the difference in orientation between pixels), average misorientation or by calculating GND densities (48). Kamaya (85) studied the correlation between the distributions of misorientations to induced macroscopic plastic strain in a stainless steel 316 specimen. The results showed that the mean value of the distribution of misorientation aligned well with the plastic strain induced within the specimens. EBSD metrics can be used to quantify misorientation change on the large scale, examples include:

- Grain Orientation Spread (GOS) (also called average intragrain misorientation (AMIS) in some studies) is the average deviation in orientation between each data point in a grain compared to the average orientation of the grain. This method assigns the same value to every scan point within a grain (51,86–89). Figure 2.19 shows a schematic of the equation used in GOS calculations,
- Grain Average Misorientation (GAM) measures the average misorientation between two neighbouring points within a grain (89,90). This technique is sensitive to step-size, therefore as step-size decreases, the misorientation also decreases between points.

- Kernel Average Misorientation (KAM) is like GAM, however, it is calculated within a kernel (a small region) instead of grain (90). A kernel may include a grain boundary causing large values of misorientation; therefore, a threshold value is specified, above which the values of misorientation are excluded (typically a misorientation above 15°). The equation for the KAM EBSD metric is shown in Figure 2.20.



$$GOS = \frac{\sum_{i=1}^n (q_m - q_i)}{n} \quad (2-18)$$

q_i = crystal orientation at point i

q_m = average orientation of the grain

Figure 2.19: Schematic calculation of GOS (49)

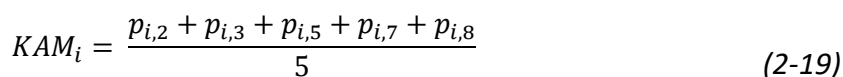


Figure 2.20: Schematic illustration of calculation by KAM (49).

32

research found GOS to be the best EBSD metric in identifying the strain-free grains from the deformed grains.

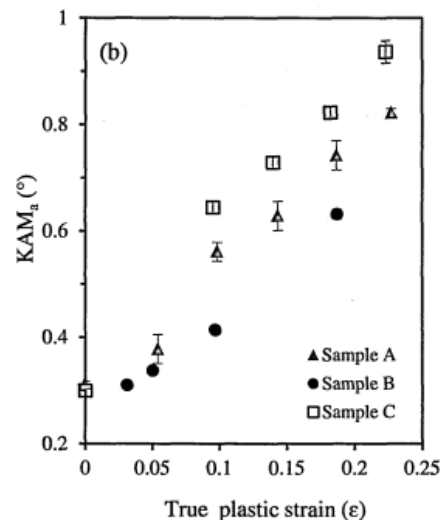


Figure 2.21: A comparison between the True plastic strain and KAM of three SS316 samples. Sample A is subjected to a strain rate (s^{-1}) 2.0×10^{-4} and a grain size of 98 ± 8 , Sample B has a strain rate (s^{-1}) of 2.0×10^{-4} and a grain size of 93 ± 12 , Sample C has a strain rate (s^{-1}) of 1.5×10^{-3} and a grain size of 35 ± 1 . By comparing Sample A and Sample B, with the same strain, it shows that is an increase in KAM values with the increasing KAM (91).

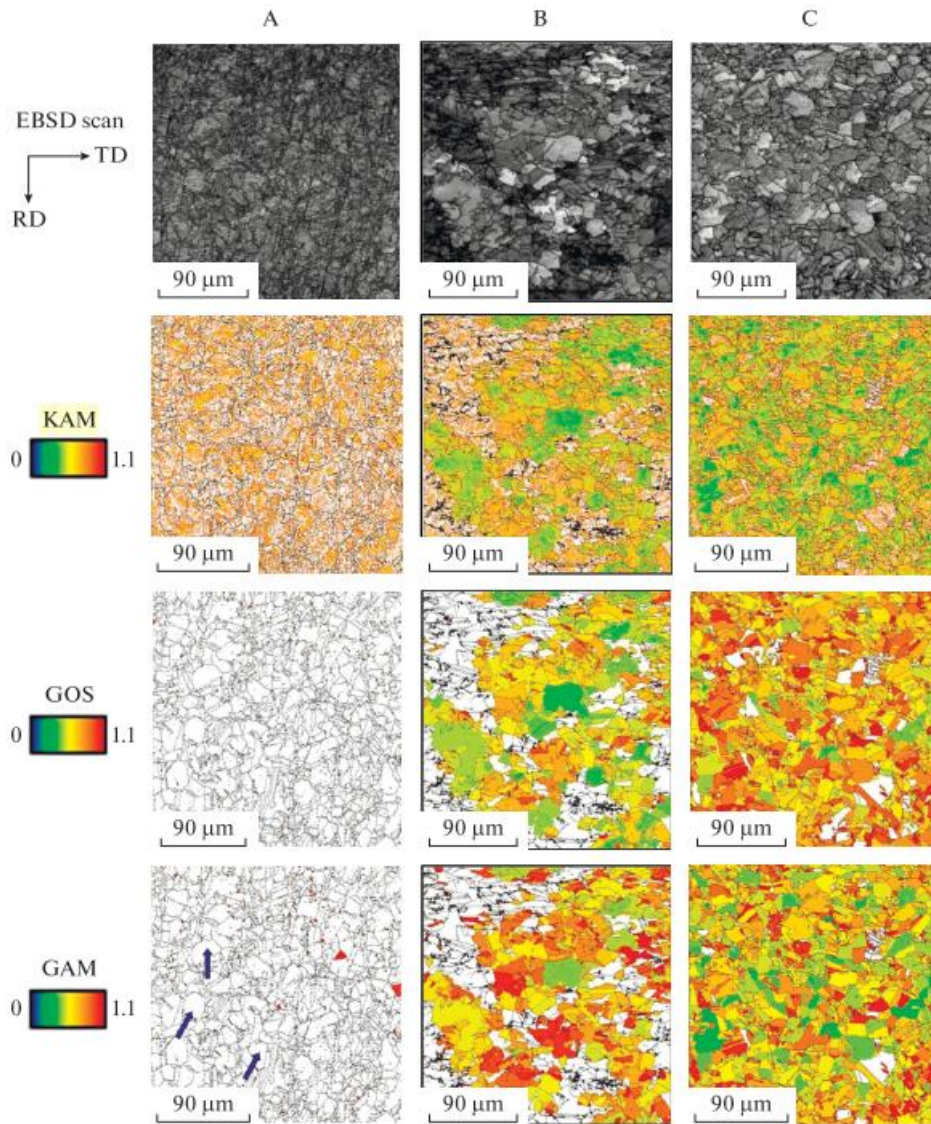


Figure 2.22: 'Comparison of IQ, KAM, GOS, and GAM maps for (A) deformed (B) partially recrystallized and (C) fully recrystallized samples. The misorientation spread $> 1.1^\circ$ is marked as white and indicated with the blue arrows' (90).

Additionally, EBSD analysis can be used to study the evolution of deformation structures throughout loading. Biroasca (92) used post-mortem EBSD analysis on a failed tensile test specimen of RR1000 nickel-based superalloy to study GND in both soft and hard grains. This showed a high GND content at the grain boundary of the soft grains and on the slip plane traces with hard grains. Yvell et al. (93) used *in situ* EBSD tensile tests to study the evolution of deformation structures throughout the loading of a high-nickel austenitic stainless steel. This work found an increase in both low- and high-angle boundaries as well as orientation changes in individual grains.

2.6.2. Diffraction techniques

Diffraction techniques provide a non-destructive method of measuring elastic strain. These techniques use Bragg's law of diffraction (shown in Equation (2-7)) to measure the lattice spacing within the crystalline structure of a specimen. Elastic strain can be determined by calculating the difference in lattice spacing from a loaded specimen to a loaded specimen. As plastic deformation permanently changes the crystal lattice, these techniques cannot directly measure plastic strain. Neutron diffraction, X-ray diffraction and x-ray synchrotron diffraction are examples of diffraction techniques which are widely used to measure strain and are shown in Figure 2.18 as primarily a bulk measurement technique due the relatively large region they can assess within a specimen.

Diffraction techniques typically require little sample preparation before strain measurements and compared to microscope-based techniques, can provide information on a larger volume of the sample. However, access to suitable diffraction instruments can be difficult as laboratory x-ray diffraction instruments have a very limited depth of penetration. This can be overcome by using high-energy synchrotron x-rays which can penetrate thousands of times deeper than laboratory x-rays (81) but can only be found at a few national facilities around the world. As neutron diffraction is used within this project, it will be discussed in detail within the following section.

2.6.3. Neutron Diffraction

Neutron diffraction uses neutrons in the incident beam, these are uncharged particles which can penetrate deep into the material. This technique was originally developed from X-ray diffraction which was limited by the penetration depth of the charged photons and would only provide information on lattice spacing near the surface. As shown in Figure 2.18, neutron diffraction is a bulk strain measurement technique, however it can be used to measure the average elastic strain for grain subsets. Because Neutron diffraction uses Bragg's law it can be used to determine the strain for a particular group of grains which a similar crystallographic orientation.

2.6.3.1. Neutron Sources

Neutron generation at neutron diffraction facilities can be divided into two distinct groups: reactor sources and spallation sources. Reactor sources use neutrons generated by nuclear fission reactions; the most common fuel being uranium alloy enriched to 3-5% U_{235} (94). During the fission reaction, a neutron collides with a uranium atom, causing the atom to split into two. This process generates more neutrons, which collide with more uranium atoms, causing a nuclear chain reaction. The high-speed neutrons produced in this process are slowed down using moderators before they are used for diffraction experiments. On the other hand, a spallation source generates neutrons by firing a

beam of highly accelerated protons at a heavy metal target (for example, Lead, Tungsten or Tantalum) (1,95). As the high-energy protons strike the target material, neutrons are emitted, this is a process called spallation. Many neutrons are produced from each proton, which is then reduced in energy to within the thermal range by moderation processes. This process is repeated many times a second.

The important parameters to consider when performing neutron diffraction experiments are the flux of neutron, intensity and speed of neutron generation. Typically, reactor sources produce continuous neutron beams which are monochromatic, whereas spallation sources produce pulsed neutron beams which are polychromatic. Choppers can be used to reduce the duration between the neutron pulses in both reactor sources and spallation sources (96,97).

2.6.3.2. Time of Flight Technique

Neutron diffraction can be used to measure the lattice spacing between the planes within the crystalline structure, the method is called the time-of-flight (ToF) technique as it uses the flight time of neutrons from a pulsed polychromatic neutron source (98). By using *in situ* neutron diffraction with tensile testing the changes in the spacing between crystalline planes can be measured throughout the application of an external load. The ToF technique produces a spectrum of diffraction peaks from the same sets of crystallographic planes in multiple similarly orientated grains, called a grain family (99). The process begins with a pulsed beam of neutrons passing through a moderator to slow fast neutrons into thermal neutrons. The beam of neutrons then reaches the sample, where the diffracted neutrons are recorded using suitably positioned detectors. The flight time of the neutrons, t , over a known flight path, l , is recorded, this can be used to determine the neutrons velocity, v . Then, De Broglie's equation (100) can be used to relate the velocity of the neutron (v) to the wavelength (λ).

$$\lambda = \frac{h}{mv} \quad (2-20)$$

Where m is the mass of a neutron and h is Planck's constant. Then, by substituting this equation into Bragg's Law Equation (2-7), Equation (2-21) can be derived.

$$\frac{h}{mv} = 2d_{hkl} \sin \theta_{hkl} \quad (2-21)$$

As the neutrons travel a distance, l in a time of t , using speed = distance/time. Equation (2-21) can be rewritten as

$$\frac{ht}{ml} = 2d_{hkl} \sin \theta_{hkl} \quad (2-22)$$

From this, the lattice spacing d_{hkl} for a grain family can be calculated. By comparing the relative change of the d_{hkl} spacing to its initial stress-free measurement $d_{0\ hkl}$ (the lattice spacing measured prior to loading) lattice strains ϵ_{hkl} can be calculated (Equation (2-23)).

$$\epsilon_{hkl} = \frac{d_{0\ hkl} - d_{hkl}}{d_{0\ hkl}} \quad (2-23)$$

2.6.4. Diffraction Peak Profile Analysis

Like all diffraction-based techniques, the peaks produced in neutron diffraction analysis are a widely used method for characterising the microstructure of crystalline materials. This is termed diffraction peak profile analysis (DPPA) and can be used to determine details about a sample that includes, the micro-strain, crystal size or dislocation cell size, dislocation density and arrangement, the number of planar faults and dislocation slip system population (63,101).

2.6.4.1. Full-Width Half Maximum

The full-width half-maximum (FWHM) is the width of the spectrum curve at the point where the y-axis is at half its maximum. This measurement can be used as an indication of plastic strain or a change in grain size within a material during *in situ* neutron diffraction tensile tests.

2.6.5. Limitations of Diffraction Techniques

Diffraction techniques provide a method of analysing the strain within the bulk of a metallic component yet there are drawbacks to using these techniques. The nature of strain measurement through diffraction techniques means the specimen is required to contain a crystalline microstructure, this limits the materials which can be evaluated by this method (55). Diffraction techniques are not able to show the spatial effects of deformation anisotropy between neighbouring grains, as the strain data is presented in diffraction peaks equated to a grain family. Therefore, to understand the full effects on the microstructure it must be accompanied by microstructural strain analysis, using a microscopic technique such as EBSD. An additional limitation of neutron diffraction is that it can only be performed in a limited number of national facilities, which can be expensive and require granted access (55).

2.6.6. Digital Image Correlation

Digital image correlation (DIC) was developed by researchers at the University of South Carolina in the 1980s (55,102–105). It is a noncontact, full-field optical metrology technique used to measure two-dimensional (2D) and three-dimensional (3D) deformation (106). DIC is an image processing technique which requires an applied pattern so that the software can pattern track between a deformed image and a reference image (107). Therefore, DIC requires the test specimen to have either a natural surface texture or an applied speckle pattern to track each selected pixel from the reference image to the deformed image. DIC is also known as the digital speckle correlation method (DSCM), texture correlation, computer-aided speckle interferometry (CASI) and electronic speckle photography (108). The work in this project solely focuses on 2D DIC, therefore, the aspects of this technique will be covered in detail within the following sections.

2.6.6.1. Image Acquisition Methods

Due to the versatility of DIC, a variety of image acquisition techniques can be used to produce images suitable for DIC. The choice of image acquisition technique is dependent on the length scale of the analysis required. Examples include an optical lens, a telecentric lens or an SEM. Even though an optical lens can be used for DIC it can be disadvantageous due to the effect of small out-of-plane motion of a test specimen and the sensor target (caused by self-heating) as well as geometric distortion of the imaging lens, these effects can lead to significant errors in displacements and strains measured by DIC (109). To mitigate these effects a telecentric lens can be used instead. Pan et al. (109) found by comparing a telecentric lens to a standard optical lens, it was shown that the telecentric lens was insensitive to the out-of-plane motion of the test subject and the self-heating of the camera. Additionally, there was negligible lens distortion found in the telecentric lens results.

2.6.6.2. Theory of DIC

By collecting images before and after deformation, DIC can provide full-field displacements and subsequently full-field strain measurements (108). This allows strain to be measured throughout the surface of a material (full-field strain). To achieve local surface variations that are trackable, it is important to apply a speckle pattern or use the natural surface texture. The method of applying a texture is dependent on the material type and the length scale of the DIC. Examples of speckle patterns include gold remodelling, which can be used at the microscale within a scanning electron microscope (SEM) and spray paint which works for the macroscale.

At the single pixel level, it can be difficult to match the deformed surface to the reference image, therefore, the surface is divided into an evenly spaced grid, shown in Figure 2.23. Usually, a square subset with a size of $(2M + 1) \times (2M + 1)$ pixels (where M is the midpoint of the subset) which contains sufficient local intensity variations is selected from the reference image, this can then be used to track the corresponding location within the deformed image. Locating the subset within the deformed image can be achieved by using predefined criteria and a certain optimization algorithm (106–108,110–112). Examples of optimization algorithms include cross-correlation function and normalised sum-squared difference (SSD) which can be used to help evaluate the degree of similarity between the reference and deformed subsets. Each sub-region produces a displacement vector (this is shown in the diagrams in Figure 2.24). This is performed at positions throughout the entire image to produce a full displacement vector field, describing the deformation of the imaged sample.

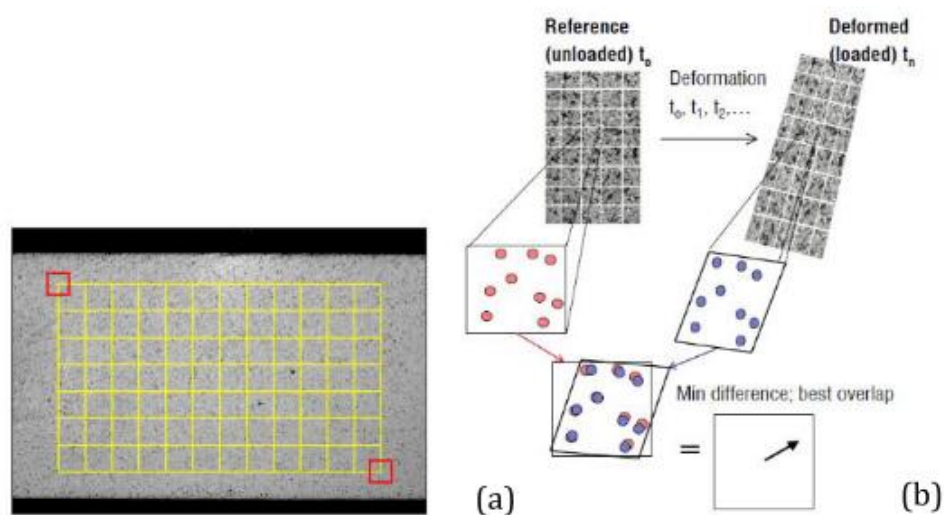


Figure 2.23: (a) Reference Image, with an imposed grid to divide the surface into subsets, (b) diagram showing the subset tracking procedure (108).

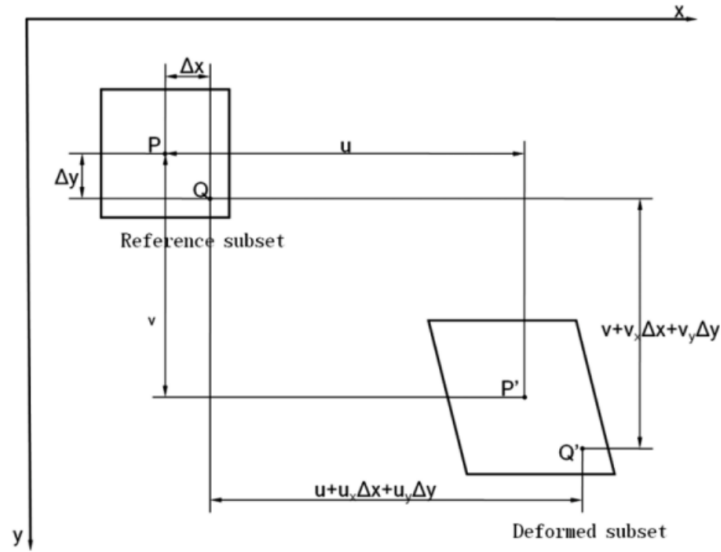


Figure 2.24: Schematic illustration showing a reference subset before deformation and the deformed subset following deformation (113).

2.6.6.3. Sum-squared difference

During deformation the subset is likely to deform along with the rest of the material, examples of such can be seen in Figure 2.24 and Figure 2.25. However, the set of neighbouring points defined in the original subset will remain neighbouring points in the deformed image. Therefore, the sampling region in the deformed image is moved and distorted to include the neighbouring points from the reference image. Figure 2.24 shows how the point Q around the subset centre P can be mapped in the deformed image subset using a correlation function.

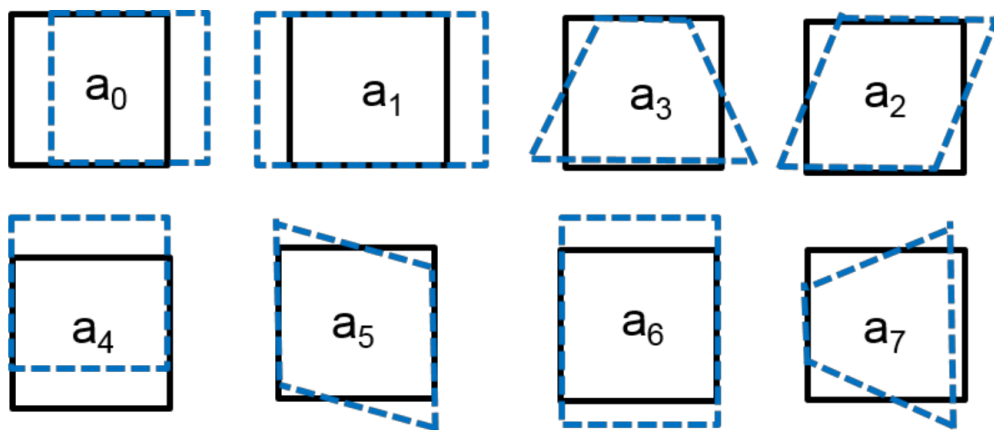


Figure 2.25: A schematic of the possible changes in shape that a subset may experience during deformation. Translation stretch, shear and distortion are shown here (55,114).

There are multiple options which can be used to find the degree of similarity between the reference subset and the deformed subset, for example, the cross-correlation function or sum-squared difference (SSD) (107). As SSD is used in this project, this will be discussed in greater detail below. SSD works by calculating the grey level within an individual subset, the deformed subset can be matched to the original image. The peak position of the distribution of the correlation coefficient helps with this matching procedure. The position of the deformed subset is determined when the correlation coefficient extremum is detected (this is the optimal scenario). However, in practice several threshold parameters are defined, and when these are reached (or the maximum number of iterations are completed), the answer is found. By using Figure 2.25 as a reference, Equation (2-24) shows how finding the minimum of the correlation function gives the best match between subsets at different strain increments (55).

$$C_{SSD} = \min_{a_0, \dots, a_7} \sum (I_1(x, y) - I_2(a_0 + a_1x + a_2y + a_3xy, a_4 + a_5x + a_6y + a_7xy))^2 \quad (2-24)$$

Where C_{SSD} is the correlation coefficient, a_0 and a_4 indicate the x and y component of displacement vector of the subset being tracked (see Figure 2.25) and a_1, a_2, a_3, a_5, a_6 and a_7 are the affine transforms (see Figure 2.25).

2.6.6.4. Strain Calculation from DIC

The DIC analysis produces full-field in-plane displacement maps $u(x_1, x_2, 0)$ where the plane is x_1x_2 and the normal is x_3 . Therefore, the displacement gradient tensor which describes the in-plane deformation can be written as

$$\frac{\partial u_i}{\partial x_j} = \begin{bmatrix} \frac{\partial u_1}{\partial x_1} & \frac{\partial u_2}{\partial x_1} \\ \frac{\partial u_1}{\partial x_2} & \frac{\partial u_2}{\partial x_2} \end{bmatrix} \quad (2-25)$$

The effective shear strain g_{eff} can then be calculated

$$g_{eff} = \sqrt{\left(\frac{\frac{\partial u_1}{\partial x_1} - \frac{\partial u_2}{\partial x_2}}{2}\right)^2 + \left(\frac{\frac{\partial u_1}{\partial x_2} + \frac{\partial u_2}{\partial x_1}}{2}\right)^2} \quad (2-26)$$

This can be used to plot strain as it reflects the shearing characteristic of slip and reduces some of the ambiguity caused by the absence of out-plane displacement data in DIC measurements (20).

2.6.6.5. High Resolution Digital Image Correlation

DIC can be adapted for use at many different length scales as the technique can be used on images obtained in a variety of ways. High-resolution digital image correlation (HR-DIC) is the name generally used by the community for DIC at the sub grain scale. To study strain at the grain scale, appropriate imaging devices need to be used. Various studies have coupled 2D DIC with optical microscopy (115,116), laser scanning confocal microscopy (117), scanning electron microscopy (14,15,22,118–120), atomic force microscopy (121) and scanning tunnelling microscopy (122–124) to yield microscopic strain data.

To track deformation correctly using HR-DIC it is important to have a tracking pattern which is an appropriate size compared to the scale of the image. Some examples of surface preparation techniques include etching the surface (14), gold remodelling (15,118,125) or fine colloidal silica particles (22).

By imposing the strain map collected through HR-DIC onto an EBSD map, the data can be segmented to study specific spatial effects. Orozco-Caballero et al. (20) studied AZ31 Magnesium alloy using ex-situ tensile tests using a micro tensile tester, this showed the very heterogenous deformation at the grain scale. Di Gioacchino and Da Fonseca (118) used HR-DIC to study the strain associated with slip bands with grains. This showed that the formation of slip bands is not strictly related to crystallographic orientation and seems to be affected by the constraint of neighbouring grains. Di Gioacchino and Da Fonseca (125) used HR-DIC in conjunction with EBSD analysis to measure strain and distinguish between material rotation and lattice rotation in austenitic stainless steel. This work showed the formation of microscale plastic strain and highlighted the correlation to lattice curvature at high global strains. When studying the effect of dislocation channel-grain boundary intersections in irradiated stainless steel, McMurtrey et al. (126) used electron backscatter imaging to determine the grain boundaries for DIC analysis. When displacement vectors obtained through DIC were compared to possible slip direction vectors along the active slip plane, found through EBSD, 64% of the total slip could be accounted for. Harte et al (21) compared grain-scale DIC to EBSD metric analysis to study the relationship between misorientation and plastic strain accumulation. This work showed that a high resolution DIC map was able to locate individual slip bands, including single slip, double slip, triple slip, cross slip, and diffuse slip (Figure 2.26).

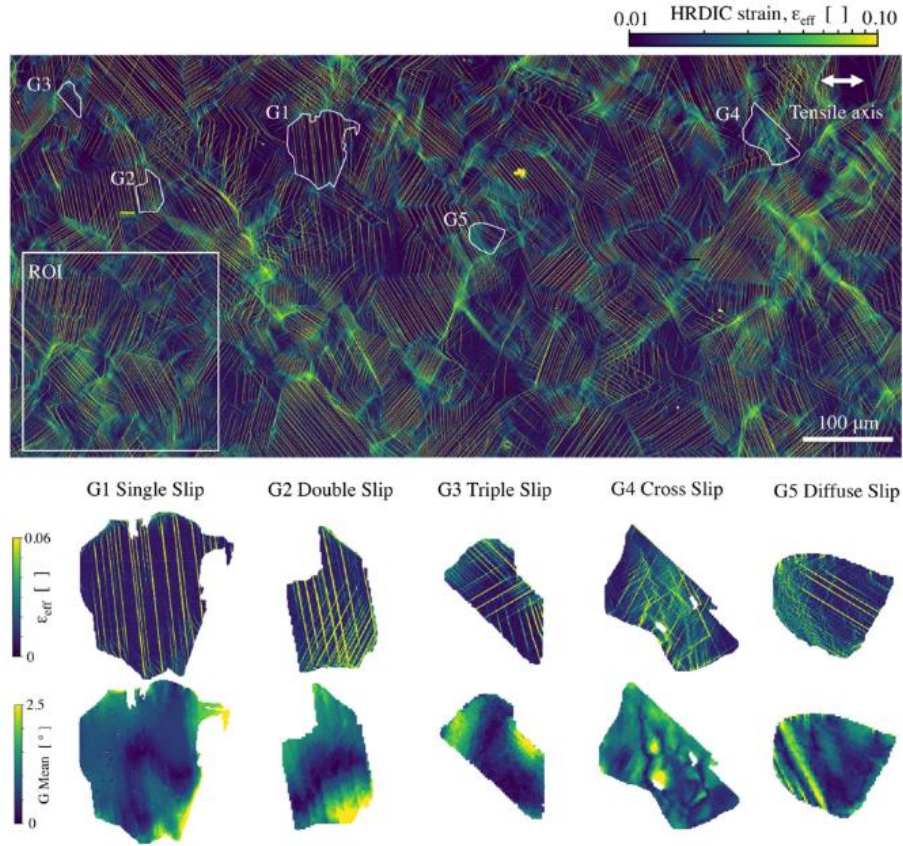


Figure 2.26: The HRDIC effective strain (ϵ_{eff}) map at macroscopic $\epsilon_{xx} \sim 0.02$, field of view 1×0.5 mm, spatial resolution 0.117 nm. G1-G5 highlight grains with different slip character and the effect of this on HRDIC ϵ_{eff} and EBSD lattice misorientation (grain reference orientation distribution mean) (21).

Das et al. (15) used *in situ* HRDIC for tensile tests performed in an SEM, which were directly compared to EBSD mapping from the same region acquired prior-to and post tensile testing. These tests were performed on samples of stainless steel 301 and by comparing the EBSD results to the HR-DIC strain data, local strain data could be related to plastic deformation and phase transformation. The HR-DIC and EBSD analysis confirmed that grains with two slip systems with similarly high Schmid factors would slip. Additionally, the disparity in strain values for individual strains compared to the global average strain, was also shown at 5% and 10 % global strain in histogram plots found in Figure 2.27. Due to the use of *in situ* HR-DIC within an SEM the image acquisition was limited to 6 images throughout the tensile test, this is shown in the stress-strain curve in Figure 2.28. This meant that using HR-DIC would not be able to produce accurate strain values throughout the entirety of the test and could not yield a complete stress strain curve.

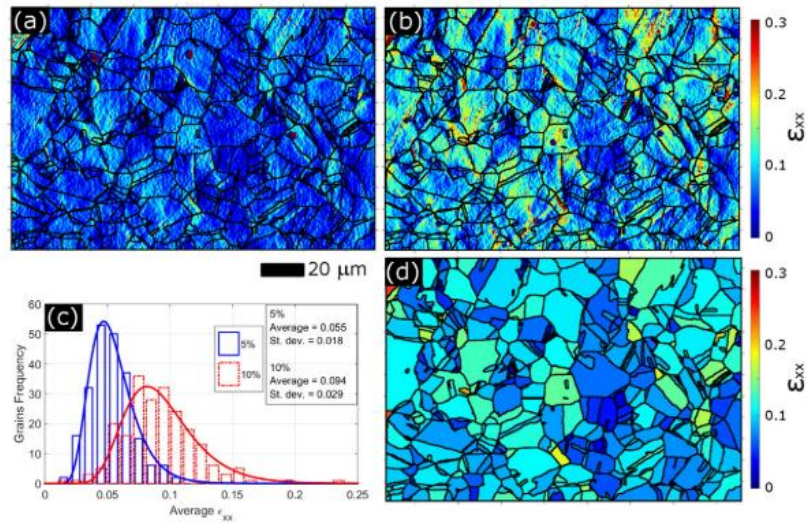


Figure 2.27: Low magnification strain maps overlaid with EBSD grain boundary maps, showing the heterogenous nature of strain accommodation within individual grains. Panels (a) and (b) show ϵ_{xx} at 5% and 10% applied strain respectively. (c) Histogram plot of ϵ_{xx} for individual grains at 5% and 10% macroscopic global strain. (d) Map of the average strain in the loading direction (ϵ_{xx}), averaged over each grain at 10% global strain used for producing (c) (15)

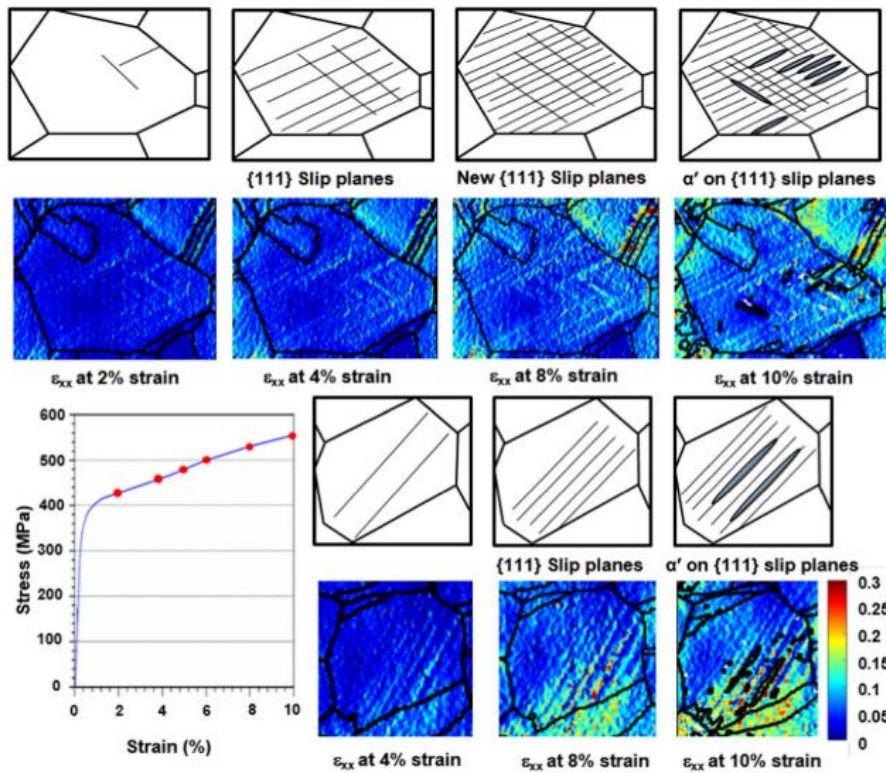


Figure 2.28: Mechanisms for martensitic phase transformation in fully austenitic grains. Grain 1 (top) and grain 2 (bottom) are shown with the corresponding DIC strain maps, made at various strain increments represented by red dots on the stress-strain curve (15).

Forsey et al. (14) studied the effect of anisotropy on additively manufactured nickel superalloys by performing two tensile tests, the first on a meso-scale using a telecentric lens and the second using a

micro tensile tester and an SEM. By plotting the results at the same local strain value, the mesoscopic deformation could be linked to the microstructural features (Figure 2.29). This work showed the deviation from the average macro stress strain for two distinct neighbouring regions in the meso-scale. In addition, strain concentrations were related to the crystallographic structure by directly comparing EBSD analysis to the spatially resolved map of the principal strain angle.

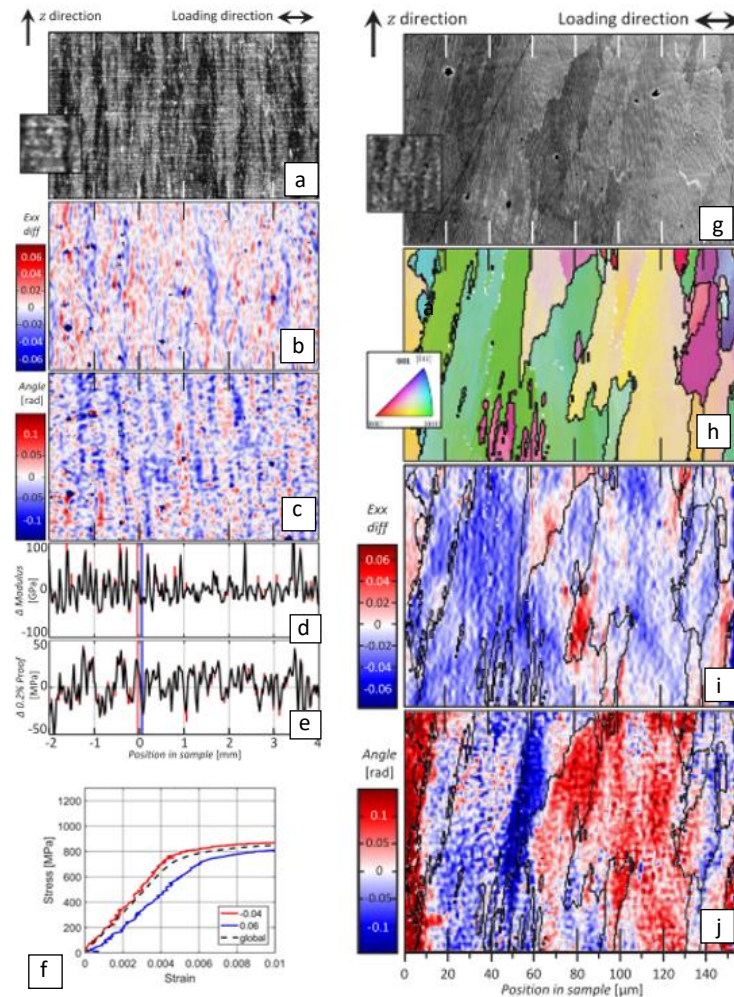


Figure 2.29: Meso-scale DIC results (a-f), a) an example image used for analysis with insert showing pixel definition, b) spatially resolved map of loading direction strain (E_{xx}) difference to global value at 0.075 strain, c) spatially resolved map of principal strain angle with respect to the loading direction at the same strain value, d) variation of elastic modulus along the length of sample gauge and e) variation of 0.2% proof stress along the length of sample gauge, f) Tensile curve to 0.01 strain of meso-scale sample, with curves from the red and blue regions highlighted in d) and e). Micro-scale DIC results (g-j), g) an example image used for analysis with insert showing pixel definition, h) Inverse pole figure EBSD orientation map of area tested using DIC i) spatially resolved map of difference in loading direction strain (E_{xx}) to sample average (of 0.075 strain) and j) spatially resolved map of principal strain angle with respect to the loading direction (14).

2.7. Summary

This section has discussed the fundamental principles that will be used for this project as a way of verifying the accuracy of using HR-DIC and EBSD to analyse the microstructure of the material. It has been shown that neutron diffraction is a well-established technique which can be used to find the strain data for the bulk of a material. However, due to its high cost and limited availability, it can be difficult to gain access. Additionally, HR-DIC has proven to be effective at deciphering grain scale variations in strain. Although, HR-DIC has yet to be utilised as a technique that can yield strain data for the bulk of a material.

3. Research Questions

The literature review has shown the importance of understanding the microstructural mechanics that occur during the deformation of polycrystalline structures. The anisotropy in deformation that occurs can lead to vastly different strain values throughout a material. Neutron diffraction is well understood as a method to measure this throughout the material; however, it is expensive only available at several national facilities and does not give information on the spatial variations from grain to grain. HR-DIC has primarily been used to study the effect of loading on individual grains or very small groups of grains, however, with suitable optics and sufficient camera resolution and by imposing the strain map data onto a large EBSD map strain in many grains can be assessed. The produced aggregate data results could offer comparative insights into neutron diffraction and produce a bulk measuring technique which is more easily accessible and less expensive.

As this project is comparing strain measurement techniques, a known metallurgical phenomenon was selected to be studied in all three strain measurement analyses, in this project it was the effect of SFE energy on deformation mechanics.

The key question for the research project is, therefore,

- Is the data collected from high-resolution digital image correlation sufficient to measure the influence of stacking fault energies on deformation mechanics?

This can be separated into smaller questions which will be answered in this project.

- Can neutron diffraction be used to show the effects of SFE on the deformation behaviour of three materials: SS316, INVAR and nickel?
- To what extent can post-mortem EBSD be used to calculate strain within a subset of grains which consist of a similar crystallographic orientation?
- Can HR-DIC be used to yield statistical results comparative to neutron diffraction without losing the spatial data?
- How do the strain analysis techniques, neutron diffraction and EBSD metrics compare to the results of the HR-DIC?

4. Investigating the Influence SFE on Deformation Mechanics using *in situ* Neutron Diffraction

4.1. Overview

Stainless steel 316 contains multiple elements and phases leading to a complex structure which can lead to microstructural instabilities when conducting testing at high temperatures (127). Therefore, it is often useful to select a 'model material' which is more simplistic in structure but still holds many of the same attributes as the complex material that is to be studied. SS316 contains the highest constituent percentage of iron, however, pure iron has a BCC microstructure and therefore, the deformation behaviour is vastly different from an FCC material (128). SS316 also contains a substantial amount of nickel and as nickel is an FCC material that has similar lattice parameters to SS316, this has been suggested as a potential alternative. However, nickel has a high SFE and therefore plastically deforms by slip whereas SS316 has a low SFE and deforms primarily by twinning (33). In this project INVAR (FeNi36) has been proposed as an alternative as it contains a simplistic microstructure as it is a binary alloy, yet also has a low SFE. Neutron diffraction conducted during *in situ* tensile tests was performed on SS316, pure nickel and INVAR, these were modelled using elastic-plastic self-consistent (EPSC) modelling. This section will discuss the methodology used in these procedures and present the results of the *in situ* neutron diffraction and EPSC modelling. These tests have been conducted to form the baseline of comparisons for future tests reported in later chapters.

4.2. Methodology

This section will outline the methods used in this chapter for the *in situ* neutron diffraction tensile tests undertaken during this project. In addition, it will describe the methods used in the set-up of the EPSC modelling of the neutron data. As well as showing the preparation methods used for the texture analysis which were performed using EBSD.

4.2.1. Materials

The first material selected for the *in situ* neutron diffraction tensile tests was SS316. This stainless-steel alloy is typically used in high-pressure and temperature environments due to its ability to withstand these conditions. Nickel has been suggested as a 'model material' for SS316, this is due to the percentage of nickel and chromium in the SS316 chemical composition (Table 4.1) and the effect on the expected microstructure. The influence of the percentage weight of chromium and nickel on stainless steels can be found in Figure 4.1. This shows that the combination of Ni and Cr in an SS316 leads to an FCC structure. However, this does not consider the effect of SFE on the deformation

behaviour. As stainless steels typically have a low SFE, whilst pure metals have a high SFE (shown in Table 2.1), the deformation behaviour between SS316 and pure nickel is likely to be vastly different (the influence of SFE on the stress strain response of steels is shown in Figure 2.4). Therefore, INVAR, also known as FeNi36, has been suggested as an alternative due to its simple chemical composition and low SFE (Table 2.1). INVAR is a binary alloy known for its ability to reduce thermal expansion which occurs when an alloy is heated. The chemical composition of INVAR used in this project can be found in Table 4.2. Additionally, the pure nickel used in this project had a purity of 99.99%. All metals were forged and sourced by Smiths metal and had been obtained for previous projects. The grain sizes for the materials are measured and presented in Table 4.7.

Table 4.1: The chemical composition of the SS316 samples used in this test.

Chemical Composition (weight %)									
	C	Cr	Mo	Si	P	S	Ni	Mn	Fe
min		16.5	2.00				10.0		Bal
max	0.08	18.5	2.50	1.00	0.05	0.02	13.0	2.00	Bal

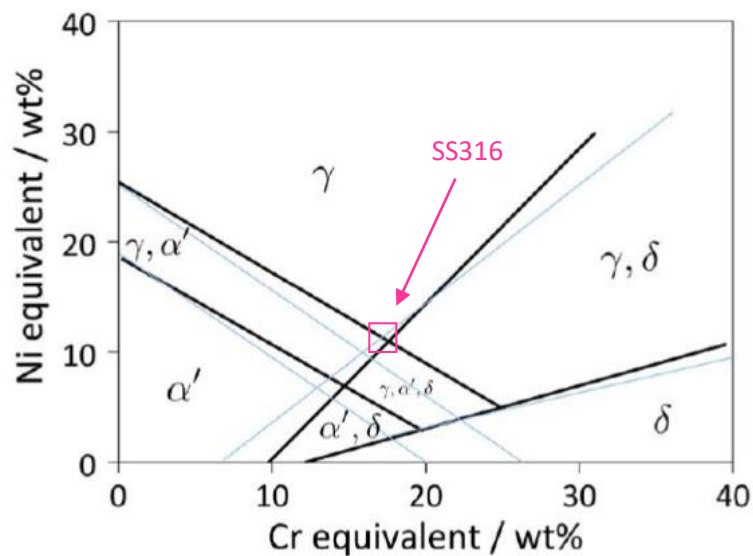


Figure 4.1: A Schaeffler diagram showing the microstructure expected by the weighted percentages of chromium and nickel in stainless steels. Here the black lines are for castings and the blue is for welds (128). Using the chemical composition for SS316 from Table 4.1, the expected microstructure can be seen.

Table 4.2: The chemical composition of the INVAR samples used in this test.

Chemical Composition (weight %)	
Fe	Ni
64	36

SS316 and pure nickel have very different behaviours during deformation but are both well understood. However, INVAR's deformation behaviour has not been studied to the same extent. Therefore, the addition of the Ni to Fe may have effects on the deformation such as resulting in twinning-induced plasticity (TWIP) (129).

4.2.2. *In situ* Tensile Testing at ENGIN-X

Mechanical testing using *in situ* neutron diffraction was used to characterise the stress-strain properties of materials with different stacking fault energies. Tensile tests involve applying a load in one direction to deform the sample. These tests discussed in this section were load-controlled meaning the load increased at a constant rate throughout the test. The neutron diffraction measurements were conducted using the ENGIN-X neutron diffractometer at the Rutherford Appleton Laboratory ISIS facility. Figure 4.2 shows a schematic of the designs used for *in situ* neutron diffraction tests.

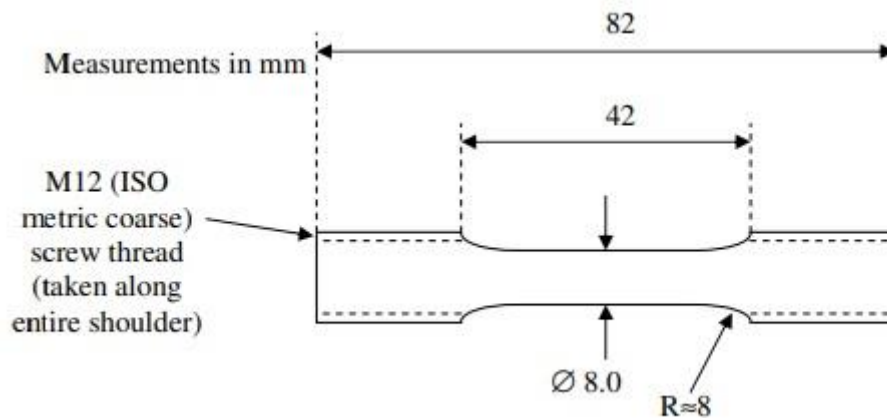


Figure 4.2: A schematic showing the tension test specimen design for the *in situ* neutron diffraction tests. Measurements are in mm.

4.2.2.1. ENGIN-X Neutron Diffractometer

Neutron diffraction can produce lattice strains for subsets of grains with similar orientations. These are predetermined by which orientations satisfy Bragg's Law. Figure 4.3 shows the diffraction pattern for a stainless steel specimen collected at ENGIN-X (97). Each peak corresponds to an (hkl) family of grains, characterised by the crystallographic plane contributing to the diffraction signal, as given by Bragg's Law of diffraction. Each of these families is a small fraction of the crystallites within the sampled volume. The lattice strains are recorded by two detectors and therefore give the lattice strain in the loading direction (longitudinal) and parallel to the loading direction (transverse).

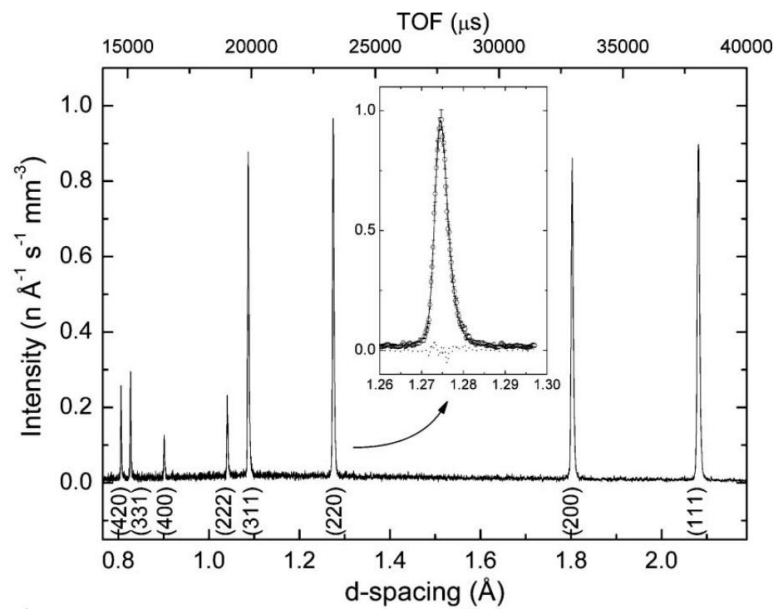


Figure 4.3: A typical diffraction spectrum for a stainless steel specimen measured at ENGIN-X (97).

The neutron diffraction experiments for this project were conducted using the ENGIN-X neutron diffractometer at the Rutherford Appleton Laboratory ISIS Facility. Where ENGIN-X is a time-of-flight neutron diffractometer and ISIS is the pulsed spallation neutron source. This section will briefly discuss the operational procedure of the instrument, but further information can be found in (97) and (96). Figure 4.4 shows a diagram of the set-up used at ENGIN-X for neutron diffraction. The specimen is placed at a 45° angle to the incident beam of neutrons, this is to align the loading direction with the direction of strain measurement. The slit can be adjusted both horizontally and vertically to limit the height and breadth of the neutron beam. The depth of the neutron beam is controlled by the position of the radial collimators. The overall size of the gauge volume is governed by a combination of the slit size and the collimator size (97). Behind the radial collimators sit the two diffraction detector banks at $\pm 90^\circ$ angle to the incident beam. Both banks contain 1200 ZnS/ ^6Li scintillator detector elements (96). These are arranged in 5 units which are stacked vertically above one another, comprising 240 horizontally stacked elements. The individual data banks are focused on a single angle with a resolution of $\sim \pm 7.5$ degrees.

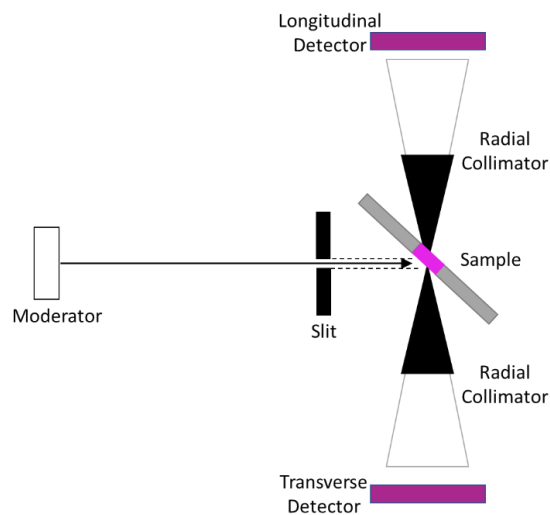


Figure 4.4: Schematic showing the neutron beam path and relative positions of the specimen and the detectors, which are used to record the longitudinal and transverse strains, in the ENGIN-X diffractometer.

4.2.2.2. Tensile Testing Rig at ENGIN-X

The ENGIN-X diffractometer contains specialist equipment to simulate specific sample environments, this includes a custom-designed mechanical stress rig, a high-temperature furnace, and a cryogenic chamber. For this project, the mechanical stress rig was used to conduct in situ tensile tests in the neutron beam. The Instron servo-hydraulic stress rig has a maximum loading

capacity of 100 kN (97). The stress rig and its relation to the neutron beam can be seen in Figure 4.5 and Figure 4.6. The sample design used for these experiments can be found in Figure 4.2. To ensure the sample was within the line of the neutron beam a telescope was used. These experiments used 4 mm collimators and 4 mm slits. The count time used was ~ 10 microamps. To analyse the results of the *in situ* neutron diffraction tensile tests, the Open GENIE program (130) was used at the ISIS facility.

The *in situ* tensile tests were performed on samples of SS316, pure nickel and INVAR, where the specimens were taken to 3% strain before unloading. As time was limited at the ENGIN-X facility, 3% strain was selected to ensure there was as many data points as possible in the low strain region. The lower strain values were required to compare the results to the HR-DIC tests, as it was unknown if the HR-DIC experiment could measure high strain values.

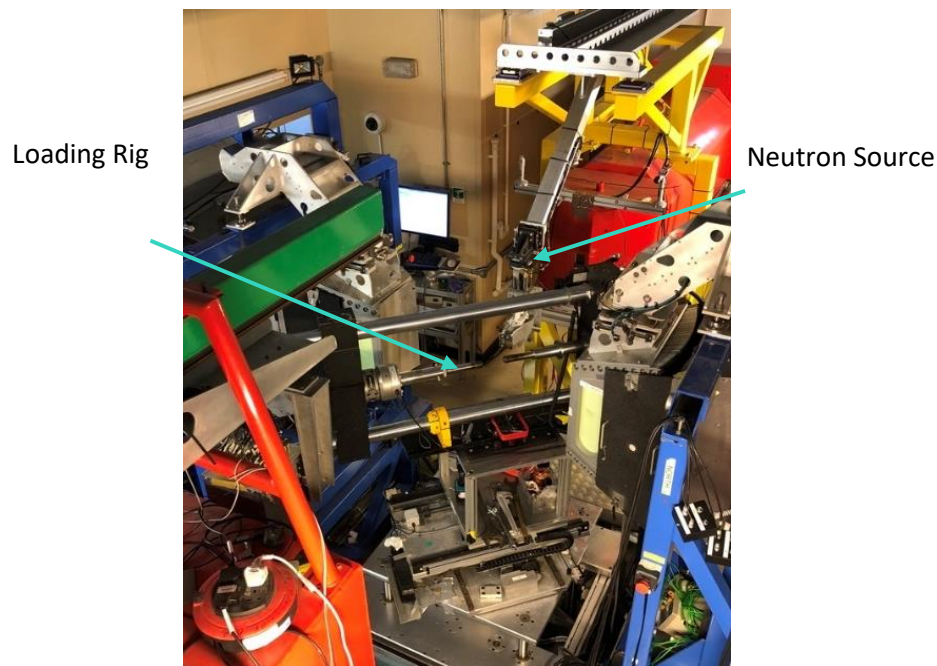


Figure 4.5: An image showing the angle of the tensile testing machine and the source of the neutrons at ENGIN-X.

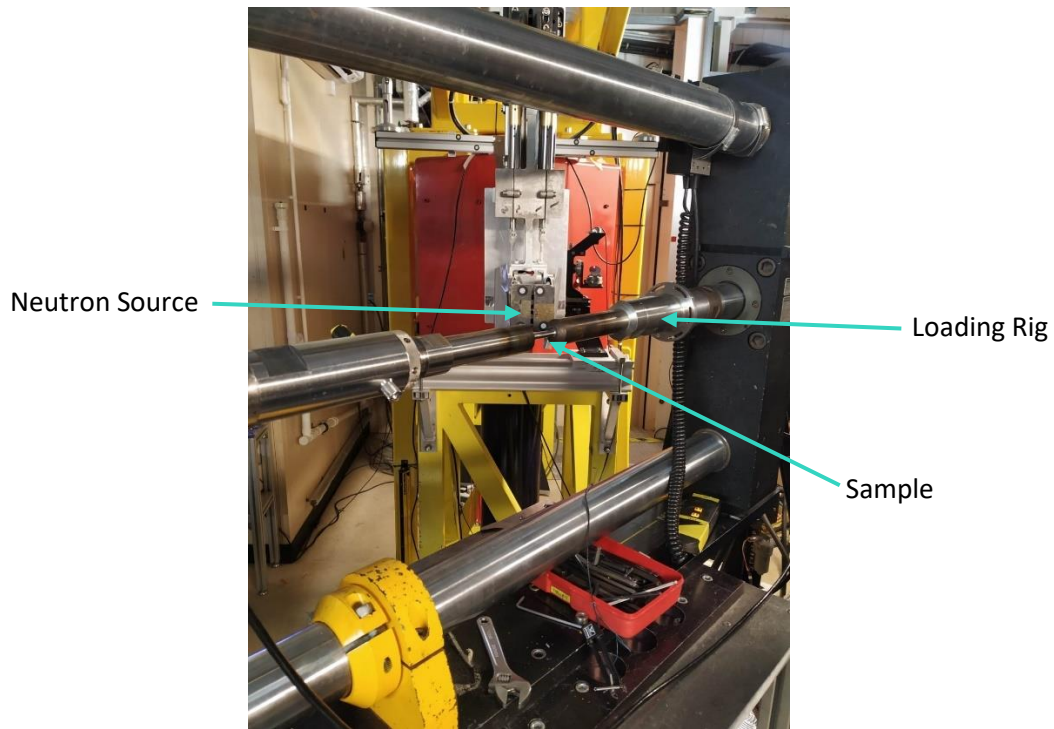


Figure 4.6 Set-up of the in-situ mechanical testing stress rig at ENGIn-X beamline.

4.3. Texture Analysis using EBSD

For polycrystalline materials, the texture will be present if the orientation of the grains within the material is not completely random (131). Texture can influence the deformation of metal as many of the mechanical properties of polycrystalline materials are anisotropic (131). Additionally, the EPSC and VPSC models rely on an accurate input texture file to yield the most accurate results. EBSD was selected over other texture analysis methods, such as x-ray diffraction, as it provides spatially resolved texture analysis and has higher resolution.

When preparing samples for EBSD analysis, the surface must be uniformly flat as any variations in the topography of the surface can disrupt the Kikuchi patterns (54,56). However, preparation methods which can produce a planar surface can cause varying degrees of damage, observed in the form of micro-strain in metals (132). This effect can be reduced by carefully choosing the grinding and polishing stages in the preparation process. Colloidal silica (SiO_2) is often regarded as the standard abrasive used in the final stages of polishing to produce a finish suitable for EBSD analysis (54). This is because the colloidal silica grinding papers can be slowly decreased in particle size to result in a deformation-free surface. However, due to the depth of the deformation layer on the surface of some metals, particularly soft metals which readily undergo oxidation on the surface, an additional step may be required. Electropolishing can be used in the final stages of polishing, this is because it is not an abrasive technique and, therefore, produces surfaces with a low micro-strain (54).

EBSD analysis was used in this project to characterise the microstructure of the tensile test samples. After the tensile tests, cross-sectional disks were cut from neutron diffraction samples using EDM. To conduct EBSD analysis on deformed and undeformed regions of the samples, a cross-section of the sample was cut within the gauge length and a disk of nominally identical undeformed material could be cut from the region within the threads of the samples. To ensure comparability in terms of orientation could be maintained between the two regions, a notch marker was created using an EDM before cutting the disks from the tensile specimens. The grinding and polishing procedures are outlined in Table 4.3 and

Table 4.4 respectively. Following these steps, electrolytic polishing was carried out as the final stage before characterisation. The electrolyte solution used consisted of 85% ethanol, 10% 2-butoxyethanol and 5% water (branded as Struers A2 electrolyte). The electropolishing solution and parameters were kept the same for all specimens and were a voltage of 22V, flowrate 20 and a time of 45 seconds.

Table 4.3 Specimen grinding guidelines used in the preparation of the specimen for EBSD analysis

Grinding paper	Grit size (μm)	Time (minutes)
P800	22	5
P1200	15	5
P2500	8.5	5
P4000	5	5

Table 4.4: Specimen polishing guidelines used in the preparation of the specimen for EBSD analysis

Polishing Cloth	Diamond particle size (μm)	Time (minutes)
MD-pan	9	5
MD-pan	3	5
Multicloth M	1	5

Post-mortem EBSD analysis was performed on the tensile test specimens for SS316, INVAR and pure nickel. The machine used was a Zeiss Supra 55VP field emission gun scanning electron microscope using an oxford instruments detector. The parameters used in the EBSD analysis can be found in Table 4.5. The EBSD maps for all specimens were 0.9 mm by 1.2 mm in size and had a step size of 1 μm .

Table 4.5: Shows the EBSD measurement parameters used.

Accelerating voltage	Working distance	Tilt Angle	Mode	Aperture Size
20 kV	15 ± 0.1 mm	70°	High current	120 μm

4.3.1. Grain Size Measurements

To measure the average grain sizes of the neutron diffraction specimens, the standard line interception method was used (133). To achieve this, the image analysis software, ImageJ (134,135), was used on the EBSD maps collected through post-mortem EBSD analysis (Figure 4.8). By using the length scale shown on the EBSD images, random lines could be drawn within the image and the number of intersections was counted, by averaging these values throughout the image the average grain size could be estimated.

4.4. Elastic Modulus Measurements

The elastic modulus is an intrinsic property of any metal and provides a measurement of resistance against mechanical deformation when subjected to an external load. When considering the modelling of metal, it is important to have accurate elastic modulus values. Hence, to run the EPSC models effectively in this project elastic modulus values were calculated for the samples of SS316, INVAR and pure nickel. When calculating the elastic modulus using the neutron diffraction tensile test data it was found that the elastic modulus for the specimens was significantly different that what had been recorded in other papers. Therefore, an independent measurement of the elastic modulus was required. To achieve this, 'natural frequency' tests were performed on specimens of these materials to determine the dynamic elastic modulus of the materials. Natural frequency tests involve striking the material with a mass and measuring the resonance of a sample.

The basic principle behind the impulse excitation technique is that the materials elastic modulus is directly proportional to the resonance frequency of flexural vibration (136,137), determined by the velocity of wave propagation, and the density of the material (138),

$$E = \rho v^2 \quad (4-1)$$

where E is the elastic modulus, ρ is the density of the material and v is the velocity of wave propagation. For a rectangular-shaped beam, such as the ones used in this project the dynamic elastic modulus is computed from the expression (138),

$$E = 0.945m \left(\frac{f}{t}\right)^2 \left(\frac{l^4}{b}\right) T_i \quad (4-2)$$

where m is the mass, f is the resonance frequency and l , b and t are the specimen length, width and thickness, respectively. T_i is the correction factor given by

$$T_i = 0.585(1 + lt) \quad (4-3)$$

These equations highlight the importance of accurate geometrical dimension and mass measurements of the test specimens to achieve precise elastic modulus measurements (139).

4.4.1. Sample Preparation for Elastic Modulus Tests

The specimen preparation for elastic modulus measurements of the SS316, INVAR and pure nickel specimens were carried out to the ASTM E1876-15 standard (139). Rectangular specimens were machined using an electro-discharge machine (EDM) to a very fine surface finish of 0.01mm. The dimensions of the test samples were measured eight times using a Digital Vernier Caliper, with the average of the values presented in Table 4.6. The results for these tests are found in section 4.6.2.

Table 4.6: Specimen dimensions (an average taken from 8 measurements) for the dynamic elastic modulus.

Material	Length, l (mm)	Width, b (mm)	Thickness, t (mm)	Mass, m (g)
SS316	50.083	4.988	2.988	5.924
INVAR	50.037	4.991	2.989	6.038
Nickel	50.019	4.991	2.989	6.596

4.5. EPSC modelling

The EPSC model (65), discussed in section 2.5.2.2, was used in this project to predict the lattice strain response of the neutron diffraction data collected for SS316, INVAR and pure nickel. To accurately predict the behaviour of the materials, texture analysis of the undeformed specimens was required. Therefore, EBSD was performed was conducted on undeformed regions of the three material specimens, details of the EBSD analysis parameters can be seen in section 4.3. Following this, a MATLAB code was created to convert the raw EBSD data into an ODF approximation of the texture file, this was then input into the EPSC code as an initial texture file. Additionally, the elastic constants measured in the elastic constant tests (discussed in section 4.4) were also used to tailor the EPSC models to each of the selected materials. Once the EPSC model was set up for each material, the model required optimisation using the experimental macro stress-strain curves recorded by the *in situ* neutron diffraction tensile tests. Details of the optimising process will be discussed in the following section.

4.5.1. Optimisation

The neutron macro stress-strain results were used to construct EPSC models by using a least squares-based MATLAB lab code to optimize the input parameters τ_0 , θ_0 , θ_1 , τ_1 . The optimisation method is shown in Figure 4.7, where the experimental data is the macro stress-strain curves calculated from the *in situ* neutron diffraction tensile tests. To find the optimal values the fit for not only the macro stress-strain curve was considered but also the lattice strain. By studying the lattice strain, each of the parameters was individually varied while the others were fixed, and it was seen that the position of onset plastic deformation was dominated by the τ_0 value. Therefore, the optimal value was found for τ_0 and then fixed and then the least squares algorithm was run for the remaining variables.

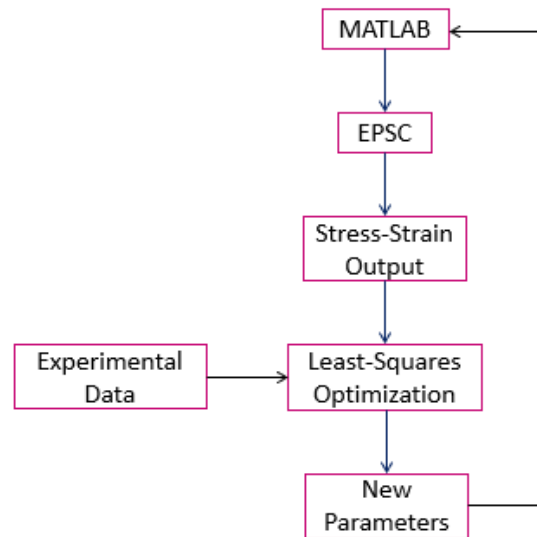


Figure 4.7 Flow chart of parameter optimisation routine utilizing built-in MATLAB least-squares optimization capability.

4.6. Results

This section will present the results of the *in situ* neutron diffraction tensile tests used to investigate the influence of SFE on the deformation of three materials with differing SFEs. The materials selected were SS 316, INVAR, and pure nickel. The results of the EPSC model are also presented in this section which uses the results of *in situ* neutron diffraction tensile tests to optimise the macro stress-strain data.

4.6.1. EBSD Analysis

EBSD analysis was performed on the tensile specimens following the tensile tests. To find the texture before loading, a sample was taken from the grip region of the sample. The EBSD analysis was used in the EPSC models to give the initial texture file. The results of the EBSD analysis for the undeformed regions of SS316, INVAR and pure nickel samples can be found in Figure 4.8 (a), (b) and (c) respectively. These EBSD maps were only indexed for 1 phase, this was nickel for pure nickel and for Fe-FCC for both INVAR and SS316. Evidence of a second-phase particle is shown as an unindexed point on the maps. Additionally, the results of the grain size measurements calculated using the standard line intersection method and ImageJ (method discussed in section 4.3.1) are shown in Table 4.7. This table also shows the estimated number of grains imaged by the EBSD analysis by using the map size (0.9 mm by 1.2 mm) and the grain lengths. The grain size of the SS316 is significantly larger than the other specimens, this was due to SS316 being provided by industry.

Although a smaller grain size would be better to compare to the other materials and provide lattice strain data on a larger number of grains, as the lattice strains had been measured using neutron diffraction SS316 in previous work (9), this ensured a level of verification for SS316 if the large grain size influenced the results. Therefore, to ensure the best neutron diffraction data could be collected for INVAR and pure nickel samples, the as-received grain size was kept for these two materials.

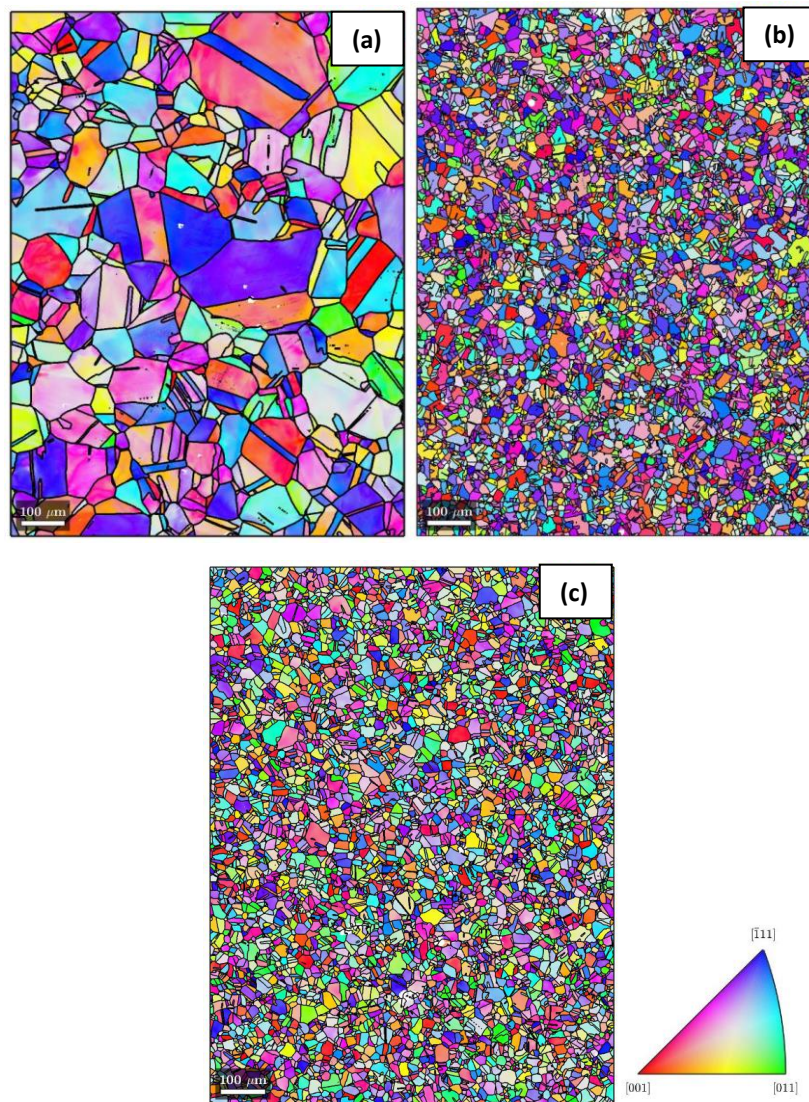


Figure 4.8: EBSD maps with ipf colouring of the undeformed region used to provide the initial texture files for the EPSC model for (a) SS316, (b) INVAR and (c) pure nickel.

Table 4.7: The grain size measurements for the SS316, INVAR and pure nickel samples.

Material	Average Grain Length (μm)	Estimated Number of Grains Imaged
SS316	69.5	223
INVAR	16.57	3911
Pure Nickel	15.24	4650

4.6.2. Dynamic Elastic Modulus

The results for dynamic elastic modulus tests for the SS316, INVAR and pure nickel samples can be found in Table 4.8. These results were calculated using Equations (4-2) and (4-3) with the dimensions and mass values found in Table 4.6 for each material. Here it can be seen that the INVAR sample has an elastic modulus which is much smaller than the other samples.

Table 4.8: The dynamic elastic modulus results for the SS316, INVAR and pure nickel.

Material	Elastic Constant (GPa)
SS316	198.94
INVAR	144.38
Pure Nickel	210.02

4.6.3. In situ Tensile tests

This section presents the results of the macro stress-strain results from the *in situ* neutron diffraction tensile tests (method discussed in section 4.2.2) of samples of SS316, INVAR and pure nickel. Figure 4.9 shows the stress and macro-strain results recorded for these three specimens during the loading process. The SS316 specimen is shown by the pink markers in Figure 4.9, here yield occurs at ~ 350 MPa. Post-yield the SS316 specimen shows an increase in the slope of the gradient. The INVAR specimen is shown by the green markers in Figure 4.9. Yield occurs at ~ 150 MPa and post-yield the gradient shows an increase. For the nickel, shown in this figure by the blue markers, here yield is ~ 200 MPa and post-yield the Ni specimen shows little change in gradient with the gradient being horizontal.

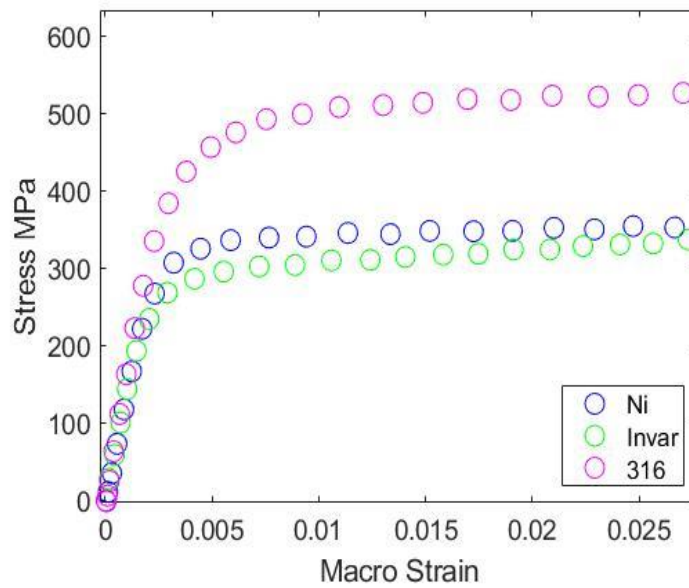


Figure 4.9: Macro stress-strain curves obtained during the *in situ* neutron diffraction tensile tests for the SS316, INVAR, and pure nickel specimens.

4.6.3.1. Lattice strain

Figure 4.10 shows the longitudinal and transverse lattice strains for the SS316 sample, which were obtained using *in situ* neutron diffraction as described in section 4.2.2. SS316 has an FCC crystallographic microstructure (highlighted in Figure 4.1), therefore the orientation subsets which were studied were the {111}, {220} and the {200}. Engin-X, the neutron diffractometer used in this project, has a resolution of $\sim \pm 7.5$ degrees, therefore, the subsets are within this degree of the given orientation. As neutron diffraction shows solely the elastic strains it can be assumed that when the lattice strain ceases to increase with increased stress that plastic deformation has occurred. This is particularly noticeable in the {220}-orientation subset in the loading (longitudinal) direction. The highest strain value recorded for the {220} subset in the loading direction is 0.0017 and in the transverse direction is -0.000964. The {111} orientation in the longitudinal direction shows a continued linear increase in the strain values as stress is increased, showing elastic strain to be constant throughout loading. The maximum strain value the {111} subset increases to in the loading direction is 0.0019 and in the transverse direction, it is -0.000579. The {200}-orientation subset shows an increase in strain with increasing stress, this subset increase linearly up to 300 MPa, however, at this point the line curves, with strain increasing more as stress increases. The maximum value recorded for the {200} subset is 0.0047 in the loading direction and in the transverse direction it is -0.0011.

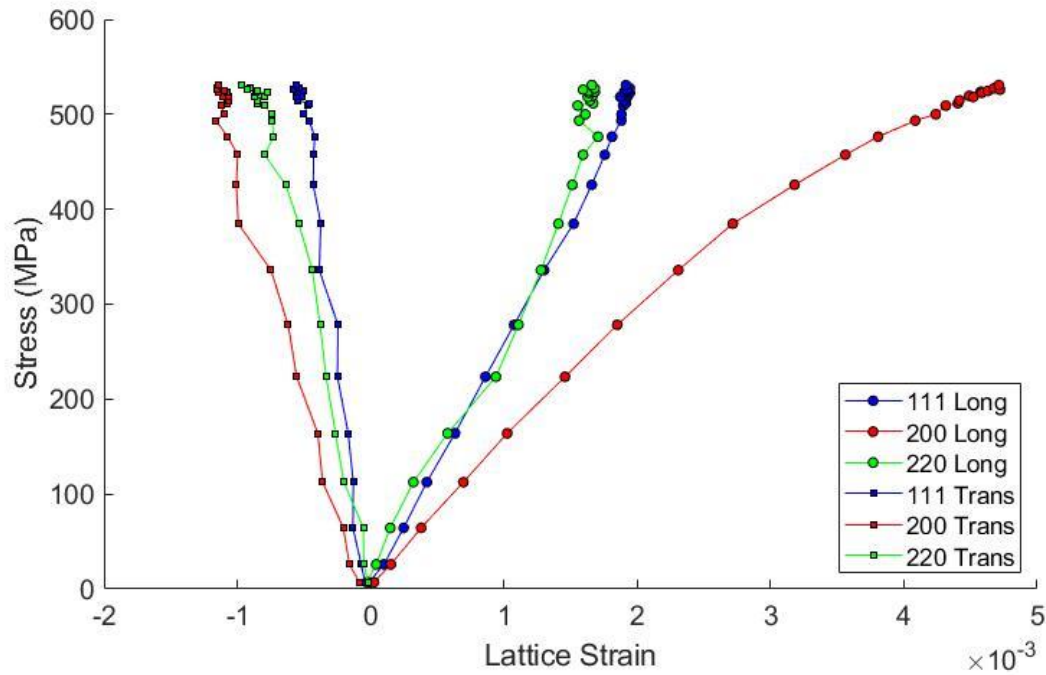


Figure 4.10: Plot showing the lattice strain for SS316 in the grain subsets: 111, 220 and 200. These are seen in both the transverse and longitudinal directions.

Figure 4.11 shows the longitudinal and transverse lattice strains for the INVAR sample. The {111} orientation subset shows a linear increase in strain with increasing stress up until a stress value of ~ 40 MPa, beyond this point the gradient steepens. At a global strain value of 0.03, the {111} subset has a strain value of 0.0017 in the loading direction and a strain value of -0.00042 in the transverse direction. The {220} subset shows a linear increase in strain with stress up to a stress value of ~ 200 MPa. At a strain value of 101 MPa, there appears to be an anomaly in the strain value recorded. At a global strain value of 0.03, the {220} subset has a strain value of 0.015 in the loading direction and -0.00083 in the transverse direction. The {200} subset shows there to be a linear increase in elastic lattice strain as the stress increases up until a value of 145 MPa, beyond this the gradient decreases leading to a non-linear increase in strain with increasing stress values. At a global strain value of 0.03, the {200} subset has a lattice strain value of 0.004 in the loading direction and a lattice strain value of -0.0011 in the transverse direction.

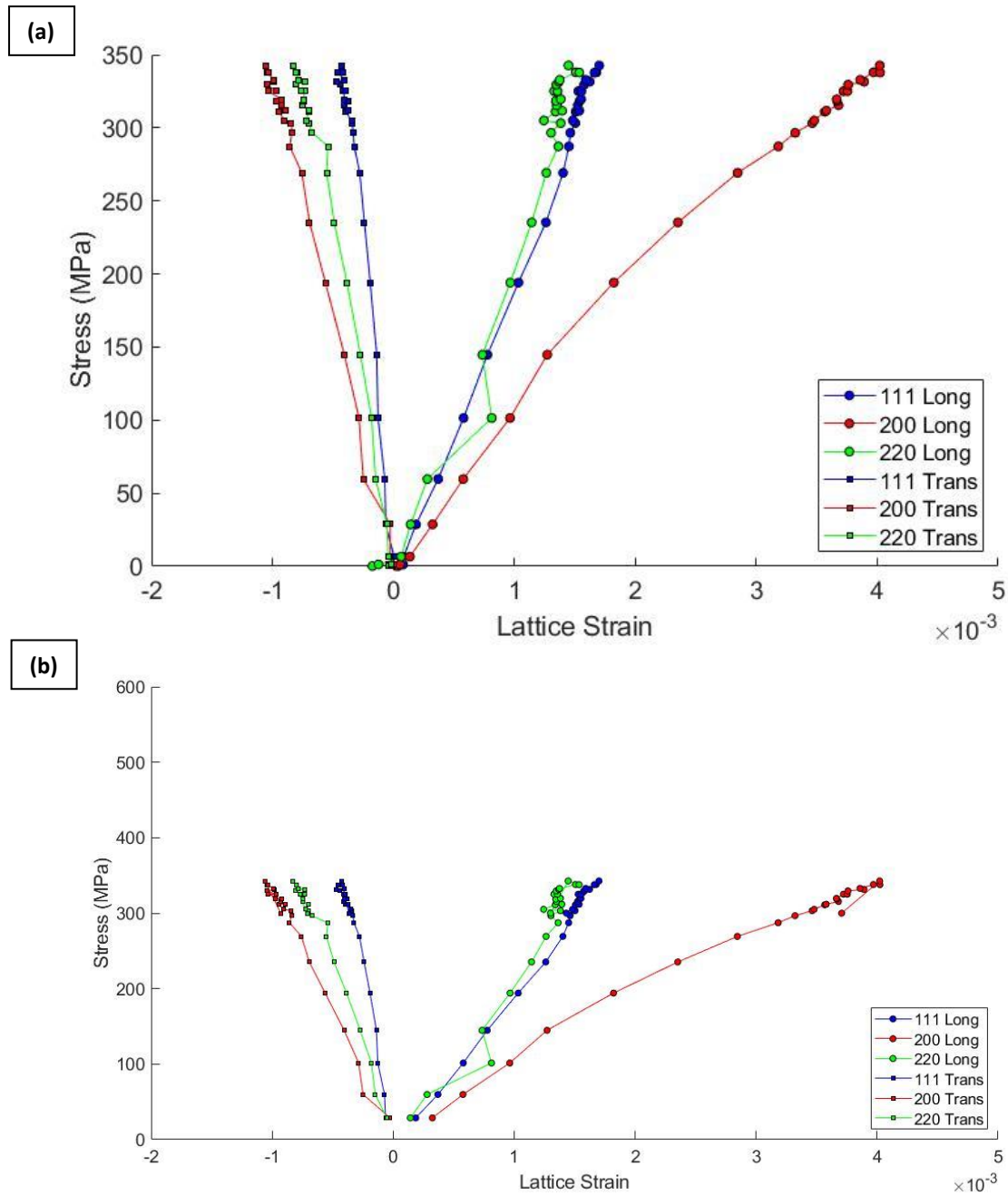


Figure 4.11: Plot showing the lattice strain for INVAR in the grain orientation subsets: 111, 200 and 200, in the transverse and longitudinal directions. Here (a) is the best fit scale to highlight the behaviours of the different orientation subset and (b) shows the comparative scale (same y-axis) to the SS316 specimen in Figure 4.10.

Figure 4.12 shows the average longitudinal and transverse lattice strains for the pure nickel sample in the {111}, {220} and {200} orientations. For the {111} subset, the change in strain by increasing stress showed a linear increase up at a stress of 74 MPa, beyond this, a non-linear increase begins. At a global strain value of 0.03, the {111} subset had a lattice strain value of 0.0013 in the loading direction and a value of -0.000432. The {220} doesn't show a clear linear increase in the elastic region, however at a stress value of 168 MPa the gradient of the curve decreases. At a global strain

value of 0.03, the {220} subset has a lattice strain value of 0.0013 and a value of -0.00052 in the transverse direction. The {200} subset shows a linear increase in strain up to a stress value of 118 MPa, however, beyond this point there is not the same clear decrease in gradient which is observed in the SS316 and INVAR data sets. At a global strain value of 0.03, the {200} subset has a lattice strain value of 0.0022 in the loading direction and -0.00052 in the transverse direction.

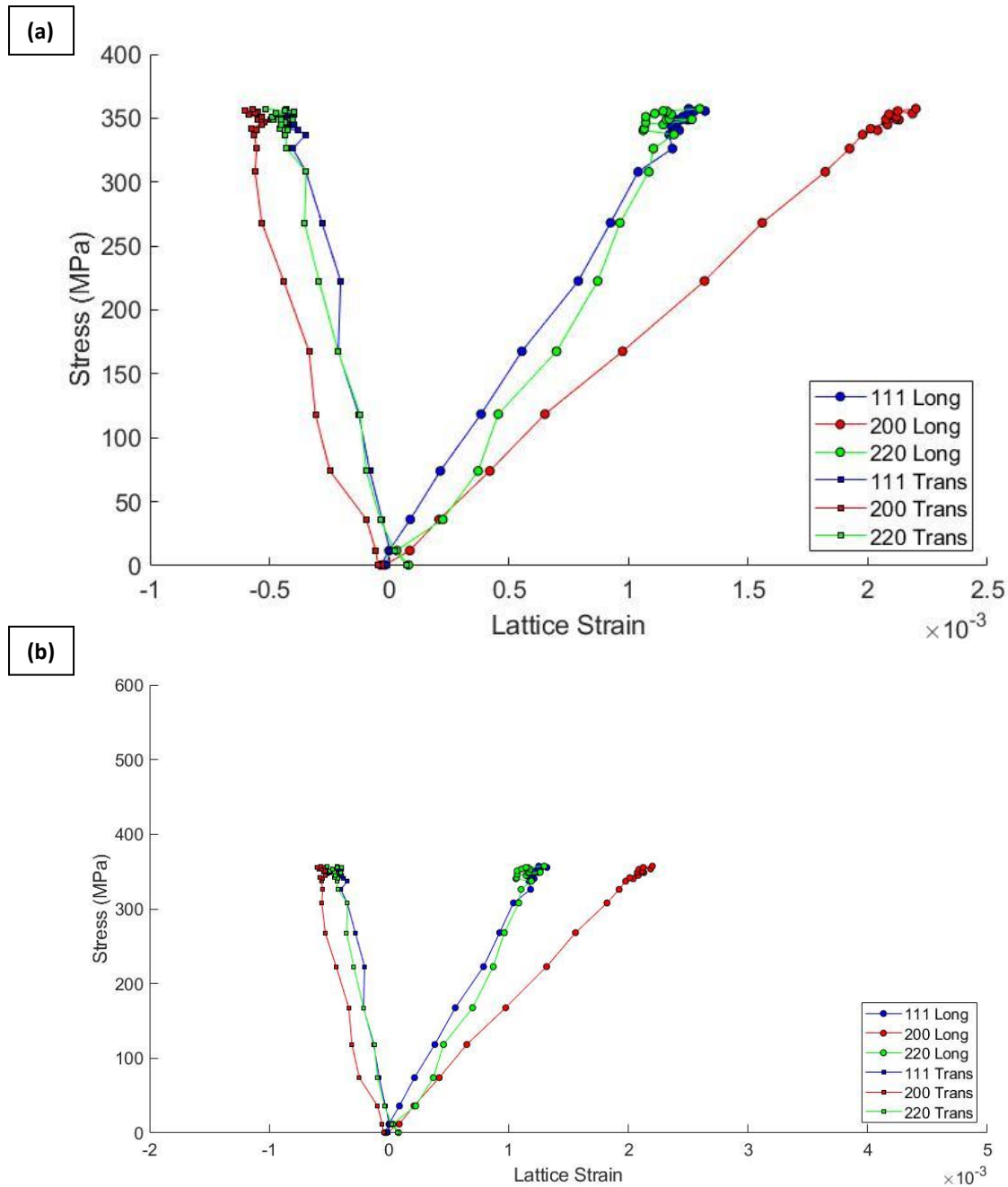


Figure 4.12: Plot showing the lattice strain for pure nickel in the grain subsets: 111, 200 and 200, for the transverse and longitudinal directions. Here (a) is the best fit scale to highlight the behaviours of the different orientation subset and (b) shows the comparative scale (same y-axis) to the SS316 specimen in Figure 4.10.

4.6.3.2. Full-Width Half Maximum

The change in the spread of the diffraction peaks collected through neutron diffraction can be linked to both grain size and plastic deformation. The change in peak width can be measured by calculating the FWHM (discussed in section 2.6.4.1) during the application of mechanical stress. Figure 4.13 shows the FWHM for the SS316 sample. For the {111} subset of grains, the FWHM is ~ 140 throughout the increase in stress. The 200 subset of grains shows FWHM to be ~ 140 up until 450 MPa, at that point the FWHM escalates to ~ 160 . The {220} subset shows more deviation in FWHM value during loading, however, there appears to be an increase in the value above 500 MPa.

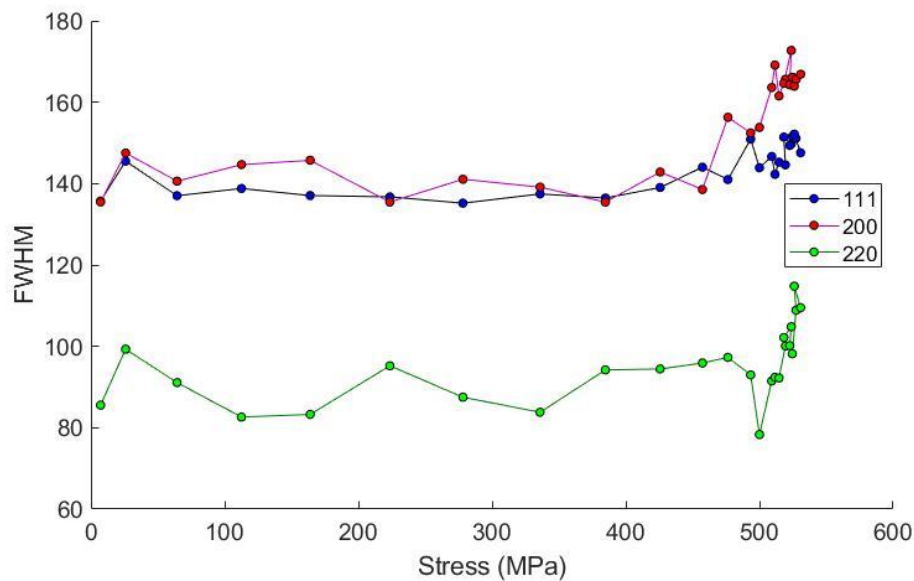


Figure 4.13: Plot of the FWHM compared to stress values for the *in situ* neutron diffraction tensile tests for the selected subsets of grains with crystallographic orientations within 7.5 degrees of the 111, 200 and 220 for SS316.

Figure 4.14 shows the FWHM for increasing stress for the INVAR sample. The 111 and 220 subsets show little change in the FWHM during the loading up to 300 MPa. The 111 subset remains between 130 and 135 FWHM up until 300 MPa where the FWHM is around 140 FWHM. The 220 subset shows an increase from 80 to 90 FWHM after around 300 MPa. The 200-orientation subset of grains shows a larger increase, from 0 to 300 MPa the FWHM is at 120 but beyond 300 MPa it increases to 140.

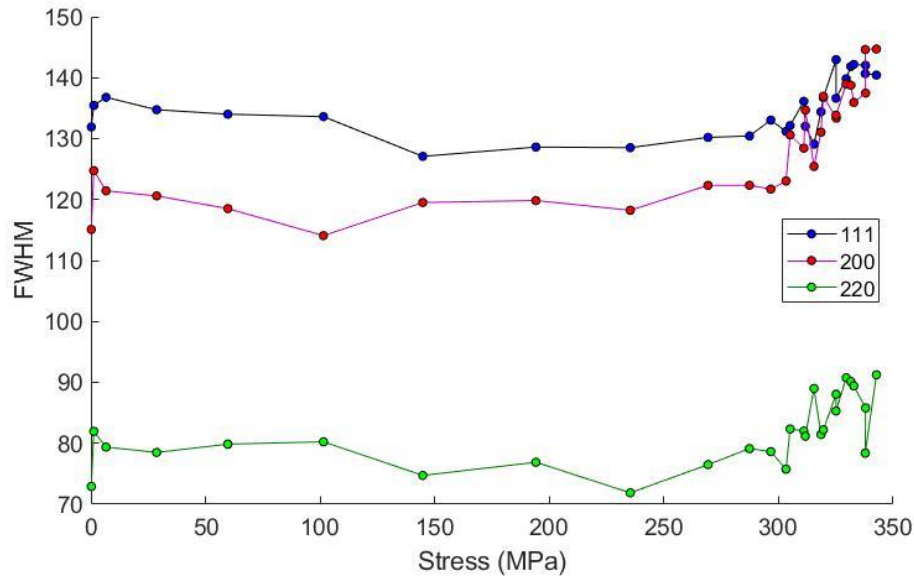


Figure 4.14: Plot of the FWHM compared to stress values for in situ neutron diffraction tensile tests for the selected subsets of grains with crystallographic orientations within 7.5 degrees of the 111, 200 and 220 for INVAR.

Figure 4.15 shows the FWHM for increasing stress for the pure nickel sample. The FWHM shows more variation for the subsets throughout loading than observed for the other materials. The 220 shows some increase in the average FWHM value, from 0 to 325 MPa the average is ~80 above 325 MPa the average is around 90 FWHM. The 111 shows the least deviation during the lower stresses with the average FWHM being ~ 135 but increasing to ~ 140 above 350 MPa. The 200 subset of grains shows little change in the FWHM throughout the test and even beyond yield at 325 MPa, the average remains at around 125 but with some values showing an increase.

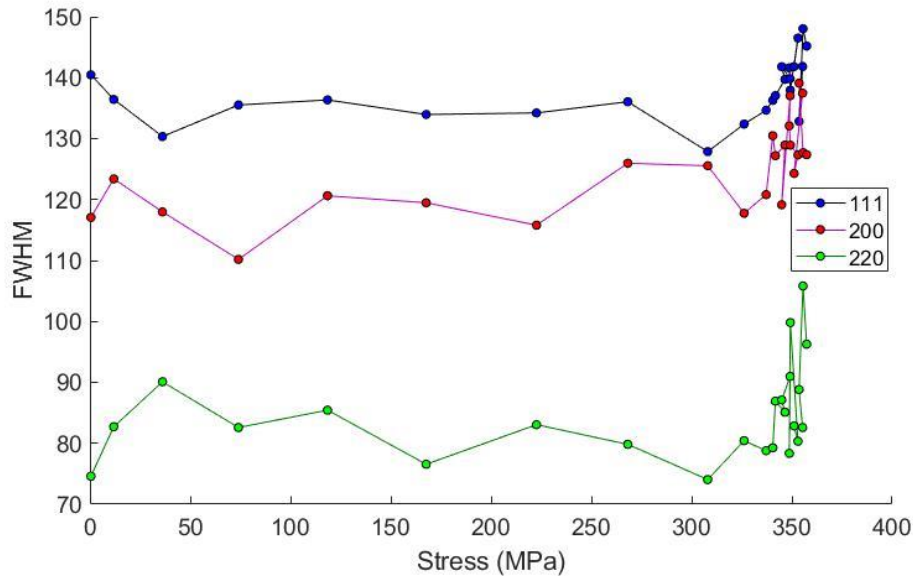


Figure 4.15: Plot of the FWHM compared to stress values for *in situ* neutron diffraction tensile tests for the selected subsets of grains with crystallographic orientations within 7.5 degrees of the 111, 200 and 220 for pure nickel.

4.6.4. Validation using the EPSC model

The section will present the results of the EPSC model and compare them to the experimental data collected through *in situ* neutron diffraction. The EPSC model is explained in section 4.5 and the process of using the experimental data to optimise the model is found in Figure 4.7. The EPSC model contains four fixing parameters, these values were optimised using MATLAB to write a code to fit the model by using the least-squares method. The EPSC model requires an initial texture file of the sample, which was collected for each sample using EBSD analysis, the process of collecting the texture analysis is discussed in section 4.3. Additionally, the EPSC model required accurate values of elastic constants, the values used in the model can be found in Table 4.8. It was found by fixing each parameter individually that the τ_0 value dominated the fitting. Therefore, by doing an initial fitting to find the $\tau_0, \tau_1, \theta_0, \theta_1$ values and then fixing τ_0 and then optimising the $\tau_1, \theta_0, \theta_1$ values it was found to achieve the best fit. The values of $\tau_0, \tau_1, \theta_0, \theta_1$ used to optimize the EPSC model can be found in Table 4.9.

Table 4.9 The fitting parameters used in obtaining the best fit between the EPSC model and the experimental data.

Material	τ_0 (MPa)	τ_1 (MPa)	θ_0 (MPa)	θ_1 (MPa)
Nickel	89	9	6564	145
Invar	84	12	9948	180
SS316	137	23	9331	73

By looking at the macro stress-strain graph for SS316 in Figure 4.18, the EPSC model shows reasonable agreement with the experimental data. The elastic region is seen between 0 MPa and 300 MPa where yield is observed at 300 MPa. The fit of the plastic region is also smooth, this is to be expected as the model is designed to work on stainless steel alloys which behave similarly to SS316 during loading.

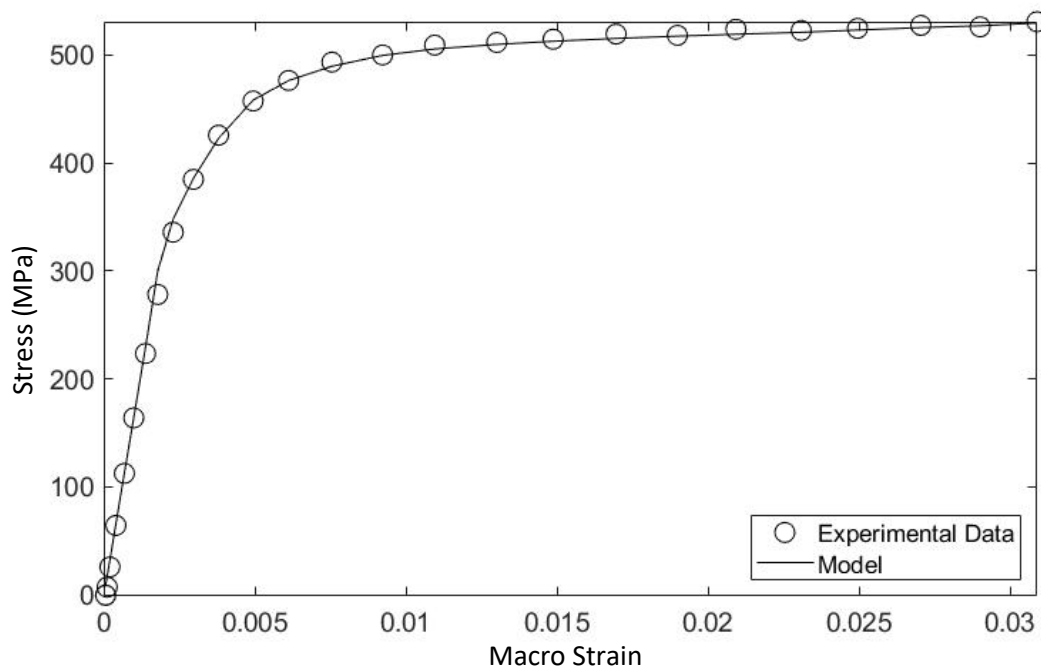


Figure 4.16: Macro stress-strain graphs for SS316, showing the comparison between the experimental in situ neutron diffraction tensile tests (markers) and the EPSC model results (line).

Figure 4.17 shows the macro stress-strain results for the EPSC model for INVAR. Due to some outlying values below 25 MPa, they have been excluded to ensure they do not affect the fit of the model. The elastic region of the model between 0 and 200 MPa shows to be in excellent agreement with the experimental data. The model seems to struggle to fit the yield as there is a sharp change in gradient at 260 MPa. The plastic region predicted by the model shows reasonable agreement with the experimental data. The EPSC model's prediction of the INVAR specimen shows some difficulty aligning with some of the data points from the experimental data, this is likely due to INVAR not being a stainless-steel alloy like SS316 and so behaves differently in the plastic region.

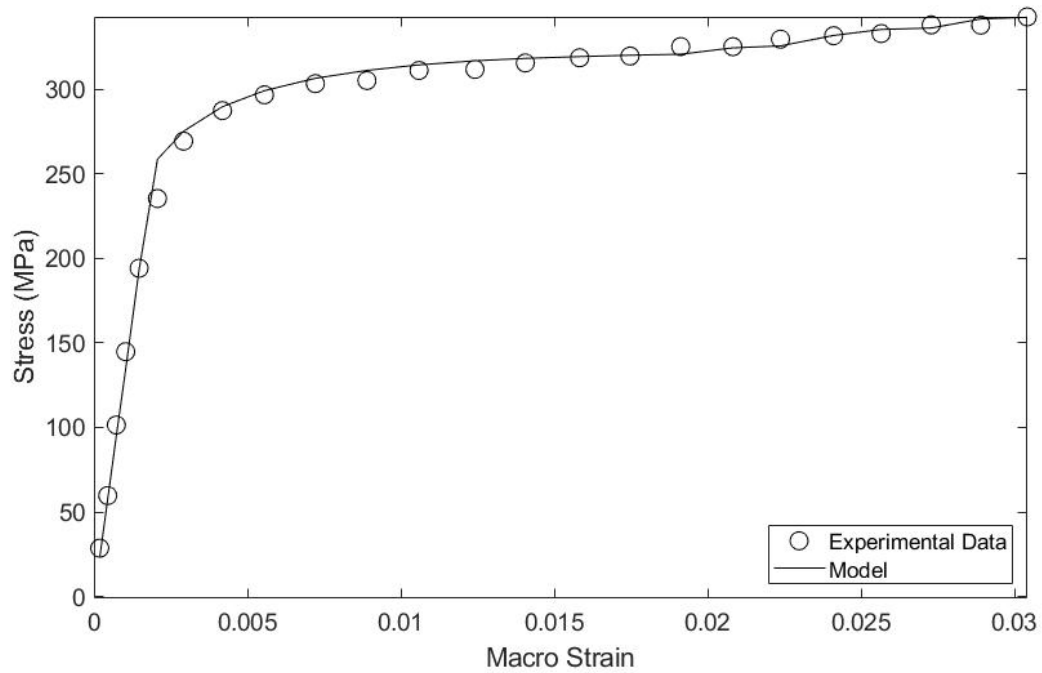


Figure 4.17: Macro stress-strain graphs for INVAR, showing the comparison between the experimental in situ neutron diffraction tensile tests (markers) and the EPSC model results (line).

Figure 4.18 shows the macro stress-strain curves calculated for the pure nickel sample. Before yield, at stress values below ~ 175 MPa, the model under-predicts the increase in strain with the applied stress. Additionally, yield the model underpredicts the stress value at yield. Following yield, the model shows an increase in the stress-strain slope, this indicates work hardening, however, pure nickel doesn't show this in the experimental results. Therefore, the model starts at a stress value below the experimental data at a value of ~ 325 MPa but increases to ~ 360 MPa by the then of the test but the experimental data shows there to be constant stress following yield at ~ 450 MPa.

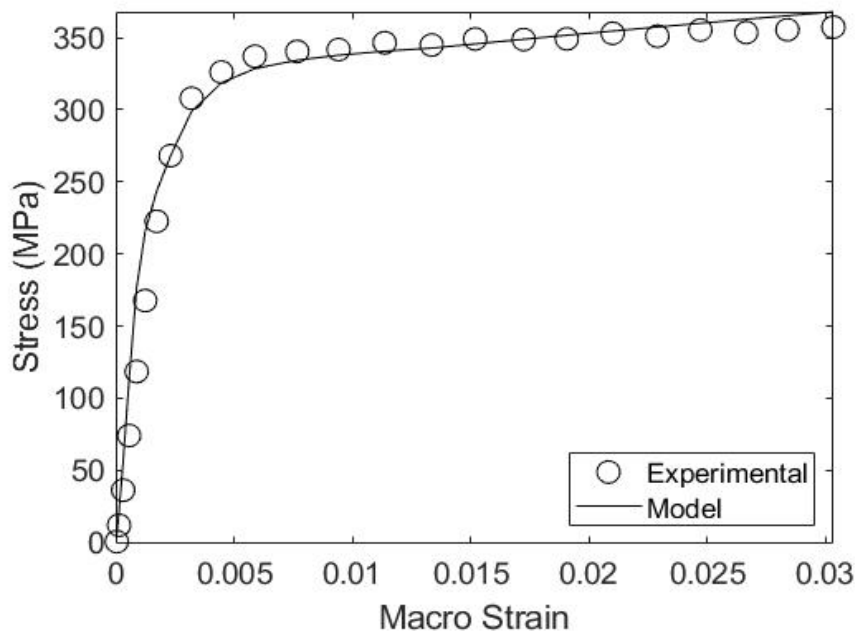


Figure 4.18: Macro stress-strain graphs for pure nickel, showing the comparison between the experimental in situ neutron diffraction tensile tests (markers) and the EPSC model results (line).

4.6.4.1. Comparison of the Measured and Modelled Lattice Strain

Once the parameters were found for each material using the macro stress-strain neutron data to optimise the model, the lattice strain predicted by the EPSC model could be plotted. However, it was noted that the elastic constants determined from the neutron diffraction tests for both SS316 and nickel were lower than the recorded elastic constants found in other sources. Therefore, additional elastic constant tests were performed and the values for these are shown in Table 4.8.

The results of the lattice strain data, showing the comparison plots between the EPSC model and the experimental neutron diffraction data for the {111}-, {220}- and {200}-orientation subsets of grains can be seen in Figure 4.19. The 111-orientation subset of grains showed the shapes of the curves for the model and the experimental data to be in reasonable agreement, however, the experimental data shows a steeper gradient. The model reflected the linear increase in the strain seen in the experimental data which is caused by elastic deformation. The {220}-orientation subset shows a deviation in the longitudinal direction towards a greater strain for the model than is seen in the experimental data. However, the shapes of the curves are very similar. The {200} family of grains shows the elastic region to be linear and then, following yield the gradient decrease and strain increases with increasing stress. opposite effect where it essentially allows for more strain to take place as stress increases. For this orientation, the model is in good agreement with the shape of the model however over predicts the strain values in this direction, at 3% global at the end of the test

the model predicts strain values of ~ 0.0056 whereas the experimental data predicts lattice strain values of ~ 0.0048 .

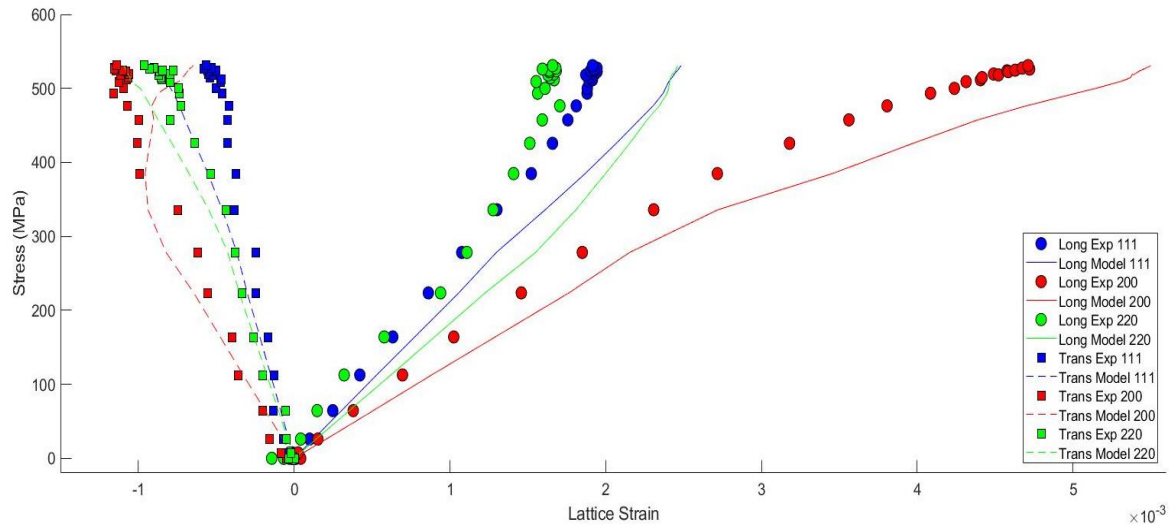


Figure 4.19: Graphs comparing the lattice strain obtained through in situ neutron diffraction tensile tests (markers) to that predicted by the EPSC model for SS316 for the grain families with orientations within 7.5 degrees of the 111, 220 and 200 orientations. The lattice strain values parallel (long) and perpendicular (trans) to the loading direction are shown in this figure.

The results of the EPSC model for the lattice strains of INVAR compared to the experimental data can be found in Figure 4.20. First looking at the lattice strain values in the loading direction which is labelled as 'long' in the figure, the 200 subset shows to be in reasonable agreement with the experimental data with the first three data points being perfectly aligned. The change in gradient observed in this orientation in the neutron diffraction data at around a strain value of 0.002 is also seen in the results of the EPSC model. For the 111-orientation subset in the loading direction, it can be seen that the EPSC model somewhat over-predicts the values of strain for the higher values of stress. However, the shape of the line created can be seen to be reflective of the experimental data as there is no change in gradient which indicates the subset continues deforming elastically. This is a similar result to the 220-orientation subset of grains in the loading direction, where the model over-predicts the values of strain, but shows the same overall shape witnessed in the neutron diffraction. The 220 subset deforms plastically before the other subset and plastic deformation is observed when the values of strain cease to increase with increasing load, this is seen in the 220 subset model above values of stress greater than ~ 225 MPa.

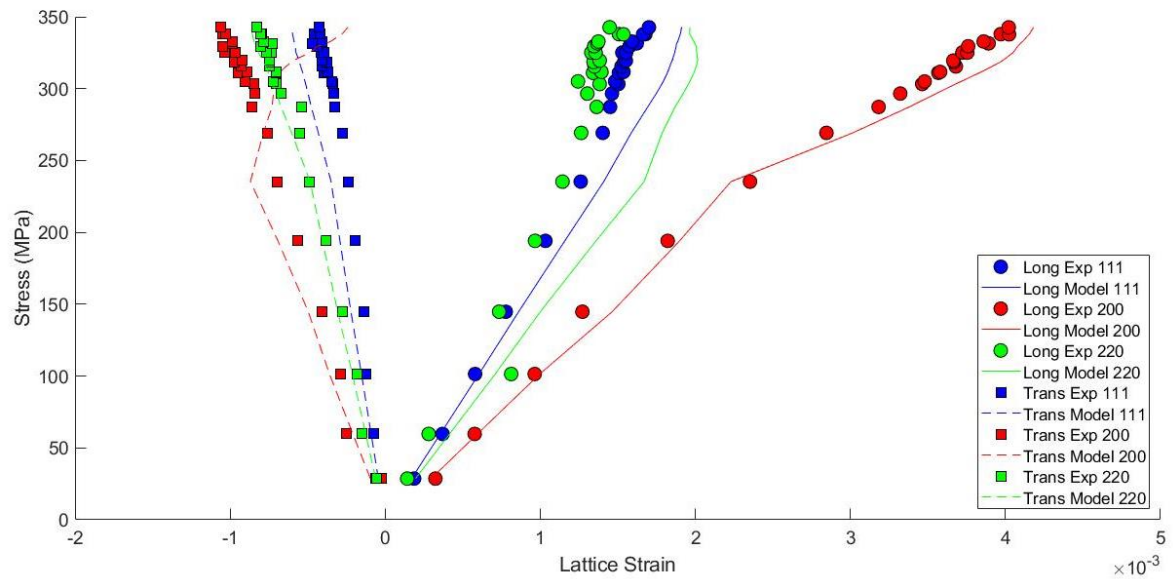


Figure 4.20: Graphs comparing the lattice strain obtained through in situ neutron diffraction tensile tests (markers) to that predicted by the EPSC model for INVAR for the grain families with orientations within 7.5 degrees of the 111, 220 and 200 orientations. The lattice strain values parallel (long) and perpendicular (trans) to the loading direction are shown in this figure.

The results for the pure nickel lattice strain values in the EPSC values can be found in Figure 4.21. Pure nickel shows a much linear increase in the experimental lattice strain values as the stress increase for all subsets than seen in the INVAR and SS316 samples. For the EPSC model results in the loading direction (long) the 200 subset is in good agreement with experimental data up to a strain value of 0.001 but beyond this value, the model over-predicts the strain values. The 220 subset shows the same pattern as the experimental data but over-predicts the values of strain. The 111 subset shows the largest over-estimate in the longitudinal direction and the shape is not as linear as the experimental data. In the transverse direction, the 111- and 220- orientation subsets are shown to be in good agreement with the experimental data up to 150 MPa, however, beyond this, the model predicts a decrease in gradient which is not observed in the experimental data. The 200 subset shows similar behaviour to the SS316 and INVAR where the model curves away from the neutron data, but again shows relatively good agreement between the model and the neutron data up to 150 MPa.

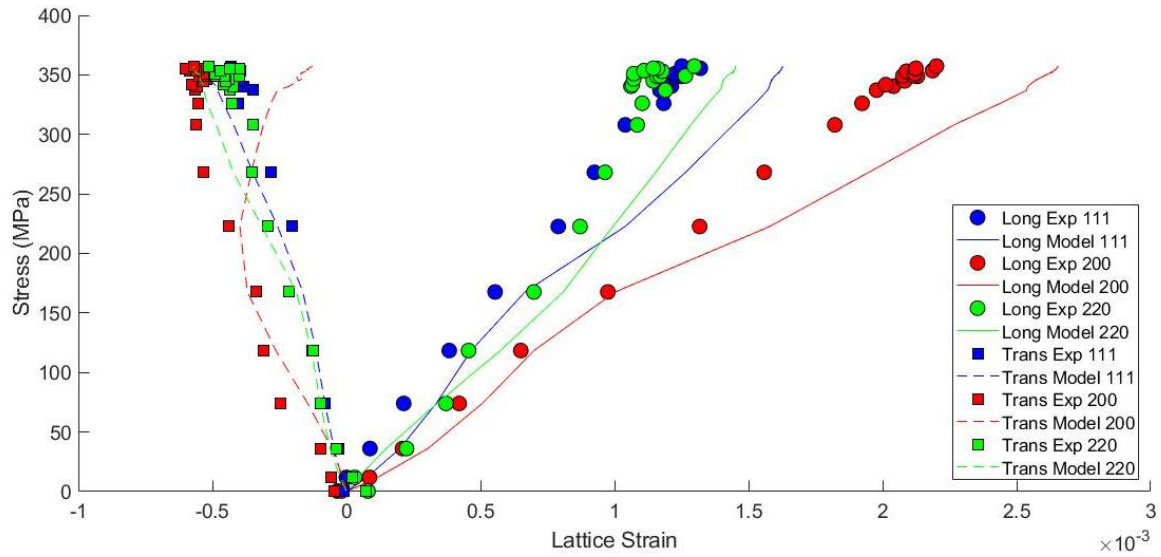


Figure 4.21: Graphs comparing the lattice strain obtained through *in situ* neutron diffraction tensile tests (markers) to that predicted by the EPSC model for pure nickel for the grain families with orientations within 7.5 degrees of the 111, 220 and 200 orientations. The lattice strain values parallel (long) and perpendicular (trans) to the loading direction are shown in this figure.

4.6.5. Post-Mortem EBSD Analysis

A post-mortem EBSD Analysis was performed on a cross-section through the centre of the tensile specimens subjected to *in situ* neutron diffraction tensile testing. Figure 4.22 (a) shows the grains subjected to 3% strain after the neutron diffraction tensile test, the grains show a random texture and a grain size which is like that in the undeformed region in Figure 4.8 (a). Figure 4.22 (b) shows the EBSD analysis for INVAR, the sample still shows a random texture and no change in grain size compared to the undeformed region in Figure 4.8 (b). Figure 4.22 (c) shows the EBSD analysis for the pure nickel sample, the grain size is unchanged from the undeformed region. Pole figures for the SS316, INVAR and pure nickel specimens (for both the deformed and undeformed regions) are shown in Figure 4.23, Figure 4.24 and Figure 4.25 respectively. Further analysis of the post-mortem EBSD analysis is covered in Chapter 5.

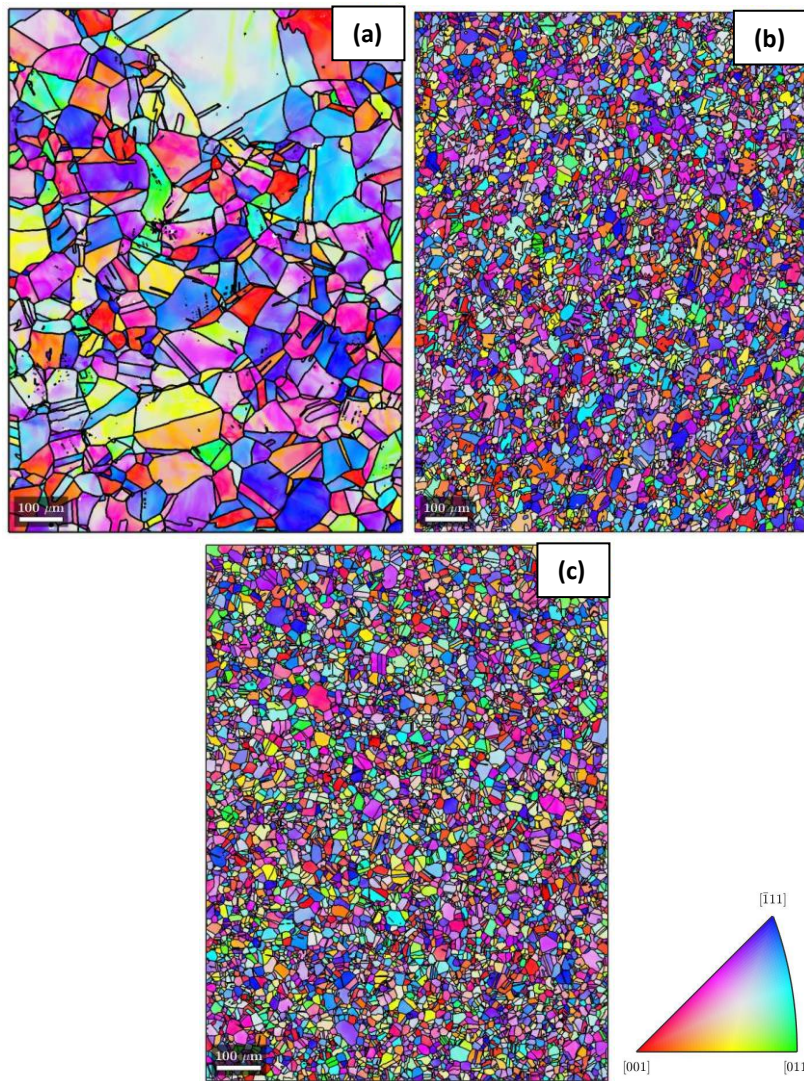


Figure 4.22: EBSD analysis of tensile test specimens (3% strain) after in situ neutron diffraction tensile testing for materials: (a) SS316, (b) INVAR and (c) pure nickel.

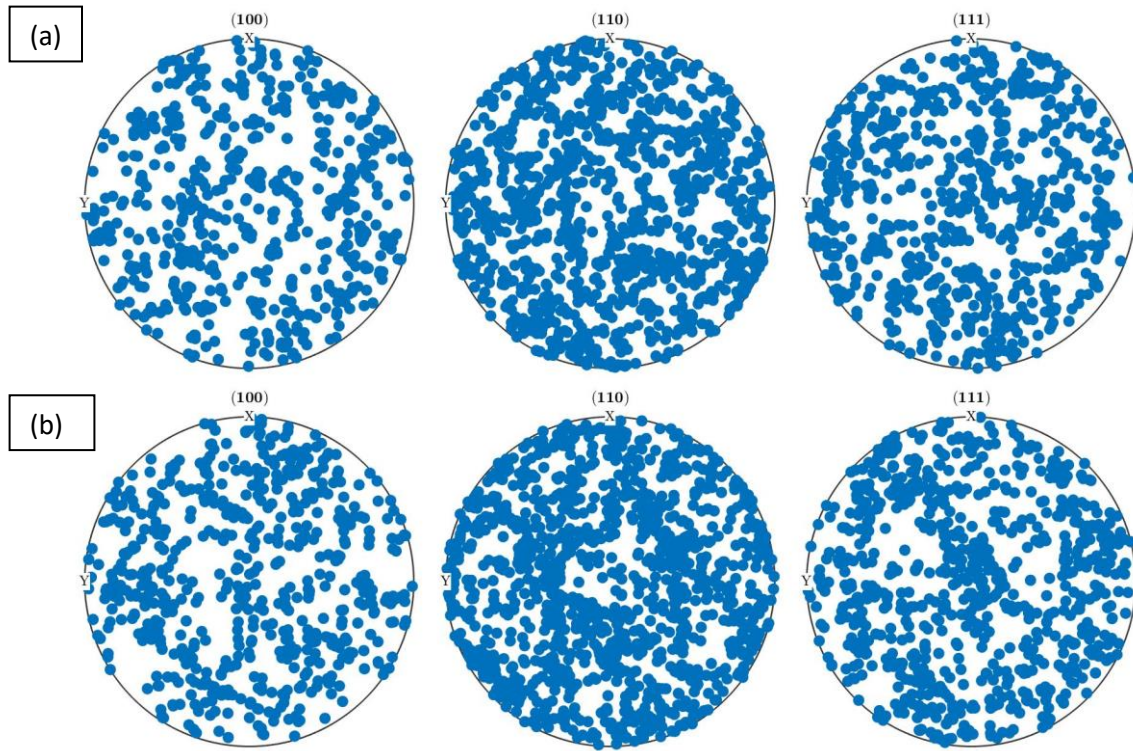


Figure 4.23: Pole figures for (a) undeformed and (b) deformed regions of the SS316 specimen.

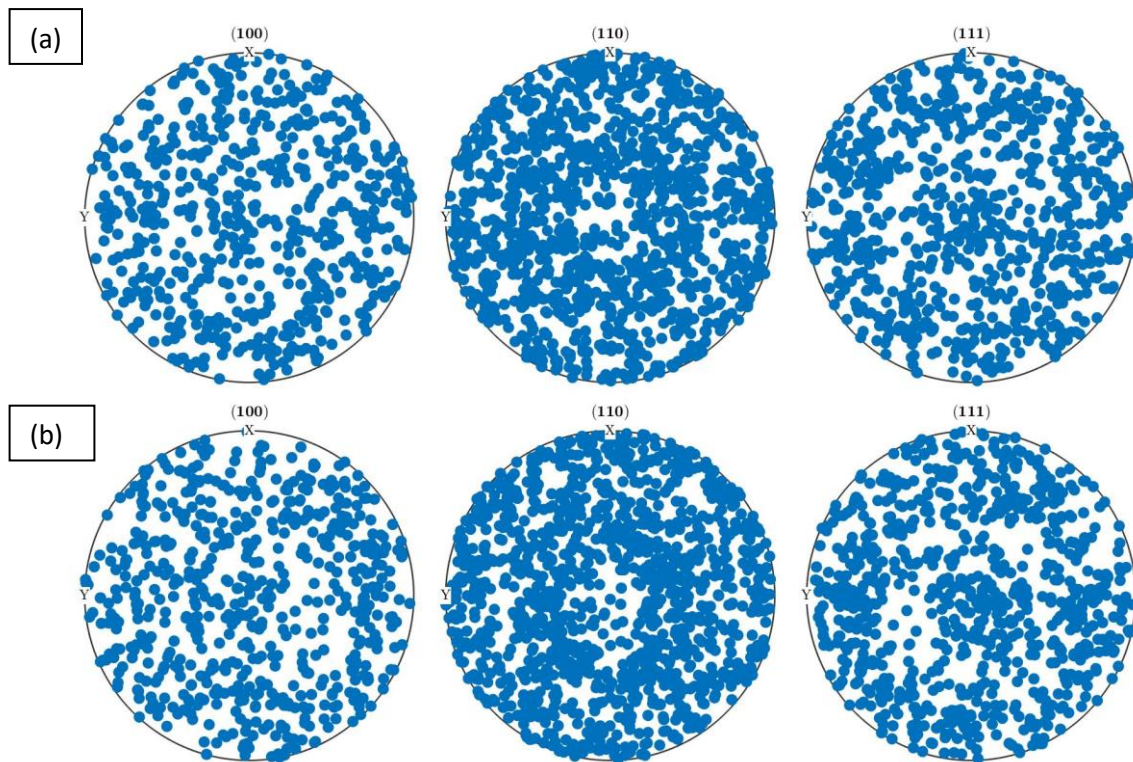


Figure 4.24: Pole figures for (a) undeformed and (b) deformed regions of the INVAR specimen.

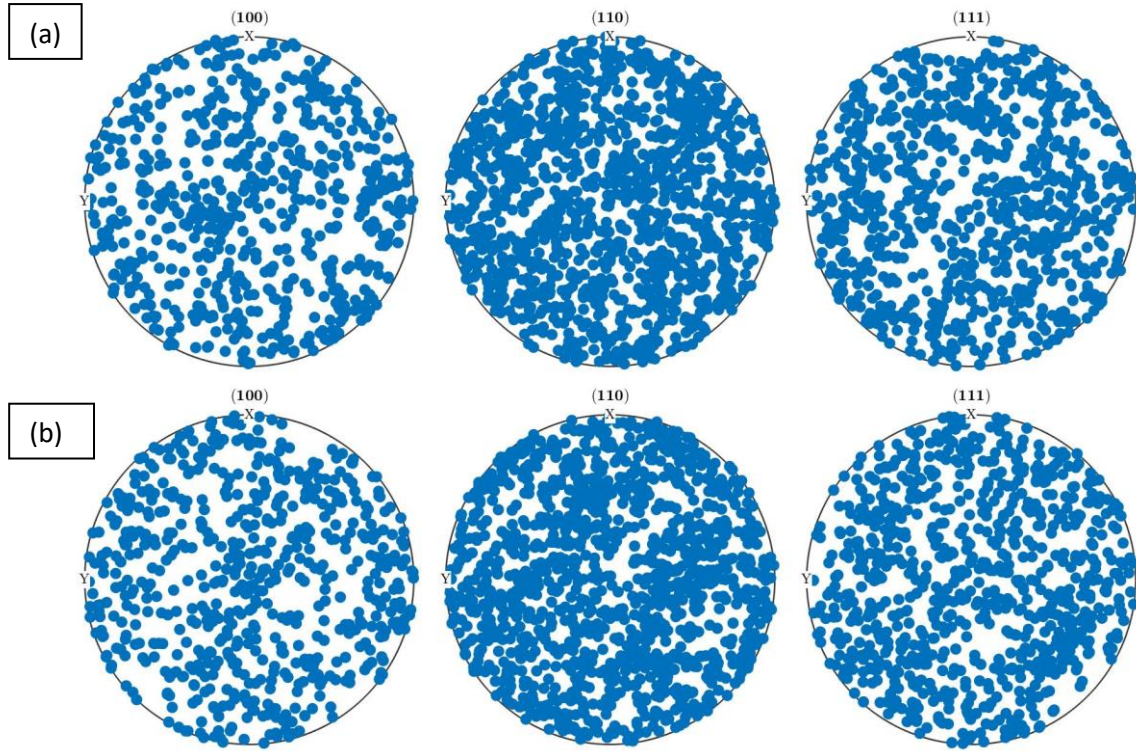


Figure 4.25: Pole figures for (a) undeformed and (b) deformed regions of the pure nickel specimen.

4.7. Discussion

This section will discuss the results of the *in situ* neutron diffraction tensile tests performed on SS316 INVAR and pure nickel to study the influence of SFE on deformation. It will then go on to discuss the results of the accompanying EPSC models. In previous work, the EPSC model had shown agreement with experimentally acquired neutron diffraction lattice strains (9,13,69,70), this was also found to be the case for the neutron diffraction tests and EPSC model in this project.

Figure 4.9 shows the macro stress-strain curve collected through *in situ* neutron diffraction for the SS316, Invar and pure nickel. SS316 and INVAR both indicate that work hardening has occurred after yield as indicated by a slight increase in the stress required to increase strain throughout loading. This is to be expected as both SS316 and INVAR have low SFE values, and therefore are susceptible to dislocation pile up during loading leading to work hardening (30). However, even though work hardening is present within the pure nickel sample the effect is to a lesser extent. Pure nickel has a high SFE, thus cross slip can occur with relative ease, meaning dislocation pile-up isn't present during deformation. As a result, work hardening is observed to a lesser extent, and this is shown in Figure 4.9 for the pure nickel sample.

Neutron diffraction only measures elastic strain. If treating each peak individually, elastic strain for subsets of grains with orientations which satisfy Bragg's law can be isolated, allowing the influence of anisotropic deformation to be quantified. The ENGIN-X neutron diffractometer contains detectors with a 7.5 degree solid angle, essentially averaging the data collected from ± 7.5 degrees from the given strain vector orientation. The crystallographic subsets analysed in this chapter are for grains within 7.5 degrees of the 111, 220 and 200 crystallographic orientations. The influence of SFE on deformation can be seen by studying the lattice strain values for the longitudinal and transverse directions shown in Figure 4.10, Figure 4.11 and Figure 4.12 for SS316, INVAR and pure nickel respectively. For SS316 (shown in Figure 4.10), the 220 subset of grains stops increasing in lattice strain beyond a strain value of around 1.5×10^{-3} and a stress value of 450 MPa, even as the stress continues to increase. This indicates the onset of plastic deformation in the 220 orientation subset of grains. However, the 111-orientation grain family shows a linear increase in lattice strain with stress, even at stresses above yield which is ~ 50 MPa, this shows that this subset is still deforming elastically beyond yield. The 200-orientation subset of grains shows a shift to allowing more elastic strain with an increase in stress, this implies that this grain subset is allowing for the anisotropic grain deformation by continuing to behave elastically for longer. For the INVAR specimen in Figure 4.11, the lattice strain values for the 200-orientation subset of grains in the loading direction have the same decrease in gradient observed in the SS316 sample following yield. In the elastic region before yield at ~ 200 MPa, the 200-subset deforms linearly, however after yield the strain increases more for each stress increment. This implies that after plastic deformation has occurred in some of the grains within the material, the 200-orientation subset is allowing for the mismatch in orientation deformation and elastically deforming more. This same effect is seen in the paper by Daymond and Bouchard (9) which can be seen in Figure 2.15. The 111- and 220-orientation subsets also show a similar progression throughout the loading as the SS316 specimen, with the subsets deforming elastically throughout the lower stress values. After yield the 220 subset shows a slight shift away from increasing strain with increasing stress, indicating the onset of plastic deformation. Figure 4.12 shows the lattice strain values for the transverse and longitudinal directions of the pure nickel specimen for the 111, 220 and 200 orientations subsets. The {200} orientation subset in the loading direction does not show the decrease in gradient that is seen in both the SS316 and INVAR samples and remains linear throughout. This indicates that deformation is occurring at a constant rate throughout the test and the load sharing which is observed in the SS316 and INVAR specimens is not present in the pure nickel sample. The 220 orientation subset shows the strain values cease to increase with increasing strain indicating the onset of plastic deformation and the 111 subset remains linear throughout implying that grains with this orientation are still deforming elastically.

The FWHM for the peaks in the neutron diffraction tests can be used to indicate a change in grain size or the onset of plastic deformation (63). By looking at the EBSD maps from Figure 4.8 and Figure 4.22 for the specimens of SS316, INVAR and pure nickel before and after loading, there was no observable change in grain size after deformation for any of the samples. This implies that the increase in FWHM of the diffraction peaks during loading was likely related to plastic deformation. However, as these regions were taken from separate parts of the sample during post-mortem EBSD analysis, any change in grain size could not be directly recorded. By looking at Figure 4.13, which shows the FWHM for SS316, even after the macro stress-strain response reached yield and is deforming plastically overall the 111 subset of grains continues to deform elastically and the FWHM remains relatively constant. Figure 4.14 shows the FWHM progression during loading of the INVAR specimen within the 111, 200 and 220 subsets of grains and shows the largest change from the beginning of loading to the end to be in the 200-orientation subset. The results of the FWHM for pure nickel are shown in Figure 4.15, this specimen showed the most fluctuation in peak width during loading for all subsets. These results do not align with the lattice strain data obtained for these materials in the given subsets, for example, it is seen in the strain data that the 220-orientation subset has begun to show plastic deformation and therefore this should show the greatest change in the FWHM, yet this is not the case. As the FWHM shows an increase in values when macroscopic yield starts, this implies that it is a good indicator of plasticity but is unable to quantify the anisotropic yielding of the orientation subsets. Additionally, the lack of FWHM change for the elastic regions may show that for low SFE materials which experience deforming by twinning, the FWHM varies less, whereas for high SFE materials the FWHM varies more.

The EPSC model was used in this project to predict the lattice strain values for the 111, 220 and 200 orientation subsets. The model required the macro stress-strain data and the initial texture file of the specimens to predict the lattice strain values in the 111, 220 and 200 orientation subsets for the SS316, INVAR and pure nickel samples. The macro-stress strain curve for SS316 Figure 4.16, this material showed an excellent fit between the experimental data and the EPSC model. This is to be expected as the model is designed to model stainless steel alloys with low SFEs and therefore the fit after yield is perfectly matched. Figure 4.17 shows the macro-stress strain curve for INVAR, this shows a good fit in the elastic region, but the model seems to struggle to replicate the plastic region. However, the overall fit is in reasonable agreement with the experimental data, this is likely due to INVAR having a low SFE so experiences work hardening after yield. Figure 4.18 shows the macro-stress strain curve fit for pure nickel, this shows the largest deviation from the stress-strain curve in the experimental data to the EPSC model. The optimisation code was unable to find a local minimum for the coefficients and therefore struggled to fit the model to the experimental data. Multiple runs

of the optimisation were performed using the optimum values from the previous test as well as fixing some of the parameters, however, the values continued to vary with each test. This could be a result of the model predicting there to be strain hardening, which is common in many alloys, but since Ni is a pure material, this phenomenon is not observed and, therefore, the model cannot match the experimental data. The EPSC model uses the Voce hardening model, this model fits well for the low SFE materials SS316 and INVAR, but like pure nickel, the INVAR specimen did not reach a local minimum even though the fit was much better. This may be because INVAR is a binary alloy and not a complex alloy such as SS316, therefore, the Voce hardening model does not accurately fit the deformation behaviour.

The results of the EPSC model for the lattice strain values for SS316 and INVAR specimens are shown in Figure 4.19 and Figure 4.20. For these specimens, the model was able to accurately predict the curve of the lattice strain, correctly indicating the change in gradient following yield. Figure 4.19 showed that in the loading direction the model over-predicted the values of strain for the SS316 for all subsets but correctly estimated the shapes of the curves. In the 220 orientation subset, the model accurately predicted the onset of plastic deformation, which is shown by the strain values no longer increasing near the end of the test. For INVAR, the 200 subset is in good alignment with the experimental data, however, the 220 and 111 subsets are over-predicted in the longitudinal direction. For the EPSC lattice strain predictions for the pure nickel specimen, shown in Figure 4.21, the lattice strain 200 subsets in the loading direction fit well in the elastic region but after yield, it over-predicts the increase in strain and does not accurately reflect the change in gradient of the curve that is modelled in the INVAR and SS316 specimens. The model also struggles to predict the shapes of the 111 and 220 subsets throughout the test. For continuity between the tests, the Voce hardening model was used in the EPSC model. This worked well for INVAR and SS316 as they both have low SFE and therefore experience a larger amount work hardening after yield, however, as pure nickel has a high SFE and allows for cross slip, the model is unable to accurately predict the shape of the lattice strains. Comparing these results to the room temperature results recorded by Daymond and Bouchard (9) (shown in Figure 2.15), the EPSC model showed a similar level of accuracy to the experimental data. However, when comparing these results, it should be noted that this work contained more data points throughout the test than was used in this project, and this would have allowed a better fit to be reached. Additionally, the neutron diffraction tests in this thesis were not taken to as high strain values as the ones in the paper discussed, this may mean the model struggled with predicting the lattice strain values. Francis et al. (72) also shows a better fit between the EPSC model and the neutron diffraction data than seen in this thesis. However, this

may be again due to the higher strains the sample was taken to or that the material used was Waspaloy, which has not been investigated in this project.

The influence of SFE on deformation mechanics can be observed in both the results of the neutron diffraction results and the EPSC model. Because pure nickel has been suggested as a surrogate alloy for modelling SS316 behaviour, to reduce the required complexity of models, this chapter has presented how the difference between the SFE of the materials will influence the deformation of the materials. Materials with a low SFE, such as SS316 and INVAR, experience work hardening following yield due to dislocation pile up, whereas high SFE materials like nickel can cross-slip, therefore, do not have work hardening. These results have suggested INVAR as an alternative to pure nickel for modelling SS316, due to also having a low SFE and simplistic chemical composition. The EPSC model was selected due to its ability to model stainless steels, and in addition to predicting SS316 effectively, it was also able to predict the deformation mechanics for the INVAR specimen, whereas it struggled to model the pure nickel sample. This shows that for the EPSC model pure nickel is not a suitable alternative to SS316, however, INVAR is much closer. The outcome may be different for another model, but there does appear to be enough difference between the responses for SS316 and pure nickel that the two are not good correlates. This shows how the SFE should be considered when using a material with a simpler chemical composition to model a complex alloy.

4.8. Summary

This chapter discussed the influence of SFE on the deformation mechanics and how when selecting a material to model a complex alloy the SFE should be considered. Despite the differences in tensile strength and elastic constants for the SS316 and INVAR samples, they both have low SFEs leading to the deformation behaviour being very similar, and both specimens showed reasonable agreement with the EPSC model. Pure nickel showed very different behaviour following yield, as work hardening was not present, this meant the EPSC model struggled to fit the deformation behaviour recorded from the *in situ* neutron diffraction tests.

Ideally, deformation prediction models would be used independently of experimental procedures such as neutron diffraction. However, the results of the EPSC models in this section showed that in this case the model used is unlikely to produce sufficient information on the deformation behaviour of these three materials alone and requires external validation.

5. Using EBSD metrics to quantify plastic strain accumulation

5.1. Overview

EBSD analyses the crystallographic structure of a material by firing electrons at the surface of a specimen and observing the angle at which they are reflected. This is done point by point to create a pixel-like data set of crystallographic information across a 2-dimensional surface plane. In an idealised polycrystal, each measurement within a grain would be identical and grain boundaries show up as sudden changes in orientation. However, defects and anomalies can form when deformation occurs, this disruption in the crystallographic lattice is registered in EBSD mapping (discussed in sections 2.4.1.1 and 2.6.1.1). These defects are reflected in the EBSD as misorientation of the crystallographic structure, and the accumulation of misorientation implies the presence of plastic deformation.

The post-mortem EBSD data of the *in situ* neutron diffraction tensile test specimens (first presented in sections 4.3, 4.6.1 and 4.6.5) are further analysed in this current chapter by using EBSD metrics to interpret the accumulation of plasticity. Additionally, the EBSD data was segmented into grain subsets based on their crystallographic orientation which correlated to the diffraction peaks in the neutron diffraction tests performed at ENGIN-X (with 7.5 degrees of the 111, 220 and 200 orientations). These subsets were then compared using EBSD metrics, which are discussed in detail in section 2.6.1.1.

5.2. Methodology

To produce a comparison between the deformed and undeformed microstructure before and after, post-mortem EBSD analysis was performed on the *in situ* neutron diffraction tensile test samples. This process was discussed detail in section 4.3 in the previous chapter.

5.2.1. EBSD Analysis

Section 4.3 discusses the process of preparing the neutron diffraction specimens for post-mortem EBSD analysis, with the exact grinding and polishing stages shown in Table 4.3 and

Table 4.4 respectively. Additionally, it was found the INVAR was prone to oxidation, therefore, required surface preparation to be performed just before the EBSD analysis.

5.2.2. EBSD Metrics

EBSD Metrics can be calculated from the EBSD data using the MTEX toolbox (140,141) in MATLAB. There are three EBSD metrics studied in this chapter are the GOS, GAM and KAM, details on these

methods can be found in section 2.6.1.1. For the KAM calculations the surrounding pixels were limited to only the first order, this can be seen in Figure 5.1.

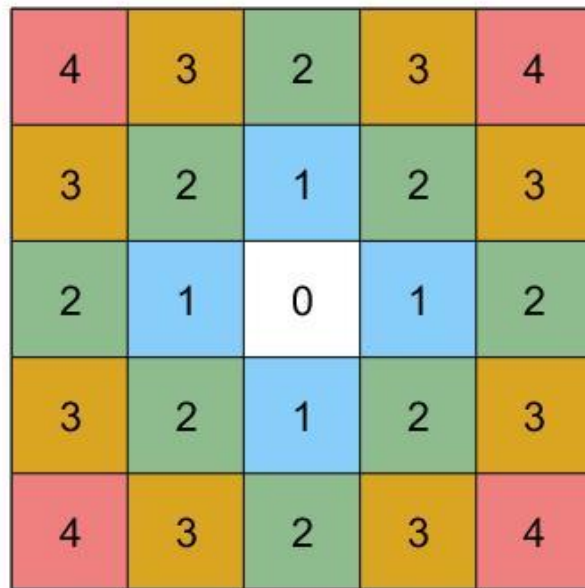


Figure 5.1: Number of surrounding pixels for KAM calculations

5.3. Results

This section will present the results of the EBSD analysis for the deformed and undeformed SS316, INVAR and Nickel samples. Firstly, figures containing the global maps of EBSD, KAM, GAM, GOS, Schmid factor and Taylor factor for each of the samples. This will be followed by histograms showing these values separated into subsets based on their orientations.

5.3.1. EBSD Raw Data

This section will display the results of the EBSD analysis and EBSD metric maps of the deformed and undeformed SS316, INVAR and pure nickel samples. The figures presented in this section are repeated from the previous chapter (shown in Figure 4.8 and Figure 4.22) to make easier comparisons between the raw EBSD data and the EBSD metric results. Figure 5.2 (a)(i) shows the region analysed to reflect a section which was undeformed in the SS316 sample. Figure 5.2 (a)(ii) shows the region selected for SS316 which had been deformed to 3% strain during in situ tensile testing as explained in Section 4.2.2. Figure 5.2 (b)(i) shows the region imaged for undeformed INVAR. Figure 5.2 (b)(ii) shows the region imaged for the INVAR sample deformed to 3% strain. Figure 5.2 (c)(i) shows the region imaged for the undeformed pure nickel. Figure 5.2 (c)(ii) shows the region imaged for the pure nickel sample deformed to 3% strain.

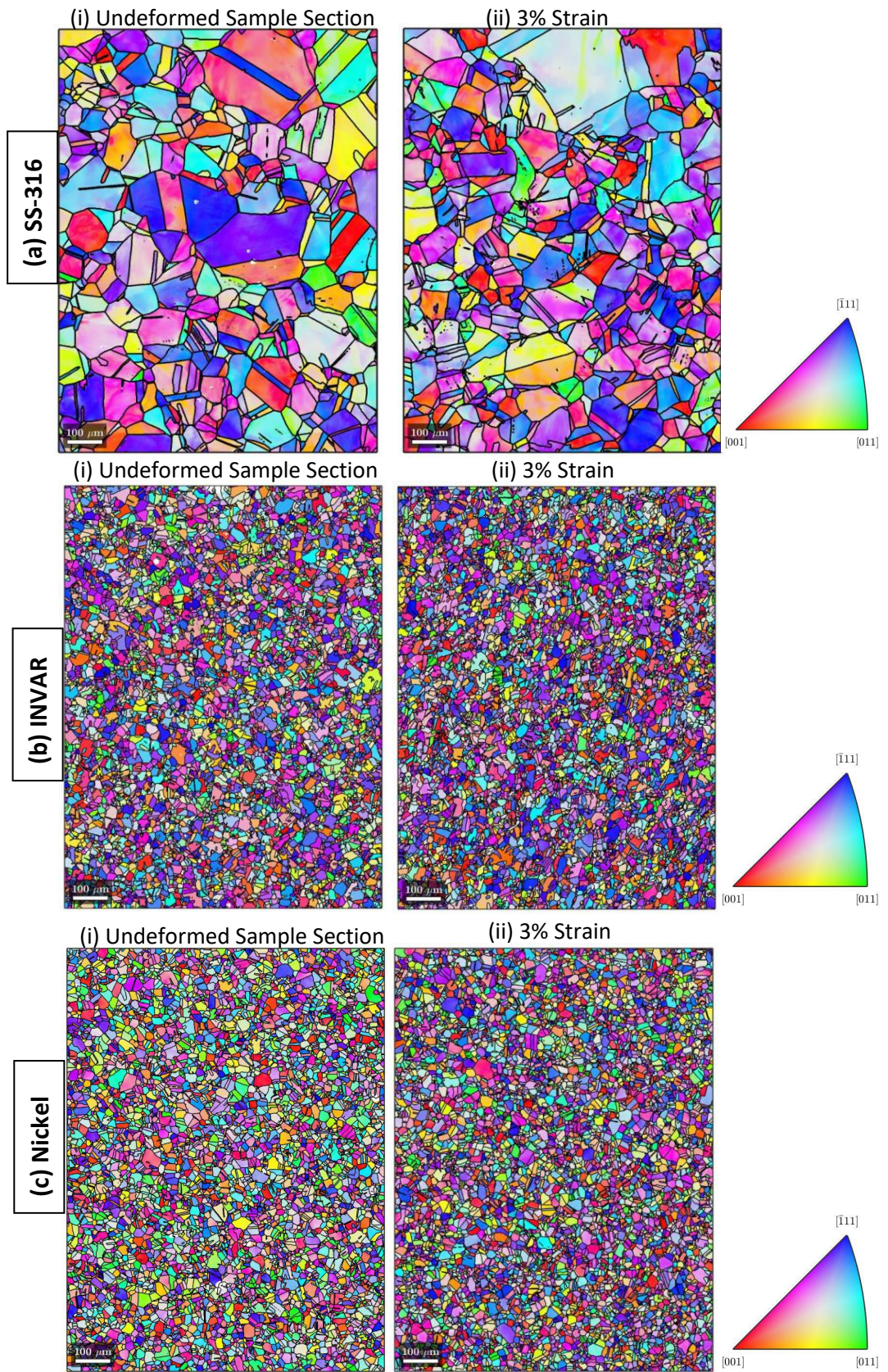


Figure 5.2: Map plots of the EBSD data for the undeformed and deformed regions for (a) SS316, (b) INVAR and (c) pure nickel.

Figure 5.3 shows maps of spatially resolved Schmid factors calculated from the EBSD shown in Figure 5.3. As all three materials show a higher concentration of grains with higher values of Schmid factor (greater than 0.45) compared to grains with a lower value of Schmid factor (less than 0.36). Figure 5.4 shows the spatial Taylor factor maps calculated from the EBSD maps from Figure 5.3. The maps show an even spread of grains with values between 2.3 to 3.7.

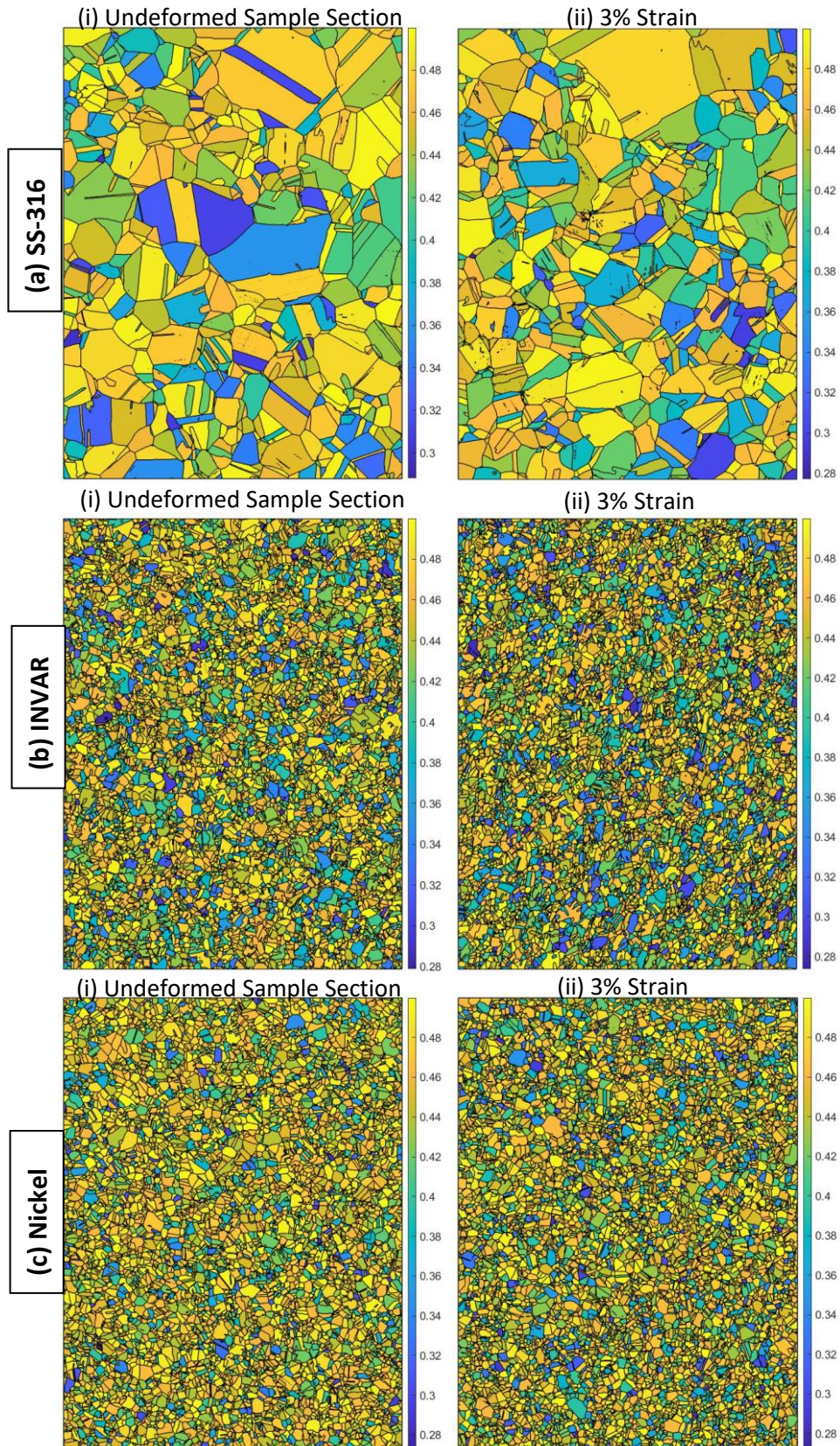


Figure 5.3: Map plots of the Schmid factor values calculated from the EBSD data are shown for (a) SS316, (b) INVAR and (c) pure nickel

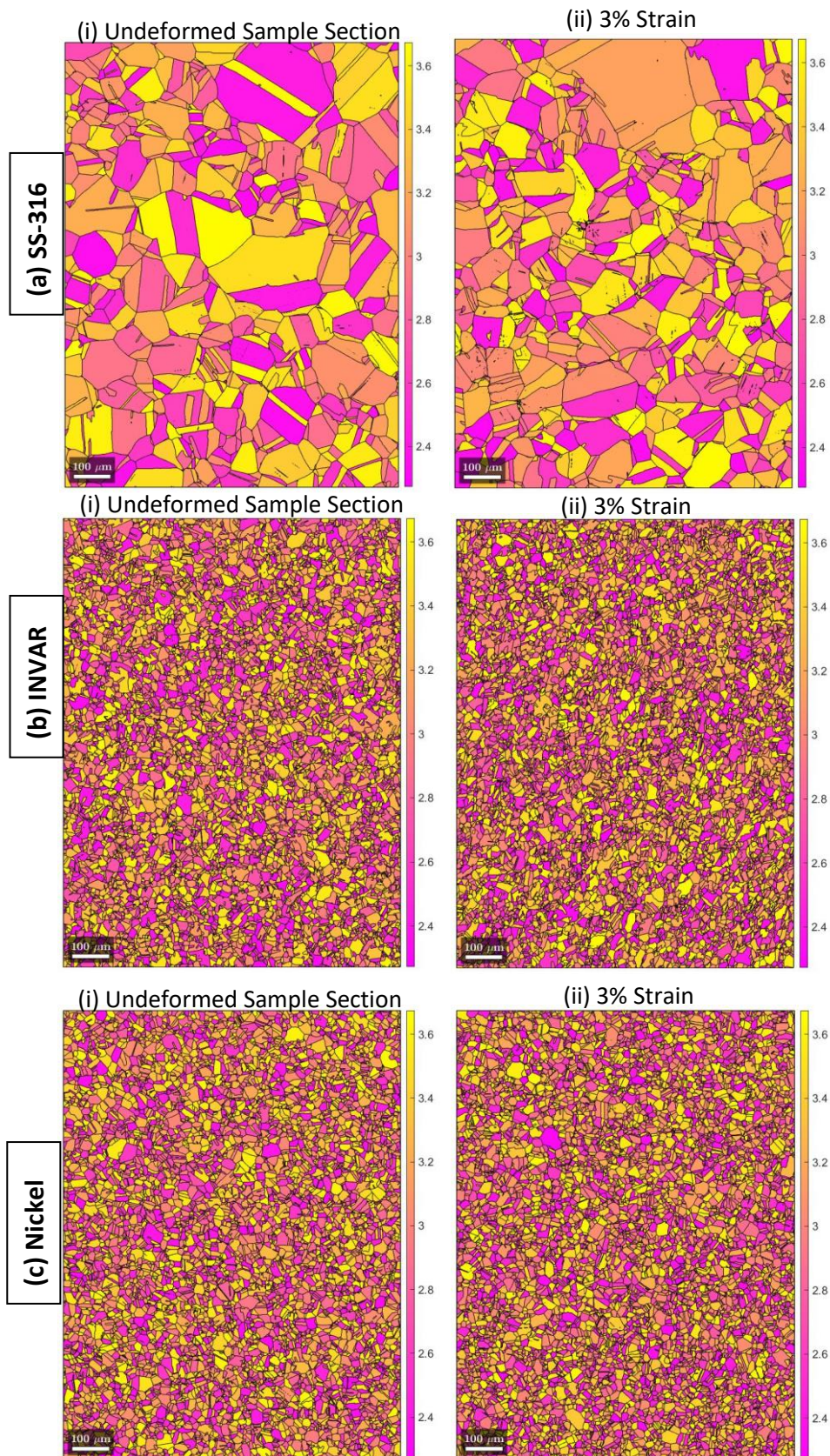


Figure 5.4: EBSD maps for Taylor factor values calculated from EBSD data from the deformed and undeformed regions cut from the samples (a) SS315, (b) INVAR and (c) pure nickel.

5.3.2. Extracting EBSD Metrics

EBSD metrics can be used to identify the concentrations of misorientation occurring in the EBSD analysis. Figure 5.5 (a)(i) shows GOS values in degrees for the undeformed region of SS316. This image shows there to be grains with values of GOS to be between ~1 degree to ~6 degrees. Figure 5.5 (a)(ii) shows the values of GOS for the grains within the region deformed to 3% strain for SS316. This image shows there to be grains with values of GOS to be up to 8 degrees and a larger percentage of grains with values greater than 5 degrees compared to the undeformed sample in Figure 5.5 (a)(i). Figure 5.5 (b)(i) shows the GOS map for undeformed INVAR. This map shows there to be mainly grains with little orientation spread and typically around between 0 and 1 degrees, with some outliers extending to 2-3 degrees. Figure 5.5 (b)(ii) shows the INVAR region which has been subjected to 3% strain. This region shows a higher percentage of grains with GOS values between 1 to 3 degrees showing there to be more orientation spread in the deformed sample than in the undeformed sample. Figure 5.5 (c)(i) shows the GOS map for the undeformed pure nickel sample. This shows there to be a range of values of GOS between 0 and 3 degrees. Figure 5.5 (c)(ii) shows the GOS values for the deformed pure nickel sample at 3% strain. The figure shows there to be a similar amount of GOS values compared to the undeformed figure, with a fractionally slight increase in grains with values between 2 and 3 degrees.

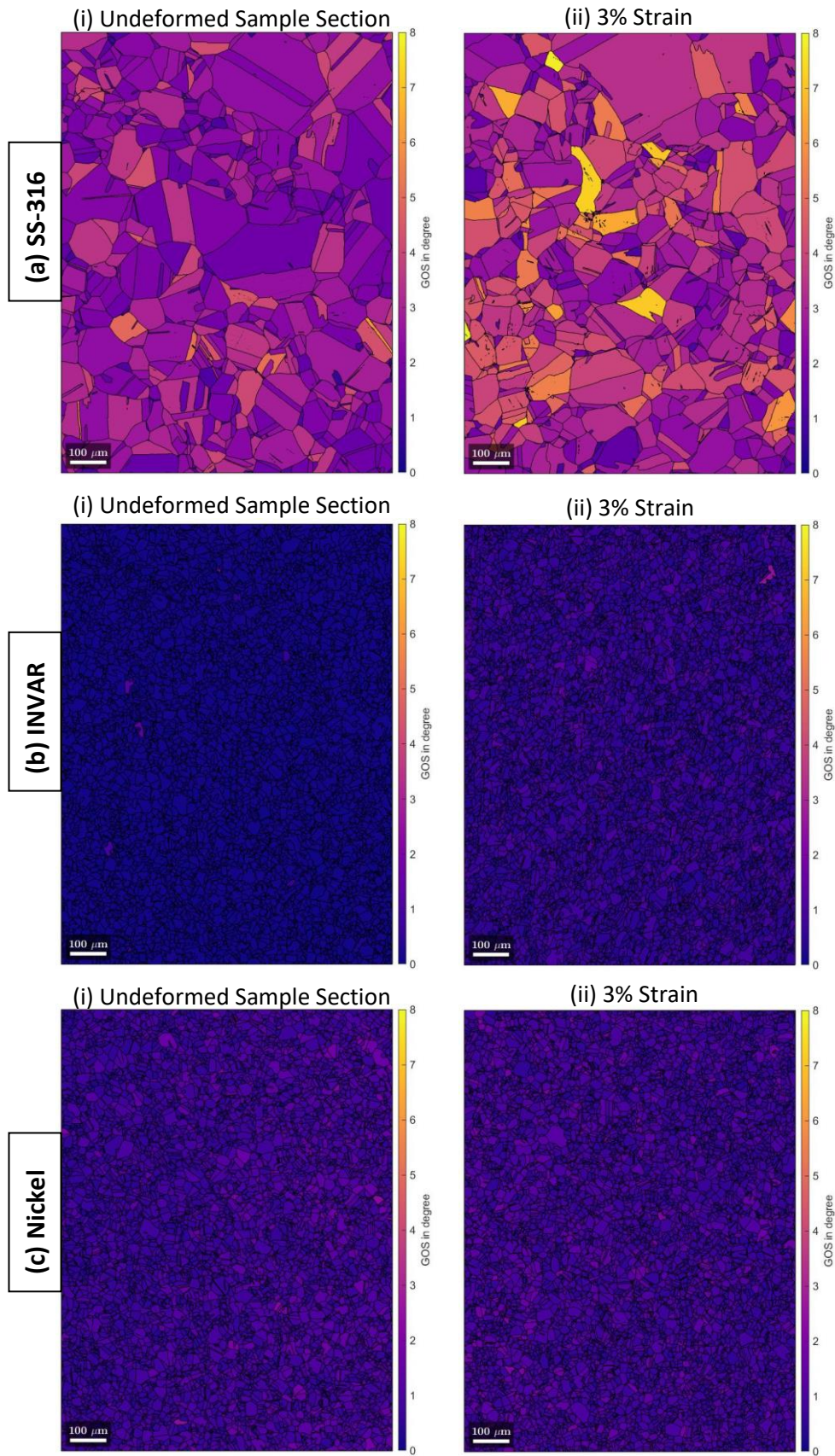


Figure 5.5: EBSD maps for GOS calculated from EBSD data from the deformed and undeformed regions cut from the samples (a) SS316, (b) INVAR and (c) pure nickel.

The EBSD metric GAM measures the average misorientation within a grain. Figure 5.6 (a)(i) shows the GAM map for the undeformed region of SS316. The figure shows there to be a range of values between 0 and 1 degrees, however, there are a larger majority of grains with values between 0 and 0.3 degrees. Figure 5.6 (a)(ii) shows the GAM map for the deformed region of the SS316 sample. Compared to the undeformed region, the deformed region shows a higher percentage of grains with GAM values greater than 0.5 degrees. Figure 5.6 (b)(i) shows the GAM map for the undeformed region of INVAR. This undeformed region shows all grains to have values of GAM to be ~ 0 degrees, showing there to be very little misorientation in the undeformed sample. Figure 5.6 (b)(ii) shows the GAM values for the deformed region of INVAR subjected to 3% strain. This shows that some grains in the deformed sample have values of GAM up to around 0.6 degrees, indicating that more misorientation is seen in the deformed region. Figure 5.6 (c)(i) shows the GAM map for the undeformed region of the pure nickel sample. This figure shows that the undeformed region of nickel has grains with GAM values between 0 and 0.6 degrees. Figure 5.6 (c)(ii) shows the GAM map for the undeformed region of pure nickel. This figure shows there for be grains with values of GAM to be between about 0 and 0.6 degrees, similar to the undeformed samples however there seems to be a slight increase in the number of grains with higher values of GAM.

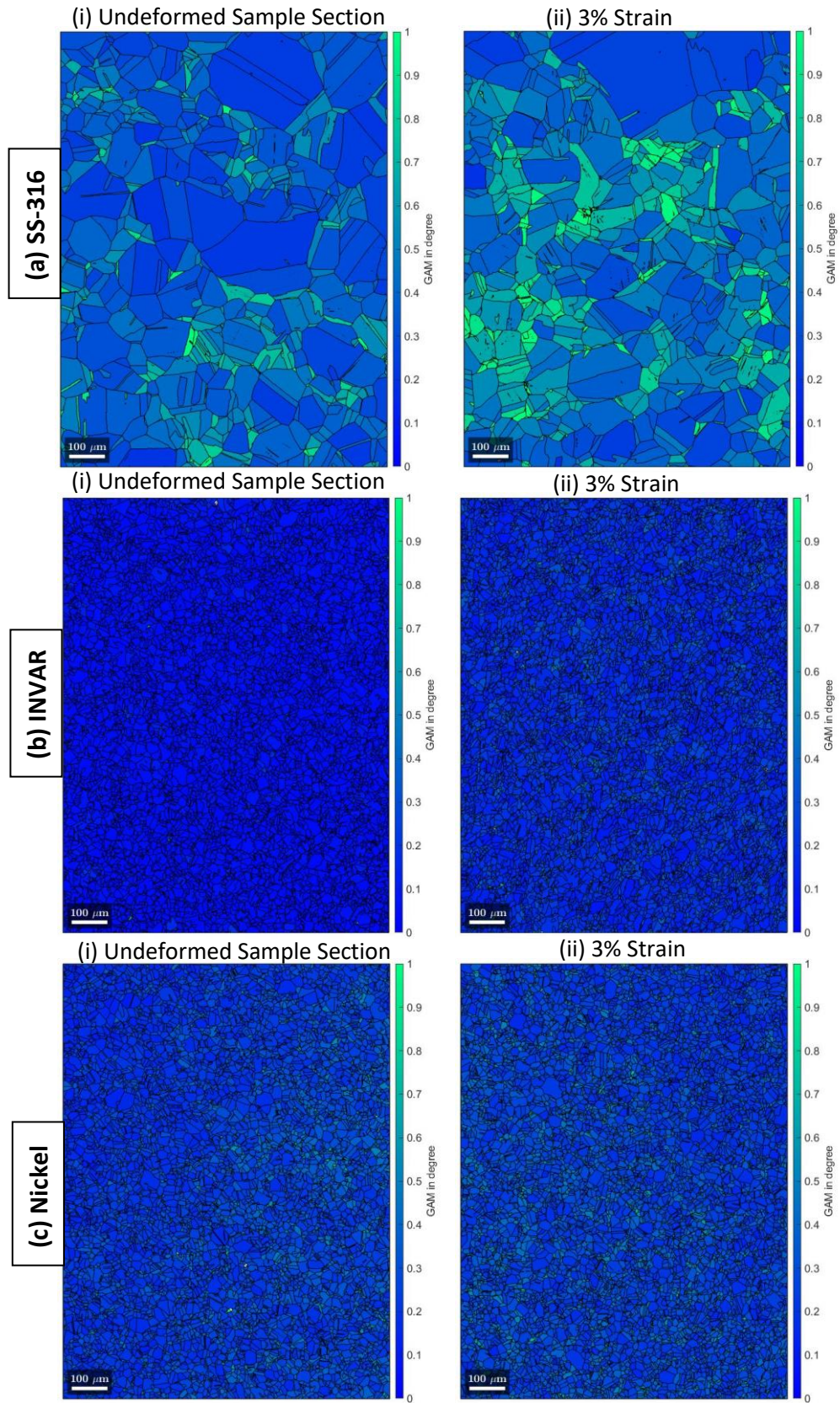


Figure 5.6: EBSD maps for GAM calculated from EBSD data from the deformed and undeformed regions cut from the samples (a) SS315, (b) INVAR and (c) pure nickel.

The EBSD metric KAM is similar to GAM but the average misorientation is averaged over a kernel as opposed to the grain. Figure 5.7 (a)(ii) shows the KAM values for the undeformed region of the SS316 sample. This region shows a concentration of misorientation to occur at the grain boundaries of grains. Figure 5.7 (a)(ii) shows the KAM values for the deformed region of the SS316 sample which was subjected to 3% strain. The deformed region shows an increased number of regions with higher KAM values than the undeformed region but is concentrated at the grain boundaries. This indicates that following deformation, the average misorientation of SS316 increases. Figure 5.7 (b)(i) shows the KAM values for the undeformed region of INVAR. This figure shows the values of KAM to be consistently around 0 degrees for this region, indicating that there is no misorientation recorded for this area. Figure 5.7 (b)(ii) shows the KAM map for the deformed region of the INVAR sample. The region shows some areas to have values of KAM up to around 0.02 degrees, indicating that following the loading of the sample increased the misorientation throughout the sample. Figure 5.7 (c)(i) shows the KAM map for pure nickel before deformation. This region shows a range of KAM values spanning between ~ 0 and 0.025 degrees. Figure 5.7 (c)(ii) shows the KAM values for the deformed region of pure nickel at 3% strain. This shows a similar range in KAM values observed in the undeformed region (between 0 and 0.025 degrees). Unlike, the SS316 and INVAR samples the change between the undeformed and deformed sample is far less noticeable for the pure nickel indicating that deformation does not affect the average misorientation of the sample as greatly.

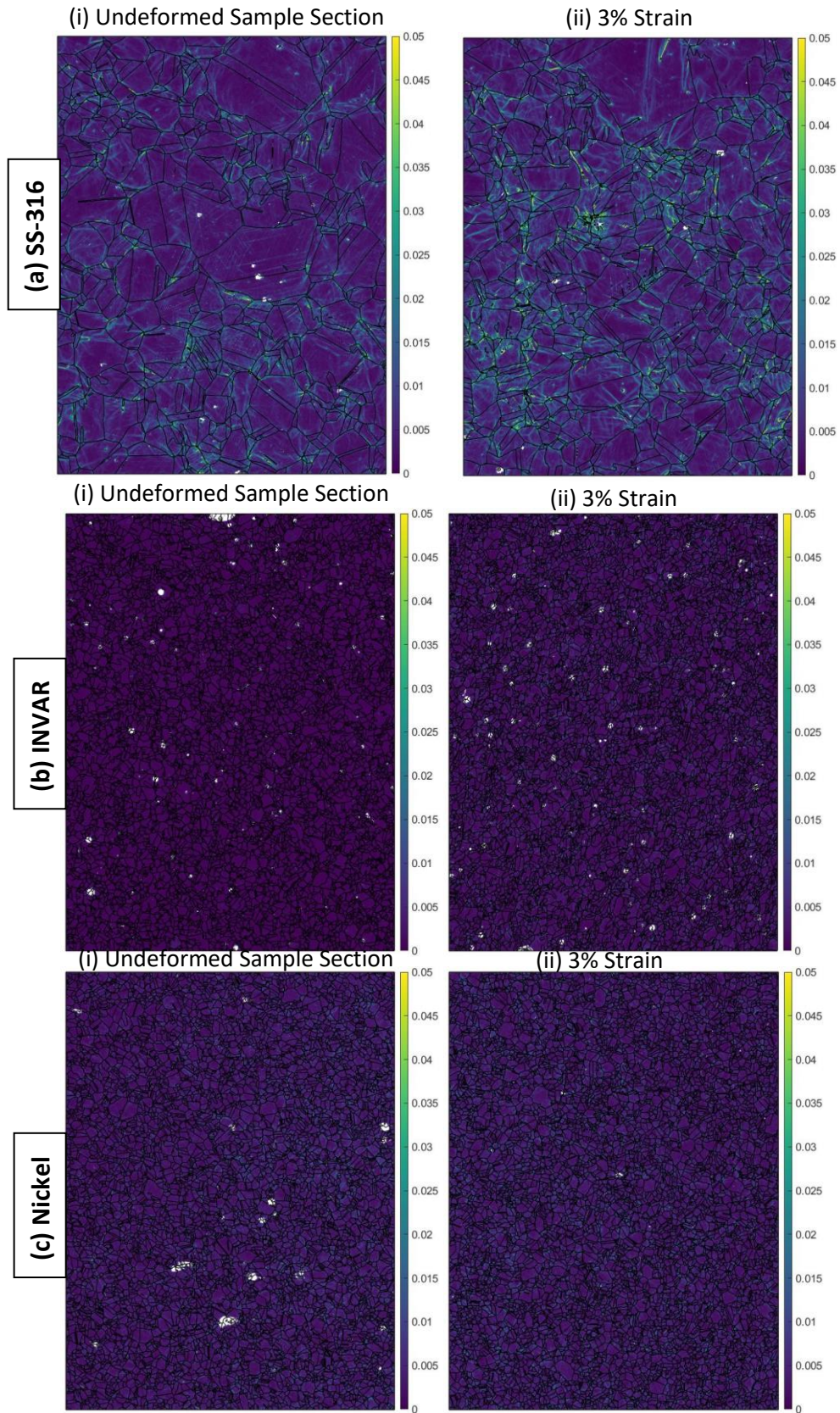


Figure 5.7: EBSD maps for KAM in radians calculated from EBSD data from the deformed and undeformed regions cut from the samples (a) SS315, (b) INVAR and (c) pure nickel. The white regions on the figures are unindexed points.

The scales for the EBSD metric map plots, found in Figure 5.5, Figure 5.6 and Figure 5.7, are kept consistent for all three materials to allow comparisons between them to be drawn. However, the scale for the INVAR and pure nickel are much smaller than the SS316, therefore, additional plots have been used to visualise the spatial variations in these metrics in a similar way to how it is possible with SS316.

Figure 5.8 (a)(i) shows the GOS map values for the undeformed INVAR sample and Figure 5.8 (a)(ii) shows the values for the deformed region of the INVAR sample, both figures have a range between 0 and 2.5 degrees. At this scale it is clearer the difference between the deformed and undeformed samples, the undeformed section contains predominately grains with an orientation spread of 0 degrees, whereas the deformed section varies between 0 and 1.5 degrees. Figure 5.8 (b)(i) shows the GAM values for undeformed INVAR and Figure 5.8 (b)(ii) shows the GAM values for deformed INVAR with a scale of 0 to 1 degree. Similar, to the GOS values, the undeformed region shows all GAM values within grains to be at 0 degrees, unlike the deformed section which shows some grains to have values above 0.6 degrees. Figure 5.8 (c)(i) shows the KAM values for the undeformed section of the INVAR sample whereas Figure 5.8 (c)(ii) shows the deformed area with scales between 0 and 1 degrees. Figure 5.8 (c)(i) shows very few instances where the KAM values are above 0 degrees, whereas Figure 5.8 (c)(ii) shows a large proportion of the map being above 0.2 degrees. This also highlights the concentrations forming around the grain boundaries which is observed at the greater length scale for SS316 in Figure 5.7 (a)(ii).

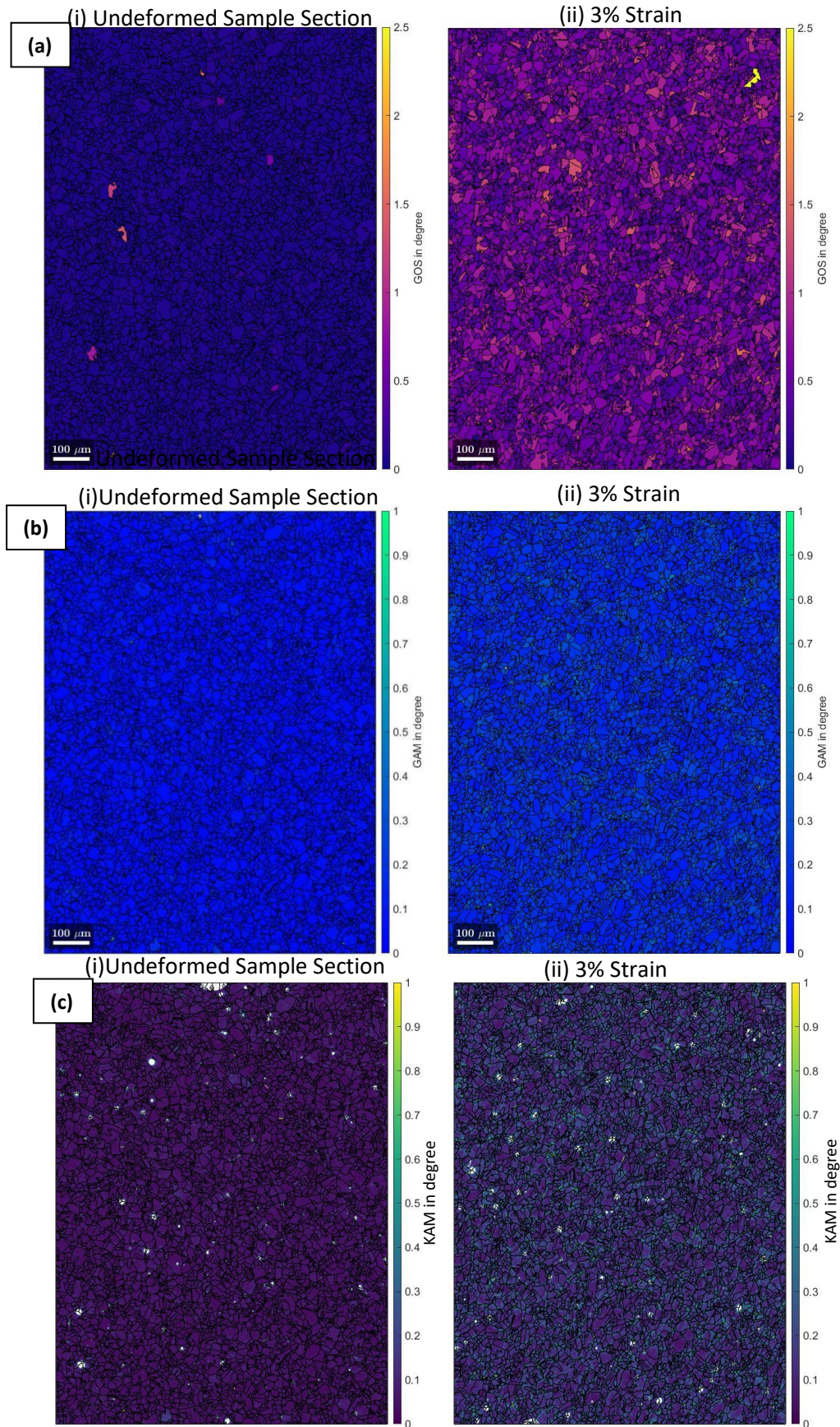


Figure 5.8: A comparison between the deformed and undeformed regions of the INVAR sample using a refined scale to highlight the change between samples for the EBSD metrics (a) GOS, (b) GAM and (c) KAM.

Figure 5.9 shows the refined scales for the GOS, GAM and KAM maps for the pure nickel specimen. Figure 5.9 (a)(i) shows the GOS values for undeformed pure nickel and Figure 5.9 (a)(ii) shows the GOS values for the deformed region, both with a length scale of 0 to 3 degrees. Both regions show areas with grains that have higher GOS values and regions with grains with lower GOS values but there seems to be little change between the two regions implying that deformation has little effect on the GOS values of pure nickel. Figure 5.9 (b)(i) shows the GAM values for undeformed pure nickel and Figure 5.9 (b)(ii) shows the values for the deformed region of pure nickel, where the length scale is between 0 and 2 degrees. The pure nickel sample shows very little change between the deformed and undeformed regions with all values for GAM in both regions remaining less than 0.6 degrees. Figure 5.9 (c)(i) shows the KAM values for undeformed pure nickel and Figure 5.9 (c)(ii) shows the KAM values for the deformed region of pure nickel. Both regions show around the same concentrations of higher peaks in KAM values. Compared to the INVAR and SS316 samples the pure nickel shows very little difference between the deformed and undeformed regions. This may imply that nickel already contains a large amount of misorientation before deformation or that deformation has little impact on increasing the misorientation of grains.

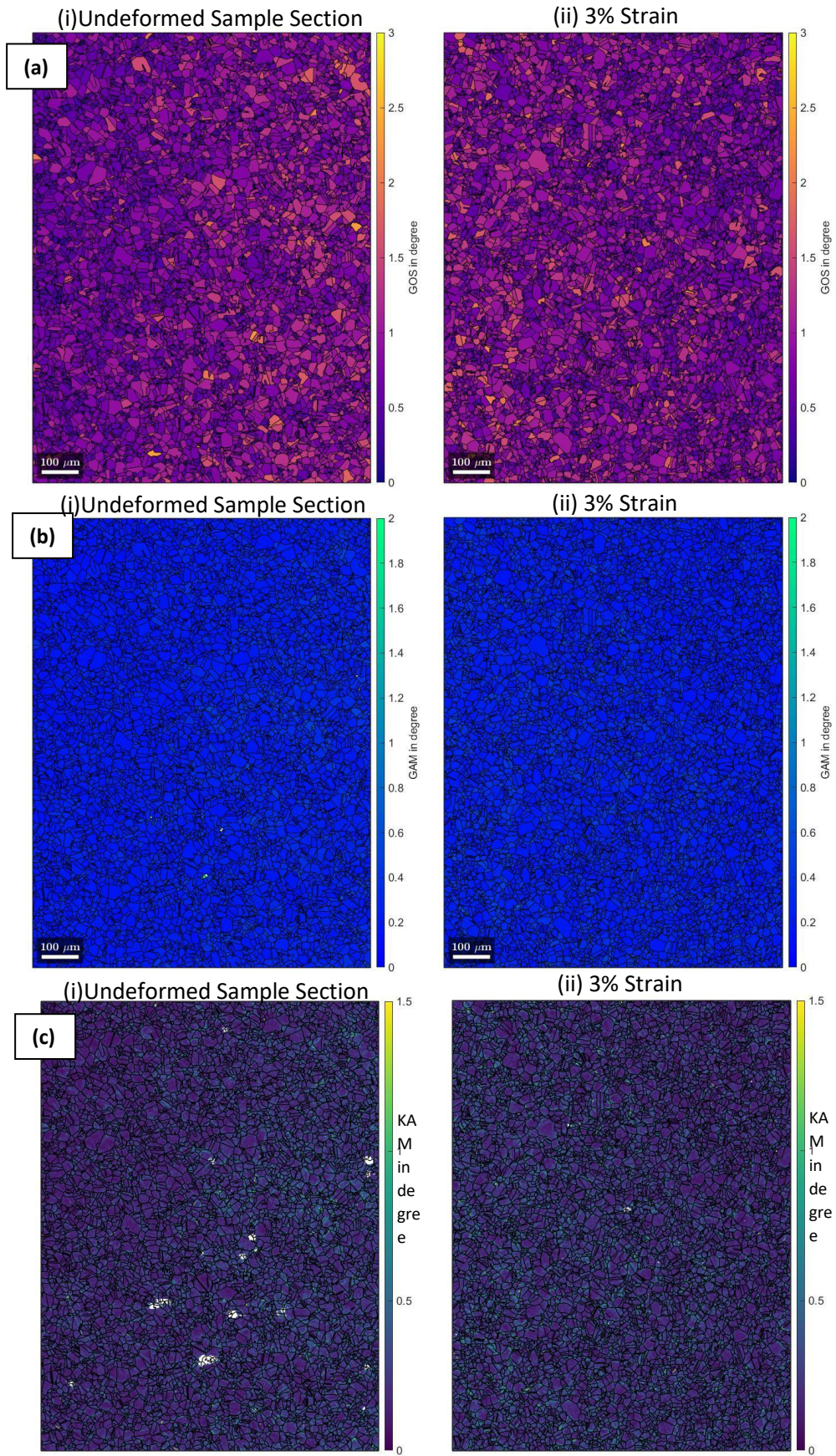


Figure 5.9: A comparison between the deformed and undeformed regions of the pure nickel sample using a refined scale to highlight the change between samples for the EBSD metrics (a) GOS, (b) GAM and (c) KAM.

5.3.3. Segmenting EBSD data

A MATLAB code was written to segment the EBSD data into subsets of grains containing similar crystallographic orientations that correspond to the grain orientations satisfying Bragg's law for each of the interesting ENGIN-X diffraction peaks. The three subsets selected were within 7.5 degrees of the 111, 220 and 200, this is because ENGIN-X has an accuracy of ± 7.5 degrees and this allowed a comparison to be drawn between the two techniques. Additionally, to ensure a comparison could be made to the neutron diffraction data, the grains selected were those that would be perpendicular to the loading direction (the same grains that would diffract in the neutron diffraction tests). This enabled a direct comparison with the neutron diffraction data presented in section 4.6.

The number of grains identified by MATLAB for each of the samples can be found in Table 5.1. Due to the regions being from different parts of the material, it is expected that these values will vary.

Table 5.1 This table shows the number of grains identified by the MATLAB for the specified crystallographic orientations

State	Material	Crystallographic Orientations		
		111	220	200
Undeformed	SS316	103	101	31
	INVAR	628	367	455
	Nickel	474	559	392
Deformed	SS316	104	193	149
	INVAR	862	371	631
	Nickel	657	439	586

To visualise the subsets selected for the EBSD metric analysis, EBSD maps with only the grains which would diffract to the given peak are presented in this section. Figure 5.10 shows segmented EBSD maps for the undeformed region of SS316, showing the grains which would diffract to the 111, 220 and 200 peaks at ENGIN-X. There are visibly more grains for the 111 orientation subset in Figure 5.10 (a) compared to the 220 and 200 subsets. The 111 subset shows a slight variation in the blue tone within the grains indicating a range of orientations, whereas the 220 and 200 subsets both have solid colours.

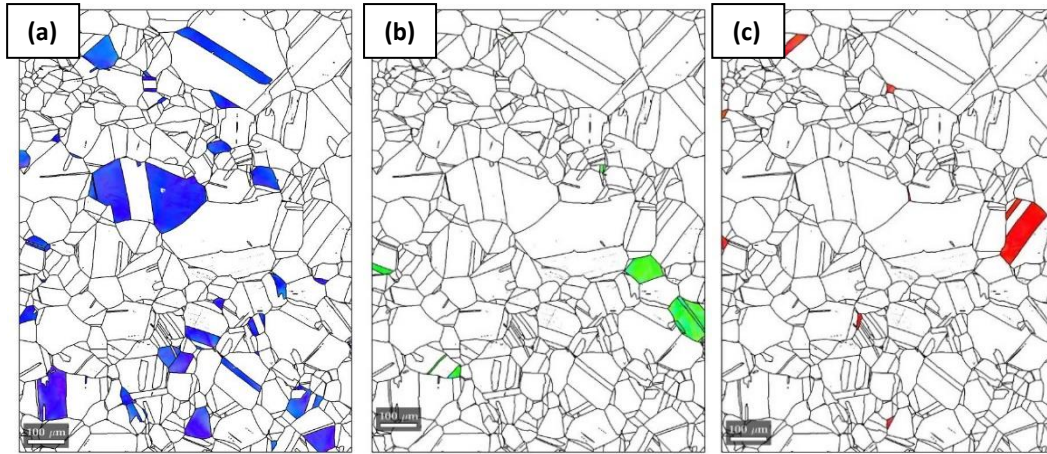


Figure 5.10: The grains selected by the MATLAB code for undeformed SS316 showing the subsets of grains within 7.5 degrees of the (a) 111, (b) 220 and (c) 200 orientations.

Figure 5.11 shows segmented EBSD maps for the deformed region of SS316, showing the grains which would diffract to the 111, 220 and 200 peaks at ENGIn-X. The grains in the 111 orientation subset show an increased colour variation throughout the grains compared to the undeformed region, indicating more range of orientations following deformation. An increase in variation is also found in the 220 subsets, particularly in the grain highlighted in Figure 5.11 (b). There is less colour variation in the 200 than in the other two subsets, additionally, more grains are observed than in the undeformed region.

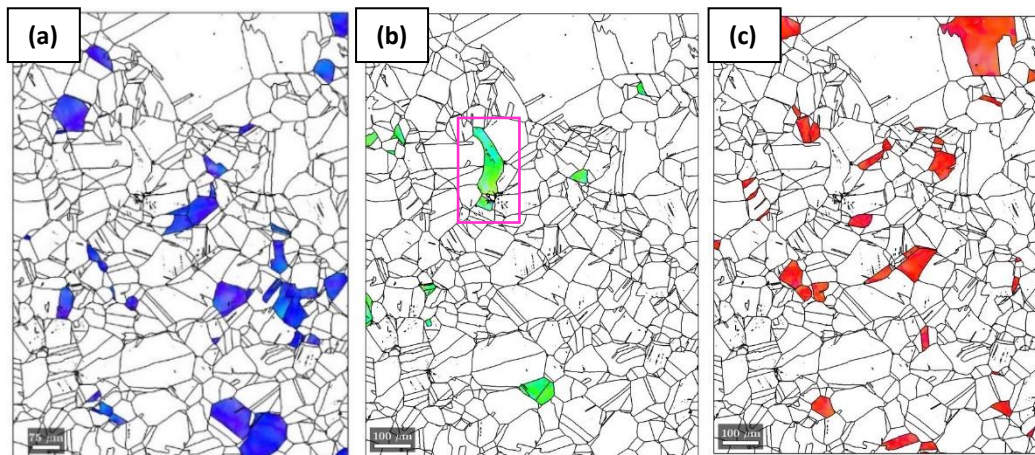


Figure 5.11: The grains selected by the MATLAB code for deformed SS316 at 3% strain showing the subsets of grains within 7.5 degrees of the (a) 111, (b) 220 and (c) 200 orientations.

Table 5.2 shows the pole figures for the selected subsets of grains with the orientations 111, 220 and 200 for both the undeformed and deformed regions SS316. The undeformed region has data points accumulated in specific regions within the pole figures, whereas the deformed sample shows the points to be spread out in all directions.

Table 5.2: Pole figures for the undeformed and deformed regions of the SS316 specimen, where the grain subsets are defined to be within 7.5 degrees of the (a) 111, (b) 220, and (c) 200 orientations. The out of plane direction is the loading direction.

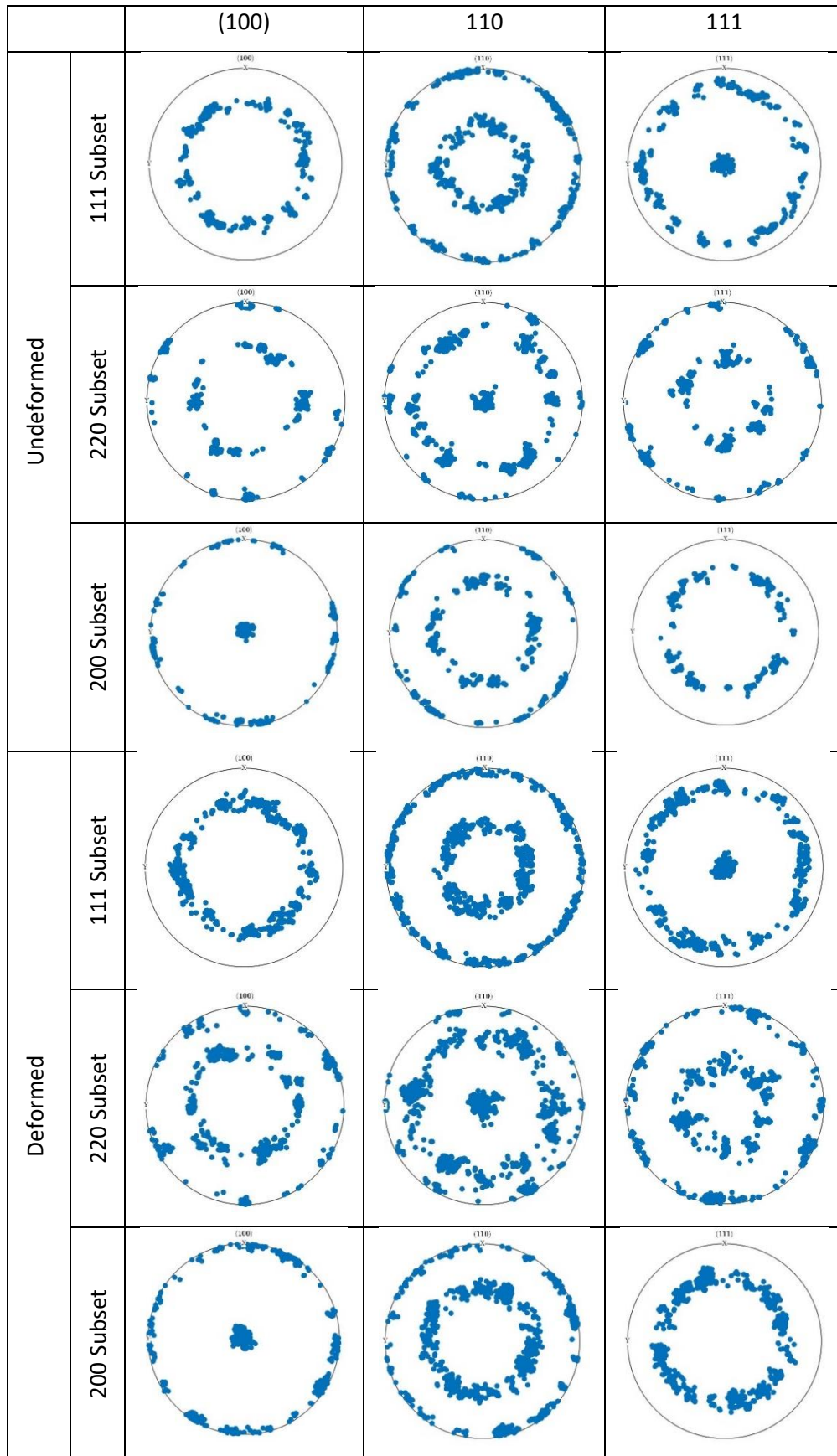


Figure 5.12 shows segmented EBSD maps for the undeformed region of INVAR, showing the grains which would diffract to the 111, 220 and 200 peaks at ENGIN-X. The grains are evenly distributed in all subsets showing the orientation is random throughout. The grains are much smaller than the SS316 sample, so it is harder to tell the colour distribution within grains, however, there is some variation between grains in the 111 orientation subset in Figure 5.12 (a). The 220 and 2000 subsets also show some colour variation between grains.

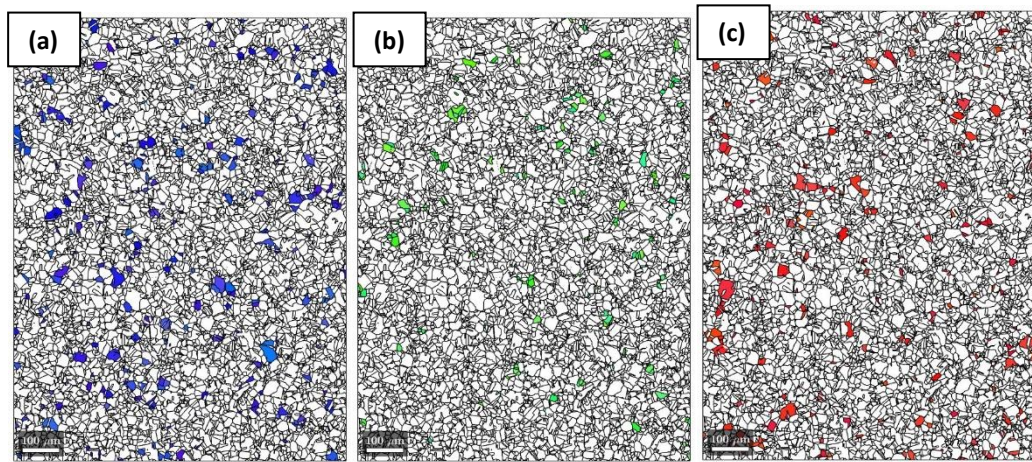


Figure 5.12: The grains selected by the MATLAB code for undeformed INVAR showing the subsets of grains within 7.5 degrees of the (a) 111, (b) 220 and (c) 200 orientations.

Figure 5.13 shows segmented EBSD maps for the deformed region of INVAR, showing the grains which would diffract to the 111, 220 and 200 peaks at ENGIN-X. The grains are uniformly distributed throughout the material, indicating a random texture. There is little change in the number of grains in each subset from the undeformed region. The colour variation between grains in each subset is also similar to that of the undeformed sample.

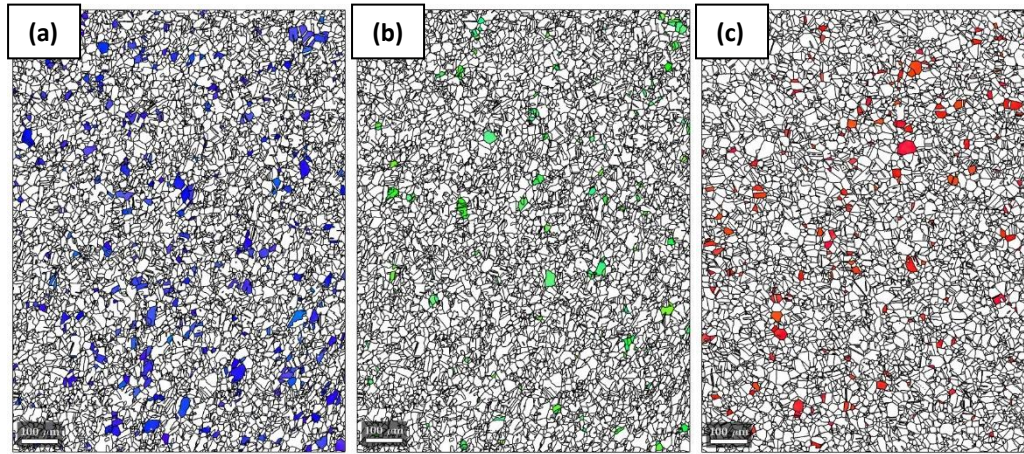


Figure 5.13: The grains selected by the MATLAB code for deformed INVAR showing the subsets of grains within 7.5 degrees of the (a) 111, (b) 220 and (c) 200 orientations.

Table 5.3 shows the pole figures for the selected subsets of grains with the orientations 111, 220 and 200 for the undeformed INVAR sample. Table 5.3 shows the pole figures for the deformed region of the INVAR sample. This verifies that the grains selected are correlated to the defined orientation.

Table 5.3: Pole figures for the undeformed and deformed regions of the INVAR specimen, where the grain subsets are defined to be within 7.5 degrees of the (a) 111, (b) 220, and (c) 200 orientations. The out of plane direction is the loading direction.

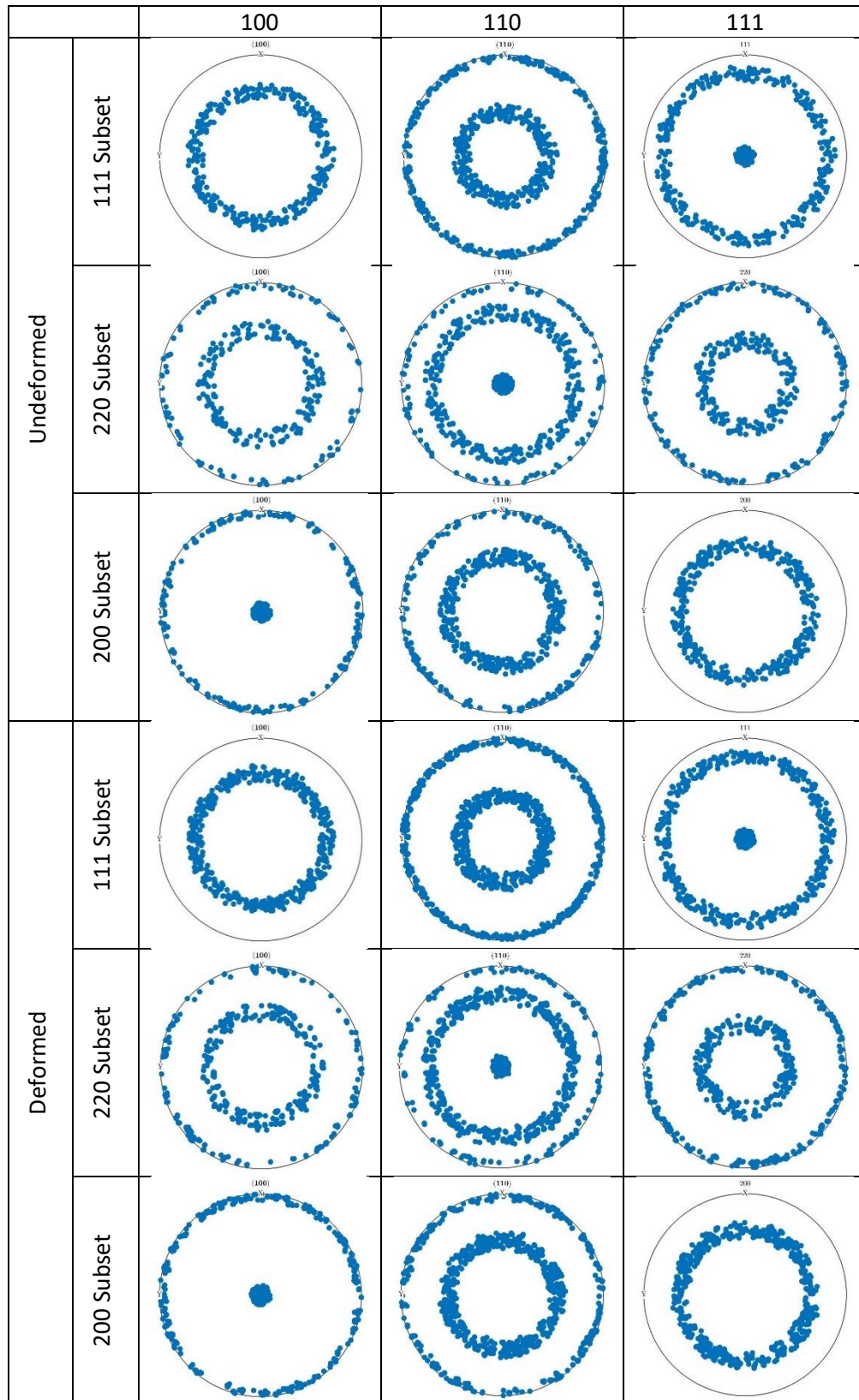


Figure 5.14 shows segmented EBSD maps for the undeformed region of pure nickel, showing the grains which would diffract to the 111, 220 and 200 peaks at ENGIN-X. Each subset shows some variation in colour within the subset, indicating some variation in orientation.

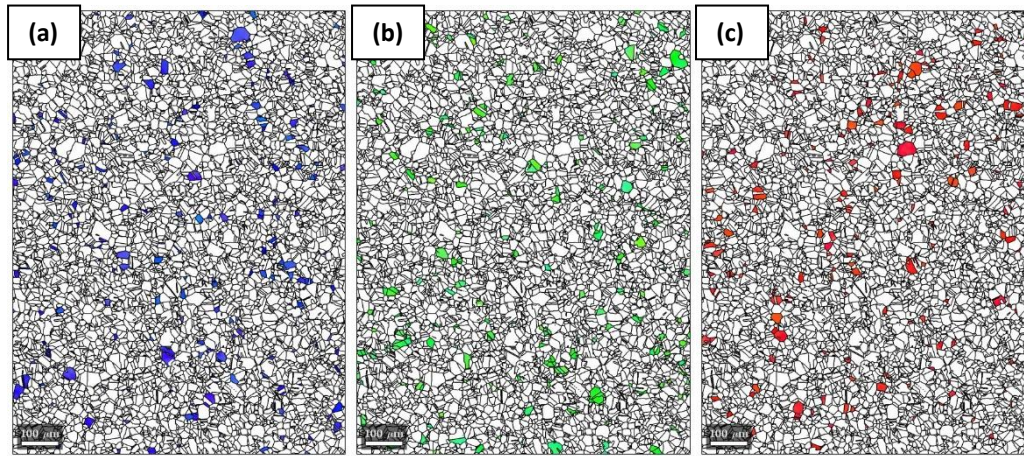


Figure 5.14: The grains selected by the MATLAB code for undeformed pure nickel showing the subsets of grains within 7.5 degrees of the (a) 111, (b) 220 and (c) 200 orientations.

Figure 5.15 shows segmented EBSD maps for the deformed region of pure nickel, showing the grains which would diffract to the 111, 220 and 200 peaks at ENGIN-X. Each subset shows some variation in colour within the subset, indicating some variation in orientation.

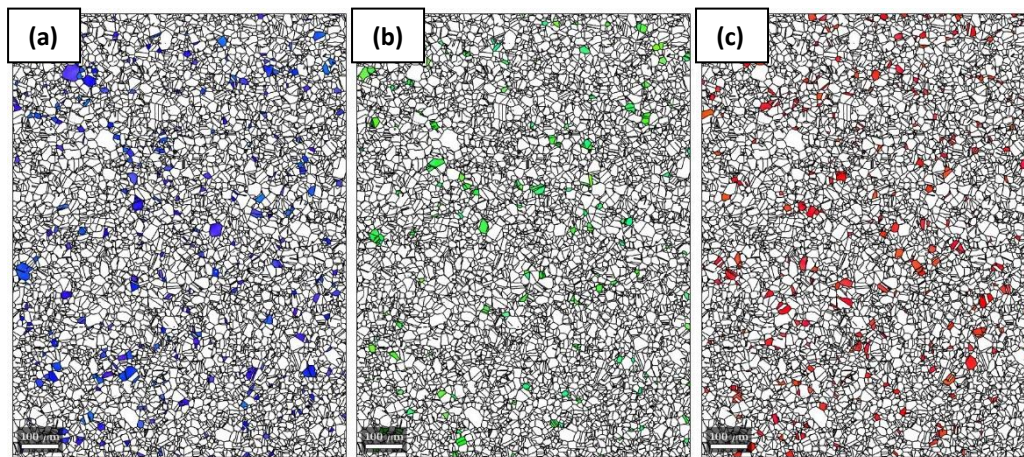
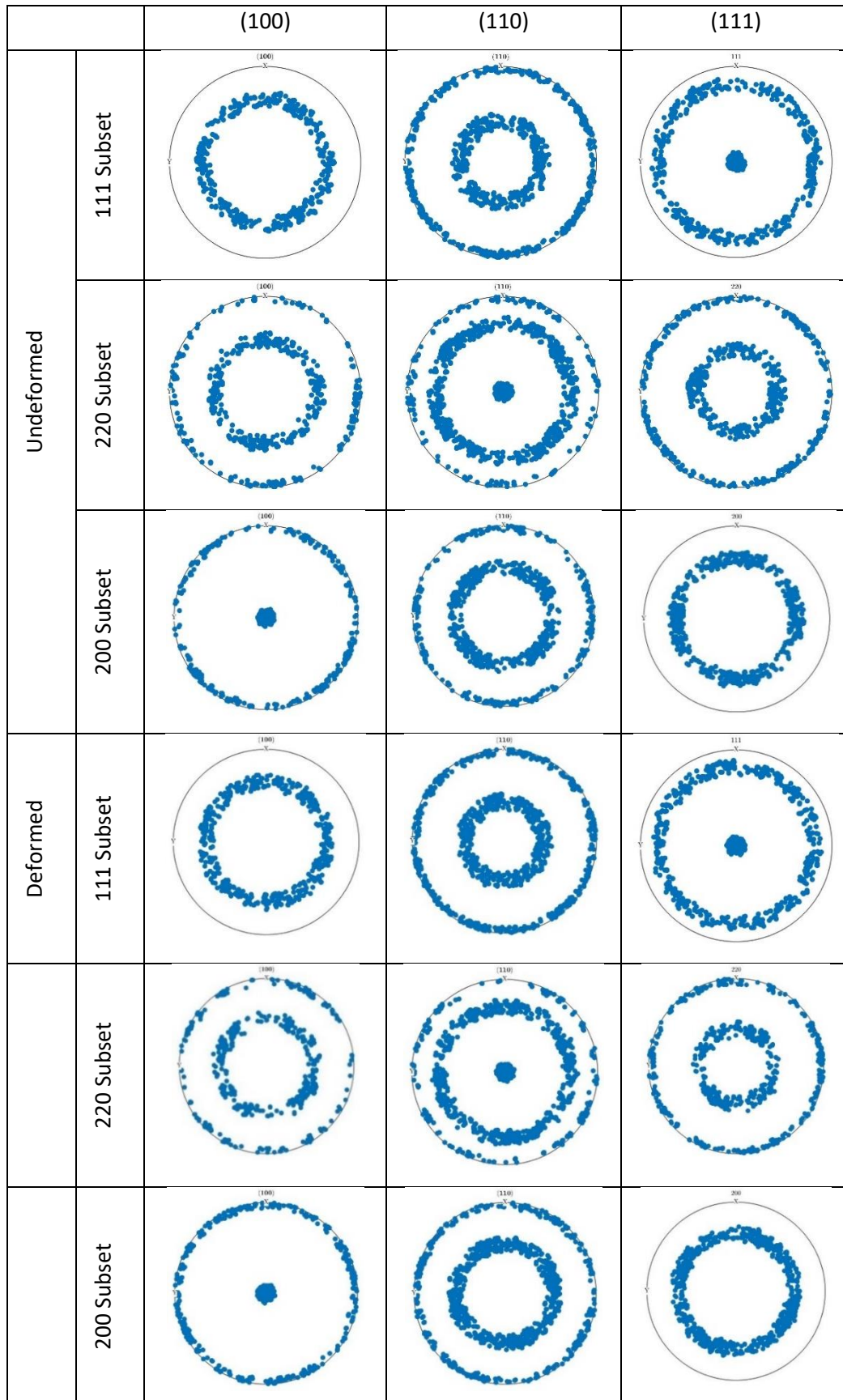


Figure 5.15: The grains selected by the MATLAB code for deformed pure nickel showing the subsets of grains within 7.5 degrees of the (a) 111, (b) 220 and (c) 200 orientations.

Pole figures for the selected subsets of grains with the orientations 111, 220 and 200 are shown for undeformed and deformed nickel in Table 5.4

Table 5.4: Pole figures for the undeformed and deformed regions of the pure nickel specimen, where the grain subsets are defined to be within 7.5 degrees of the (a) 111, (b) 220, and (c) 200 orientations. The out of plane direction is the loading direction.



5.3.4. Histograms plots of EBSD Metrics

This section will present the histogram plots for the results of the Schmid factor, Taylor Factor and EBSD metrics for the samples of SS316, INVAR and pure nickel in the deformed and undeformed states. The histogram plots are used to present a graphical representation of the spatial maps shown in the previous section, this allows for the data to be quantified and shows numerical values compared to studying the maps visually.

5.3.4.1. Schmid Factor

As discussed in section 2.3.1, the Schmid factor can be used to determine the CRSS. EBSD analysis can be used to determine the Schmid factor for all grains and grain subsets. This section will show the results of the Schmid factor analysis on the EBSD Maps on the undeformed and deformed regions of the specimens. Figure 5.16 shows the histogram plot for the deformed and undeformed regions for SS316. The values of the Schmid factor vary between 0.28 and 0.5. The 111-orientation subset makes up all the lowest values of the Schmid factor for the material, between around 0.28 and 0.35. The 220 and 200 subsets of grains have values between 0.42 and 0.46. The 200 subset shows a relative increase in the number of counts compared to the other orientation subsets.

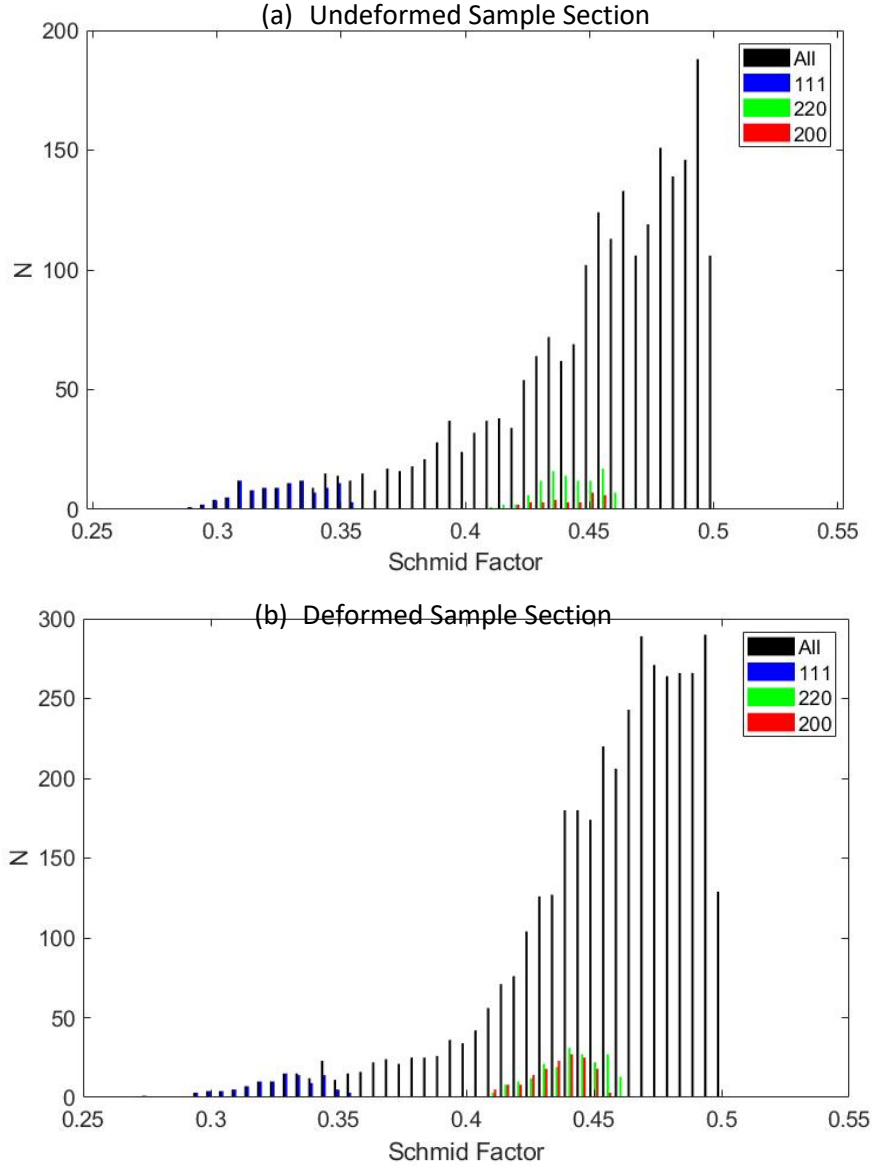


Figure 5.16: Histogram showing the number of counts (N) for each Schmid Factor for all grains, and for the subsets of grains within 7.5 degrees of crystallographic orientations 111, 220 and 200 for SS316 for the (a) undeformed and (b) deformed regions.

Figure 5.17 shows the histogram plot for the deformed and undeformed regions for INVAR. The values of the Schmid factor vary between 0.28 and 0.5. The 111 orientation subset makes up all the lowest values of the Schmid factor for the material, between around 0.28 and 0.35. The 220 and 200 subsets of grains have values between 0.42 and 0.46.

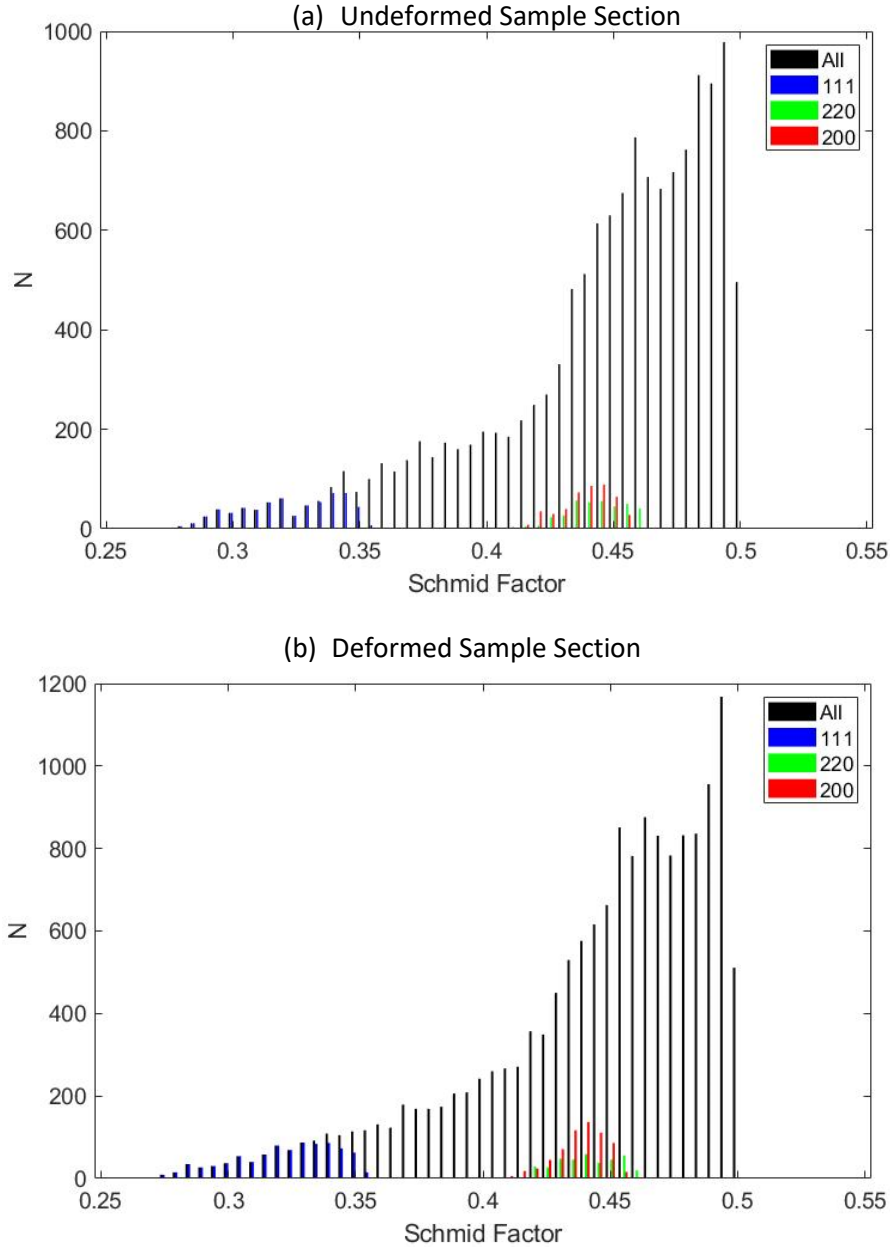


Figure 5.17: Histogram showing the number of counts (N) for each Schmid Factor for all grains, and for the subsets of grains within 7.5 degrees of crystallographic orientations 111, 220 and 200 for INVAR for the (a) undeformed and (b) deformed regions.

Figure 5.18 shows the histogram plot for the deformed and undeformed regions for the pure nickel specimen. The values of the Schmid factor vary between 0.28 and 0.5. The 111-orientation subset makes up all the lowest values of the Schmid factor for the material, between around 0.28 and 0.35. The 220 and 200 subsets of grains have values between 0.42 and 0.46.

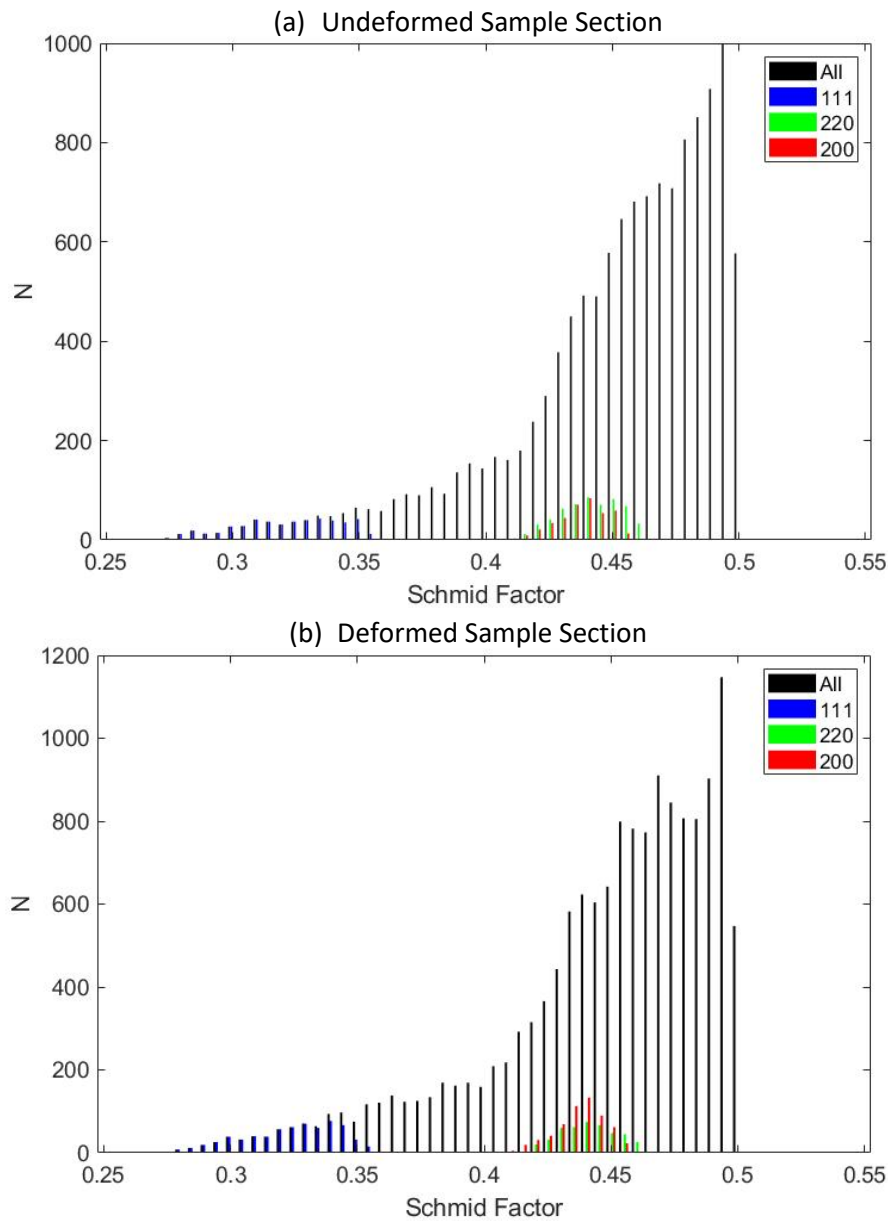


Figure 5.18: Histogram showing the number of counts (N) for each Schmid Factor for all grains, and for the subsets of grains within 7.5 degrees of crystallographic orientations 111, 220 and 200 for pure nickel for the (a) undeformed and (b) deformed regions.

5.3.4.2. Taylor Factor

This section will present the histogram plots for the Taylor factors for the undeformed and deformed samples. Taylor factor is another way of predicting the likelihood of deformation for a given crystallographic orientation. These values are the same for all FCC materials and are dependent on the orientation.

The histogram plots for the Taylor factor values for undeformed and deformed regions of SS316 are shown in Figure 5.19. This shows that the 111 and 220 subsets of grains have values at around 3.6 - 3.7 whereas the 200 subset has a much lower Taylor factor. This is seen in both the deformed and undeformed subsets, however, the number of counts increases in the deformed subset.

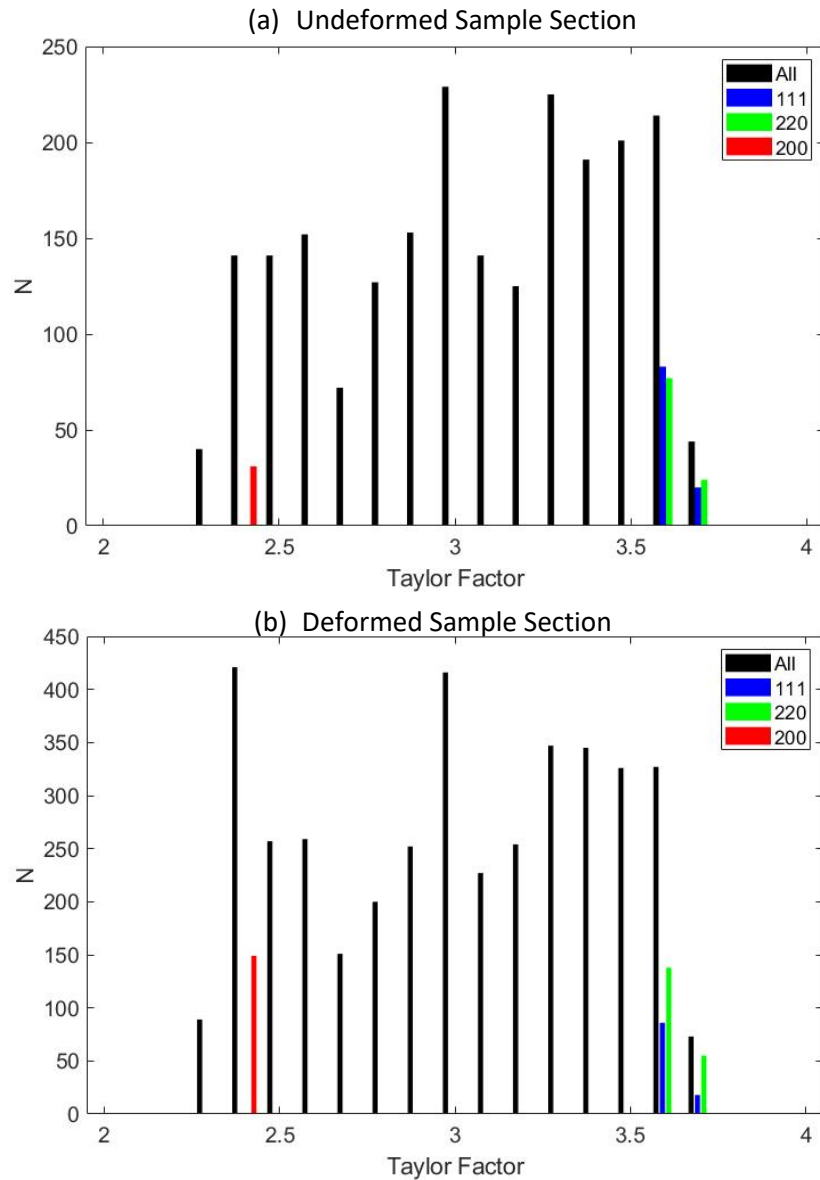


Figure 5.19: Histogram plot showing the Taylor Factor values for the total and the subsets of grains within 7.5 degrees of the 111, 220 and 200 orientations for deformed SS316

Figure 5.20 (a) shows the histogram plot for the undeformed INVAR and Figure 5.20 (b) the deformed region. The 111 and 220 orientation subsets have the same values of the Taylor factor whereas the 200 subset has a lower Taylor factor at ~ 2.4 .

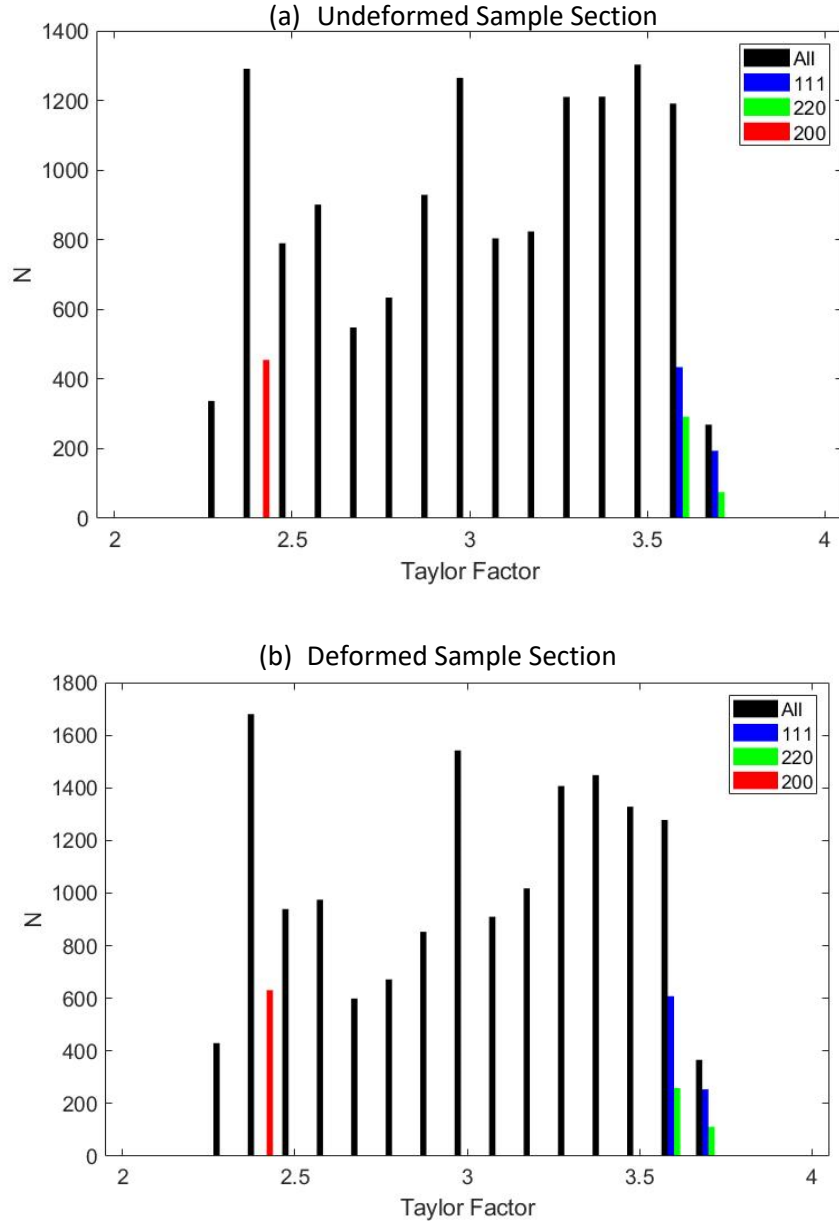


Figure 5.20: Histogram plot showing the Taylor Factor values for the total and the subsets of grains within 7.5 degrees of the 111, 220 and 200 orientations for undeformed and deformed INVAR.

Figure 5.21 shows the histogram plot for the undeformed pure nickel and Figure 5.21 (b) the deformed region. The 111 and 220 orientation subsets have the same values of the Taylor factor whereas the 200 subset has a lower Taylor factor at ~ 2.4 .

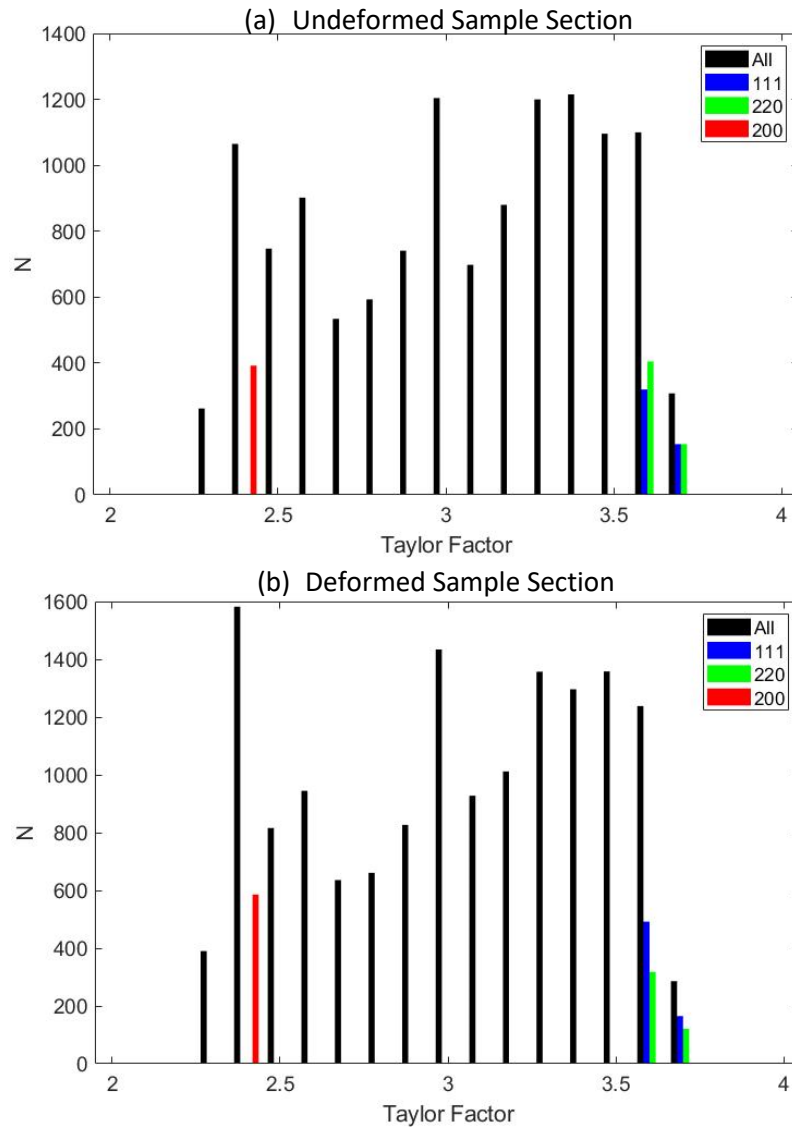


Figure 5.21: Histogram plot showing the Taylor Factor values for the total and the subsets of grains within 7.5 degrees of the 111, 220 and 200 orientations for an undeformed and deformed nickel.

5.3.4.3. Grain Orientation Spread

The EBSD metric, grain orientation spread (GOS), is the average of the misorientation angles to the grain mean orientation. The GOS was calculated for the subsets of grains which are within 7.5 degrees of 111, 220 and 200 crystallographic orientations. Figure 5.22 shows the histogram plots for GOS values of SS316 shown in Figure 5.5 (a)(i) and (a)(ii). Figure 5.22 (a) shows the GOS values for the undeformed region for the SS316 sample and Figure 5.22 (b) shows the deformed region. These figures show there to be a large amount of spread, possibly due to the large grain size found in SS316, however, it is evident that there are greater instances of grains with higher GOS values in the deformed sample. The deformed region has a peak of GOS values at 10 degrees whereas the undeformed region has a peak at 9 degrees.

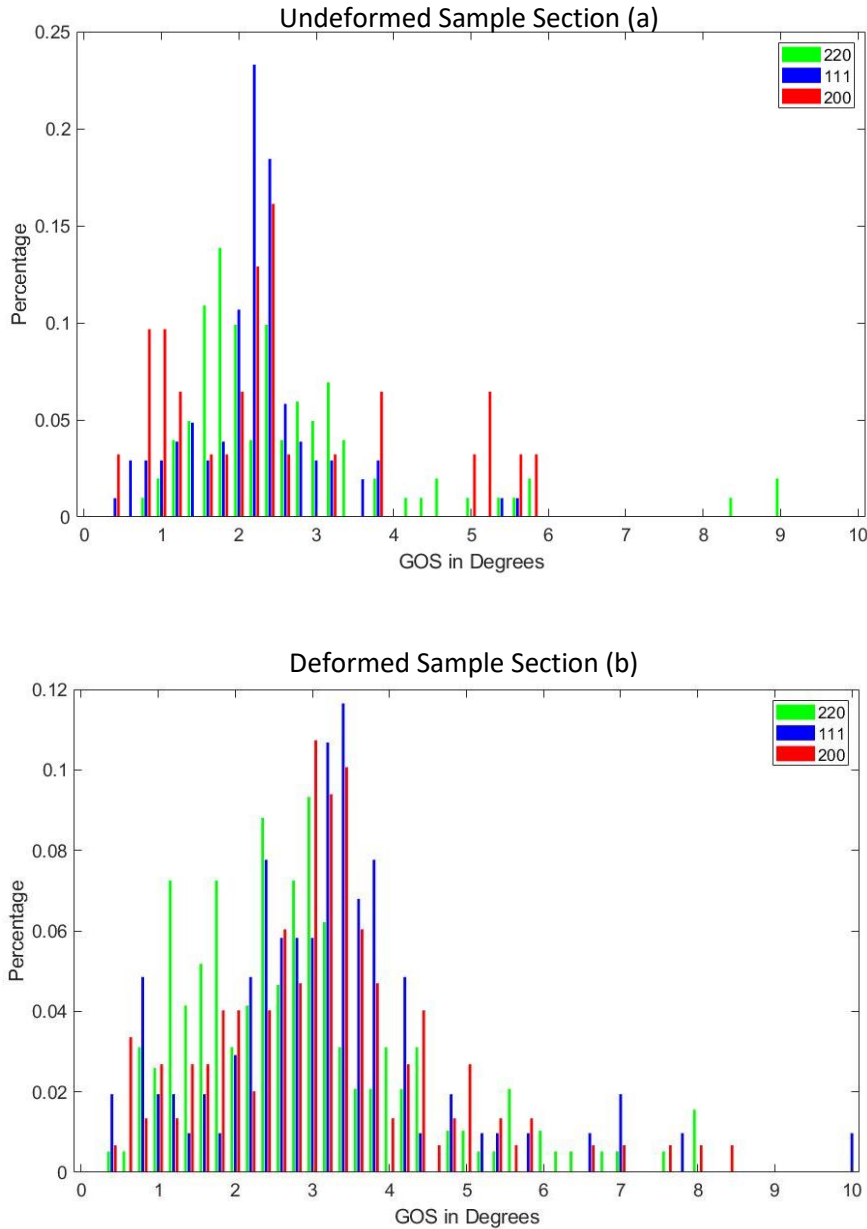


Figure 5.22: Histogram plots showing the GOS values for the grain subsets which are within 7.5 degrees of the 111, 220 and 200 orientations for the SS316 specimen for the (a) undeformed region and (b) deformed region.

Figure 5.23 (a) shows the histogram plot for the GOS values of the undeformed region of INVAR and Figure 5.23 (b) shows the histogram plot for the deformed region of INVAR. In Figure 5.23 (a), 90% of the instances of GOS for the 111, 220 and 200 subsets of grains have a value of 0 degrees, with ~10% at 0.2 degrees. The largest value is at 0.6 degrees for the 220 orientation subset of grains, this is likely to account for a singular grain. Figure 5.23 (b) shows the GOS values for the deformed region of INVAR. Here, it is noted that a larger spread is present in the data and the highest value recorded for GOS is at 1.8 degrees which is over double that of the undeformed region.

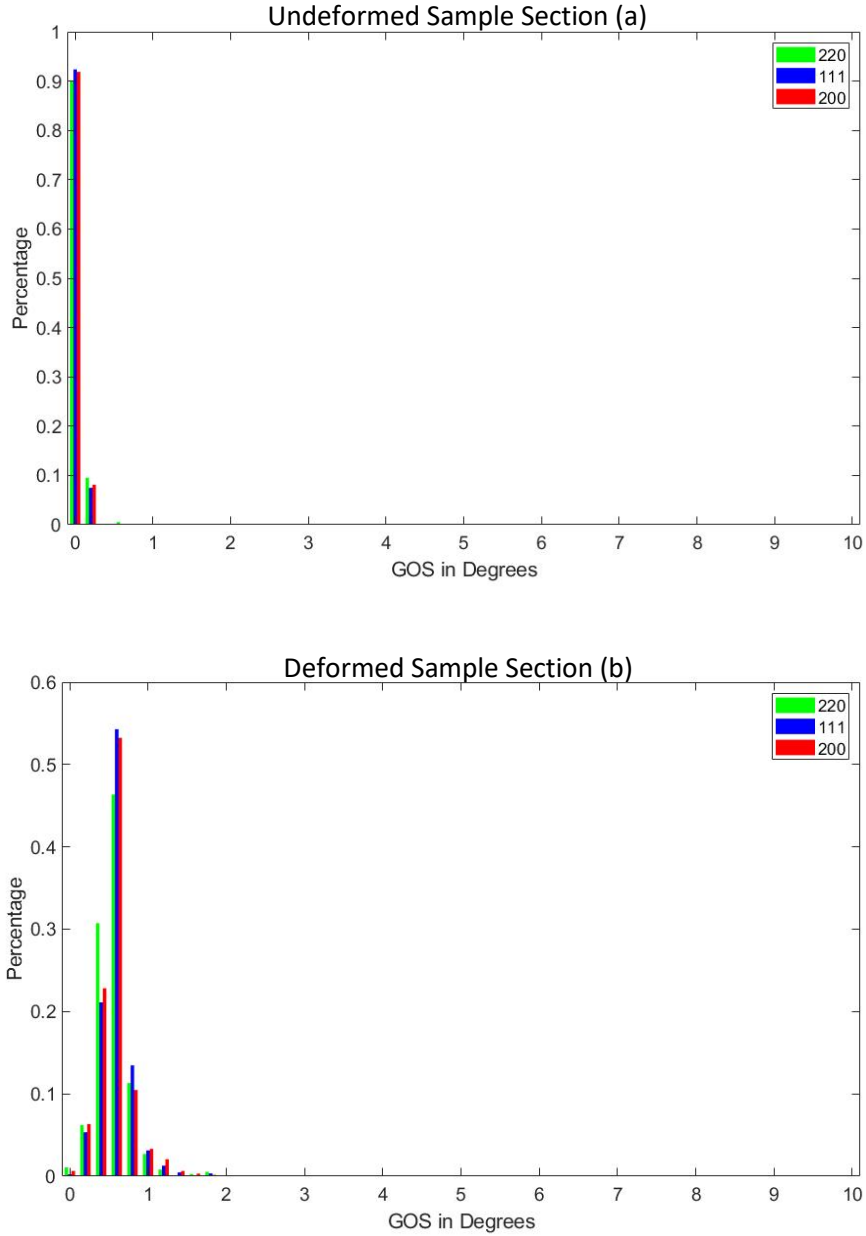


Figure 5.23: Histogram plots showing the GOS values in degrees for the grain subsets which are within 7.5 degrees of the 111, 220 and 200 orientations for the INVAR specimen for the (a) undeformed region and (b) deformed region.

Figure 5.24 (a) shows the histogram plot for the GOS values for the undeformed region of the pure nickel sample and Figure 5.24 (b) shows the histogram plot for the GOS values for the deformed section. From these histogram plots, it can be seen that there is very little difference in the range and top value of the GOS data from the deformed and undeformed regions.

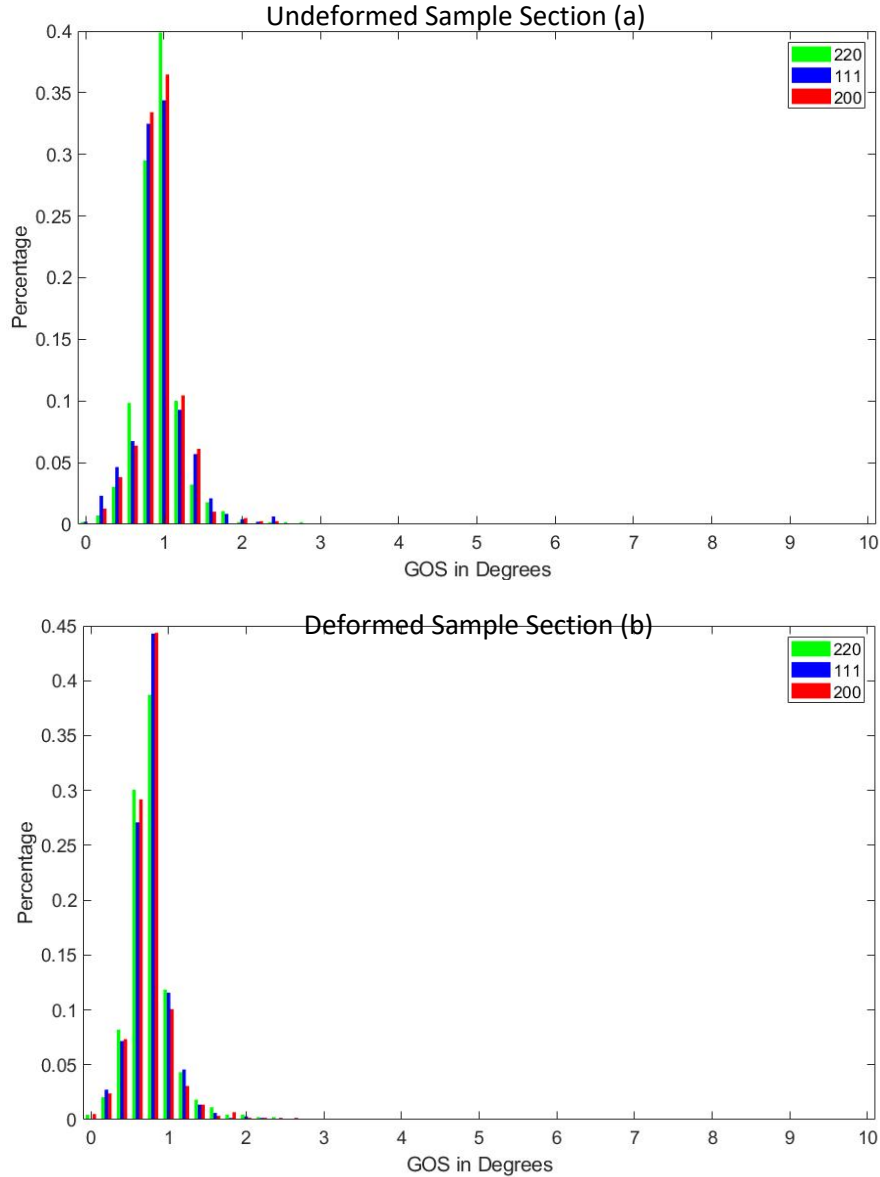


Figure 5.24: Histogram plots showing the GOS values in degrees for the grain subsets which are within 7.5 degrees of the 111, 220 and 200 orientations of pure nickel for the (a) undeformed region and (b) deformed region.

5.3.4.4. Grain Average Misorientation

Another EBSD metric is GAM which the average misorientation calculated over each individual grain. The GAM histograms for SS316 can be found in Figure 5.25 where the units are given in degrees. Similarly, to the GOS histograms for SS316 shown in Figure 5.22, the GAM histogram plots show a lot of noise in the results, this is again likely caused by the large grain size found in SS316 causing a large amount of variation throughout the grains. Figure 5.25 (a) shows the results of the GAM analysis for the undeformed region of the SS316 sample and Figure 5.25 (b) shows the deformed region of the SS316 sample. For the deformed region, there are more instances of grains with GAM values above 1.5 degrees indicating that deformation increases the value of GAM for SS316. However, due to the

noise in both regions, it is hard to identify how the 111, 220 and 200 subsets are affected by deformation, as there are values recorded for all subsets between 0 and 2.5 degrees.

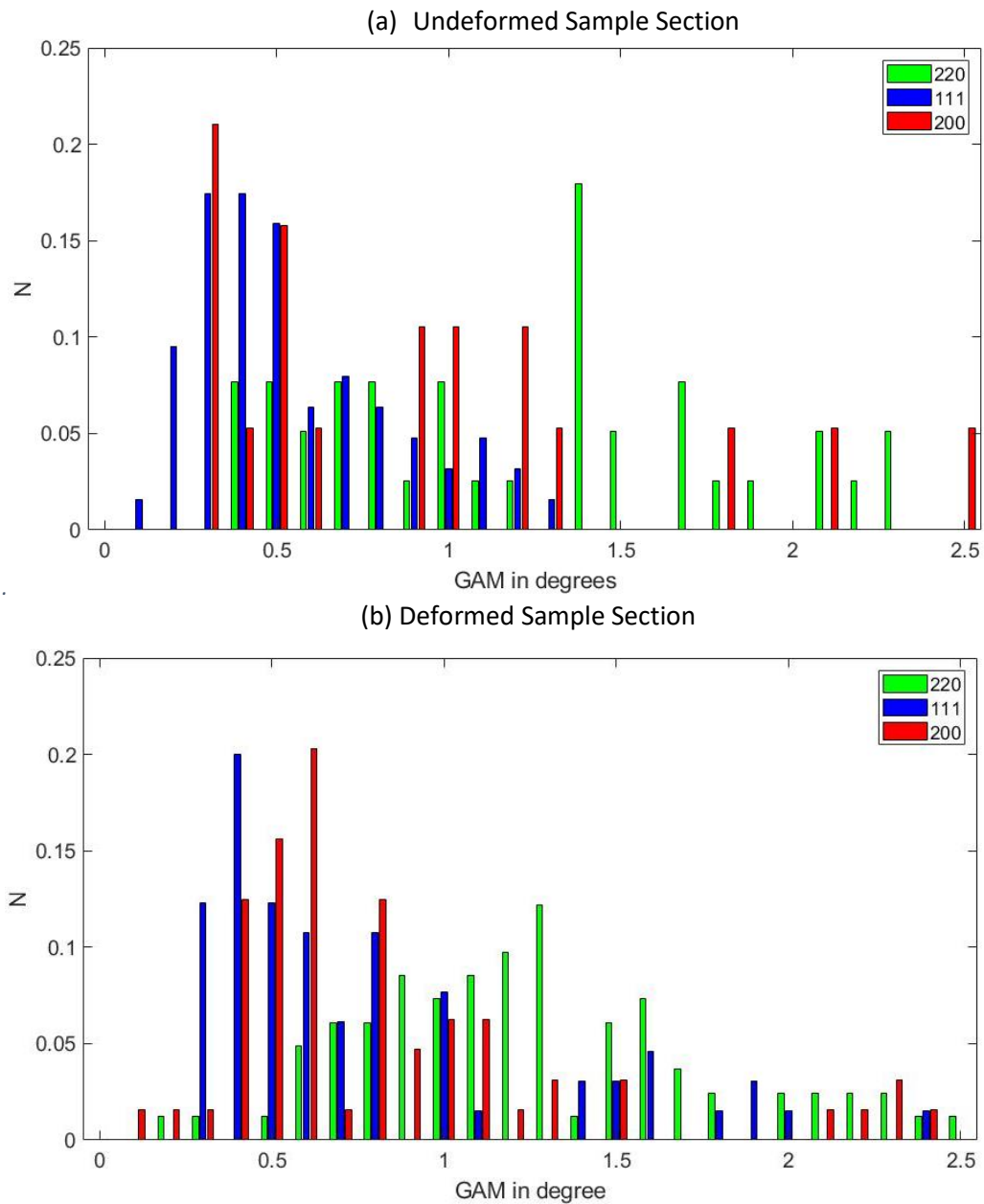


Figure 5.25: GAM histogram for SS316 (a) undeformed region and (b) deformed region, where the subsets of grains are defined as being within 7.5 degrees of the 111, 220 and 200 orientations.

The histogram plots for the GAM values recorded for the undeformed region in INVAR are shown in Figure 5.26 (a) and the deformed region to 3% strain in Figure 5.26 (b). The same levels of noise observed in the SS316 are not seen in these figures and are likely due to the grain sizes being smaller. Figure 5.26 (a) shows that most GAM values are found at 0.2 degrees for all subsets. There is also one grain which has a value of GAM greater than 0.5 degrees and this grain has the 220

crystallographic orientation. However, Figure 5.26 (b) shows an increase in the spread of GAM values and the highest value of GAM being recorded at 1 degree. This indicates that deformation has caused the GAM values of INVAR to increase.

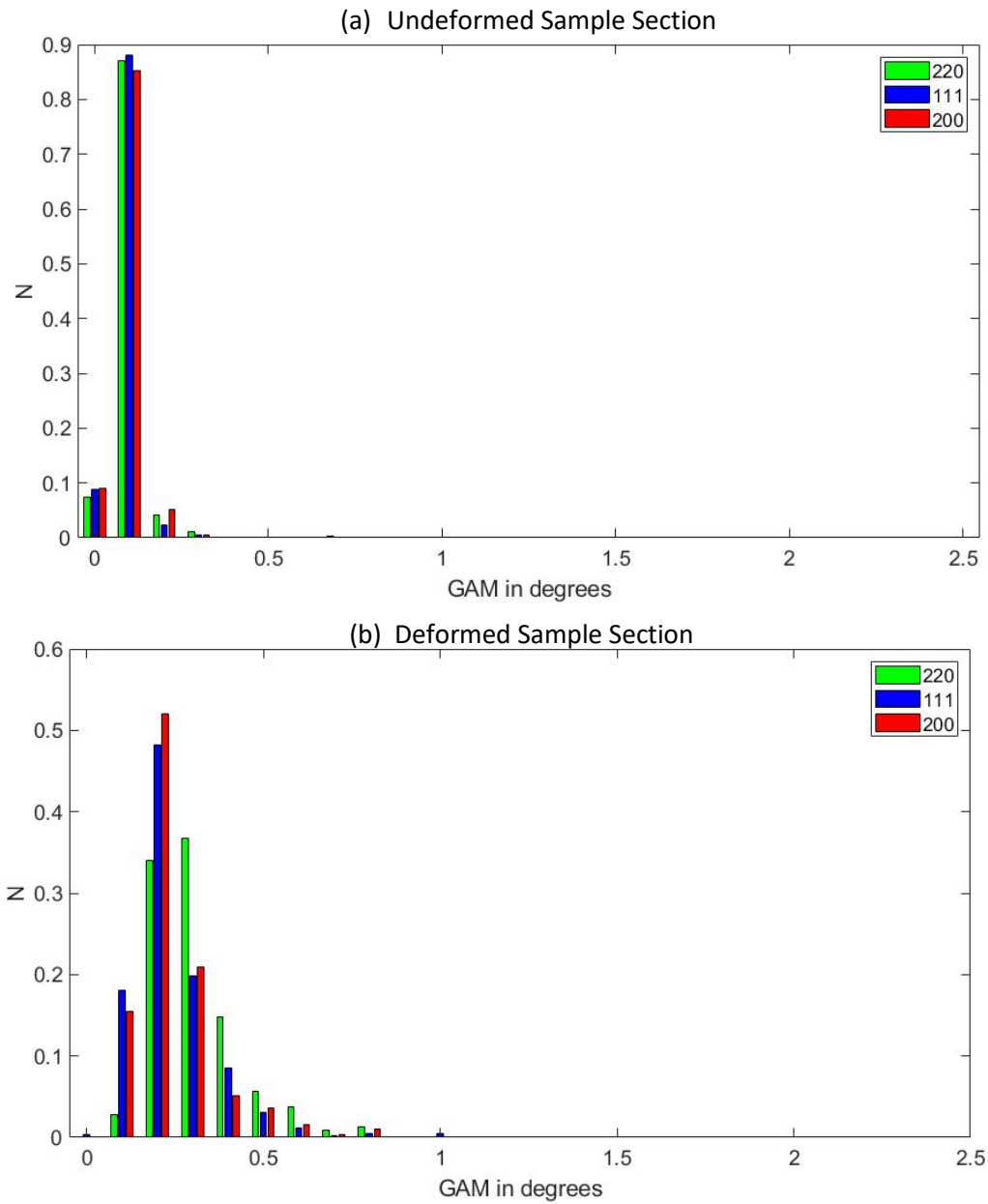


Figure 5.26: GAM histogram for INVAR (a) undeformed region and (b) deformed region, where the subsets of grains are defined as being within 7.5 degrees of the 111, 220 and 200 orientations.

Figure 5.27 (a) shows the histogram plot for the GAM values of the undeformed region of pure nickel and Figure 5.27 (b) shows the deformed region of pure nickel. These plots confirm what is predicted in the GAM map in Figure 5.9 (b), that there is very little change between the undeformed and deformed regions of pure nickel, however, Figure 5.27 (b) shows that to be an increase in the average misorientations of the 220 orientation subset of grains compared to Figure 5.27 (a).

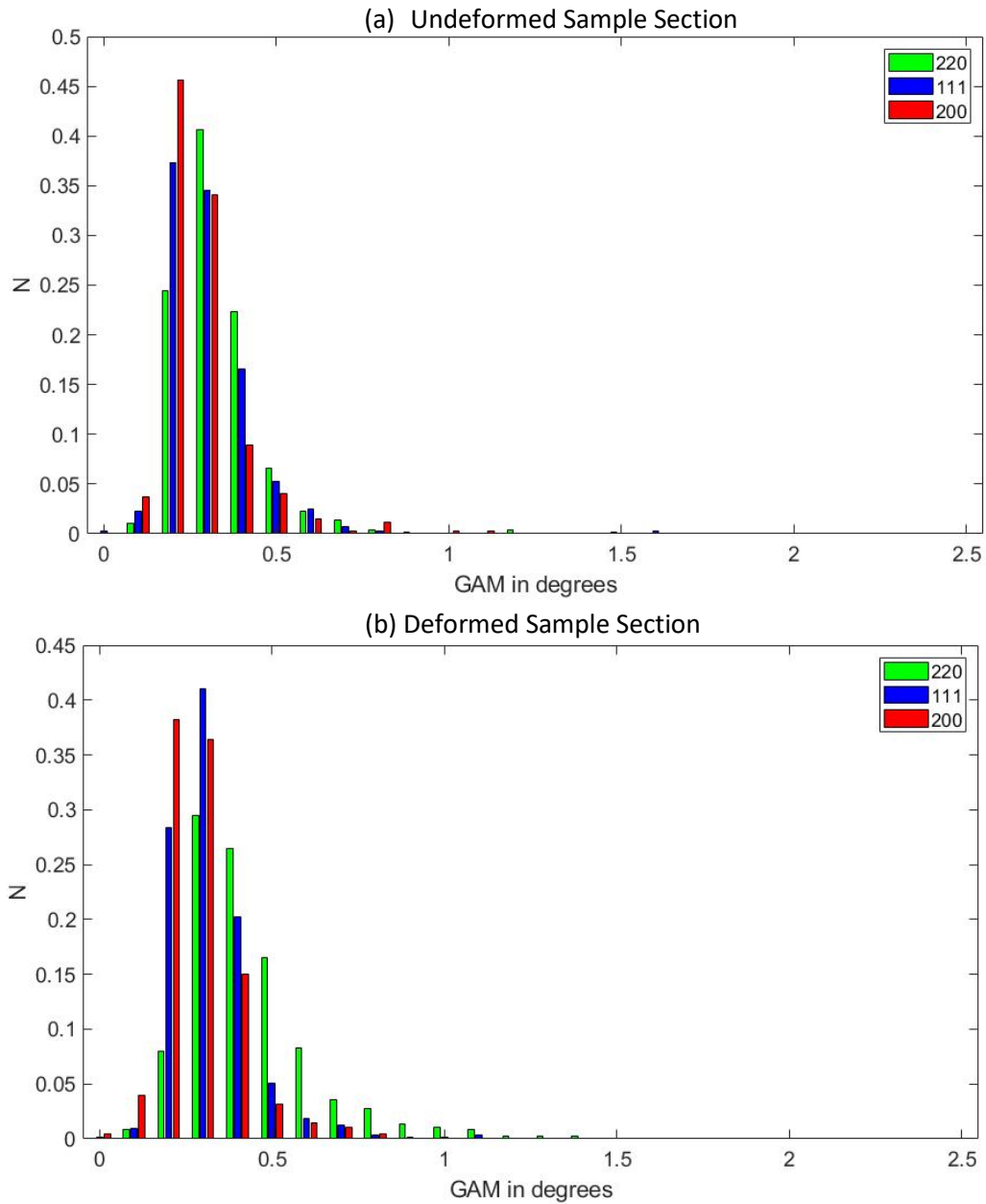


Figure 5.27: GAM histogram for nickel (a) undeformed region and (b) deformed region, where the subsets of grains are defined as being within 7.5 degrees of the 111, 220 and 200 orientations.

5.3.4.5. Kernel Average Misorientation

The kernel average misorientation (KAM) was calculated for each of the sample's EBSD data, this was then segmented into the grain subsets within 7.5 degrees of the 111, 220 and 200 orientations. Figure 5.28 (a) shows the KAM data presented as a histogram of the undeformed region of SS316 and Figure 5.28 (b) shows the deformed region of the SS316 sample. Compared to the GOS histogram in Figure 5.22 and the GAM plot in Figure 5.25 there is far less noise seen in Figure 5.28.

This makes it clearer to observe the differences between the subsets of grains. In Figure 5.28 (b) there is a clear increase in the maximum values of KAM for the 220 orientation subset of grains, with the highest being at 5 degrees but for the undeformed section, there is only a maximum of just above 2.5 degrees. The peak at 5 degrees is likely due to the maximum value of KAM being limited to 5 degrees and therefore anything above this value is grouped together. There is also a much higher number of 220-orientated grains above 1 degree. This same pattern is also seen in the 111 and 200 subsets of grains but to a lesser extent. The difference between the deformed region and undeformed region can be seen more clearly the Figure 5.28 (c), the 220 subset shows the largest change from the undeformed region to the deformed region with the peak shifting to more positive values. The 111 and 200 peaks show a slight increase from the undeformed subset but the change is much less than the 220 orientation subset.

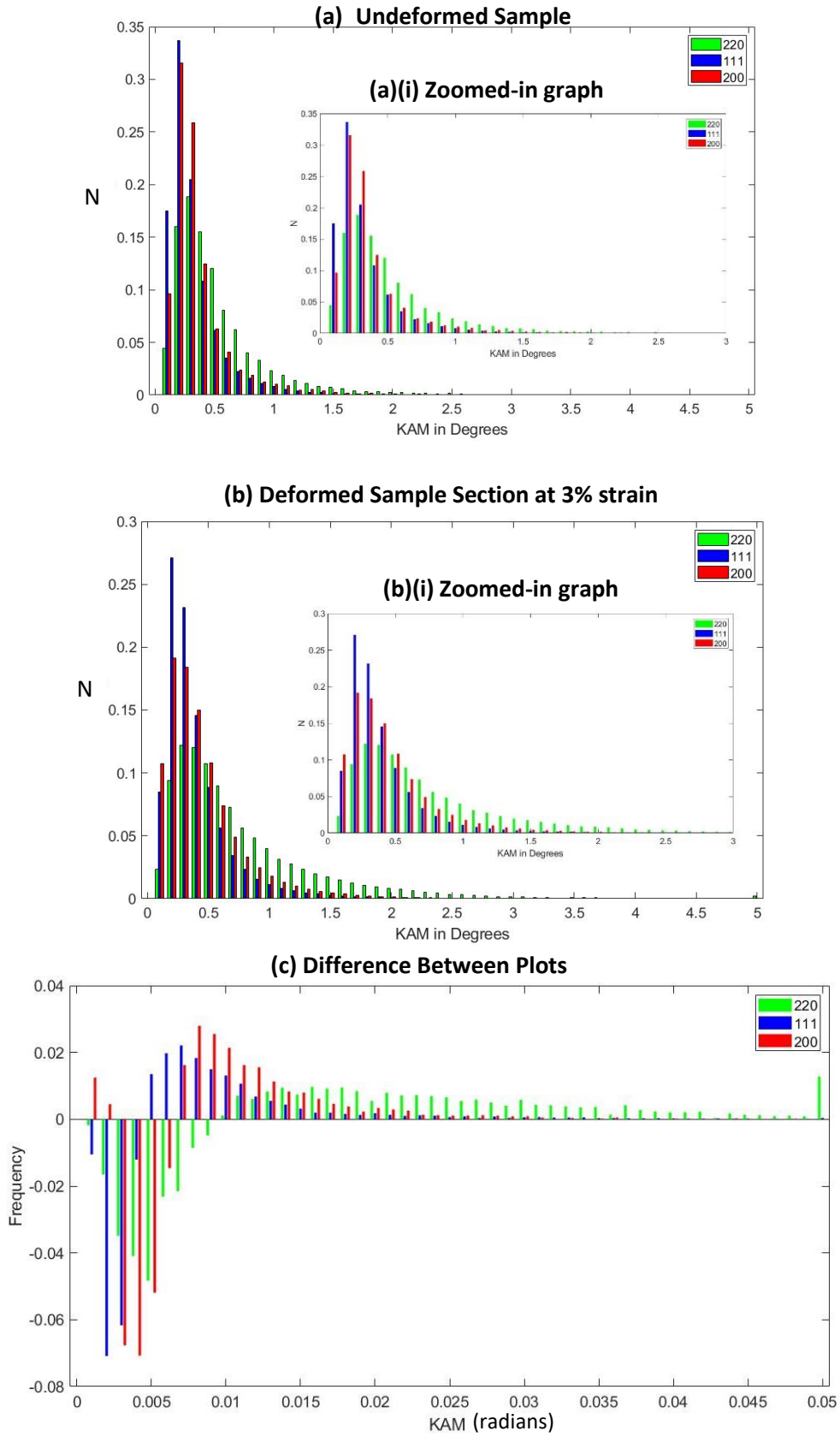


Figure 5.28: KAM histogram plot for SS316 where (a) undeformed region with the x-axis from 0 to 5 degrees and (a)(i) has an axis from 0 to 3 degrees, (b) deformed region with the x-axis from 0 to 5 degrees and (b)(i) has an axis from 0 to 3 degrees and (c) shows the difference between the two KAM values in radians, where the subsets of grains are defined as being within 7.5 degrees of the 111, 220 and 200 orientations.

The KAM histogram for undeformed and deformed INVAR is shown in Figure 5.29 (a) and (b) respectively. The undeformed section in Figure 5.29 (a) is similar to that seen in the GAM values in Figure 5.26 where the majority of values are at 0 and 0.2 degrees, this means there is little average misorientation in the undeformed region. Additionally, in Figure 5.29 (b), there is a maximum value of KAM at around 1 degree whereas the undeformed region in Figure 5.29 (a) shows there to be a maximum at around 0.5 degrees. In the deformed region, there is also a greater spread of KAM values which is not seen in the undeformed region, this can be seen more clearly seen in Figure 5.29 (c) where the difference in plots is shown. The 220 subset shows the highest increase in values of KAM to be seen of the three subsets. Compared to the SS315 values in Figure 5.28, the change in KAM values for the given subsets is far less.

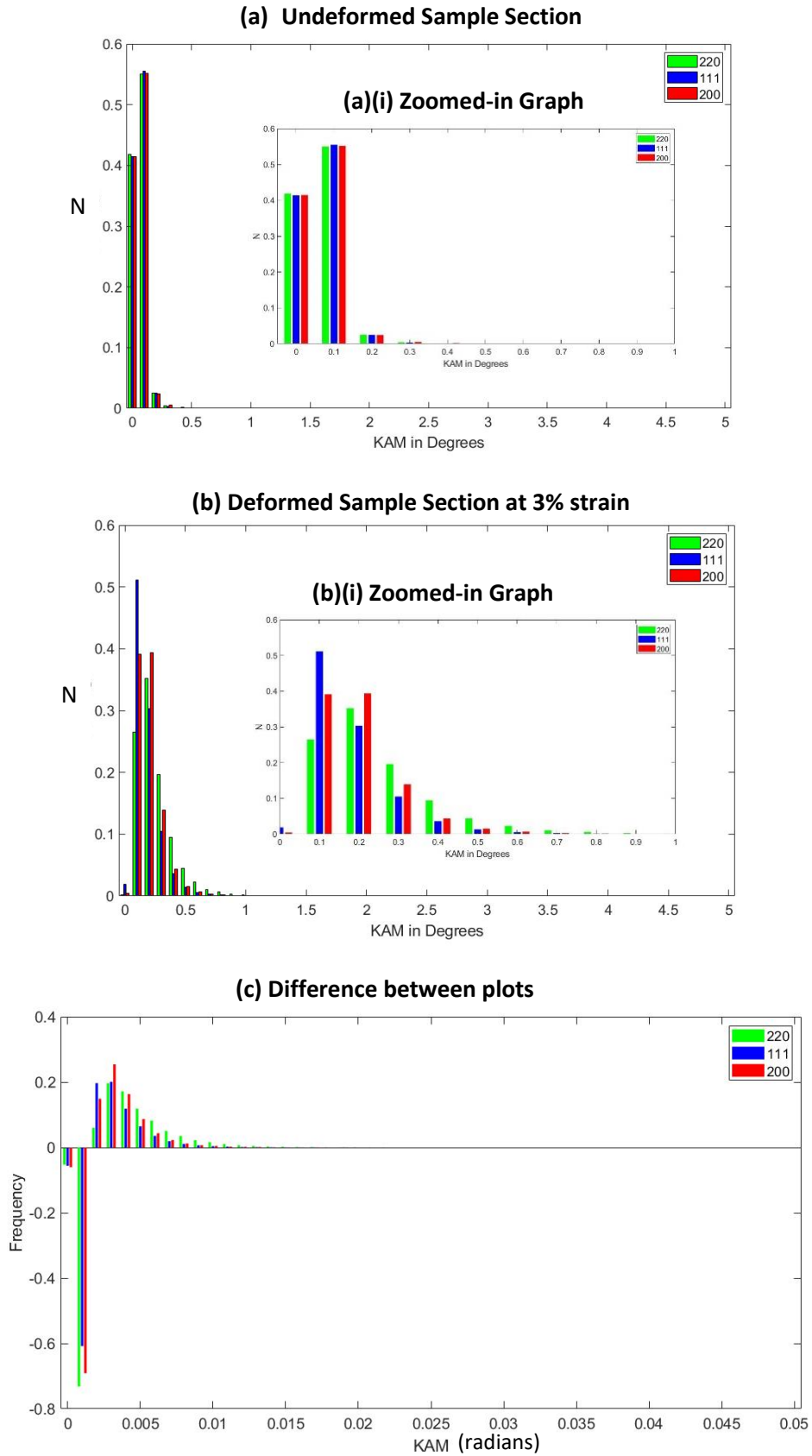


Figure 5.29: KAM histogram plot for INVAR where (a) undeformed region with the x-axis from 0 to 5 degrees and (a)(i) has an axis from 0 to 1 degrees, (b) deformed region with the x-axis from 0 to 5 degrees and (b)(i) has an axis from 0 to 3 degrees and (c) shows the difference between the two KAM values, where the subsets of grains are defined as being within 7.5 degrees of the 111, 220 and 200 orientations.

Figure 5.30 (a) shows the histogram plots for the KAM data for the grain subsets 111, 220 and 200 for the undeformed region of pure nickel and Figure 5.30 (b) shows the subsets for the deformed region. There is not a large difference between the undeformed and deformed regions which is also seen in the GOS and GAM histograms for a pure nickel. There is a slight increase in the 220 subset values as they extend to 1.5 degrees as opposed to the undeformed region which only extends to just beyond 1 degree. The change between the KAM values can be seen more clearly in the difference plot in Figure 5.30 (c), where the KAM values for the 220 orientation subset show the largest increase but are closely followed by the 111 and 200 subsets.

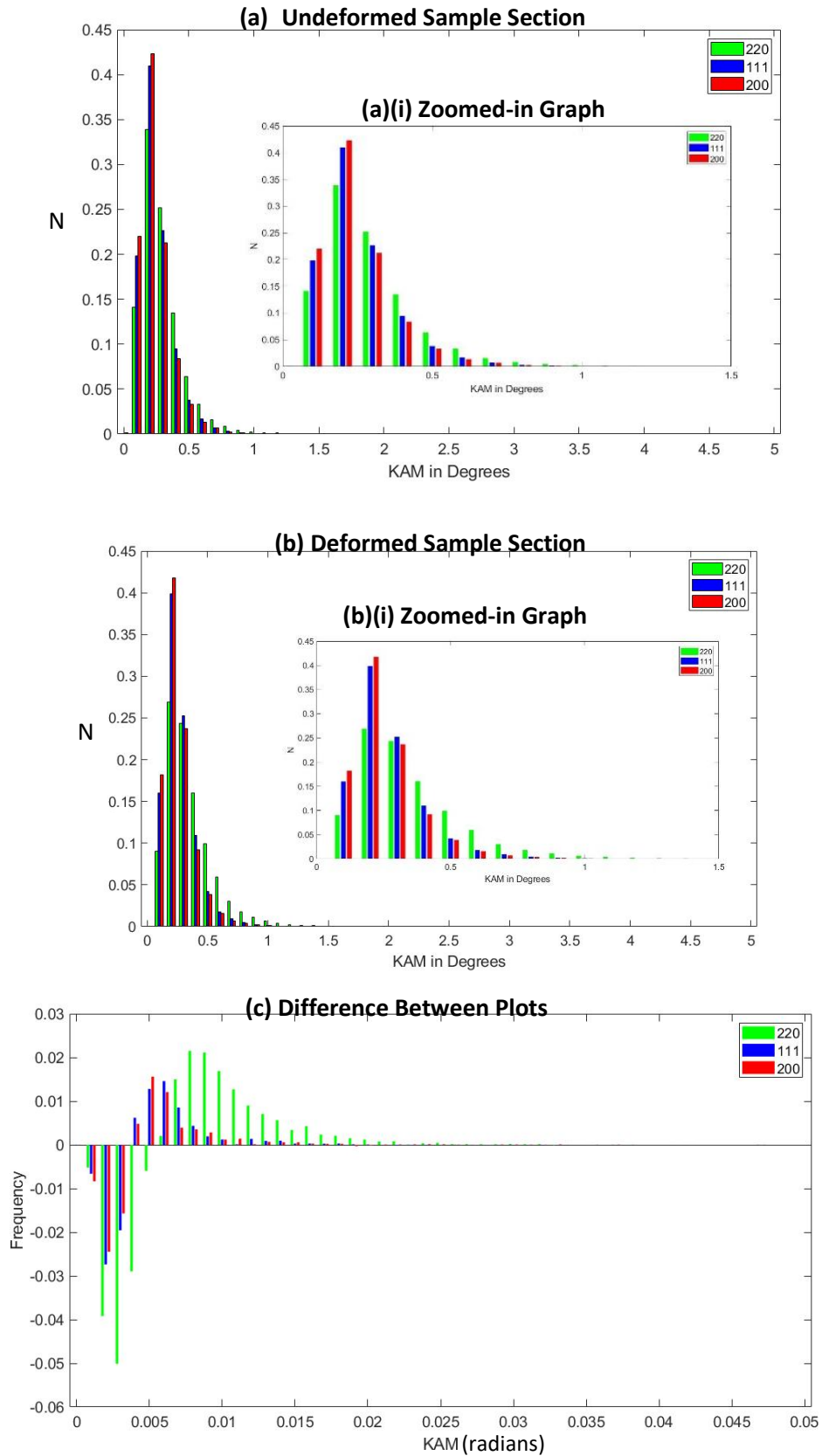


Figure 5.30: KAM histogram plot for pure nickel where (a) undeformed region with the x-axis from 0 to 5 degrees and (a)(i) has an axis from 0 to 1.5 degrees, (b) deformed region with the x-axis from 0 to 5 degrees and (b)(i) has an axis from 0 to 1.5 degrees and (c) shows the difference between the two KAM values, where the subsets of grains are defined as being within 7.5 degrees of the 111, 220 and 200 orientations.

5.3.5. Segmented KAM Spatial Maps

This chapter has presented the results for three EBSD metrics GOS, GAM and KAM devised from the EBSD maps collected from post-mortem analysis of the in situ neutron diffraction specimens. Due to the large amount of noise found in the GOS and GAM metrics for SS316 (in Figure 5.22 and Figure 5.25 respectively) only the segmented KAM maps will be presented in this section. The segmented KAM maps for SS316 are shown in Figure 5.31, the length scale used here is between 0 and 3 degrees. This figure shows that the KAM values for all subsets increase after deformation, with regions within grains showing higher values. However, the highest concentration of high KAM values can be seen in the deformed 220 orientation subset in Figure 5.31 (b). The segmented KAM maps are shown for INVAR in Figure 5.32, as discussed in section 5.3.2 the range of the KAM values for INVAR are significantly lower than SS316, therefore, to highlight the differences between the deformed and undeformed regions in the segmented maps a range between 0 and 0.6 degrees is used. All subsets in the undeformed state show near-zero values for KAM. The deformed regions all show an increase, with the largest increase being in the 220 crystallographic orientation. The segmented KAM maps for pure nickel can be found in Figure 5.33, similarly to INVAR, the KAM values are significantly lower than SS316 therefore a range of KAM is shown between 0 and 1 degrees.

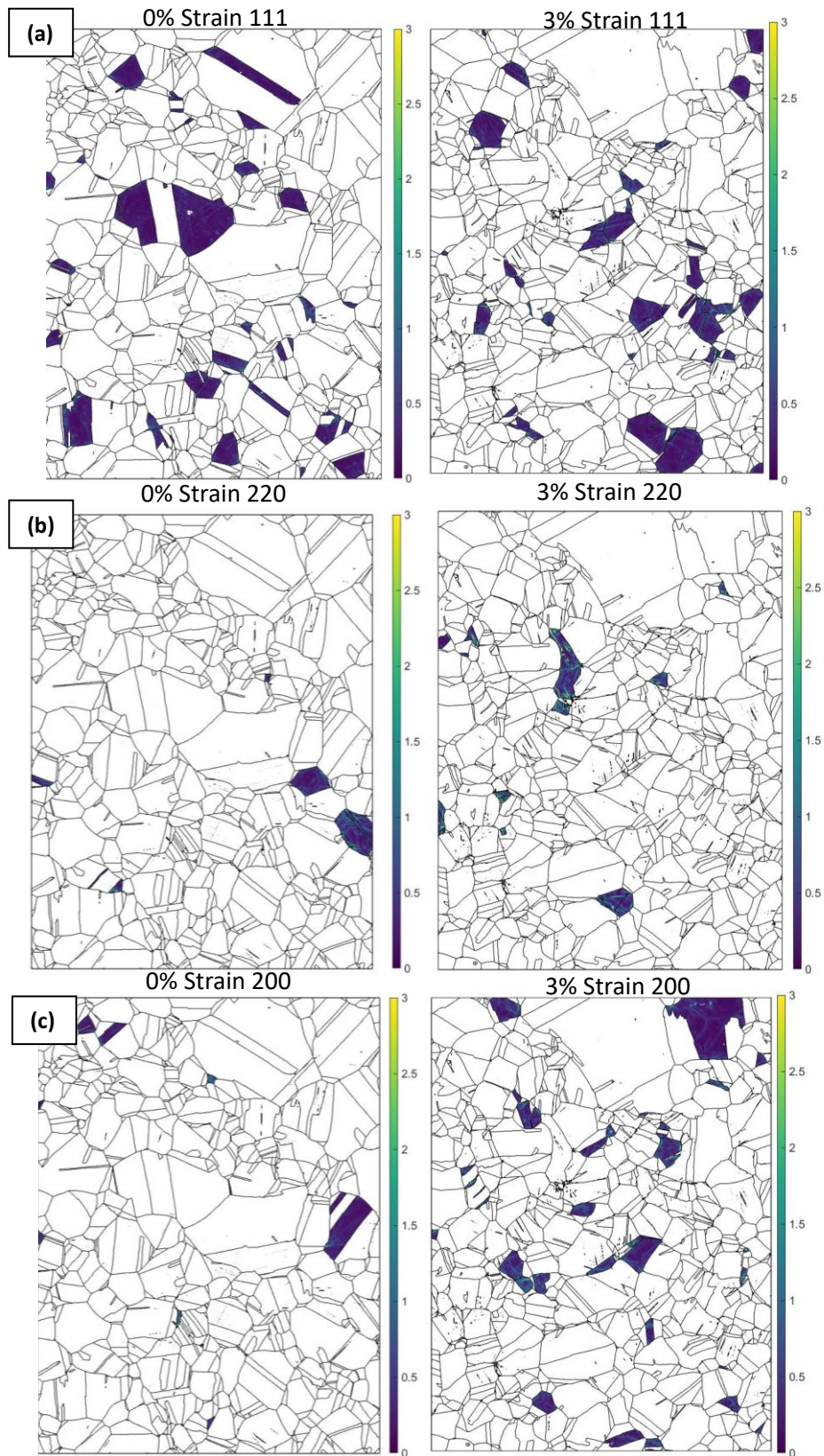


Figure 5.31: KAM spatial maps for SS316, which are segmented into the three orientation subsets (a) 111, (b) 220 and (c) 200 for both the undeformed and deformed regions, where the scale is KAM in degrees.

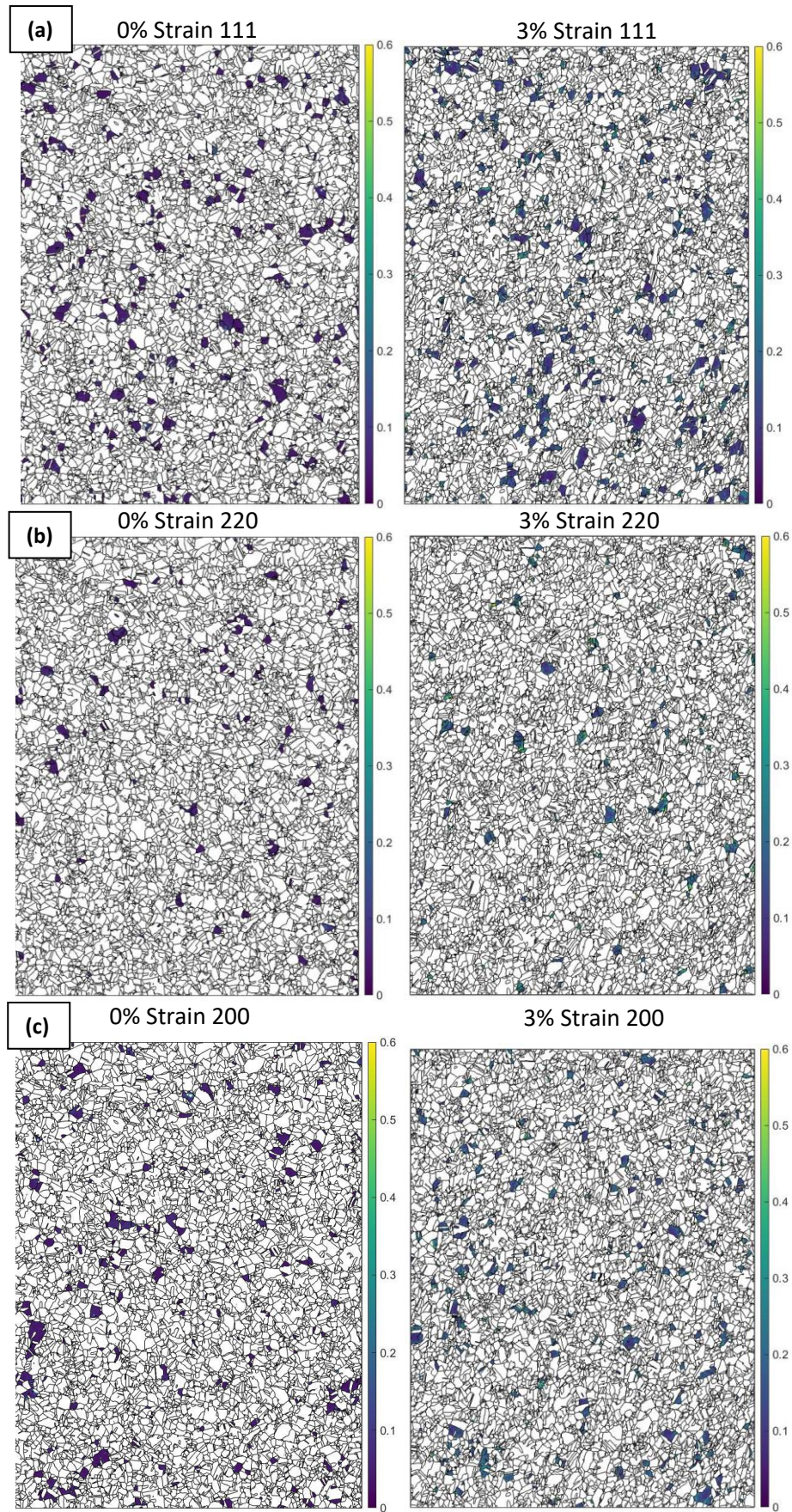


Figure 5.32: KAM spatial maps for INVAR, which are segmented into the three orientation subsets (a) 111, (b) 220 and (c) 200 for both the undeformed and deformed regions.

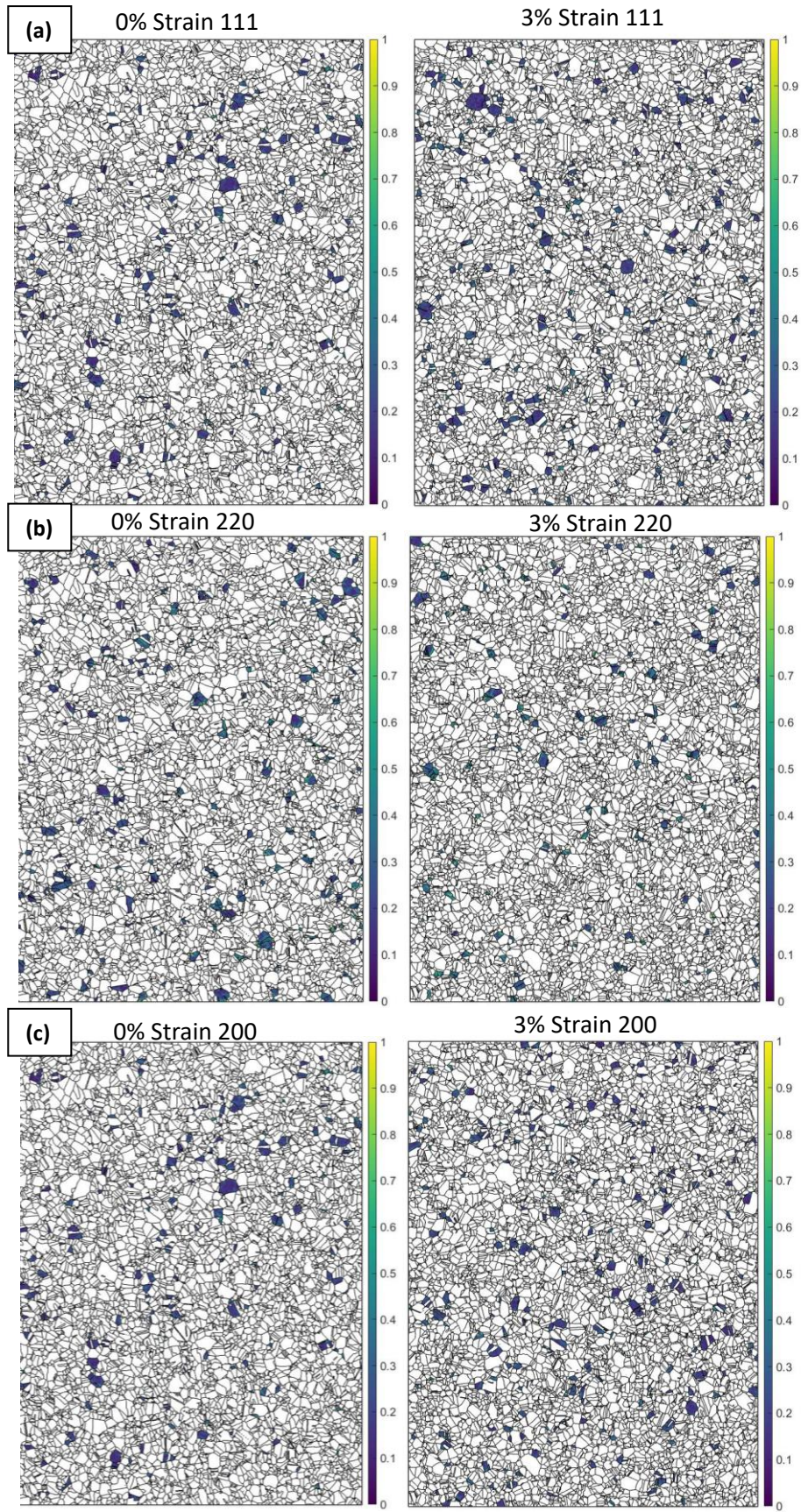


Figure 5.33: KAM spatial maps for pure nickel, which are segmented into the three orientation subsets (a) 111, (b) 220 and (c) 200 for both the undeformed and deformed regions.

5.4. Discussion

To investigate the influence of SFE on deformation behaviour in polycrystalline materials, *in situ* neutron diffraction tensile tests were performed on three samples: SS316, INVAR and pure nickel (results for these tests are presented in Chapter 4). These tests were used to investigate the influence of SFE on deformation behaviour for subsets of grains with similar crystallographic orientations. EBSD analysis was performed on the tensile test specimens. A cross-section was cut using EDM from the shoulder of the specimens and from the centre of the gauge length to show the accumulation of plasticity before and after deformation. This section will discuss the results of the EBSD analysis and EBSD metric analysis of the *in situ* neutron diffraction tensile test specimens which are presented in the current chapter (Chapter 5).

From the methodology section 5.3.3, it was discussed how the EBSD data was to be segmented into the subsets of grains which correlate to the ones recorded using the neutron diffraction data. To achieve this a MATLAB code was written with the same orientation variation allowance used in ENGIN-X (7.5 degrees). The results of the segmented EBSD data can be found in Figure 5.10, Figure 5.11, Figure 5.12, Figure 5.13, Figure 5.14 and Figure 5.15. It should be noted that the number of grains shown in Table 5.1 is significantly larger than is observed in the segmented EBSD plots, this is due to some of the grains recorded by the MATLAB data only being 1 μm in size and hence would not be visible in the plots. The same size map was chosen for each sample, however, as INVAR and nickel samples had far smaller grain sizes than the SS316, there were far more data points for both INVAR and pure nickel compared to SS316. However, even with the fewer data points for SS316, each sample produced a pole figure which gave the expected pattern for an FCC alloy, indicating that the subsets selected through this method have the same orientations as that of the subsets from the neutron diffraction tests.

The Schmid factors were calculated from the EBSD maps in Figure 5.2 and are shown in Figure 5.3. When considering Schmid factor the subset with the highest Schmid factor should activate first. When looking at the Schmid factor histograms for all three materials, before and after deformation for SS316, INVAR and pure nickel are in Figure 5.16, Figure 5.17 and Figure 5.18 respectively. These plots include the total Schmid factors for all data points, in addition to the values corresponding to each subset. It is observed that the 220 and 200 orientations have the highest Schmid factors, and the 111 orientation subset has the lowest Schmid factors. This implies that the 220 and 200 subsets of grains will deform first, followed by the 111. However, the neutron diffraction lattice strain results (Figure 4.10, Figure 4.11 and Figure 4.12), showed that the 220 orientation subset showed the onset of plastic deformation first, followed by the 111 and then the 200, which is also the order of grain

deformation observed by Daymond and Bouchard (9). The discrepancy between the neutron diffraction data and the Schmid factor calculations is likely related to cube slip system activation as this is not calculated by the EBSD maps. Therefore, the Schmid factor cannot be used alone as an indicator of strain measurement and must be compared to other strain measurement techniques.

The Taylor factor of a grain indicates the likelihood that deformation will occur, the higher the Taylor factor the more likely it will deform. Taylor factors can be calculated from EBSD data, where each data point correlates to a Taylor factor value. The complete spatial Taylor factor maps calculated for the deformed and undeformed regions of each sample are found in Figure 5.4. The Taylor factor results are also presented as histograms in Figure 5.19, Figure 5.20 and Figure 5.21 for SS316, INVAR and pure nickel respectively. An example of the segmented Taylor factor map Figure 5.34 shows the 111, 220 and 200 orientation subsets for the SS316 sample, this specimen was selected for clarity due to the large grain size. The histogram plots (Figure 5.19, Figure 5.20 and Figure 5.21) present the Taylor factor values for all data points as well as the points which correlate with the 111, 220 and 200 grain orientation subsets. For all samples, the histogram plots show that the 200-orientation subset has a Taylor factor of ~ 2.2 , whereas the 111 and 220 subsets have a Taylor factor of ~ 3.8 . This verifies the neutron diffraction data which shows that the 111 and 220 orientation subsets have ceased to deform elastically, implying plastic deformation has begun, as the 200-orientation subset continues to deform elastically.

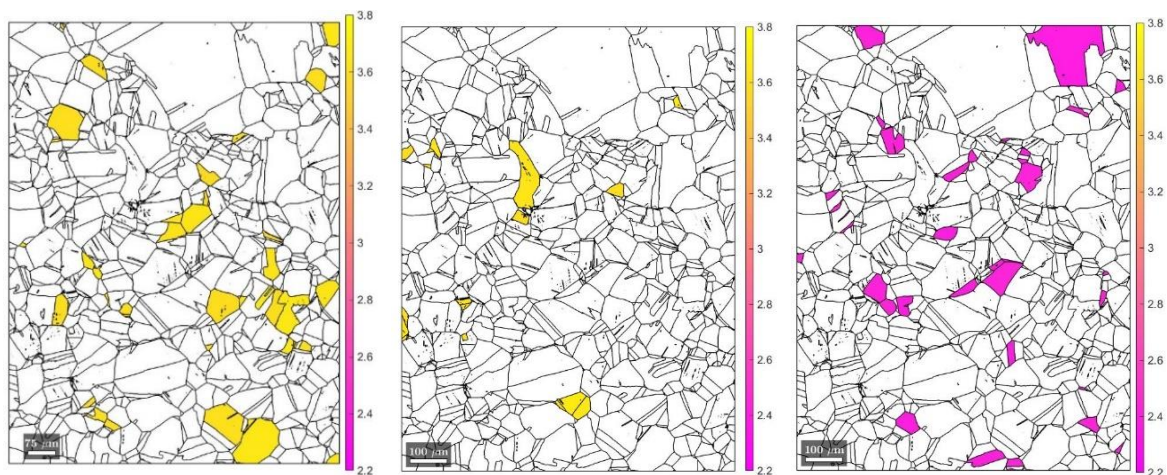


Figure 5.34: Segmented Taylor factor maps for deformed SS316 for the grain subsets (a) 111, (b) 220 and (c) 200.

The GOS values for the deformed and undeformed samples of SS316 are shown in Figure 5.5 (a). When analysing the histogram plots which represent these maps in Figure 5.22, it is noticeable that the spread shifts indicating there is an increase in the GOS once deformation has occurred. However, the spreads of both plots vary greatly for each subset, so it is hard to directly compare the two regions. This is likely caused by the size of the grains in the SS316 samples, as they are far larger than

the nickel and INVAR samples grains, the GOS is likely to vary far greater within each grain. The GOS maps for INVAR are found in Figure 5.5(b) and again in Figure 5.8 (a) with a reduced colour bar range to show the impact of deformation, with the complimentary histogram plots in Figure 5.23. In Figure 5.23(a), the deformed INVAR samples show the GOS values are consistently low for all subsets, low GOS values imply that the sample is well annealed before loading and the orientations within the grains. After deformation, there is an increase in GOS values for INVAR, shown in Figure 5.23(b). As discussed for both the INVAR and SS316, there was an increase in GOS following deformation, however, for pure nickel in Figure 5.24 there seems to be very little change or even a slight decrease in the calculated GOS values. This is also shown in the spatial plots of GOS for the pure nickel specimen at the larger scale (used for comparison to the other alloys) in Figure 5.5 (b) and the refined scale in Figure 5.9 (a). For Figure 5.24(a), the peak of the GOS values, is at 1 degree whereas in the deformed sample (Figure 5.24(b)) it is at 0.8 degrees, around these peaks the spreads remain similar between the two regions. This implies that for pure nickel the application of a load has a small impact on the GOS values.

The KAM spatial plots for SS316, INVAR and pure nickel are shown in Figure 5.7. Figure 5.7 (a) shows the spatial KAM values for the undeformed and the deformed SS316 regions, the deformed specimen shows higher KAM values throughout the region whereas in the undeformed there are fewer incidents of high KAM values throughout the region. This is also shown in the KAM histogram plots for SS316 in Figure 5.28, where the deformed region shows a clear shift to positive values of KAM. INVAR is presented in Figure 5.7 (b), which shows an increase in KAM values throughout, this is seen more clearly in Figure 5.8 (c), where the colour bar is refined. INVAR, in the pre-deformation state, produces values of KAM to be around 0 degrees (Figure 5.29 (a)), however, after deformation (Figure 5.29 (b)) the values show each subset to follow a similar spread pattern to that of SS316 (Figure 5.28). Nickel shows very little change in KAM from the undeformed to the deformed regions, this is shown at both length scales in the spatial maps in Figure 5.7 (c) and Figure 5.9 (c) as well as the histogram plots in Figure 5.30. This is likely due to nickel being a pure material and, therefore, containing a large amount of deformation before loading due to being soft. Additionally, due to its high SFE, the anisotropic deformation caused by the variation in grain orientation is not as evident as that seen in SS316 and INVAR (which both have low SFE). From looking at the histogram plots for the deformed regions of all materials (Figure 5.28 (b), Figure 5.29 (b), and Figure 5.30(b)), the highest value of KAM is seen in the 220-orientation subset of grains, implying this is the subset which contains the highest values of plasticity for all materials. This corroborates the neutron diffraction data presented in Figure 4.10, Figure 4.11 and Figure 4.12 for SS315, INVAR and pure nickel

respectively, as the neutron data showed a shift away from elastic deformation implying the onset of plastic deformation.

For the GAM values of SS316, looking solely at the spatial GAM plots in Figure 5.6 (a) there appears to be the same increase in values observed as seen in the KAM data. However, when looking at the histogram plots in Figure 5.25 (a) and (b) the results are far noisier than the KAM plots. This is likely due to the large grain size found in the SS316 sample which affects the averaging throughout the grain, as this is also observed in the histogram plots for GOS (Figure 5.22). The INVAR and nickel samples do not experience the same effect and show the same trends observed in the KAM data, showing that their smaller grain sizes are complementary to the GAM EBSD metric. For INVAR, the spatial GAM plots in Figure 5.6 (b) and Figure 5.8 (b), the undeformed section shows universally low values of GAM, even at the refined colour scale. This is also observed in the histogram plots in Figure 5.26, which are congruent with the KAM histogram plots in Figure 5.29. Additionally, the spatial GAM plot for nickel, at both the comparative (Figure 5.6 (c)) and refined (Figure 5.9 (b)) colour scales, show minimal differences between the deformed and undeformed regions. This is also reflected in the histogram plots in Figure 5.27. Similarly to the GOS plots, the nickel GAM plots also show a slight decrease in deformation between the two plots as the peak shifts negatively away from increases in GAM values. This shows that due to the nickel sample containing a large amount of misorientation before loading it is difficult to see the influence deformation has on the GOS and GAM values.

The impact that the larger grain size found in SS316 has on GOS and GAM histogram plots implies that the KAM EBSD metric is best for comparing these three materials and identifying the orientation subset which shows the largest amount of plasticity. Harshavardhana et al. (90) compared the EBSD metrics GOS, GAM and KAM for samples of pure copper and found GOS to be the best for differentiating deformed and undeformed grains. These samples had a grain size of $\sim 20 \mu\text{m}$ and hence did not have the issue of the varying grain sizes, therefore, if the three samples did have similar grain sizes the results may have been different. Additionally, Githinji (91) found a correlation between increasing grain size and increased KAM values. This relationship could have caused KAM values for the SS316 sample to be greater than if the grain sizes were of similar magnitude for all materials. However, due to the noise in the GOS and GAM histogram plot, it was decided that KAM was the only metric which could be used to investigate all three materials comparatively and hence the segmented EBSD data for the 111, 220 and 200 subsets are shown for SS316, INVAR and pure nickel in Figure 5.31, Figure 5.32 and Figure 5.33 respectively. The segmented data highlights some of the aspects shown in the histogram plots, for example, in Figure 5.31 (b) there is a clear concentration of KAM in the deformed SS316 grain which is not seen in the grains in the

undeformed region. This same change can also be seen in Figure 5.32 (b), however, the small grain sizes found in INVAR make this difficult to see. Hence, why histograms were used, as they provided greater detail on the regions.

By looking at the difference in GAM (Figure 5.26) and KAM (Figure 5.29) between the undeformed and deformed regions of the INVAR sample, it can be assumed that the sample preparation process had little effect on the misorientations recorded. This is because the undeformed region shows near-zero values of misorientation confirming that the sample has been well-annealed. As the deformed region shows higher values of misorientation and the only difference between the sample preparation was the region the samples were taken from the specimen it is fair to say this change can only be related to the loading process. This, therefore, verifies the other EBSD metric results as both the pure nickel and SS316 were subjected to the same sample preparation procedures.

As the samples were taken from the material specimens following the neutron diffraction tests, the regions do not show the same area before and after testing. Neutron diffraction requires a solid cylindrical specimen and, therefore, taking an EBSD map from the same region would be impossible. However, despite this, the results shown from the KAM EBSD metrics do reflect that of the neutron diffraction lattice strain data for the subsets of grains with 7.5 degrees of the 111, 220 and 200 orientations. Although, using EBSD metrics alone to quantify deformation can be difficult. For example, due to the soft nature of pure materials, the nickel sample shows large concentrations of misorientation prior to the tensile testing, therefore there is a less noticeable change in misorientation concentrations between the deformed and undeformed regions.

5.5. Summary

This chapter has discussed the methodology and results of the EBSD analysis on the spent SS316, INVAR and pure nickel tensile test specimens used in the *in situ* neutron diffraction tests. The EBSD analysis was performed on regions of the tensile samples which were pre-deformation and post-deformation. This data was used to calculate values of Taylor and Schmid factors of the materials, in addition to the EBSD metrics: GOS, GAM and KAM. The Taylor Factor results for the 111, 220 and 200 orientation subsets reflect the behaviours observed in neutron diffraction analysis in Chapter 4. Whereas the Schmid factor indicates the 111 and 200 will deform first, which is not the case in the experimental results as the 220 shows plastic deformation. For the EBSD metrics it was found that due to the large grain found in the SS316 specimen, the histogram plots for GOS and GAM showed a large amount of noise, therefore it was found KAM was the most suitable EBSD metric to compare

the three materials. The KAM EBSD metric showed a correlation between the results of the neutron diffraction experiments, showing that between the deformed and undeformed samples there was the greatest increase in KAM values for the grains within 7.5 degrees of the 220-orientation.

6. Using HR-DIC as a method to measure strain

6.1. Overview

So far, the effect of SFE on the deformation mechanics of SS316, INVAR and pure nickel has been investigated using *in situ* neutron diffraction and post-mortem EBSD analysis. The neutron diffraction tests showed the average elastic strain for grain subsets within 7.5 degrees of the 111, 220 and 200 orientations. This method was able to show the onset of plastic deformation in the 220-orientation subset and an increase in elasticity in the 200-orientation subset, however, with this technique the spatial response to strain was lost. The post-mortem EBSD analysis showed the highest amount of misorientation in the 220-orientation subset, indicating this subset had the highest amount of plastic deformation, which verified the neutron data. With this technique, spatial strain data was not lost, but as EBSD metrics only measure misorientation it was not able to directly measure the plastic deformation. In this chapter, the effect of SFE on deformation mechanics will be measured using *in situ* HR-DIC tensile tests. This technique maintains the spatial resolution of the strain data and measures both elastic and plastic deformation but is unable to distinguish between the two (142). To segment the HR-DIC strain data into the same orientation subsets as the neutron diffraction data, which allowed comparisons to be drawn between the strain measurement techniques, the precise locations and orientations of the surface grains need to be known. Therefore, EBSD mapping was selected as the method best for achieving this. By combining large EBSD maps and segmenting the strain data by the grain orientation subsets, the aggregate strain data results collected through HR-DIC could be compared to the neutron diffraction and EBSD metric analysis that was performed to investigate the effect of SFE in the previous chapters.

6.2. Methodology

This section will discuss the methodology used in segmenting the HR-DIC data into subsets within 7.5 degrees of the 111, 220 and 200. As the EBSD and HR-DIC techniques required different sample was prepared in a certain order. This order can be found in the flow chart in Figure 6.1. Additionally, it was important to align the regions in the analysis step, therefore fiducial markers were required. This method will be discussed in detail in the following sections.

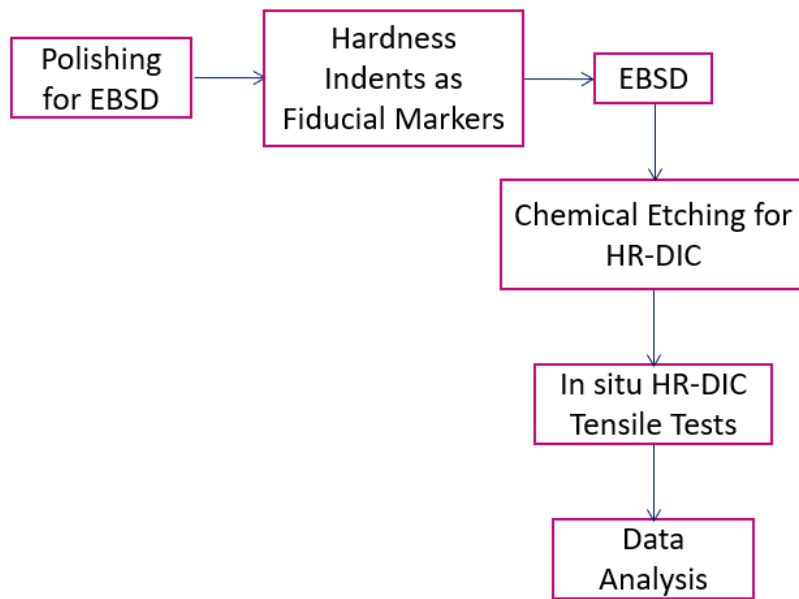


Figure 6.1: Flow chart showing the preparation steps for aligning the HR-DIC data to EBSD maps.

6.2.1. Sample Preparation

This section will discuss the methods used to prepare the samples for HR-DIC analysis. The techniques and finish required for both EBSD and HR-DIC analysis are vastly different. As was discussed in section 4.3, a mirror finish is required to produce a high-quality EBSD, however, to prepare the surface for HR-DIC a stochastic pattern is required, to achieve this the sample was etched after the EBSD map had been produced. Hardness indents were used as fiducial markers to align the EBSD map with the HR-DIC strain data.

6.2.2. EBSD Preparation

To prepare the tensile specimens for EBSD, the same preparation method steps described in section 4.3 were used. The grinding, polishing and electropolishing procedures used for these specimens were the same as was used for the post-mortem EBSD analysis on the neutron diffraction specimens, the details of these procedures can be found in Table 4.3,

Table 4.4, Table 4.5 respectively.

6.2.3. Hardness Indents

Before the EBSD mapping of the surface, hardness indents were applied to the surface. This was used as a method to cross-correlate the EBSD map to the HR-DIC data during the analysis steps. The indents were created in an 'L' shaped pattern, using a Struers Duramin-A300 machine with a spacing of 1 mm. Figure 6.2 shows an SEM image of the arrangement of the hardness indents on an etched sample of IN718 with large grains ~ 1 mm in length. This specimen and material were used as a test only to check the hardness indents that could be easily found using the SEM.

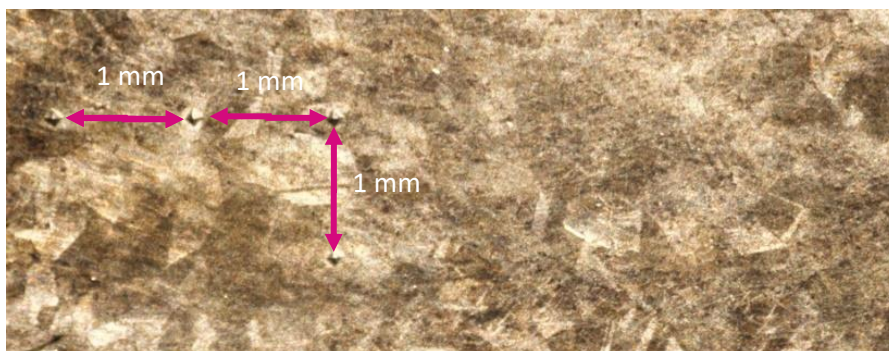


Figure 6.2: SEM image showing the hardness indents on an etched large-grain IN718 sample used as a test specimen to ensure the fiducial marker could be found.

6.2.4. EBSD Mapping and Analysis

The coordinates of all hardness indents were recorded once the sample was inside the SEM and in focus. An EBSD map was taken for each sample, to provide insight into the size and orientation of the grains. This EBSD was taken 1 mm from a hardness indent (the indent which was selected depended on the location of the 'L' to keep the map within the centre of the sample). Examples of the location of the EBSD maps with relation to the hardness indents can be found in Figure 6.3. The EBSD maps for all alloys have a size of 2 mm by 2 mm with a step size of $1\text{ }\mu\text{m}$. These samples were analysed on a Zeiss Crossbeam 550 equipped with Oxford Instrument Symmetry S2 detector.

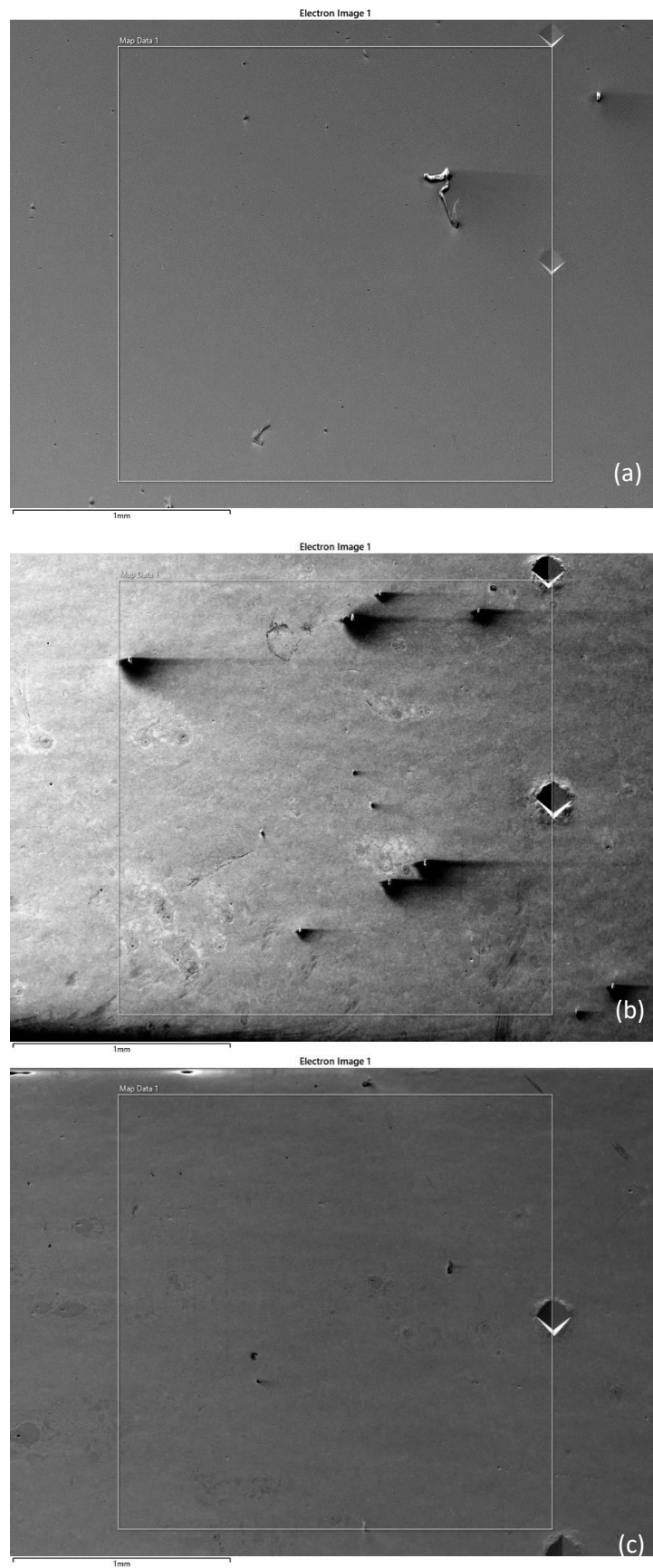


Figure 6.3: SEM images showing the ROI of the EBSD maps to the hardness indents for (a) SS316, (b) INVAR and (c) pure nickel.

6.2.5. Etching

After EBSD maps were produced for the region of interest (ROI), the samples' surfaces were prepared for HR-DIC *in situ* tensile testing. This meant a speckle pattern was required so that tracking throughout deformation could be achieved by the DIC software (this process is discussed in detail in section 6.2.9). In this project, the samples were prepared using a chemical etchant, which selectively removes material from the specimen's surface. However, whereas etching typically is used to expose the features within the crystallographic structure, for example, grain boundaries, in this instance the etchant is used to uniformly destroy the surface. This then produces a textured surface which can be tracked.

The chemical etchant used in this project was a mixture of 5 ml nitric acid, 5 ml deionised water and 15 ml hydrochloric acid. This etchant must be made up fresh for every test specimen as deionised water starts to evaporate leaving the etchant composition compromised, causing the final finish to be uneven and making the procedure less repeatable. The samples were submerged in the chemical etchant in a measuring cylinder which was filled so the chemical etchant covered the entirety of the specimen. A sonic bath was used to keep the movement of the solution constant throughout the exposure time. The exposure time was estimated using test samples of each specimen but was found to vary greatly, therefore, observation was used to ensure the best finish was achieved for each specimen. A diagram of the experimental procedure can be found in Figure 6.4. It was found that the time taken for the specimens to be etched was dependent on the material. However, external factors, such as the temperature of the lab (for example etching took less time in warmer months than in the winter), therefore, to eliminate these effects it was important to check on the specimen's progress throughout the submergence in the etchant to ensure all shine had been removed from the sample before it was removed. Photos of the resultant surfaces of the SS316, INVAR and pure nickel samples are shown in Figure 6.5, Figure 6.6 and Figure 6.7 respectively.

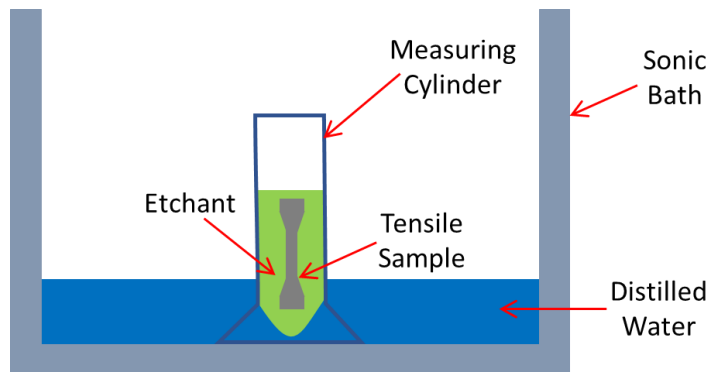


Figure 6.4 Schematic showing the procedure used to create a texture on the surface of the tensile specimens for HR-DIC analysis.



Figure 6.5: Photo of the etched surface for the SS316 sample.

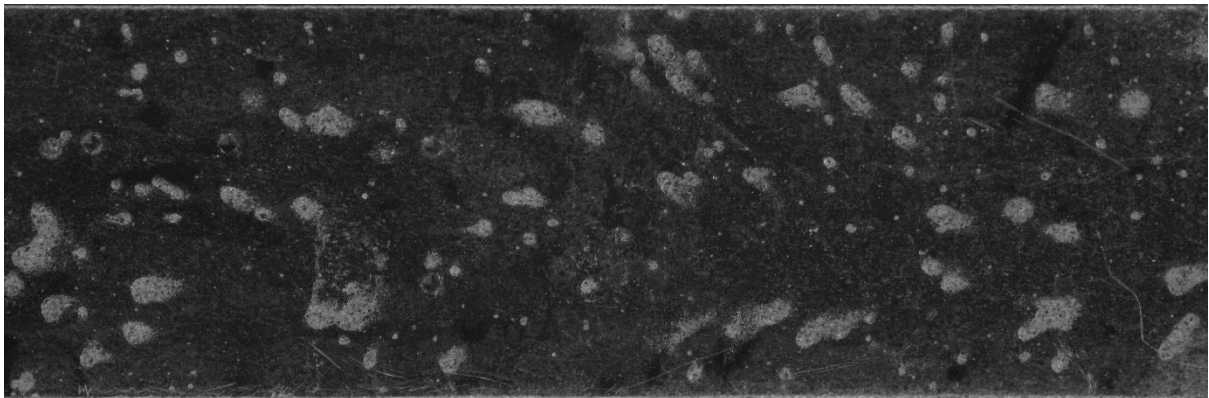


Figure 6.6: Photo of the etched surface for the INVAR sample.

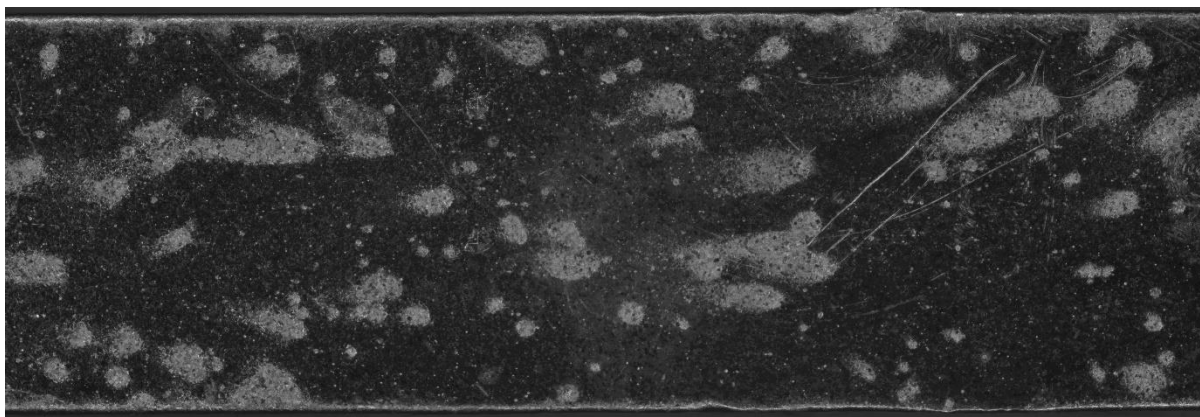


Figure 6.7: Photo of the etched surface for the pure nickel sample.

6.2.6. Mechanical Testing

HR-DIC tensile tests were performed using an opt-engineering TC16M009 4x magnification telecentric lens and a high-resolution optical Nikon D850 camera (a labelled picture can be found in Figure 6.8). The tensile tester used was an *in situ* 4.5 kN ADMET mini-tensile testing machine (Figure 6.9), this tester has been used in previous work within the department (14,15). The micro tensile tester can be used within an SEM, however, by using a telecentric lens images could be taken continuously throughout acquisition without pausing the test. The micro tensile tester was set to increase in displacement of 0.3 mm per minute, up to a total displacement of 5 mm. The total time of the tests for each test specimen is shown in Table 6.2. The camera took images every two seconds throughout the tensile test. The software used to control the micro tensile tester was ADMETs own software: MTESTQuattro.

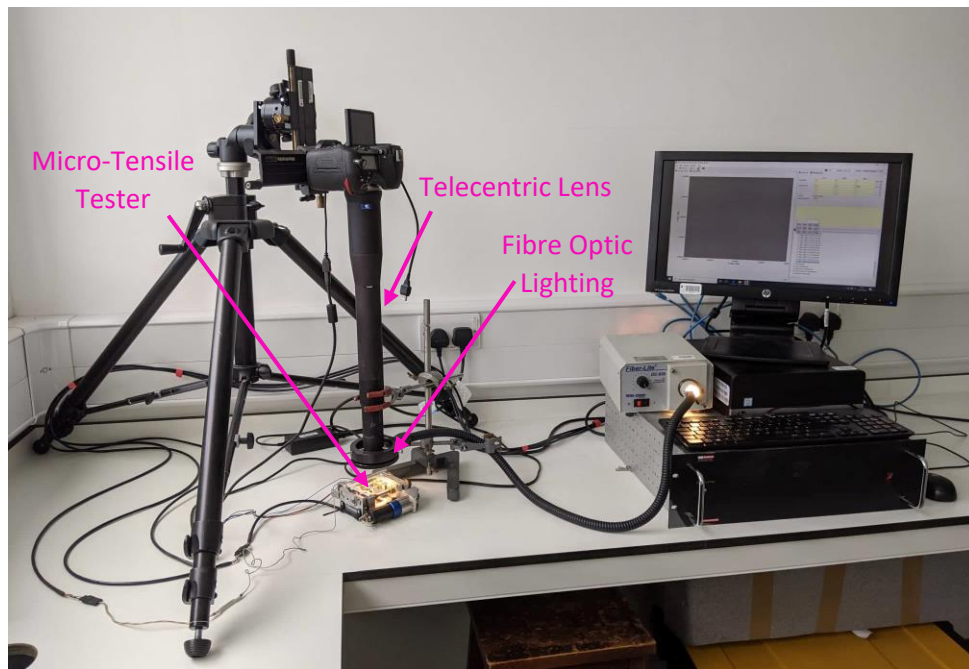


Figure 6.8: An image showing the set-up of the micro-tensile tester with the control computer, it also shows the set-up used for performing HR-DIC on a tensile sample.

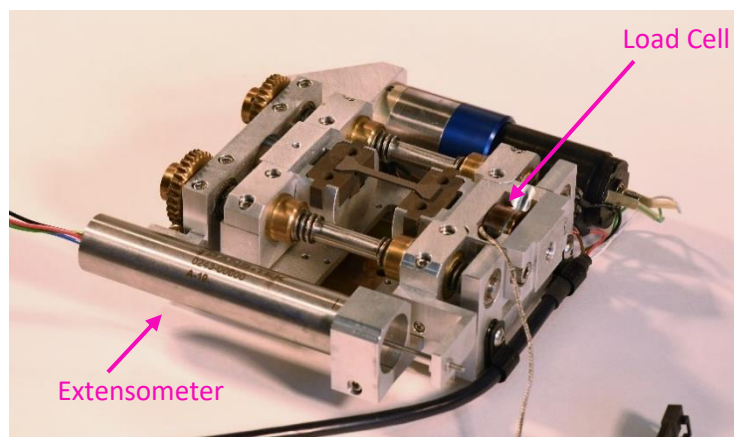


Figure 6.9: The 4.5 kN ADMET mini-tensile testing machine used for the HR-DIC tensile tests.

Table 6.1: Duration of in situ HR-DIC tensile tests.

Alloy	Test Duration (s)
SS316	1014
INVAR	1015
Pure Nickel	1006

6.2.7. Sample Geometry

Tensile test samples were cut using EDM to fit within the micro tensile tester used to perform the EBSD and HR-DIC tensile tests. Figure 6.10 shows approximate dimensions of the tensile specimens.

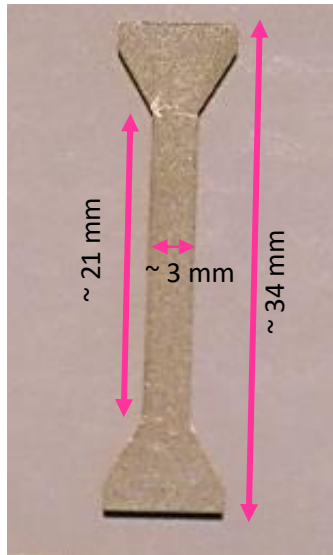


Figure 6.10: The approximate dimensions of the HR-DIC tensile test specimens.

6.2.7.1. Grip Redesign

As the SS316 alloy sample is too hard for the original serrated grip design and would therefore cause the grip to deform before the specimen, new grip designs were needed to be designed to accommodate this. Creating the same serrated grip design in a harder material would be difficult as the ridges are very small. Therefore, a jig-saw style grip design was created in which the sample will slot into and be 'sandwiched' between two blocks to keep the sample level. The new grip design required a material which had a hardness value greater than SS316, therefore, alloy X, a nickel-based superalloy was selected. A comparison between the original grip design and the new grip design can be found in Figure 6.11. Here it is shown that the outside shape of the grip was kept the same shape as the original grip so it would still fit within the tensile tester, but the sample shape and how it was held within the grip were changed. Even though the pure nickel and INVAR specimens were soft enough to use the original grip design, the new grip design was used for all specimens to ensure the tests could be compared.

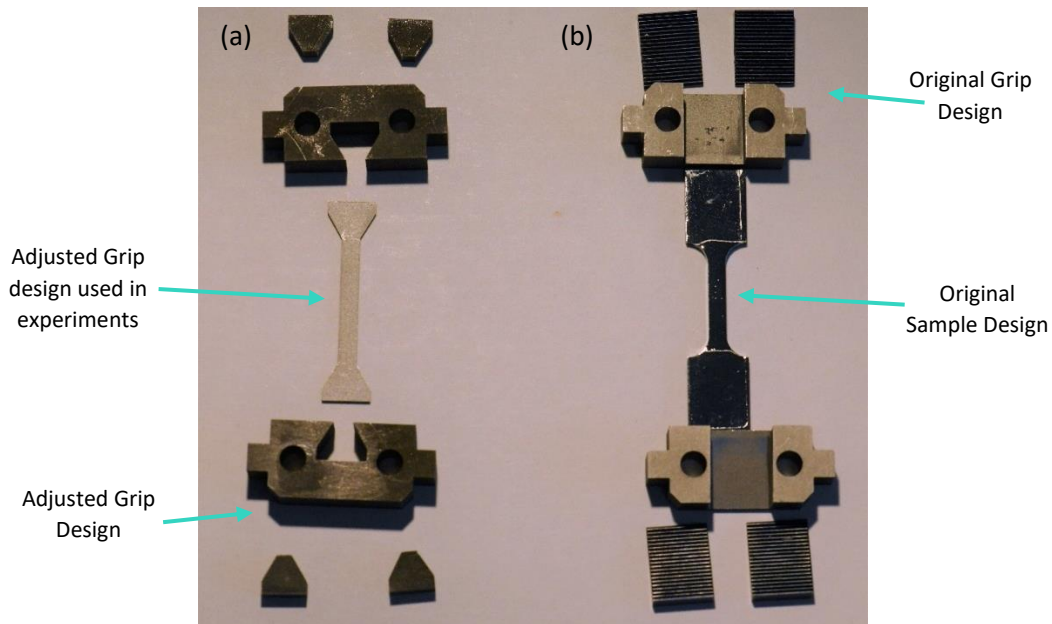


Figure 6.11: Grip re-design with annotations, here (a) new grip design EDM and (b) original grip design.

6.2.8. Telecentric Lens

A high-magnification bilateral telecentric lens is used in the experiments to acquire high-resolution images of the surface of the specimen during deformation. A telecentric lens was used over an ordinary optical lens because during the tensile test out of plane motion may occur, and HR-DIC will record this motion as a pseudo strain value, reducing the accuracy of the HR-DIC results. A telecentric lens can reduce the impact of out-of-plane motion of the test sample during loading as it consists of an arrangement of optics that, for a given range of working distances, produces little or no change in apparent magnification. Therefore, we can assume the strain values calculated by a DIC package are related to the tensile test as opposed to measuring any pseudo strain because of changes in apparent size caused by a change in working distance. The telecentric lens produced a pixel length of 1×10^{-3} .

6.2.9. Analysing DIC data

Using the commercial DIC package, DaVis 8.3 (LaVision) (143) the deformed and undeformed images of the sample's surfaces were compared. This software uses the least-squares approach to iteratively solve the sum of squared differences (SSD) correlation function (107). This technique records strain in both the loading direction (E_{xx}) and transverse to the loading direction (E_{yy}).

Once the strain data was collected it was segmented into crystallographic orientations using crystallographic data collected by EBSD on the same surface. Then using the DICE MATLAB code, which was developed by Forsey (144), the data could be divided into subsets based on their crystallographic orientations. While one of the significant differences between HR-DIC and neutron diffraction is that the strain information is available for individual grains, to compare the results of the HR-DIC to the neutron diffraction the results need to be in a similar form. Therefore, the orientation subsets for the 111, 220 and 200 families of grains were isolated as they are the subsets recorded in the diffraction peaks, and the results are presented in the following section.

6.3. Results

This section will document the results of the HR-DIC analysis of the tensile tests performed on SS316, INVAR and nickel. This includes the EBSD analysis of the ROI, followed by the strain data for the samples as well as the segmented strain data created by imposing the EBSD map onto the sample. The strain data was then segmented into subsets, which contained grains with crystallographic orientations within the 111, 220 or 200 orientations. These were then plotted using histogram plots to investigate the distribution of strains for each subset.

6.3.1. EBSD Analysis

As mentioned in the method section of this chapter EBSD analysis of ROI was required before *in situ* HR-DIC tensile to equate the strain data to the microstructure of the material. The EBSD maps for the samples with different SFEs, SS316, INVAR, and pure nickel, are presented in

Figure 6.12,

Figure 6.13, and

Figure 6.14 respectively. Here, all materials have a wide range of grain orientations, with the grains in INVAR and nickel being comparative in size, whereas the SS316 has grains significantly larger. The grain sizes for the specimens of SS316, INVAR and pure nickel are shown in Table 6.2, these values were measured using the standard line intersection method and ImageJ, discussed in detail in section 4.3.1.

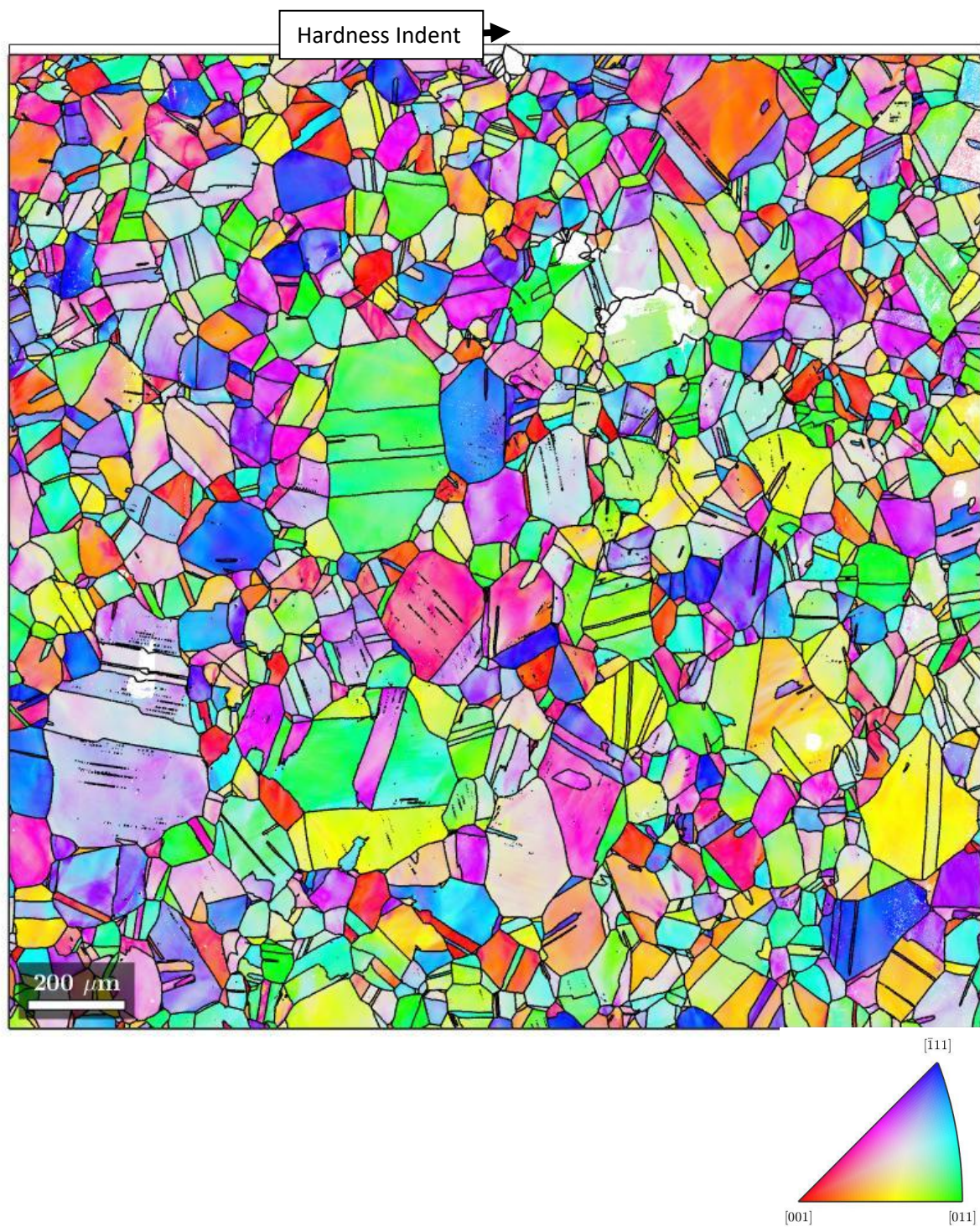


Figure 6.12: A 2 mm x 2 mm EBSD map for SS316 used in the segmentation of the HR-DIC data. The location of the hardness indent used as a fiducial marker is shown on the map.

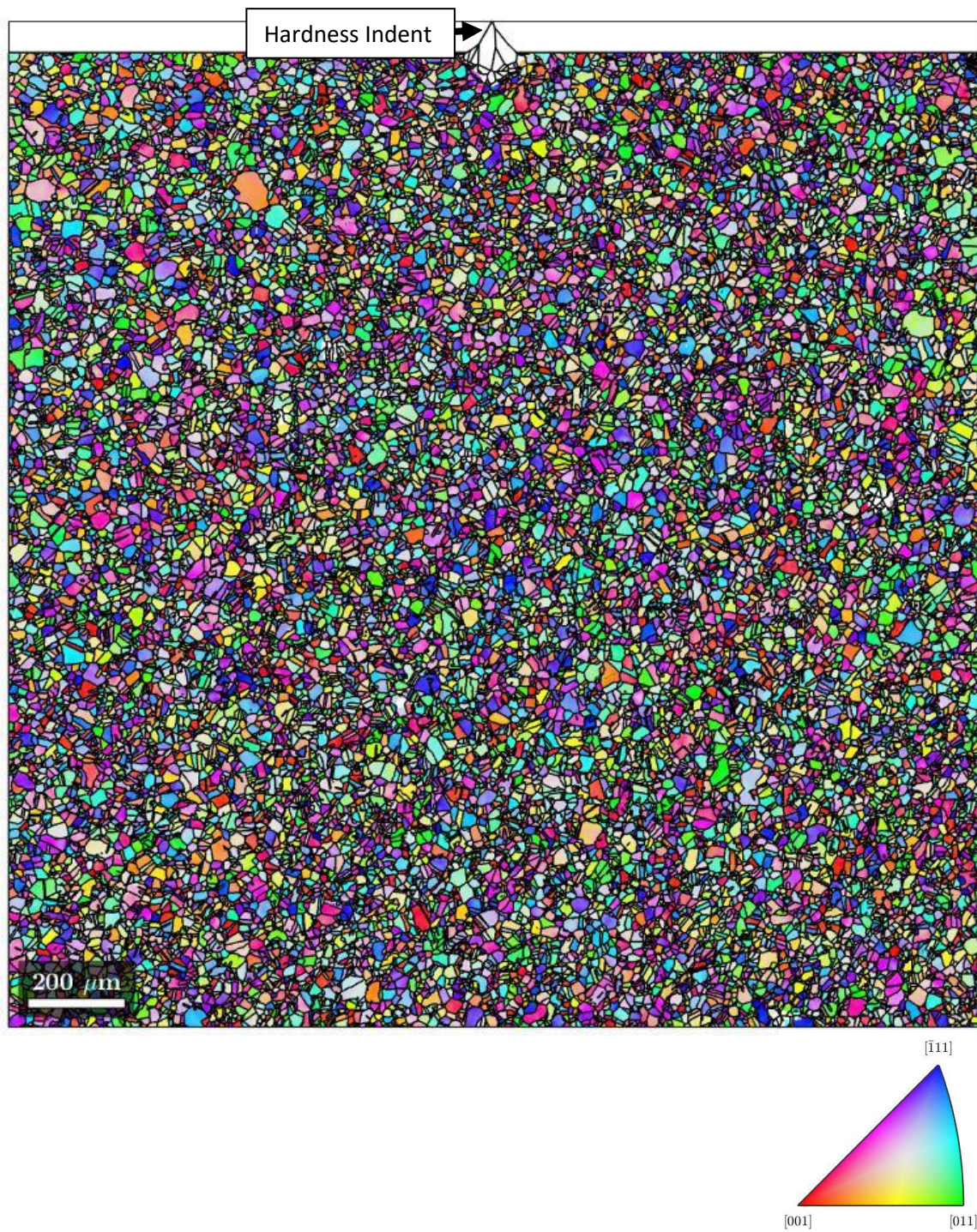


Figure 6.13: A 2 mm x 2 mm EBSD map for INVAR used in the segmentation of the HR-DIC data. The location of the hardness indent used as a fiducial marker is shown on the map.

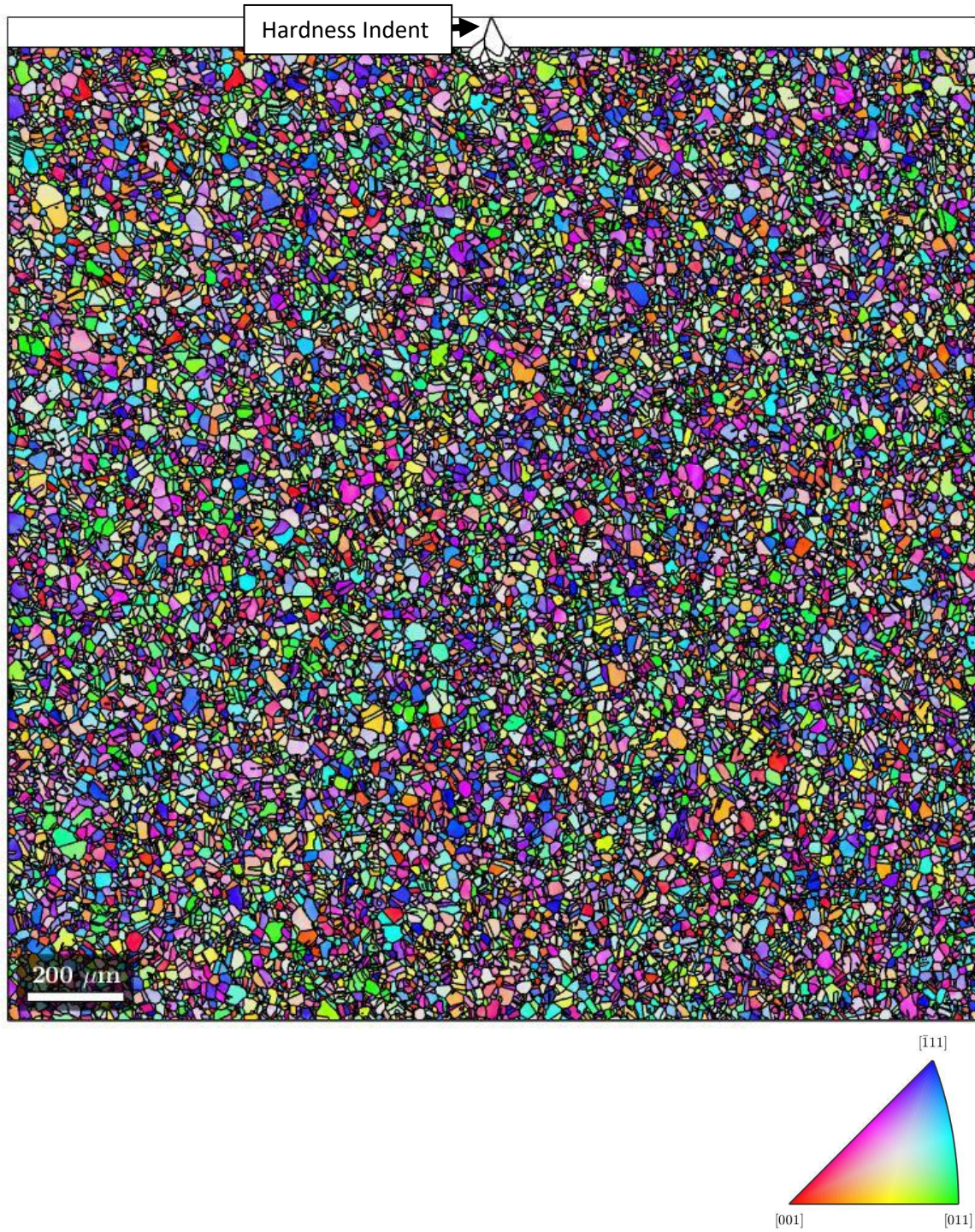


Figure 6.14: A 2 mm x 2 mm EBSD map for pure nickel used in the segmentation of the HR-DIC data. The location of the hardness indent used as a fiducial marker is shown on the map.

Table 6.2: Grain sizes for the materials used in the HR-DIC analysis.

Material	Average Grain Length (μm)
SS316	69.5
INVAR	16.57
Pure Nickel	15.24

6.3.2. HR-DIC

This section will present the results of the DIC analysis on the samples of SS316, INVAR and pure nickel. To draw comparisons with the neutron diffraction and EBSD metric results the results for DIC have been found at 3% global strain as this is the strain the neutron diffraction tests went to. To locate the image number which correlated to 3% global strain, the strain image number plots were used. The image number selected for each material can be found in Table 6.3.

Table 6.3: The image number where each sample reached 3% global strain.

Material	Image Number
SS316	184
INVAR	148
Pure Nickel	138

Figure 6.15 shows the area pictured for the SS316 tensile sample using the telecentric lens during tensile tests performed for DIC analysis. An EBSD map was taken of the region where the grains are imposed on the picture, where hardness indents were used to align the EBSD map onto the initial image. This region was then segmented using the DICE program (144).

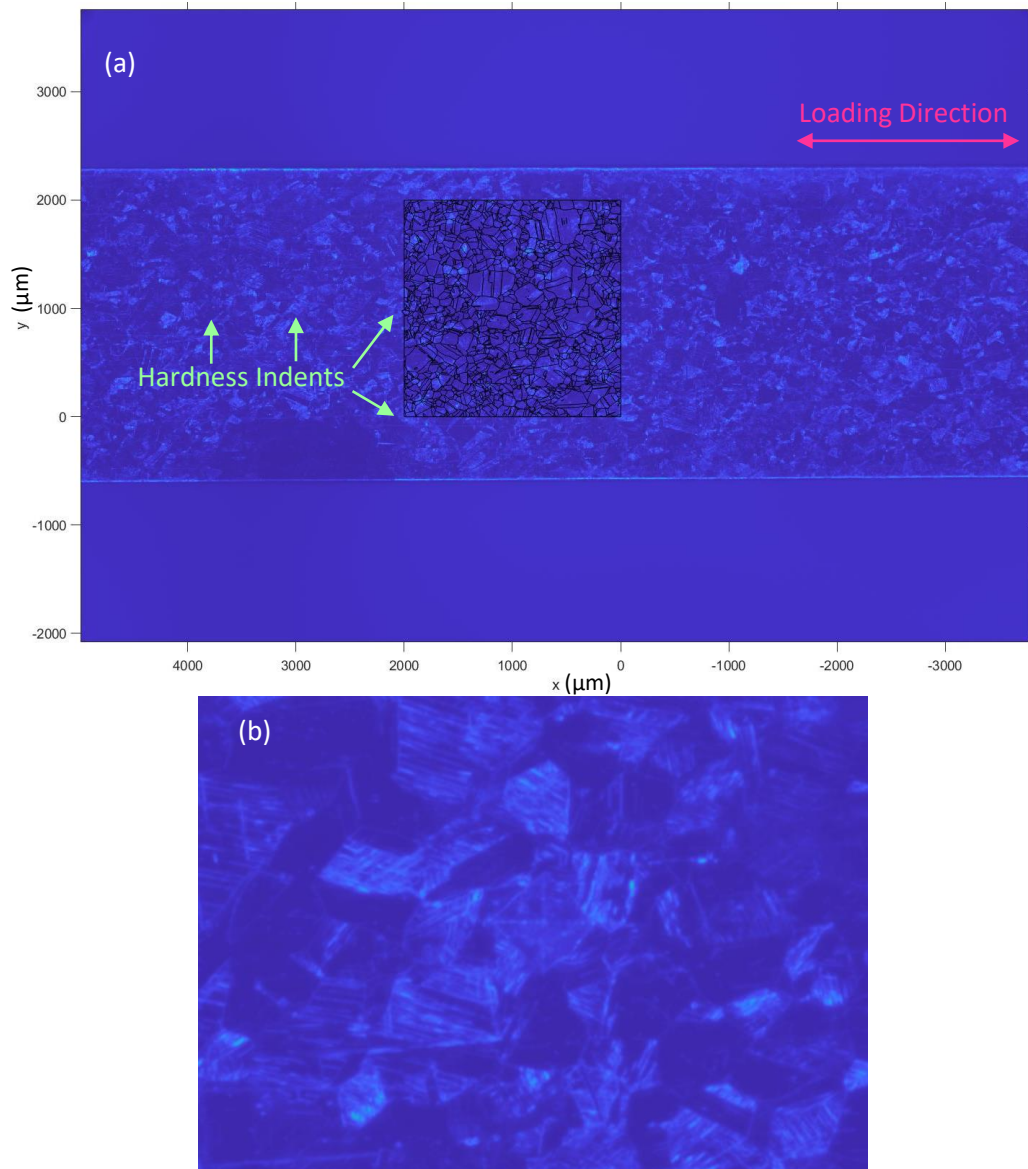


Figure 6.15: (a) DIC area for SS316 with the EBSD map region superimposed, showing how the region is segmented using the EBSD data. (b) shows a close-up image of one of the hardness indents.

The maximum nominal strain for SS316, collected from DaVis, can be seen in Figure 6.16 (a) and the maximum principle strain for SS316 for the segmented region with correlating EBSD data can be seen in Figure 6.16 (b). The E_{xx} values show the strain values in the x direction, Figure 6.17 (a) and (b) show the SS316 values at 3% strain. This shows a variation in strain values throughout the sample indicating anisotropic deformation with the regions extending between -0.15 and 0.15. There are some regions in Figure 6.17 (b) with negative strain values (blue), showing contraction. These regions are on a similar scale to the grain size of the material (observed by the imposed grains onto of the strain map), this may indicate that some grains are experiencing different extremes of deformation. Figure 6.18 shows the strain values in the y direction (perpendicular to the loading

direction). These values span between -0.15 and 0.15 and show variation throughout the area but are dominated by negative values (blue) indicating there is more contraction in this direction.

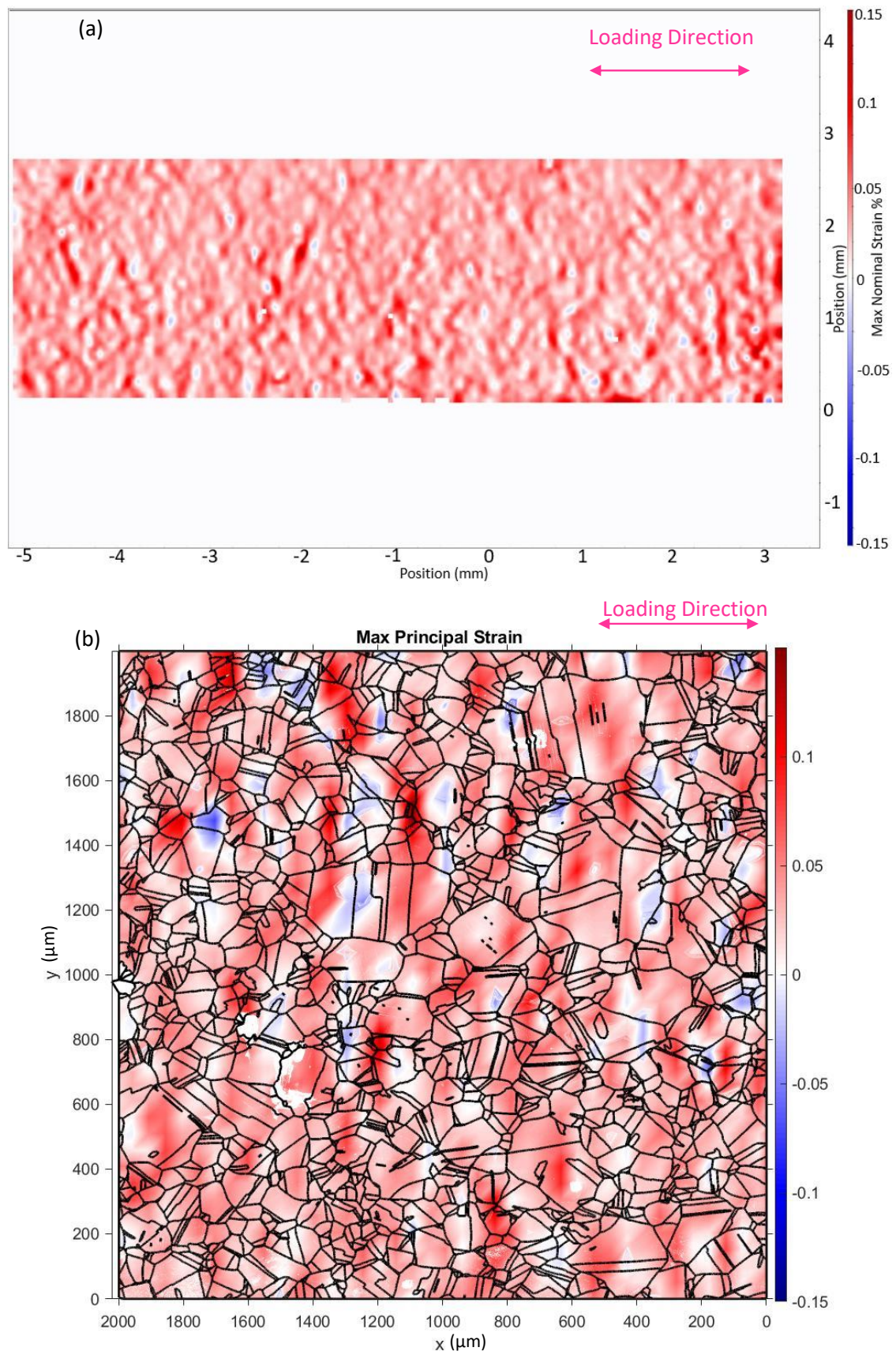


Figure 6.16: Strain maps collected through DIC for SS316 at 3% global strain showing (a) the total area showing the maximum nominal strain and (b) showing the maximum principal strain for the area within the EBSD analysis.

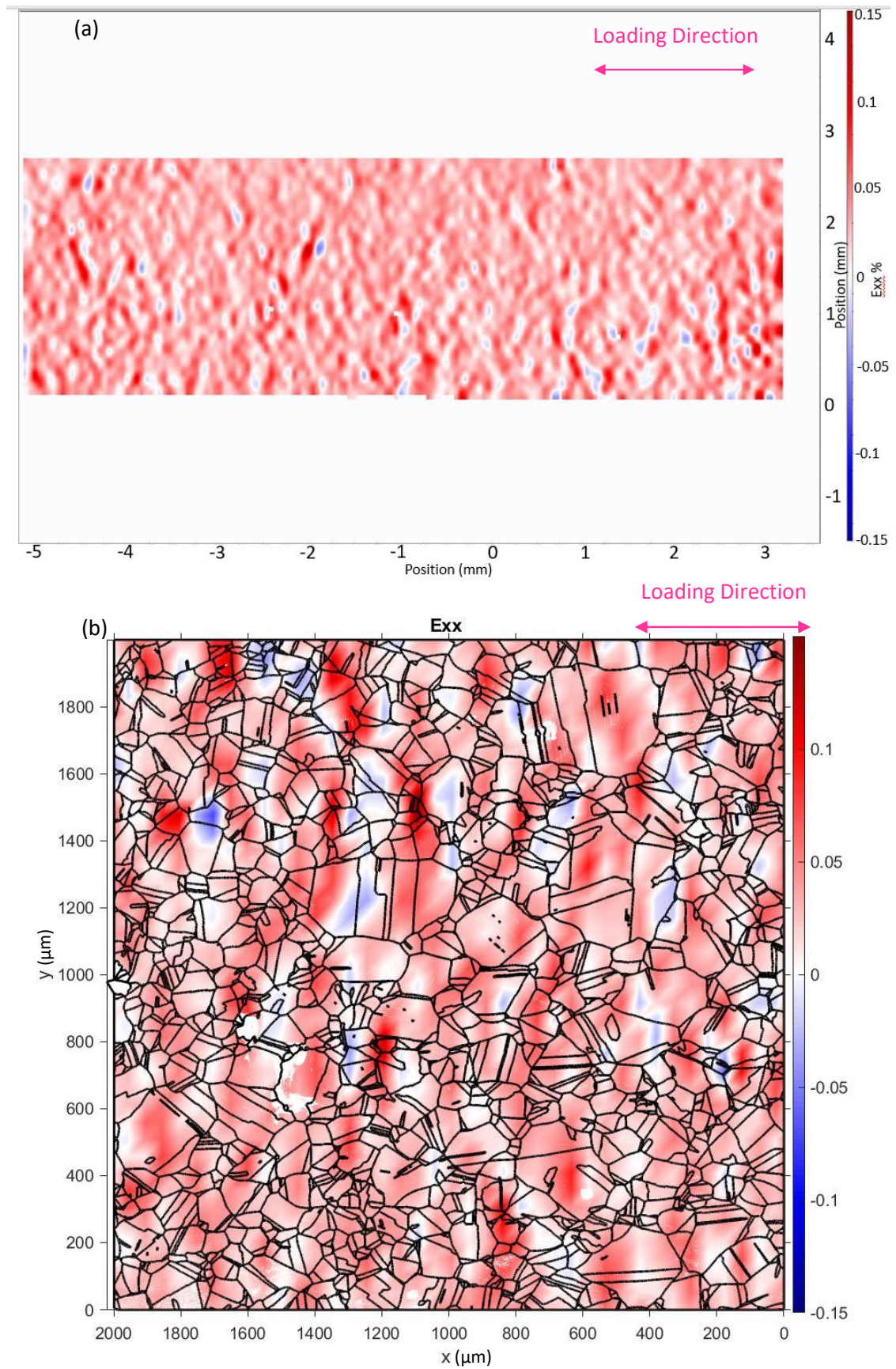


Figure 6.17: Strain map for SS316 in the loading direction (E_{xx}) at 3% global strain where (a) shows the entire region captured by the telecentric lens and (b) the segmented region calculated by imposing EBSD analysts on the DIC analysis.

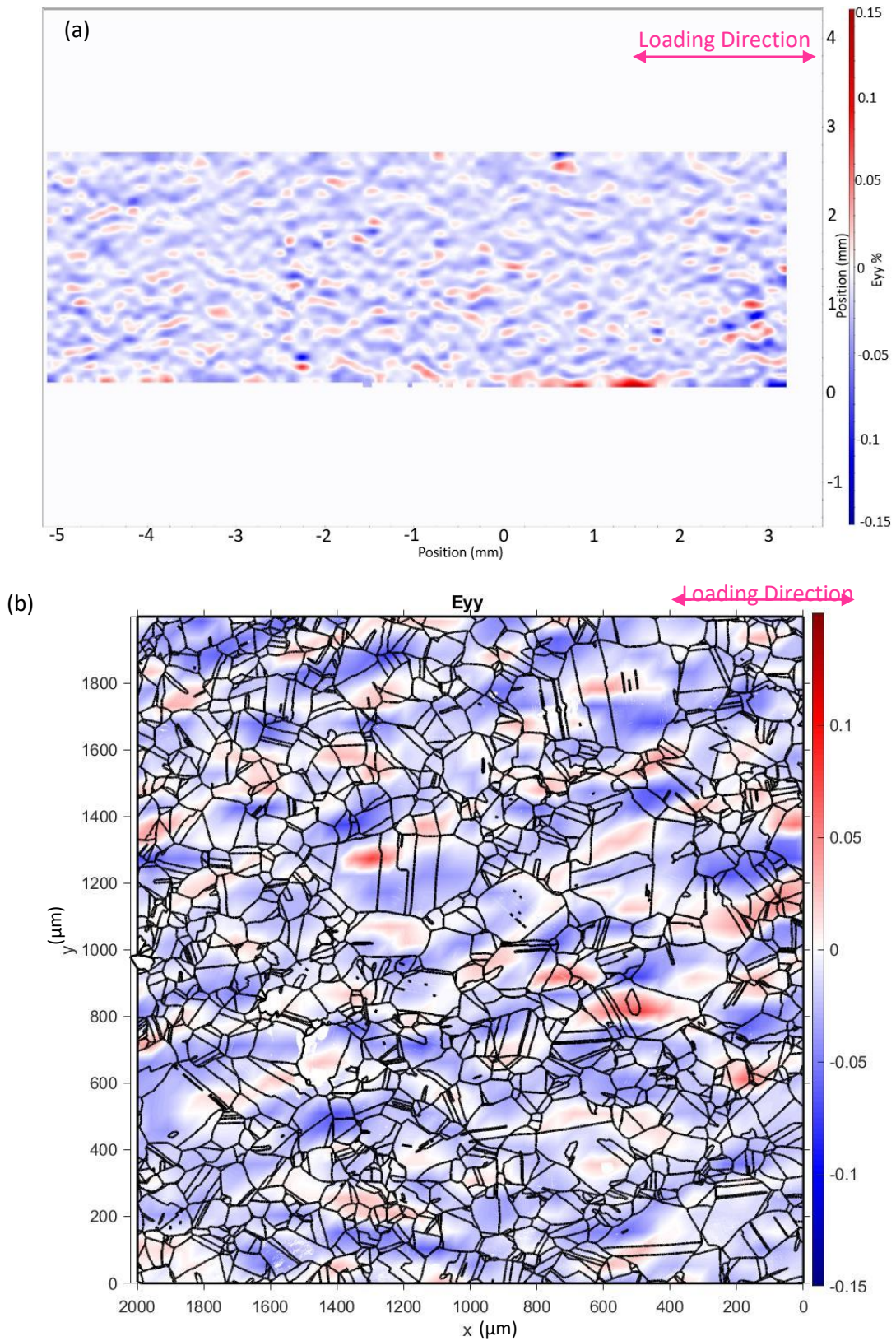


Figure 6.18: Strain map for SS316 perpendicular to the loading direction (E_{yy}) at 3% strain where (a) shows the entire region captured by the telecentric lens and (b) the segmented region calculated by imposing EBSD analysis on the DIC analysis.

Figure 6.19 shows the area pictured for the INVAR tensile sample using the telecentric lens during tensile tests performed for DIC analysis. It should be noted that the large light coloured etching features found in Figure 6.19, were a by product of the etching preparation and are not the speckle pattern used for the DIC analysis. They were found to have a significantly high contrast within them, meaning they would not effect the DIC process. An EBSD map was taken of the region where the grains are imposed on the picture, where hardness indents were used to align the EBSD map onto the initial image. This region was then segmented using the DICE program which cuts the strain data into the region selected by the EBSD analysis.

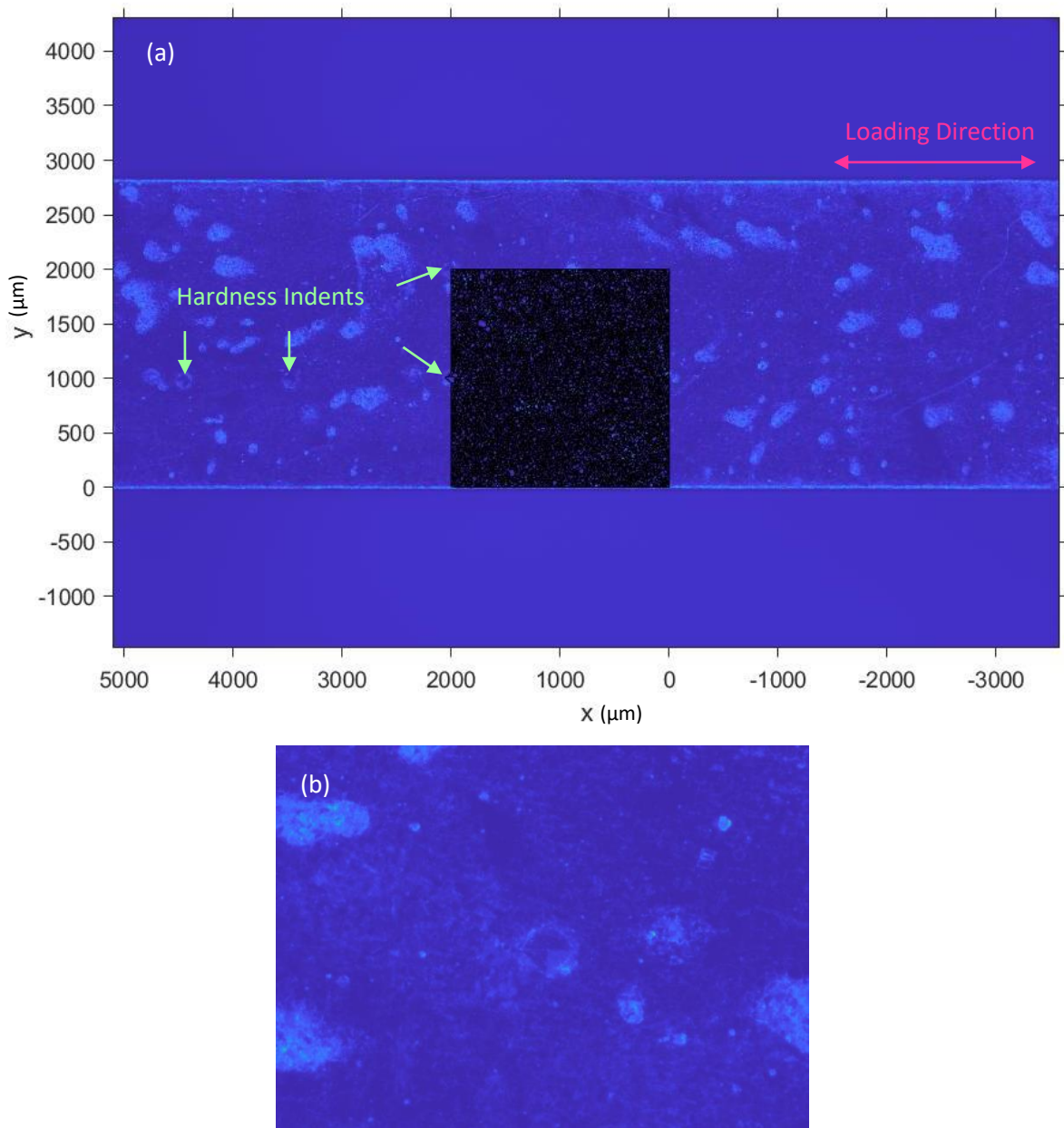


Figure 6.19: (a) Initial image collected for the DIC analysis for the tensile tests of INVAR with the EBSD map region superimposed. The hardness indents seen between 2000 and 4500 were used to align the EBSD map with the initial image to segment the strain results. (b) Shows a close-up image of one of the hardness indents.

The maximum nominal strain for INVAR, collected from DaVis, can be seen in Figure 6.20 (a) and the maximum principle strain for the segmented region using the correlating EBSD data can be seen in Figure 6.20 (b). The E_{xx} values show the strain values in the x direction, Figure 6.21 (a) and (b) show the INVAR values at 3% strain. This shows a variation in strain values throughout the sample indicating anisotropic deformation with the regions extending between -0.15 and 0.15. There are some regions with negative values (blue) showing contraction, however, the images are mainly dominated by extension due to being in the loading direction. Figure 6.22 shows the strain values in the y direction (perpendicular to the loading direction). These values span between -0.15 and 0.15 and show variation throughout the area but are dominated by negative values (blue) indicating there is more contraction in this direction.

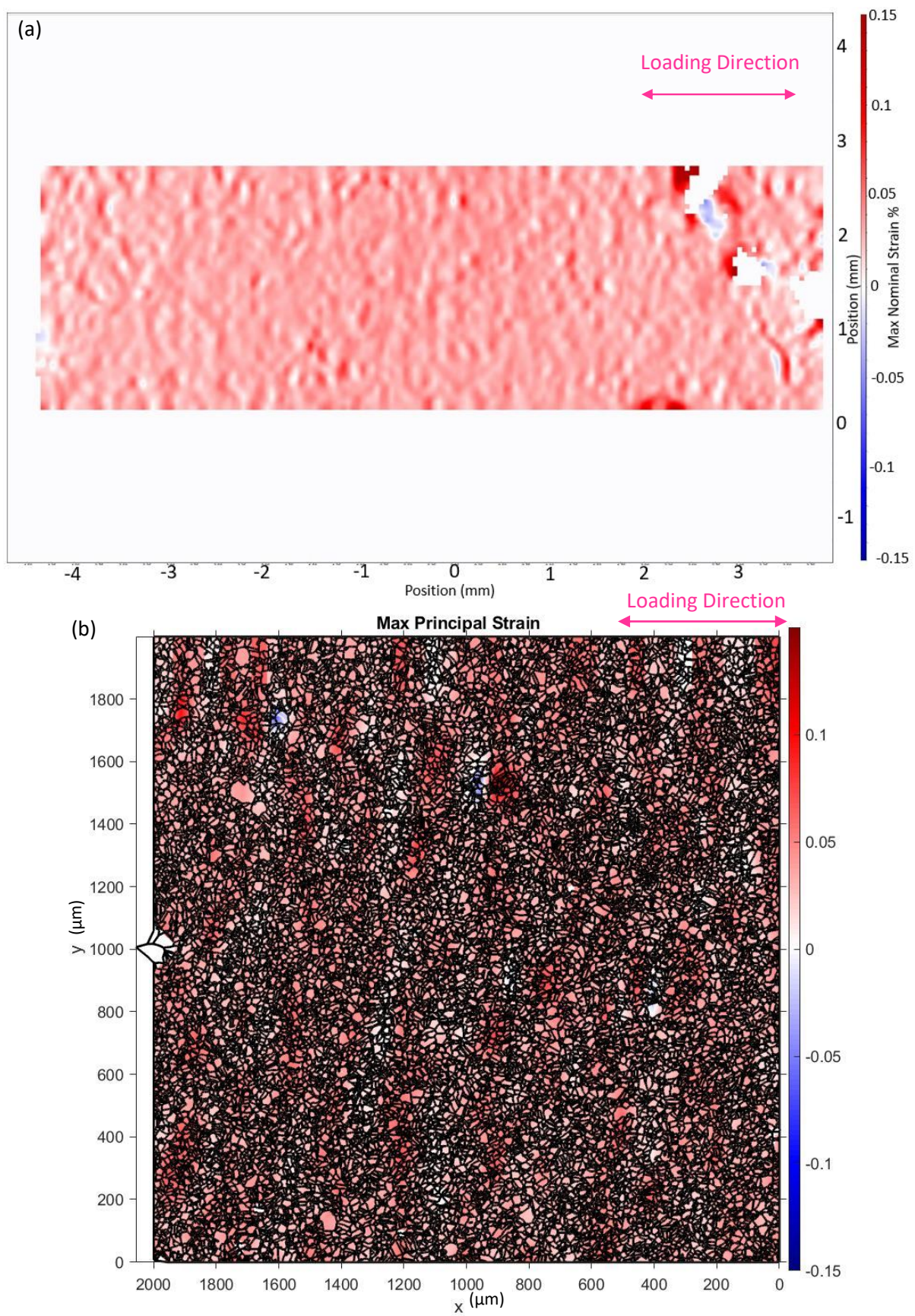


Figure 6.20: Strain maps collected through DIC for INVAR at 3% global strain, showing the (a) total area maximum nominal strain and (b) the maximum principal strain for the area within the EBSD analysis.

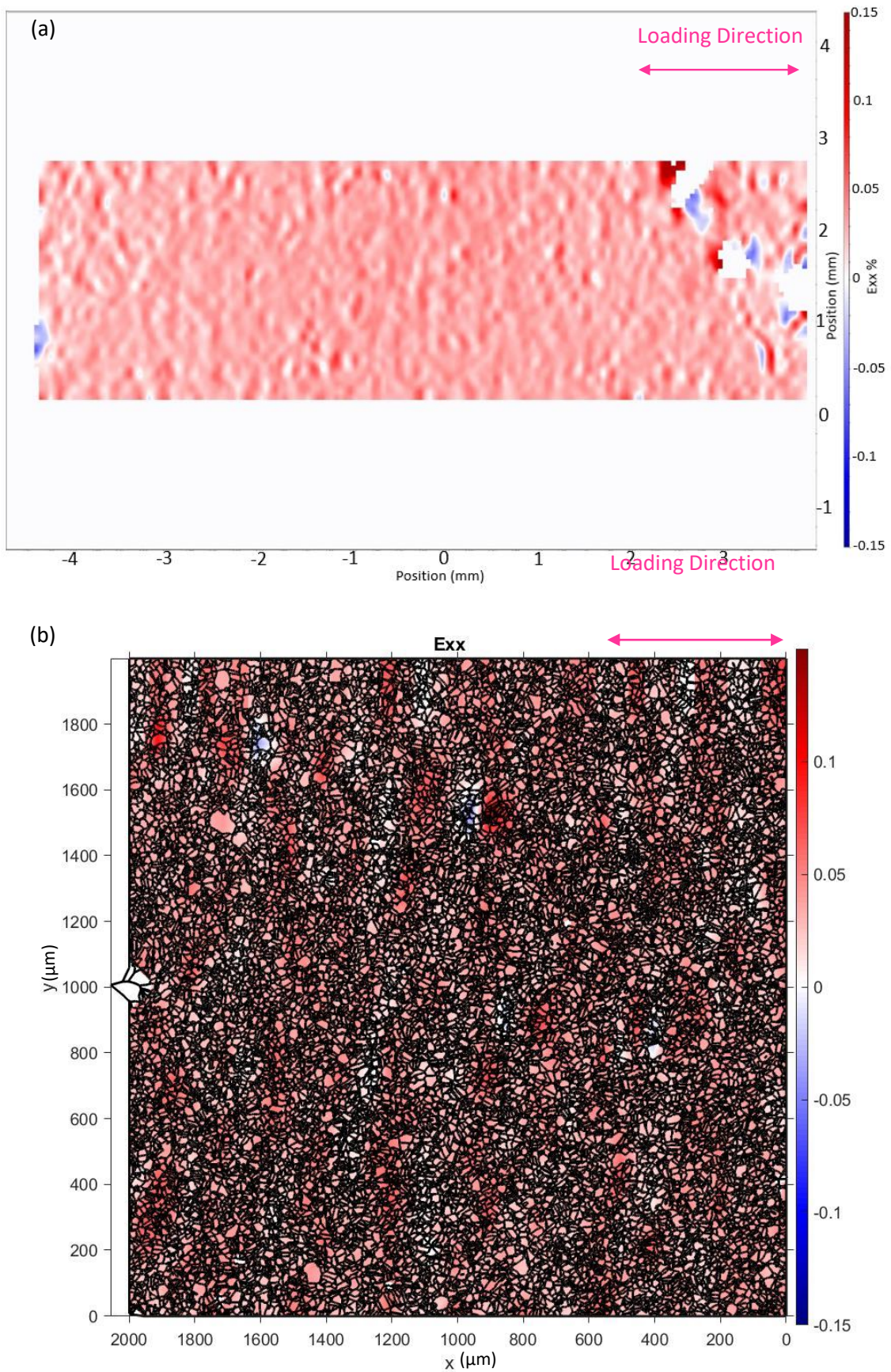


Figure 6.21: Strain map for INVAR in the loading direction (E_{xx}) at 3% global strain where (a) shows the entire region captured by the telecentric lens and (b) the segmented region calculated by imposing EBSD analysts on the DIC analysis.

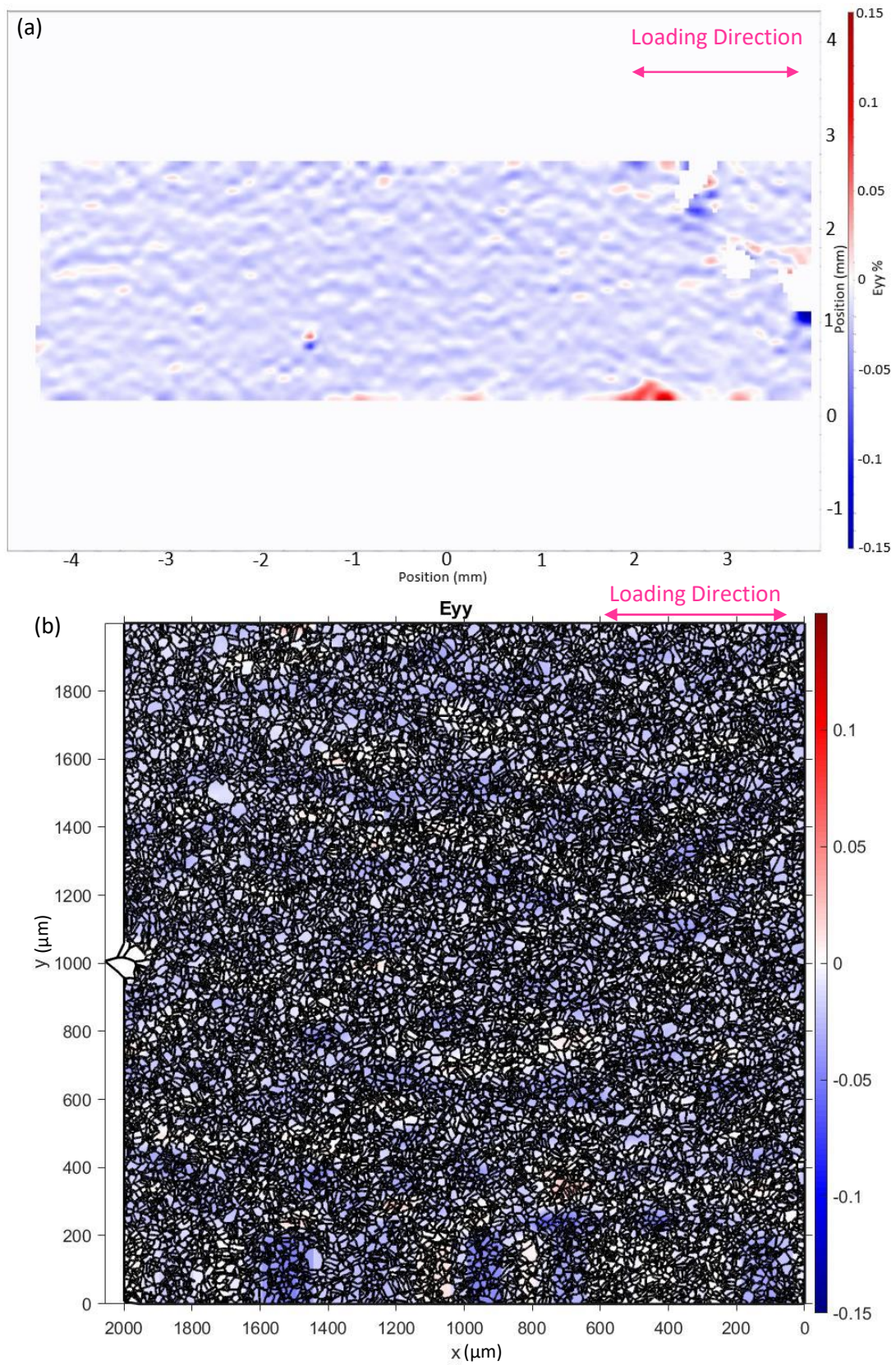


Figure 6.22: Strain map for INVAR perpendicular to the loading direction (E_{yy}) at 3% global strain where (a) shows the entire region captured by the telecentric lens and (b) the segmented region calculated by imposing EBSD analysts on the DIC analysis.

Figure 6.23 shows the area pictured for the pure nickel tensile sample using the telecentric lens during tensile tests performed for DIC analysis. Similarly to the previous INVAR specimen, it should be noted that the large light coloured etching features found in Figure 6.23, were a by product of the etching preparation and are not the speckle pattern used for the DIC analysis. They were found to have a significantly high contrast within them, meaning they would not effect the DIC process. An EBSD map was taken of the region where the grains are imposed on the picture, where hardness indents were used to align the EBSD map onto the initial image. This region was then segmented using the DICE program which cuts the strain data into the region selected by the EBSD analysis.

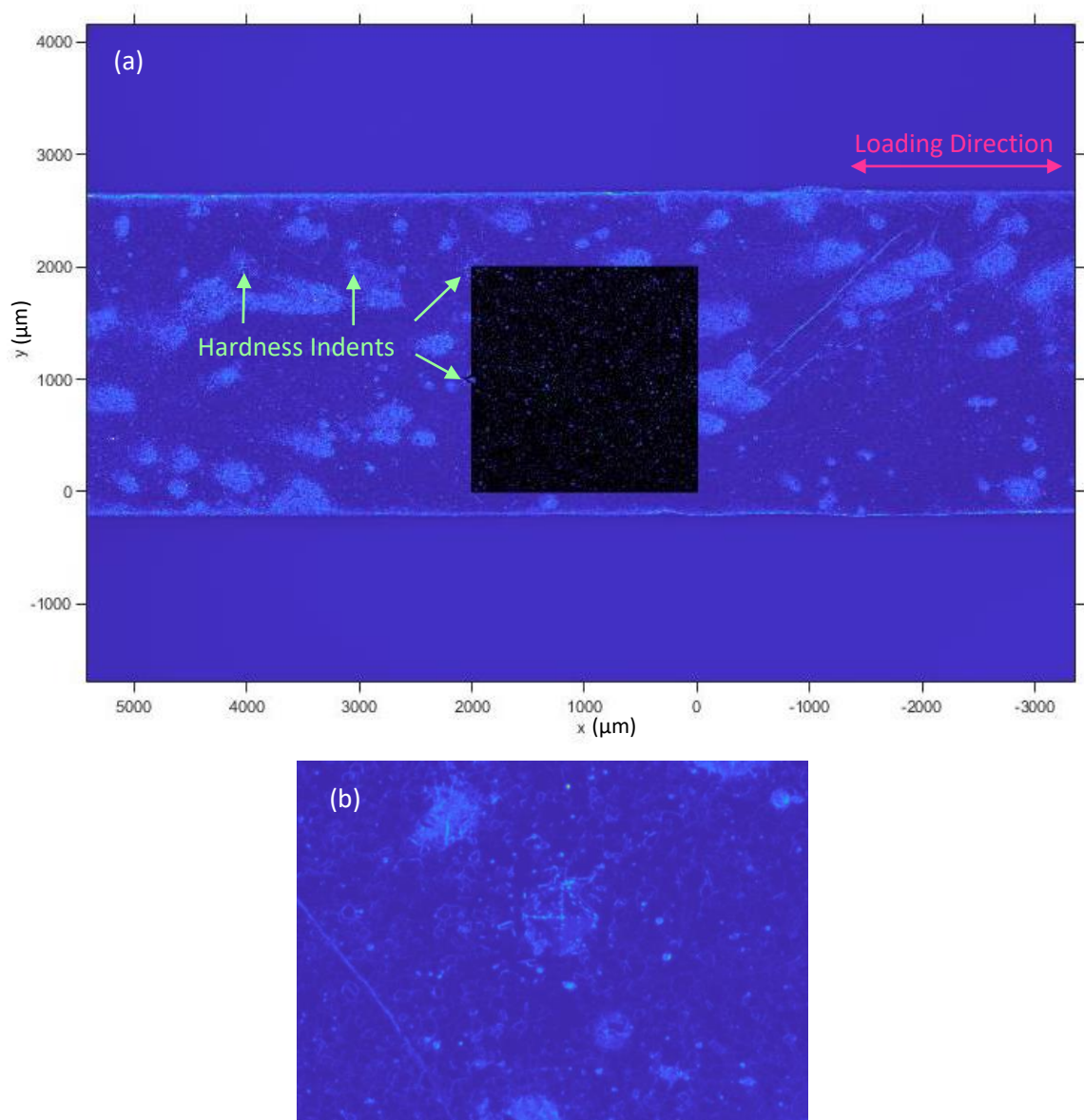


Figure 6.23: Initial image collected for the DIC analysis for the tensile tests of pure nickel with the EBSD map region superimposed. The hardness indent used to align the EBSD map to the DIC data is seen at (2000,1000). (b) Shows a close-up image of one of the hardness indents.

The maximum nominal strain for pure nickel, collected from DaVis, can be seen in Figure 6.24 (a) and the maximum principle strain for the segmented region using the correlating EBSD data can be seen in Figure 6.24 (b). The E_{xx} values show the strain values in the x direction, Figure 6.25 (a) and (b) show the pure nickel values at 3% strain. This shows a slight variation in strain values throughout the sample indicating anisotropic deformation, however, the values typically vary around 0.03 and show no negative values. Figure 6.26 shows the strain values for the E_{yy} direction (perpendicular to the loading direction) of pure nickel. These values span show very little variation throughout the area and only show some positive values at the border of the image which is likely an effect of being the edge of the sample.

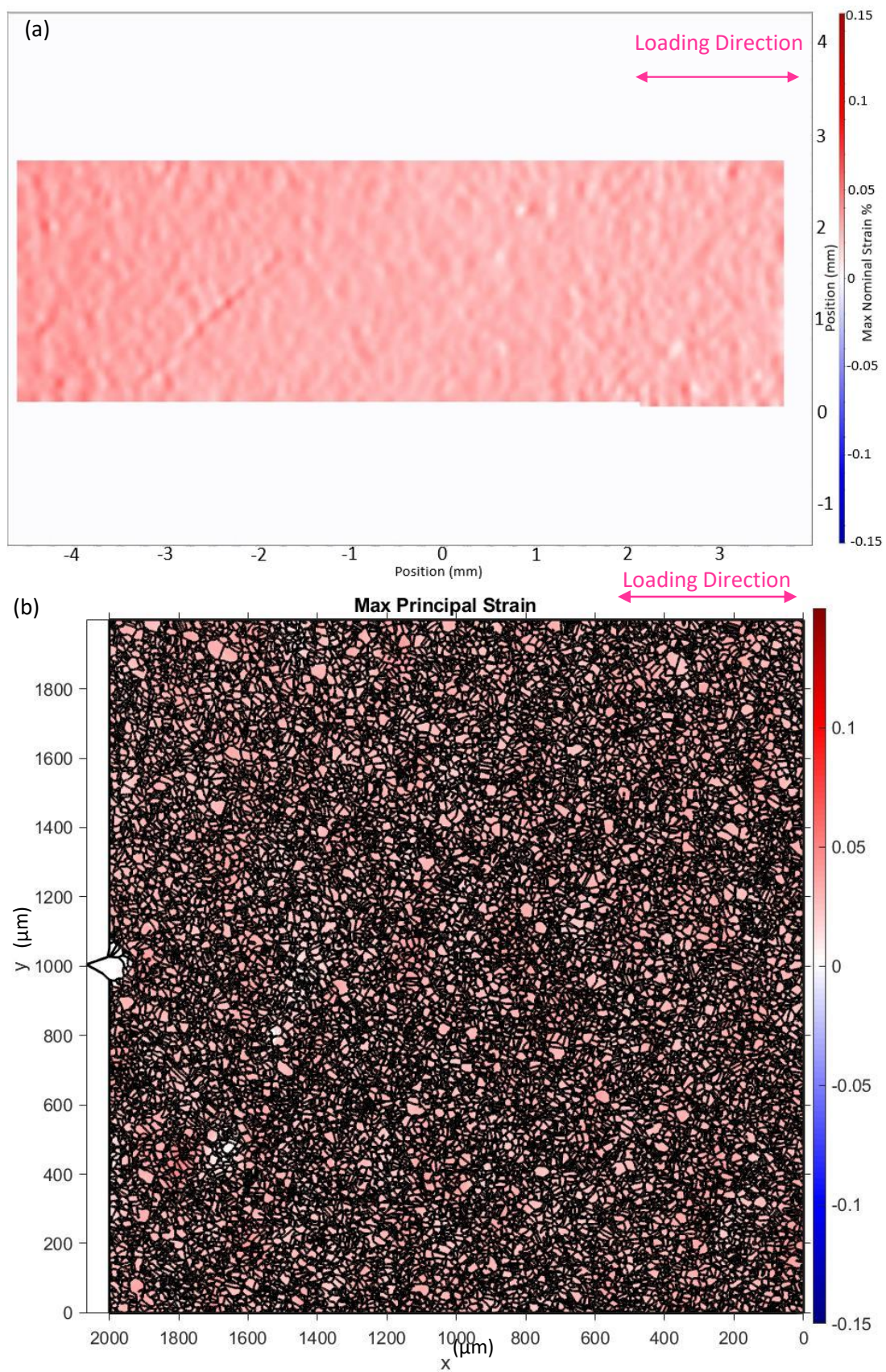


Figure 6.24: Strain maps collected through DIC for pure nickel at 3% global strain showing the (a) total area maximum nominal strain and (b) the maximum principal strain for the area within the EBSD analysis.

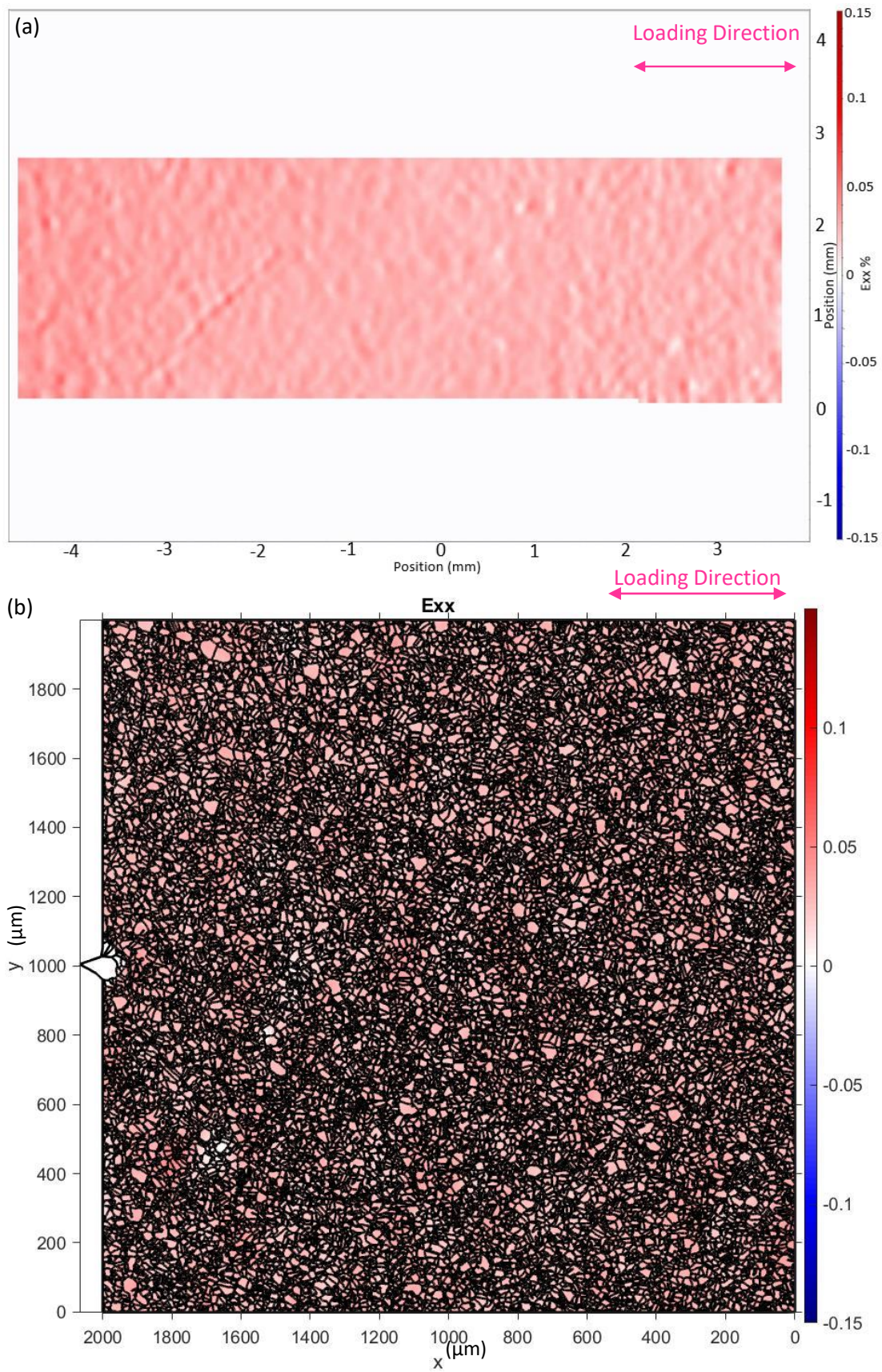


Figure 6.25: Strain map for pure nickel in the loading direction (E_{xx}) at 3% global strain where (a) shows the entire region captured by the telecentric lens and (b) the segmented region calculated by imposing EBSD analysts on the DIC analysis.

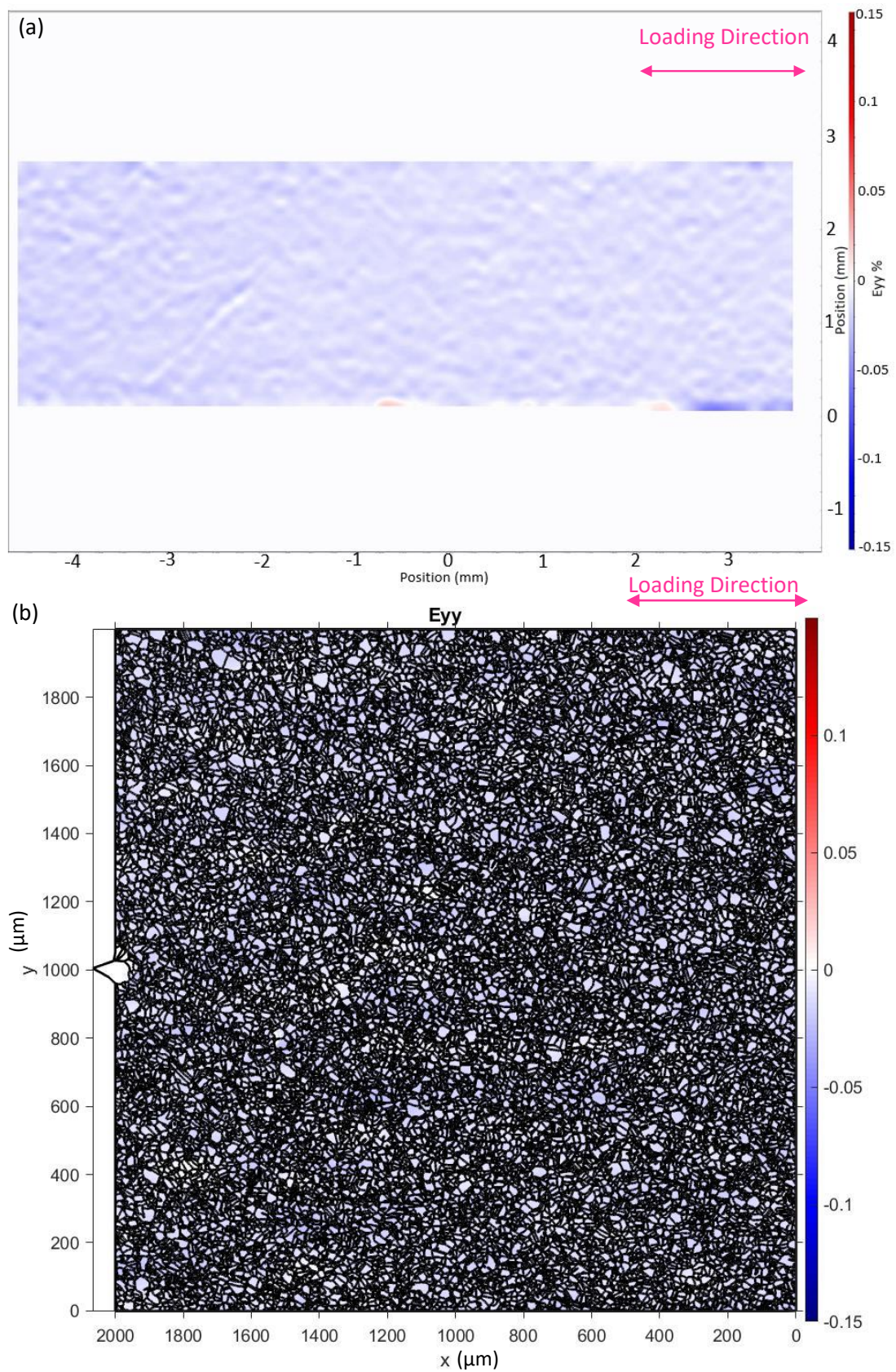


Figure 6.26: Strain map for pure nickel perpendicular to the loading direction (E_{yy}) at 3% strain where (a) shows the entire region captured by the telecentric lens and (b) the segmented region calculated by imposing EBSD analysts on the DIC analysis.

6.3.3. Segmented EBSD Maps

To compare the results of the HR-DIC strain data to the neutron data it was essential to segment the data into the same subsets recorded in the neutron diffraction tests. The same method for segmentation of the EBSD data used for the post-mortem EBSD analysis in Chapter 5 was used for this, therefore the grains selected were within 7.5 degrees of the given orientation.

Stainless Steel 316

The EBSD map for the SS316 specimen shown in Figure 6.12 was segmented to show the grains within 7.5 degrees of the 111, 220 and 200 orientations, these results are shown in Figure 6.27, Figure 6.28 and Figure 6.29 respectively.

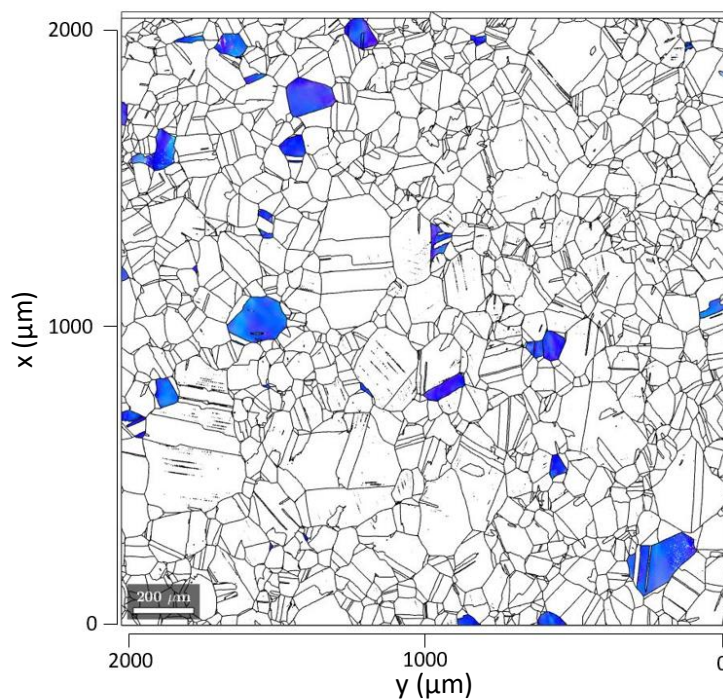


Figure 6.27: EBSD map showing only grains within 7.5 degrees of the 111 crystallographic orientation for the SS316 specimen. Here the loading direction is parallel to the x-axis.

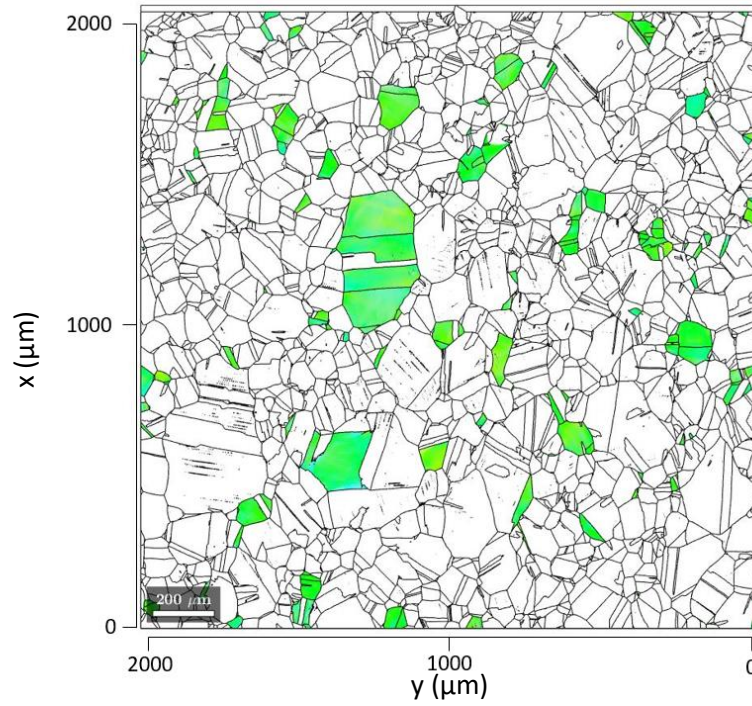


Figure 6.28: EBSD map showing only grains within 7.5 degrees of the 220 crystallographic orientation for the SS316 specimen. Here the loading direction is parallel to the x-axis.

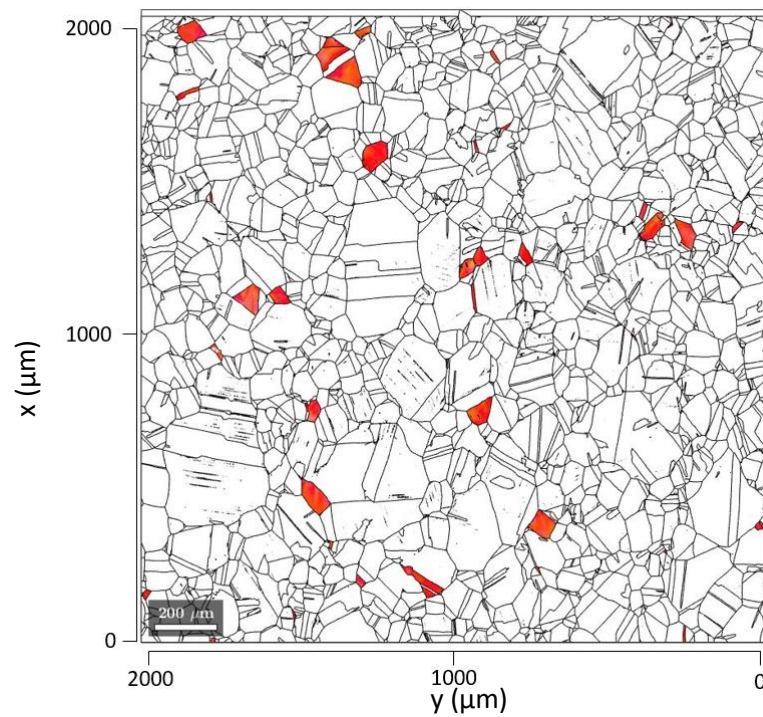


Figure 6.29: EBSD map showing only grains within 7.5 degrees of the 200 crystallographic orientation for the SS316 specimen. Here the loading direction is parallel to the x-axis.

INVAR

The EBSD map for the INVAR specimen shown in Figure 6.13 was segmented to show the grains within 7.5 degrees of the 111, 220 and 200 orientations, the results are shown in Figure 6.30, Figure 6.31 and Figure 6.32 respectively.

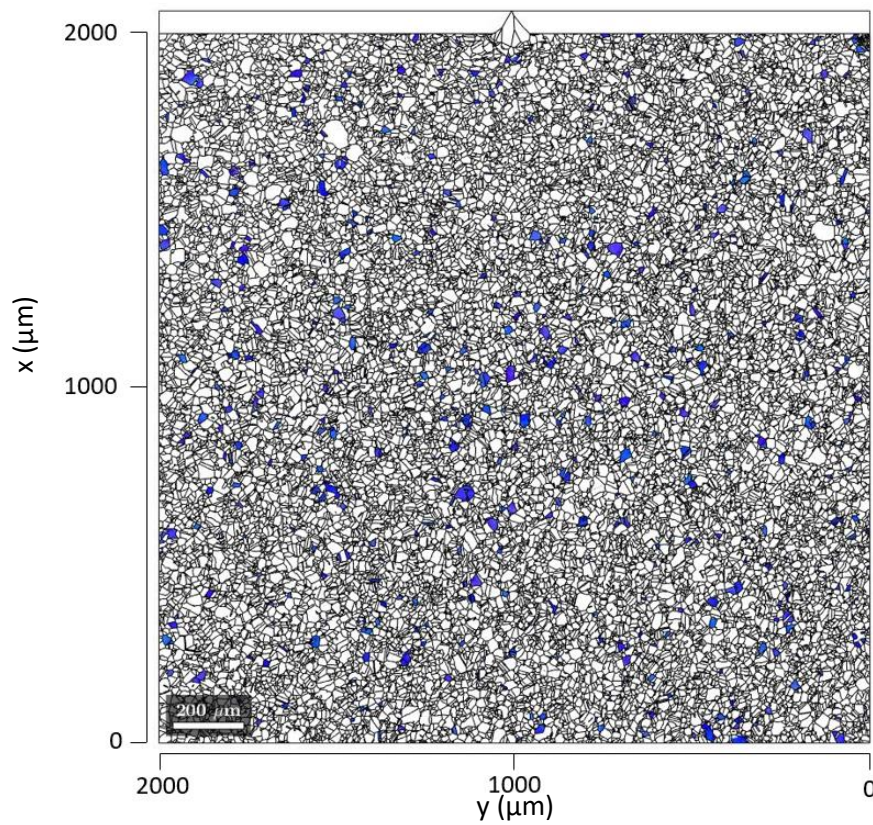


Figure 6.30: EBSD map showing only grains within 7.5 degrees of the 111 crystallographic orientation for the INVAR specimen. Here the loading direction is parallel to the x-axis.

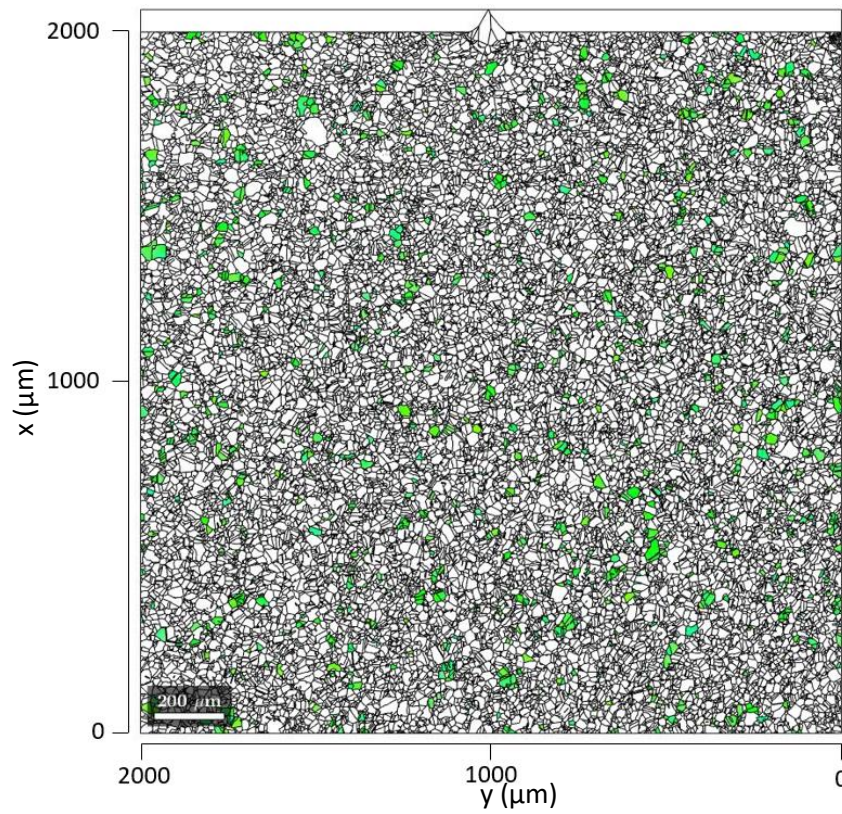


Figure 6.31: EBSD map showing only grains within 7.5 degrees of the 220 crystallographic orientation for the INVAR specimen. Here the loading direction is parallel to the x-axis.

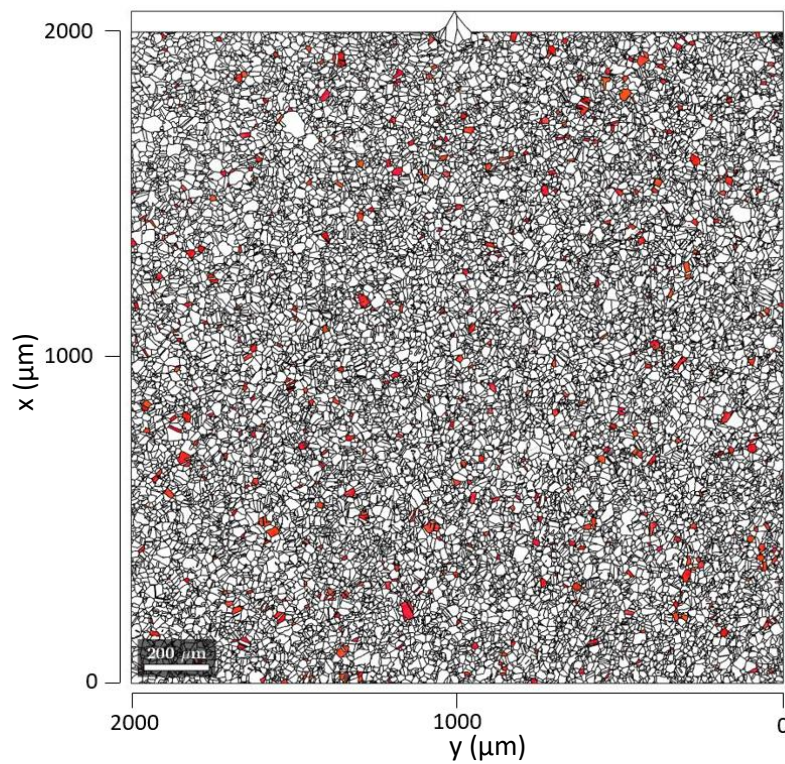


Figure 6.32: EBSD map showing only grains within 7.5 degrees of the 200 crystallographic orientation for the INVAR specimen. Here the loading direction is parallel to the x-axis.

Pure Nickel

The EBSD map for the pure nickel specimen shown in Figure 6.14 was segmented to show the grains within 7.5 degrees of the 111, 220 and 200 orientations, the results are shown in Figure 6.33, Figure 6.34 and Figure 6.35 respectively.

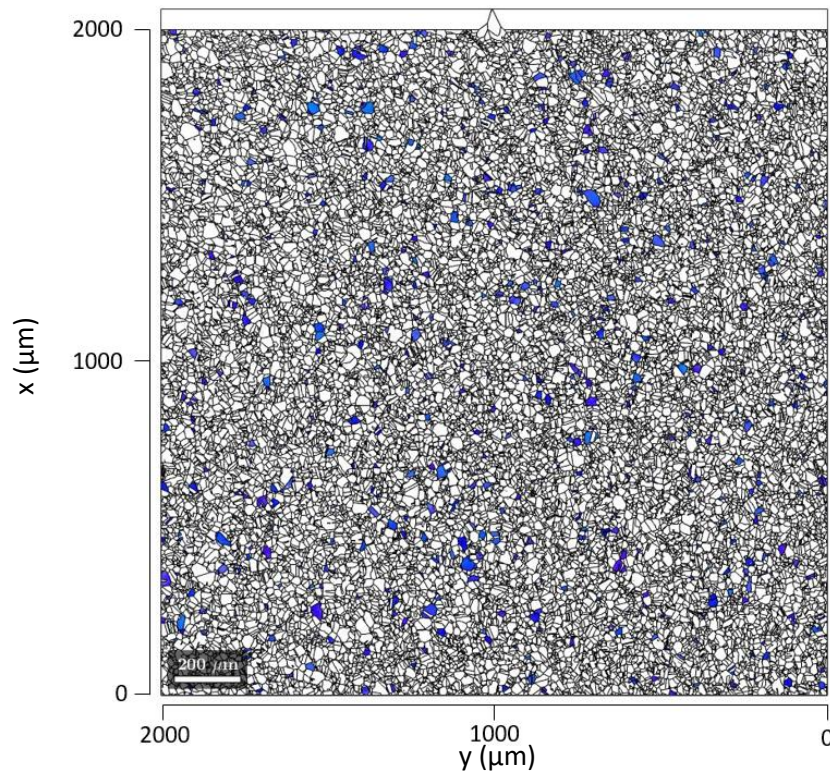


Figure 6.33: EBSD map showing only grains within 7.5 degrees of the 111 crystallographic orientation for the pure nickel specimen. Here the loading direction is parallel to the x-axis.

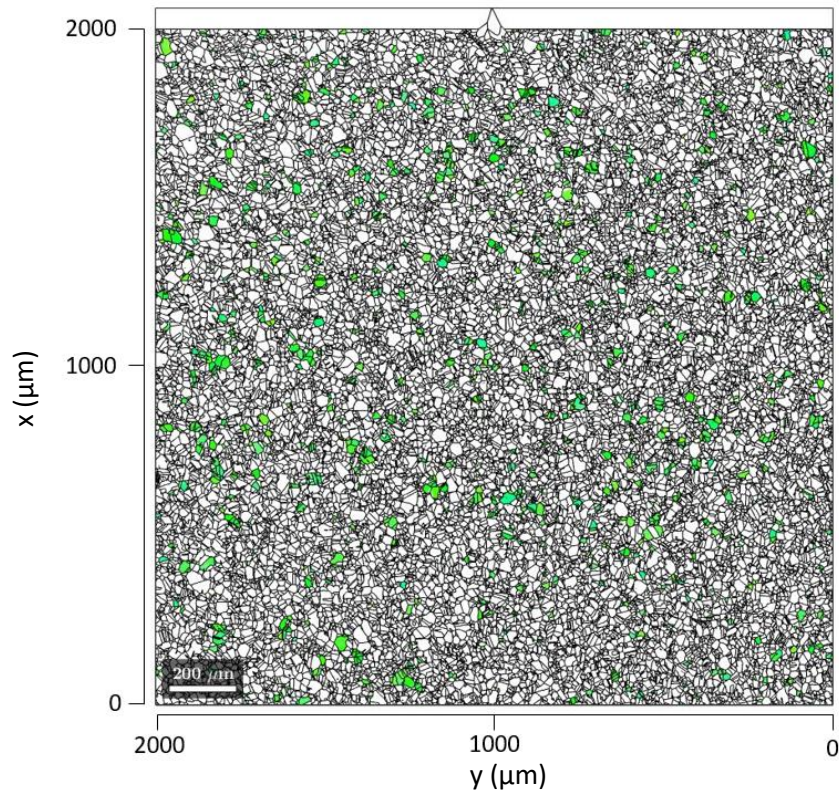


Figure 6.34: EBSD map showing only grains within 7.5 degrees of the 220 crystallographic orientation for the pure nickel specimen. Here the loading direction is parallel to the x-axis.

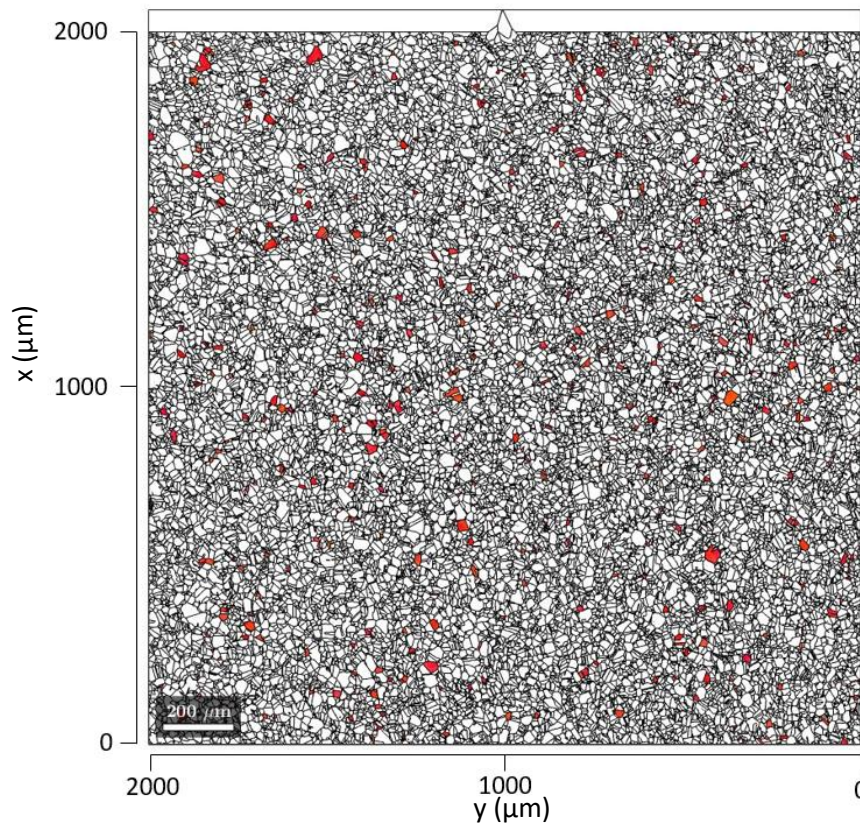


Figure 6.35: EBSD map showing only grains within 7.5 degrees of the 200 crystallographic orientation for the pure nickel specimen. Here the loading direction is parallel to the x-axis.

6.3.4. Histogram plots

By superimposing the EBSD maps onto the strain data, the grain subset regions can be defined and, therefore, split the DIC strain data into just those regions. Following the segmentation of the EBSD maps and strain maps, histogram plots have been used to visually show the difference in the stain for each subset of grains. The histogram plots present the frequency of recorded strain values for the regions determined to be within 7.5 degrees of the 111, 220 or 200 orientations. The decision to selected 7.5 degrees stemmed from the neutron diffraction analysis, where ENGIN-X has the same accuracy and therefore allowed a direct comparison of grain subsets.

6.3.4.1. HR-DIC Histogram Plots for SS316 Specimen

Figure 6.36 shows the segmented strain data in the loading direction (E_{xx}) for the SS316 specimen (using the strain map found in Figure 6.17) at 3% global strain. The strain data was segmented using the EBSD maps so the grains were within 7.5 degrees of the 111 (Figure 6.27), 220 (Figure 6.28) and 200 (Figure 6.29) orientations. The 111 orientation subset had strain values which range between - 0.045 to 0.105, with a maximum number of counts at 0.01. The 220 subset has a range of strain

values between -0.04 and 0.09, with a maximum number of counts at 0.035. The 200 subset has a range of strain values between -0.015 and 0.105, with a maximum number of counts at 0.025.

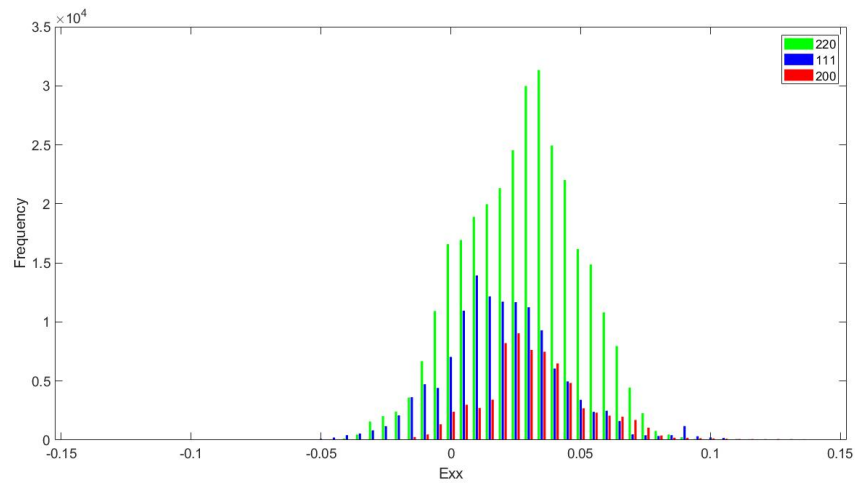


Figure 6.36: Histogram plot for the Exx strain values recorded for SS316 at 3% global strain for the 111, 220 and 200 subsets of grains.

Figure 6.37 shows the strain data for the SS316 specimen, perpendicular to the loading direction (Eyy) for the 111, 220 and 200 orientation subsets at 3% global strain. This data was segmented from the strain data presented in Figure 6.18. Each subset primarily sits in the negative values, indicating contraction in this direction. The 111 subset has a range of strain values between -0.0505 to 0.04, with a maximum number of counts at -0.01. The 220 subset has a range of strain values between -0.051 and 0.0525, with a maximum number of counts at -0.01. The 200 subset has a range of strain values between -0.0515 and 0.0505, with a maximum number of counts at -0.0105.

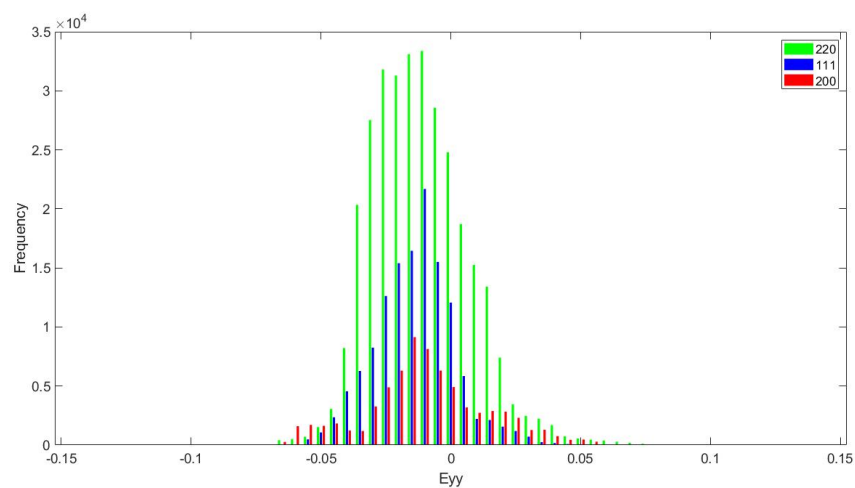


Figure 6.37: Histogram plot for the Eyy strain direction values recorded for SS316 at 3% global strain for the 111, 220 and 200 subsets of grains.

Figure 6.38 shows the spread of the strain data for SS316 for the maximum principal strain for the 111, 220 and 200 orientations of grains at 3% global strain. This data was segmented from the strain map presented in Figure 6.16. The 111 subset has a range of strain values between -0.0505 to 0.11, with a maximum number of counts at 0.0305. The 220 subset has a range of strain values between -0.05 and 0.0905, with a maximum number of counts at 0.03. The 200 subset has a range of strain values between -0.0205 and 0.11, with a maximum number of counts at 0.0205.

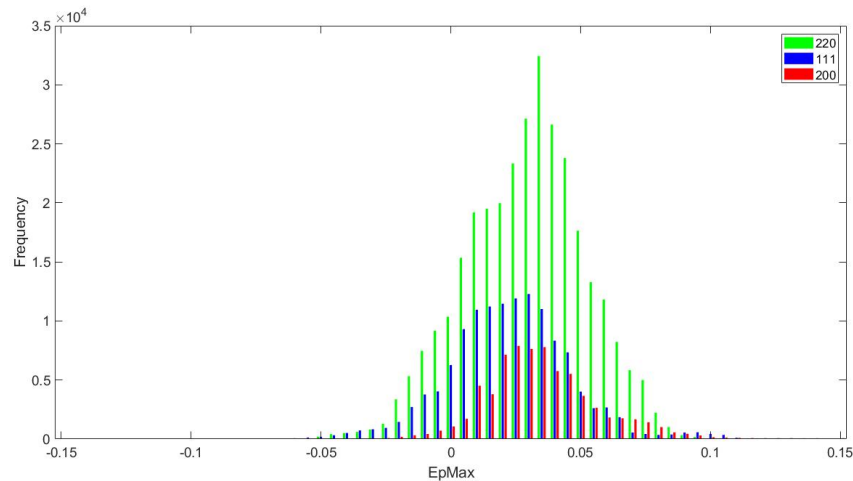


Figure 6.38: Histogram plot for the maximum principal strain values recorded for SS316 at 3% global strain for the 111, 220 and 200 subsets of grains.

6.3.4.2. HR-DIC Histogram Plots for INVAR Specimen

Figure 6.39 shows the segmented strain data in the loading direction (Exx) for the INVAR specimen (using the strain map found in Figure 6.21) at 3% global strain. The strain data was segmented using the EBSD maps so the grains were within 7.5 degrees of the 111 (Figure 6.30), 220 (Figure 6.31) and 200 (Figure 6.32) orientations. The strain values span between -0.01 and 0.08, however, they all have a maximum number of occurrences at a value of ~ 0.03 .

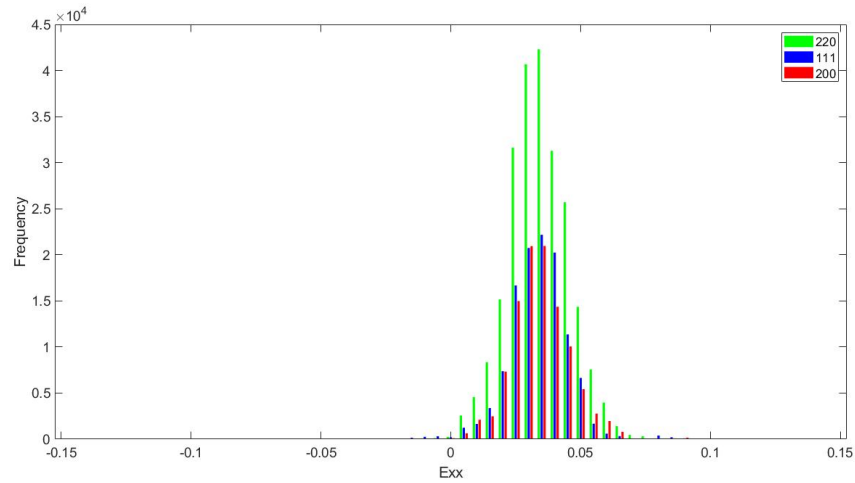


Figure 6.39: Histogram plot for the E_{xx} strain values recorded for INVAR at 3% global strain for the 111, 220 and 200 subsets of grains.

Figure 6.40 shows the strain data perpendicular to the loading direction (E_{yy}) for the grains in INVAR divided into the 111, 220 and 200 orientation subsets at 3% global strain. This data was segmented from the strain map presented in Figure 6.22. The 111-orientation subset has a range of values between -0.05 and 0.02, with a maximum number of counts at -0.015. The 220-orientation subset has a range of values between -0.05 and 0.02, with a maximum number of counts at -0.02. The 200-orientation subset has a range of values between -0.04 and 0.02, with a maximum number of counts at -0.015.

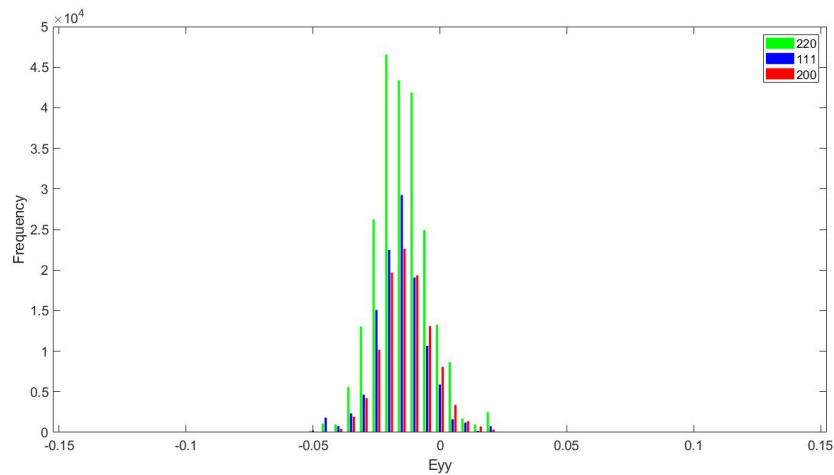


Figure 6.40: Histogram plot for the E_{yy} strain values recorded for INVAR at 3% global strain for the 111, 220 and 200 subsets of grains.

Figure 6.41 shows the spread of the strain data for INVAR for the maximum principal strain for the 111, 220 and 200 orientations of grains at 3% global strain. This data was segmented from the strain map presented in Figure 6.20. The maximum principal strain consists of all positive values which

span between 0 and 0.1. The number of occurrences of the 220 orientation subset is nearly double that of the 111 and 200 orientation subsets.

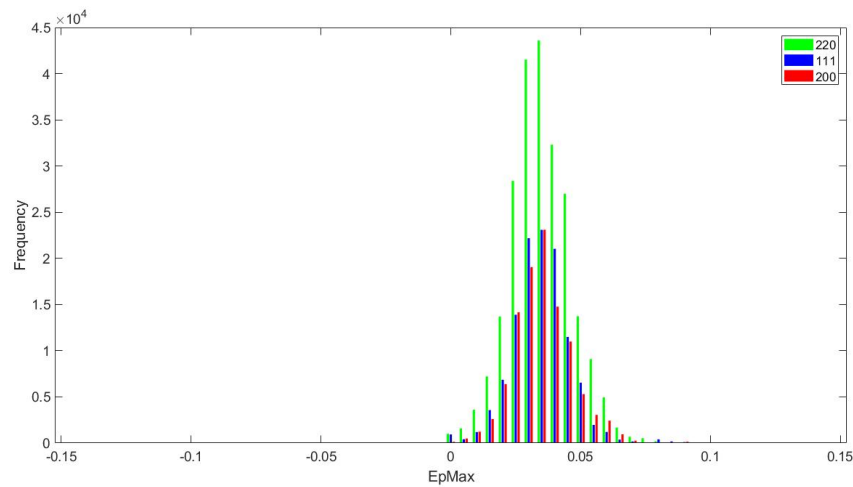


Figure 6.41: Histogram plot for the maximum principal strain values recorded for INVAR at 3% global strain for the 111, 220 and 200 subsets of grains.

6.3.4.3. HR-DIC Histogram Plots for Pure Nickel Specimen

Figure 6.42 shows the segmented strain data in the loading direction (E_{xx}) for the pure nickel specimen (using the strain map found in Figure 6.25) at 3% global strain. There is no variation in strain values between the subsets but the 220 orientation subset has a larger number of counts, followed by the 111 and then the 200. The strain values are all positive and span between 0.01 and 0.04, with a maximum number of counts at 0.03.

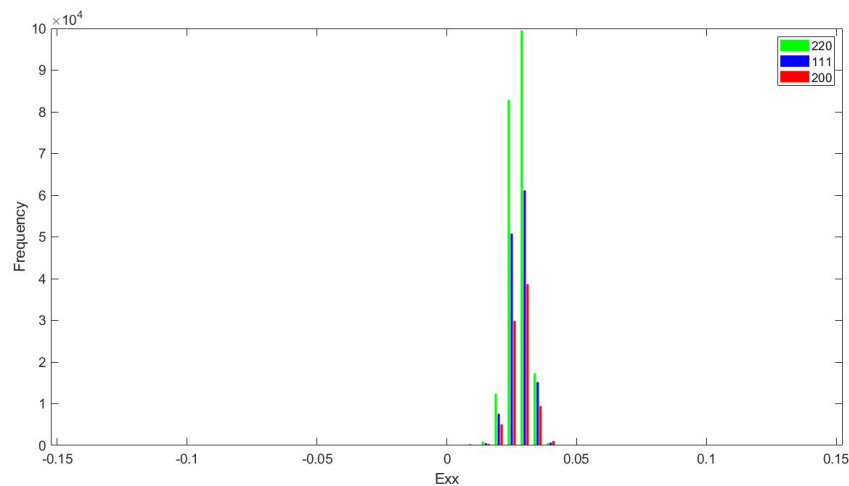


Figure 6.42: Histogram plot for the E_{xx} strain direction values recorded for pure nickel at 3% global strain for the 111, 220 and 200 subsets of grains.

Figure 6.43 shows the strain data perpendicular to the loading direction (E_{yy}) for the grains in pure nickel specimen, divided into the 111, 220 and 200 orientation subsets at 3% global strain. This data

was segmented from the strain map presented in Figure 6.26. All the subsets have the same values of strain which span between -0.025 and 0, with a peak value number of counts at -0.0125. The number of instances for 220 is the highest, followed by 111 and then 200.

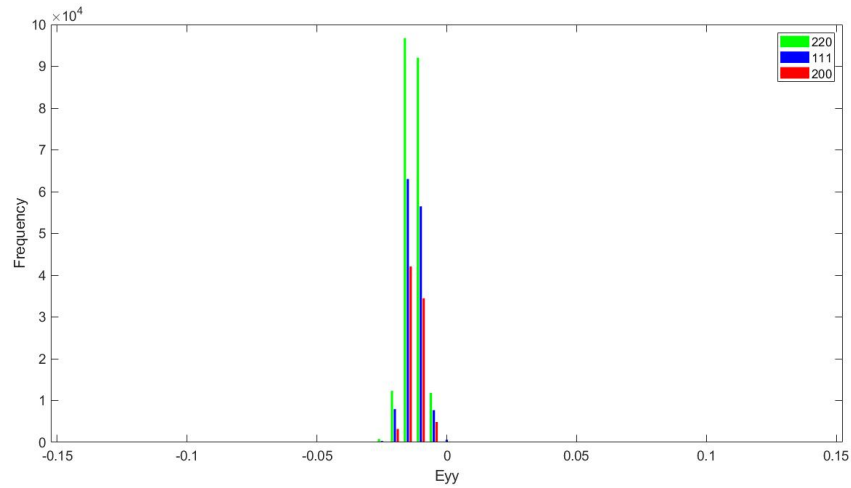


Figure 6.43: Histogram plot for the E_{yy} strain direction values recorded for pure nickel at 3% global strain for the 111, 220 and 200 subsets of grains.

Figure 6.44 shows the spread of the strain data for pure nickel for the maximum principal strain for the 111, 220 and 200 orientations of grains at 3% global strain. This data was segmented from the strain map presented in Figure 6.24. It should be noted that the length scale in y is larger in this figure than in Figure 6.42 and Figure 6.43. The values span between 0.01 and 0.04 for all subsets with the peak being at 0.03.

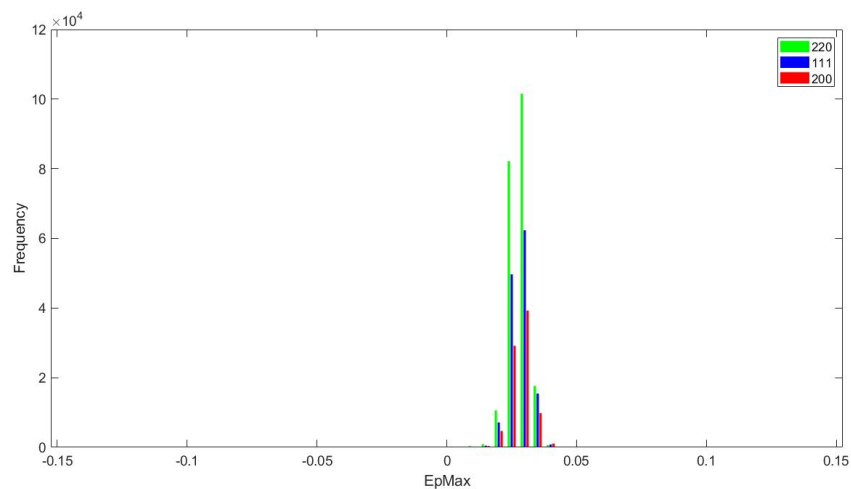


Figure 6.44: Histogram plot for the maximum principal strain values recorded for pure nickel at 3% global strain for the 111, 220 and 200 subsets of grains.

6.3.5. Regional Strain Plots

As the DICE code was not programmed to process multiple images, to produce strain progression throughout loading, regions with high concentrations of grains with the 111, 220 and 200 orientations were selected from the original, global DIC data. This process involved using the segmented EBSD maps to identify three regions that had a high concentration of grains within 7.5 degrees of the desired orientation and then using these coordinates and relating them to the DIC data coordinate system to segment the DIC data into the required region. Three regions of grains were selected to highlight any outlying values of strain and to find any patterns between the regions. The strain plot is from the start of the test to the point at which the samples reached 3% strain, where the image number indicates the time for the start of the test. An additional plot for each sample was included which had a strain scale between -0.2 and 0.2, this allowed comparisons to be drawn between the three specimens and allowed for a closer inspection of the elastic region for the SS316 and INVAR samples.

7.4.4.1. Regional strain plots for SS316

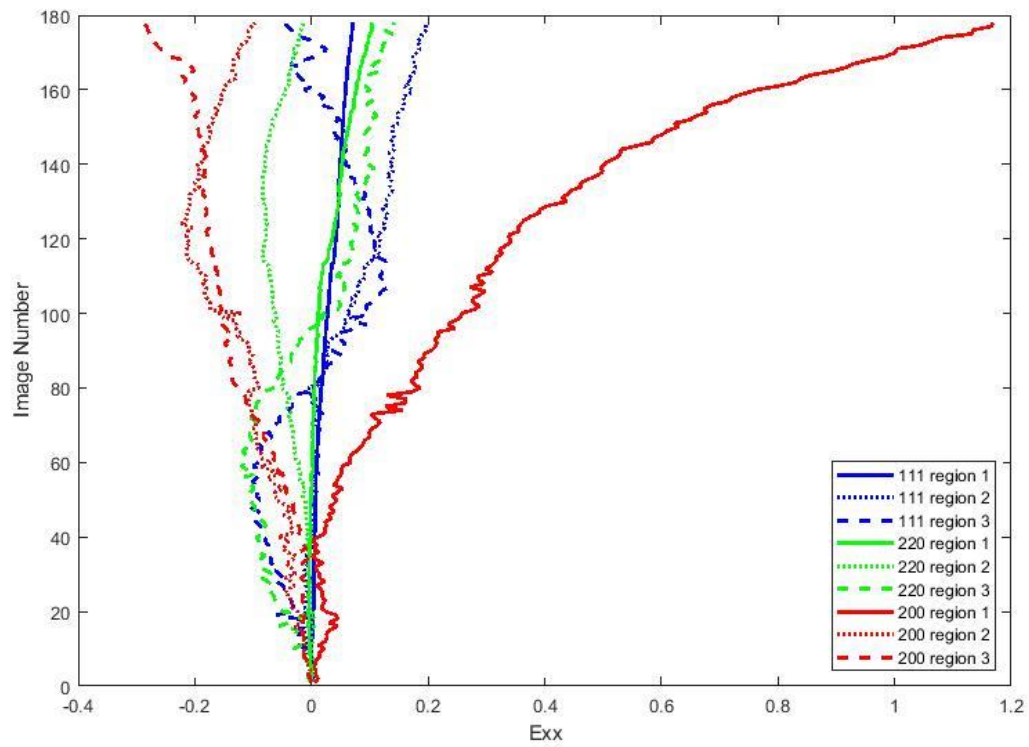
The segmented EBSD maps used to locate the grains with 7.5 degrees of the 111, 220 and 200 orientations for the SS316 specimen can be found in Figure 6.27, Figure 6.28 and Figure 6.29 respectively. The location for the regions chosen for SS316 from the EBSD coordinate which contained grains with the 111, 220 and 200 orientations are shown in Table 6.4. The regions needed to be greater than 200 μm by 200 μm to include the vector arrows from the DIC analysis, however, due to the grain size of the SS316 material this typically spanned an entire grain.

Table 6.4: Regions selected from EBSD data for SS316 which contain the largest concentration of either 111, 220 or 200 orientation subsets.

Orientation	Region	X1	X2	Y1	Y2
111	1	984	1666	1440	1640
	2	74	274	122	322
	3	1626	1826	1266	1466
220	1	958	1429	1103	1303
	2	435	635	1259	1459
	3	1597	1797	1061	1261
200	1	1760	1970	1282	1482
	2	1226	1426	212	412
	3	984	1184	1511	1711

Figure 6.45 shows the strain data progression in the loading direction (E_{xx}) for the SS316 tensile sample for the regions shown in Table 6.4. Figure 6.46 shows the strain data progression throughout loading in the perpendicular direction (E_{yy}) for the SS316 sample for the regions shown in Table 6.4. Up to image 20, all three 111-orientated regions are in reasonable agreement with one another, however above this image number a large amount of variation is shown. For the 220-orientation subset, regions 1 and 3 are in reasonable agreement up to image 20 but deviate after that, whereas region 2 is vastly different from the start of the test. The 200 subset shows reasonable agreement for the region 2 and 3 plots up to around 140, with some variation throughout, however, region 1 deviates greatly from the start of the test.

(a)



(b)

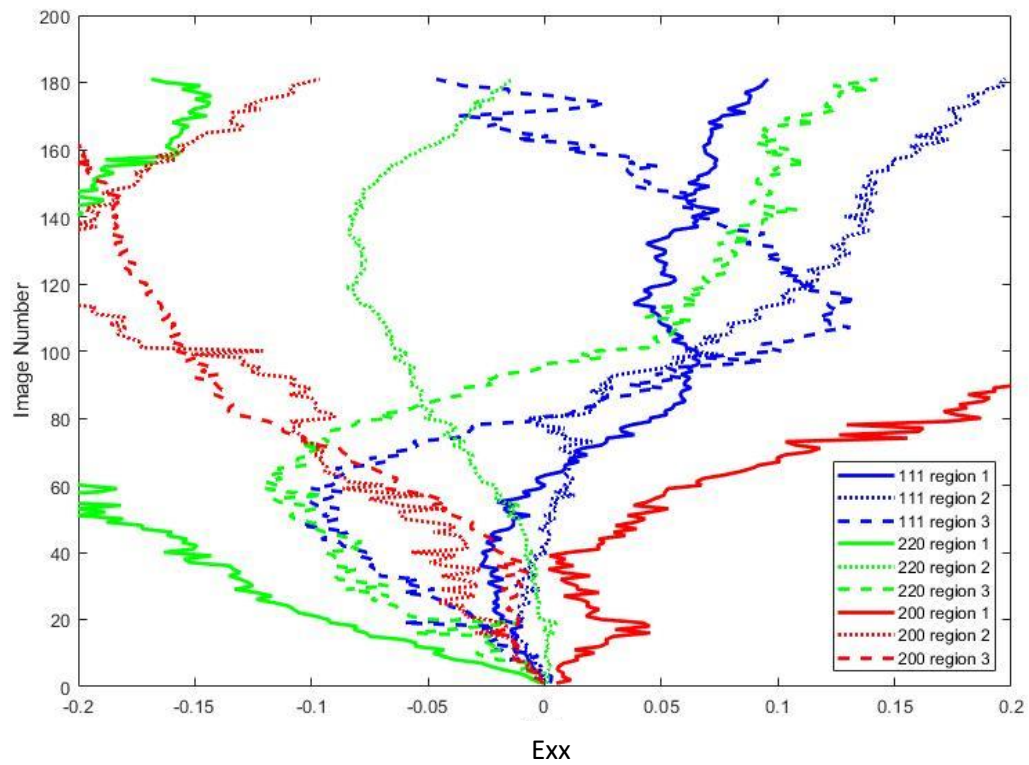
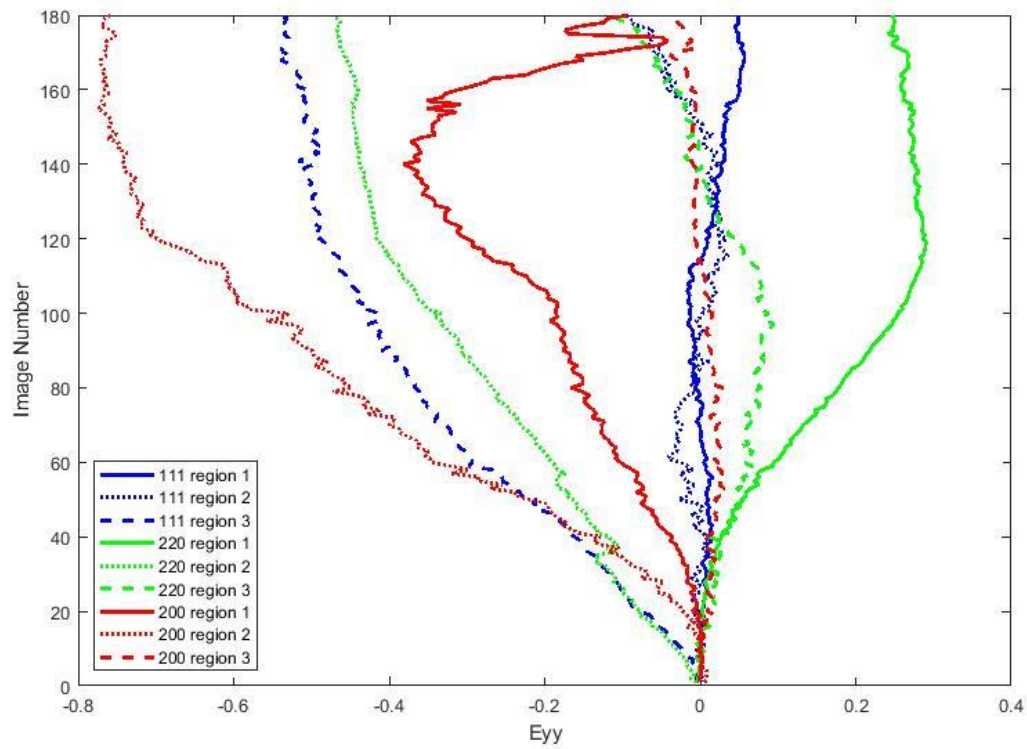


Figure 6.45: The SS316 Exx strain for regions with a high concentration of grains with the 111, 220 and 200 orientations from the start of the test to 3% strain, where (a) best fit scale and (b) is the relative scale.

(a)



(b)

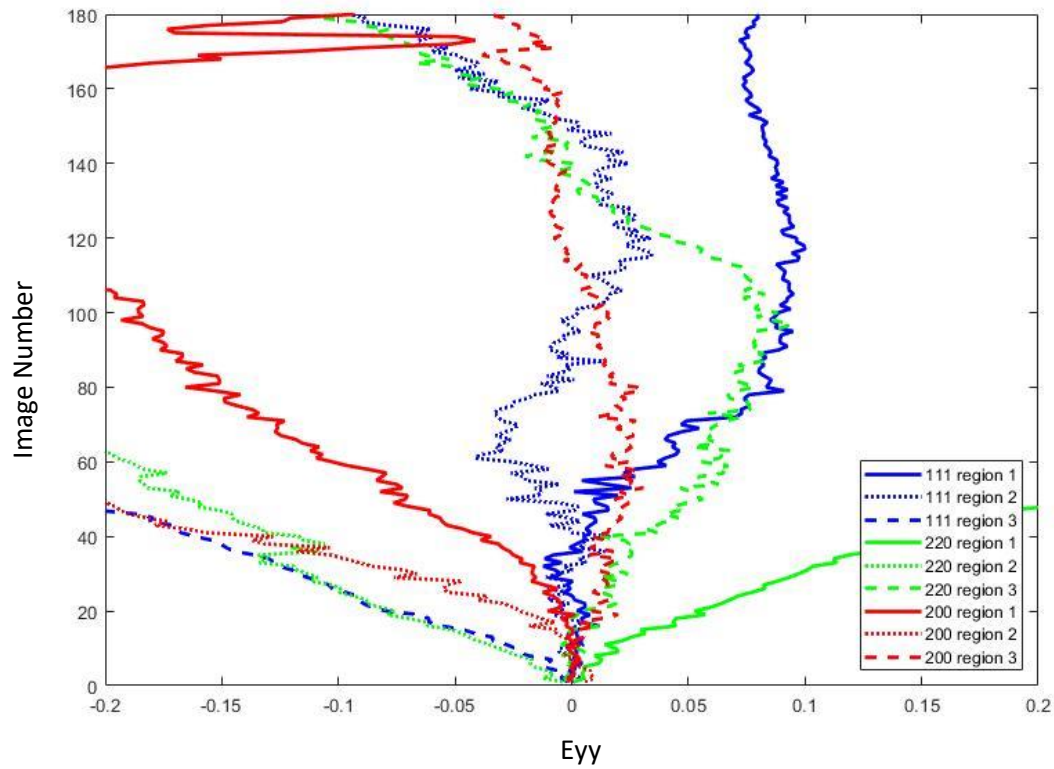


Figure 6.46: The SS316 Eyy strain for regions with a high concentration of grains with the 111, 220 and 200 orientations from the start of the test to 3% strain, where (a) best fit scale and (b) is the relative scale.

7.4.4.2. Regional strain plots for INVAR

The regions selected from the EBSD maps for the INVAR samples were chosen to include the largest concentration of grains with either the 111, 220 or 200 orientations. The segmented EBSD maps for the INVAR specimen for the 111, 220 and 200 orientations can be found in Figure 6.30, Figure 6.31 and Figure 6.32 respectively. The regions chosen for each subset are shown in Table 6.5. The regions needed to be greater than 200 μm by 200 μm and as the INVAR grains are much smaller than those found in SS316 the regions spanned multiple grains with different orientations. Therefore, the regions were selected to contain the largest percentage of the grains of the given orientation.

Table 6.5: Regions selected from EBSD data for INVAR which contain the largest concentration of either 111, 220 or 200 orientation subsets.

Orientation	Region	X1	X2	Y1	Y2
111	1	529	729	972	1172
	2	999	1248	850	1113
	3	219	460	213	466
220	1	1642	1962	81	410
	2	425	736	518	809
	3	716	1009	3	303
200	1	1672	1995	404	742
	2	560	889	1745	1993
	3	291	527	3	345

Figure 6.47 shows the strain data progression in the loading direction (E_{xx}) for the INVAR tensile sample for the regions shown in Table 6.5. Figure 6.48 shows the strain data progression throughout loading in the perpendicular direction (E_{yy}) for the INVAR sample for the regions shown in Table 6.5.

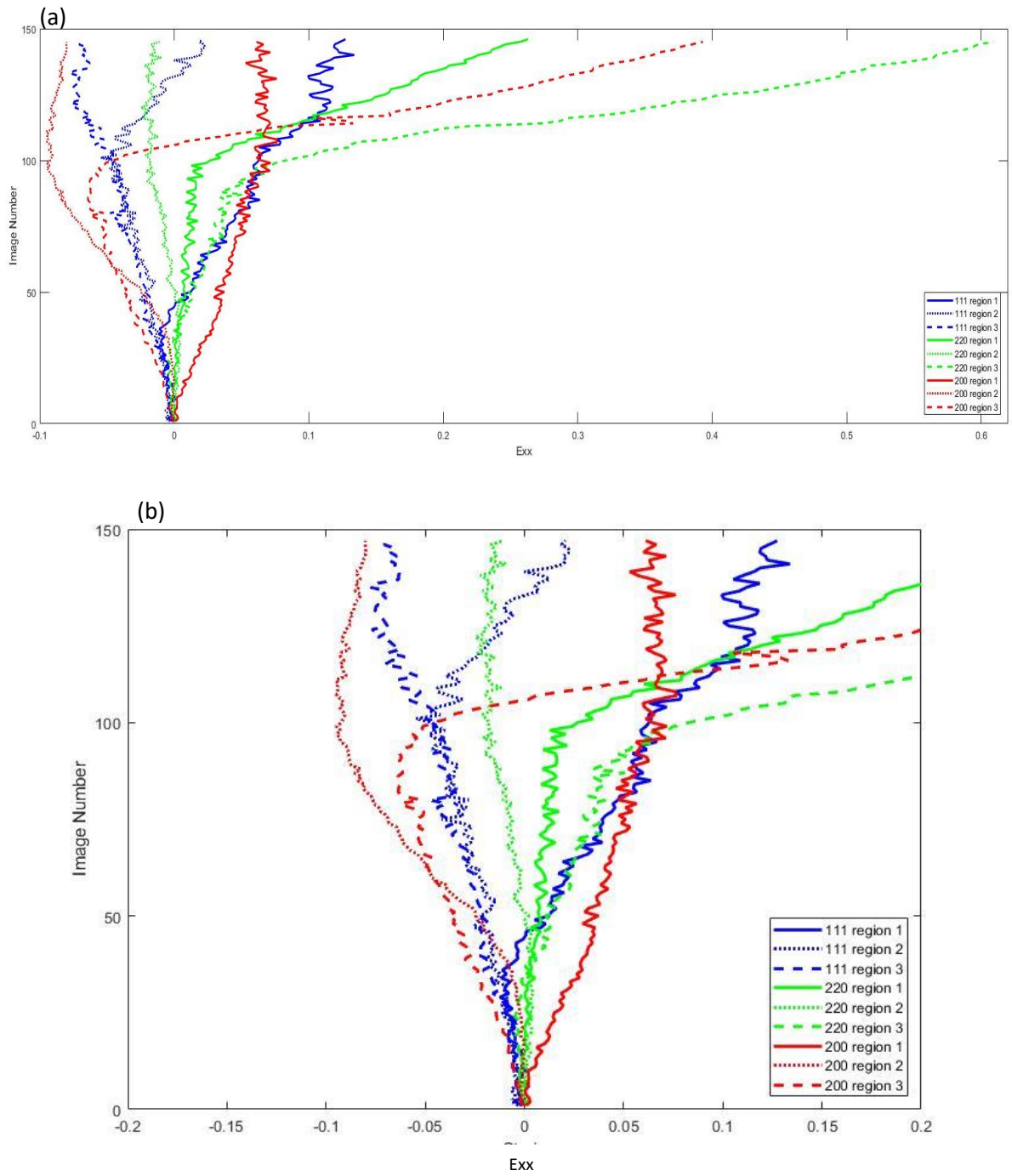


Figure 6.47: The INVAR E_{xx} strain for regions with a high concentration of grains with the 111, 220 and 200 orientations from the start of the test to 3% strain where (a) best fit scale and (b) is the relative scale.

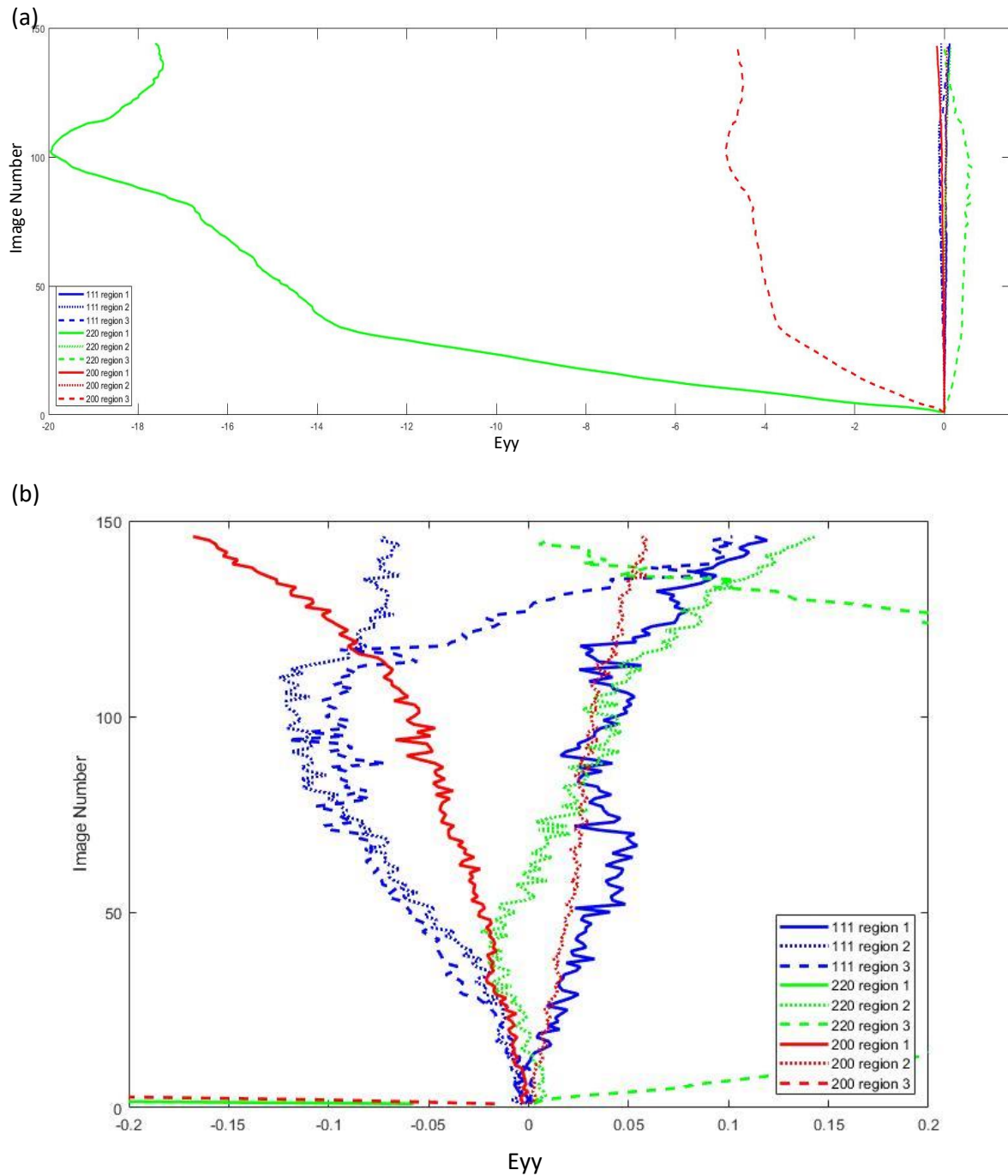


Figure 6.48: The INVAR E_{yy} strain for regions with a high concentration of grains with the 111, 220 and 200 orientations from the start of the test to 3% strain where (a) best fit scale and (b) is the relative scale.

7.4.4.3. Regional strain plots for pure nickel

The segmented EBSD maps used to locate regions with the highest concentrations of grains within 7.5 degrees of the 111, 220 and 200 orientations for the pure nickel specimen can be found in Figure 6.33, Figure 6.34 and Figure 6.35 respectively. The regions selected from the EBSD data, which contained the highest concentrations of grains with the 111, 220 and 200 orientations for the pure nickel sample are shown in Table 6.6. Like the Invar samples, the grains were significantly smaller

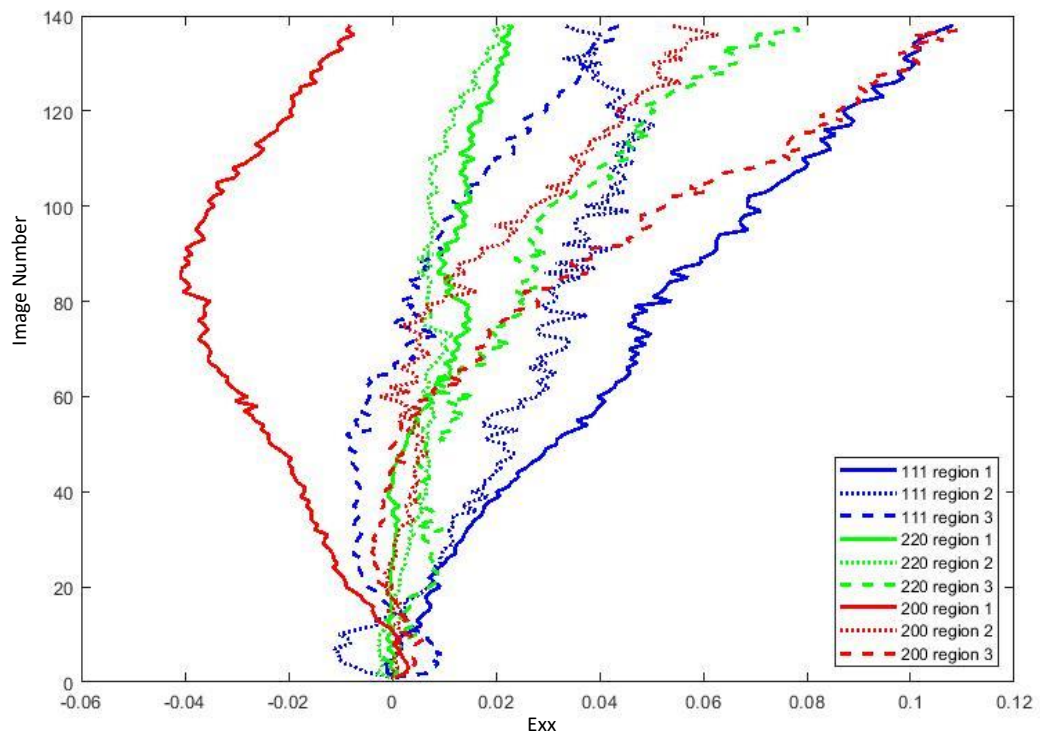
than the SS316 and therefore these selected regions contained grains without the desired orientation.

Table 6.6: Regions selected from EBSD data for pure nickel which contain the largest concentration of either 111, 220 or 200 orientation subsets.

Orientation	Region	X1	X2	Y1	Y2
111	1	331	531	972	1172
	2	1775	1975	583	783
	3	1100	1300	1700	1900
220	1	949	1149	1717	1917
	2	653	853	1703	1903
	3	1541	1741	977	1177
200	1	811	1011	1280	1480
	2	51	251	1263	1463
	3	1739	1972	1640	1896

Figure 6.49 (a) and (b) shows the strain data progression in the loading direction (E_{xx}) for the pure nickel tensile specimen for the regions shown in Table 6.6, where (a) shows the most suitable length scale for the data points and (b) is a larger length scale to show a direct comparison between this specimen and the INVAR and SS316 specimens. Figure 6.50 (a) and (b) shows the perpendicular direction strain data (E_{yy}) for the pure nickel sample for the regions shown in Table 6.6.

(a)



(b)

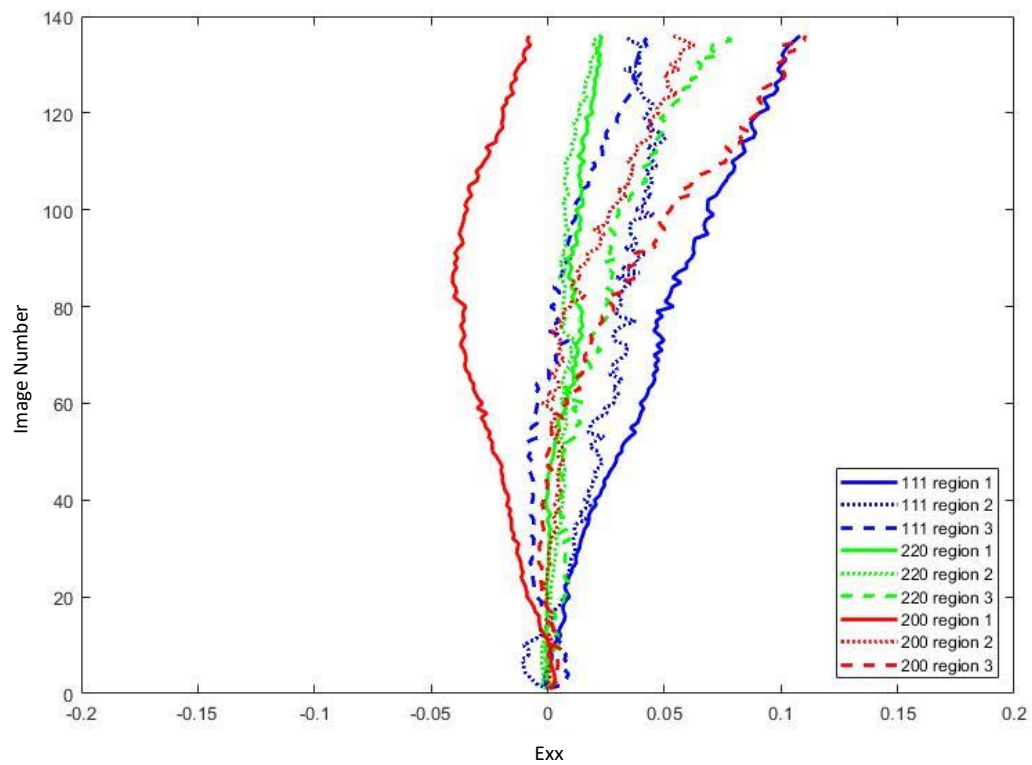
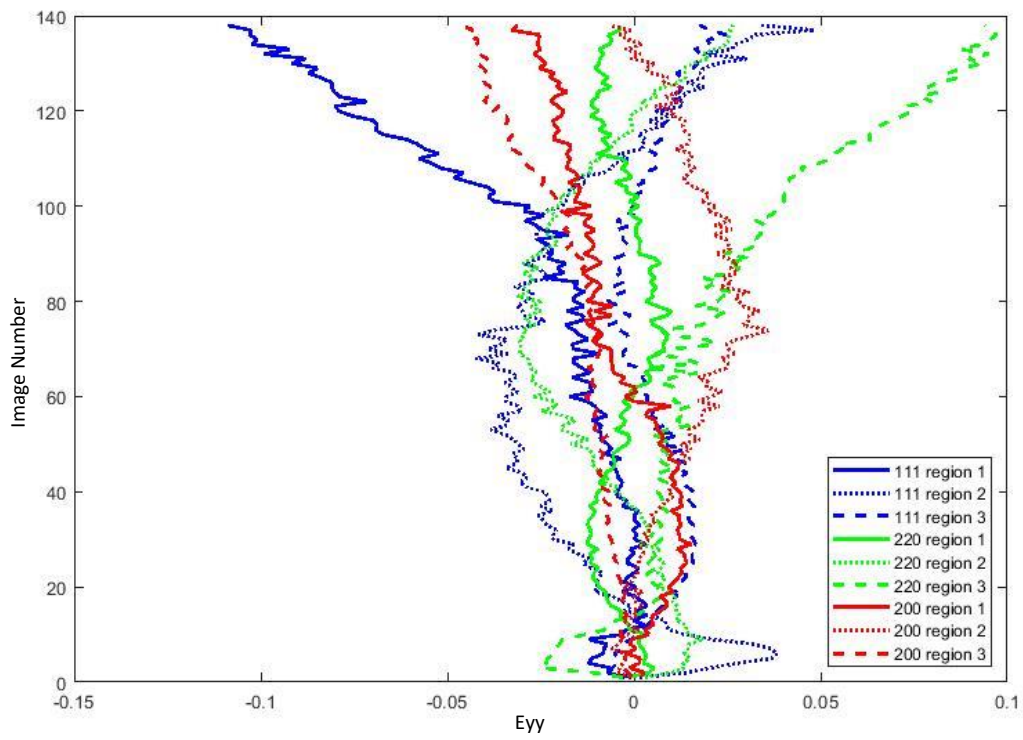


Figure 6.49: The pure nickel Exx strain plot for regions with a high concentration of grains with the 111, 220 and 200 orientations from the start of the test to 3% strain where (a) best fit scale and (b) is the relative scale.

(a)



(b)

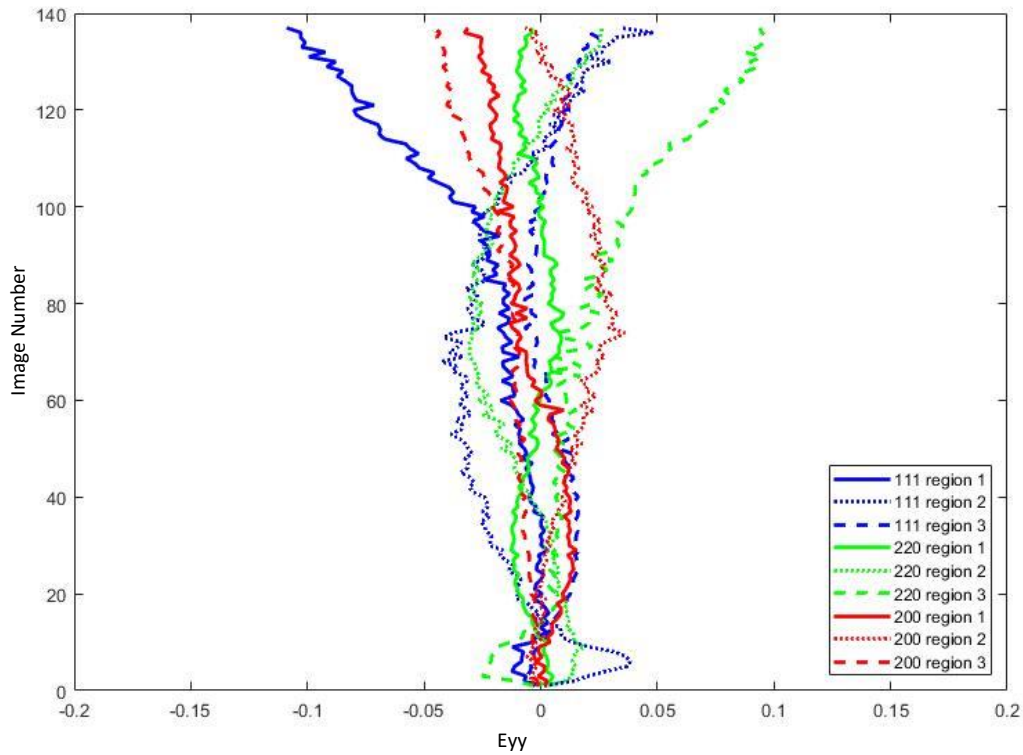


Figure 6.50: The pure nickel Eyy strain plot for regions with a high concentration of grains with the 111, 220 and 200 orientations from the start of the test to 3% strain.

6.4. Discussion

The HR-DIC tests were performed on SS316, INVAR and pure nickel samples to highlight the importance of SFE on deformation mechanics. These tests were successful in producing strain data for samples subjected to a tensile load. The results of the DIC analysis were then superimposed on top of EBSD maps to allow for the strain data to be segmented by the individual grains and divided into subsets based on their crystallographic orientations. The DIC images were chosen when the samples reached 3% strain to allow comparisons to be drawn between these results and those of the neutron diffraction tests. This was achieved by plotting the strain by image number curves for each test and finding the image number when the strain reached 3%.

To align the spatial HR-DIC data to the EBSD map, the hardness indents were used to locate the EBSD map location from the tensile test specimen. The SS316 grains were large enough that they could be clearly seen in the etched tensile specimen, this acted as an indicator of how accurate the alignment between the EBSD map and strain data would be. It was found that by using the coordinates of the hardness indents to place the SS316 EBSD map onto the HR-DIC data that the grain boundaries aligned well. Therefore, it was assumed that the same could be applied for INVAR and pure nickel, which had smaller grains that were not visible on the etched surface.

For the strain data, the Exx direction shows the strain in the loading direction and the Eyy value is the strain perpendicular to the loading direction. The Exx strains are typically much larger than the Eyy which is to be expected and the perpendicular strain is likely to show a small amount of contraction, therefore, the maximum principal strain is dominated by the Exx direction. The complete strain maps calculated from the raw images along with the segmented area plots for SS316 are shown in Figure 6.16, Figure 6.17 and Figure 6.18 for the Max Principal Strain, Exx and Eyy respectively. In Figure 6.16 (b) there is a large range in strain values throughout the surface, where there are distinct regions with high strain concentrations. The map is predominately red, indicating positive strain, however, there are some regions where negative strain values are recorded. Figure 6.17 (b) shows the Exx strain map, this has a very similar pattern with strain concentrations in the same regions. The Eyy direction strain map in Figure 6.18 (b) shows regions to be predominately negative values of strain, indicating contraction in this direction, however, there are focused regions which have positive strain values. The regions of strain concentration are of a comparative size to the grain size within the material, showing that at the grain level there is a wide range of strain values and therefore anisotropic deformation is present.

The maximum nominal strain map, Exx strain map and Eyy strain map collected for INVAR, which was cropped using a superimposed on the EBSD map of the material (

Figure 6.13), are shown in Figure 6.20, Figure 6.21, and Figure 6.22 respectively. Figure 6.20 presents nominal strain which contains a variation in strain values throughout the sample. There are stripes of strain which are prevalent in the DIC strain which is all positive but there are some regions of near 0 strain. Figure 6.21 shows the E_{xx} values in the loading direction, all values are positive and vary between 0 and 0.15. Figure 6.22 shows the E_{yy} strain map, this gives the strain values perpendicular to the loading direction, here all values of strain are negative and mostly vary between -0.1 and 0, however, there are some regions with values up to -0.15. This variation in the strain throughout the surface is similar to the SS316 sample, but the variation is less pronounced. The strain 'bands' appear to align with the grain boundaries in some areas indicating that the grain structure is causing this variation in the strain values.

The nominal, E_{xx} and E_{yy} strain maps for the pure nickel specimen can be found in Figure 6.24, Figure 6.25 and Figure 6.26 respectively. Figure 6.24 (b) shows the nominal strain for the segmented pure nickel sample, where the values range between 0.01 and 0.04, this shows much less variation compared to the SS316 and INVAR samples. This same pattern can be found in the E_{xx} figure in Figure 6.25 (b). For the E_{yy} map in Figure 6.26 (b), the strain variation is between -0.025 and 0, but the majority of the area is around an average between these numbers. These maps do not show the regions of low and high strain concentration that are found in the SS316 and INVAR, indicating that pure nickel deforms uniformly throughout the material.

Using the DICE software to impose the EBSD data on-top of the DIC strain map allowed the strain data for the crystalline subsets 111, 220 and 200 to be shown in histogram plots. For all the histogram plots in section 6.3.4, each material for the E_{xx} , E_{yy} and nominal strains shows there to be the largest number of occurrences for the 220 orientation subset of grains. This is conclusive with the theory for FCC polycrystals, as the 220 subset has higher multiplicity than the 200 and the 111. This implies that the EBSD data has accurately segmented the DIC strain data into the orientations correctly.

Figure 6.36 shows the histogram plots of the loading direction (E_{xx}) strain values for the SS316 specimen in the 111, 220 and 200 orientation subsets. This shows three distinct curves for each subset, from this figure it can be seen that the 220 subset generally has higher values of strain. Figure 6.37 shows the strain values perpendicular to the loading direction, here the values are predominately negative, and the magnitude is less than in the loading direction. Figure 6.38 shows the histogram plot for the maximum principal strain values for SS316. The SS316 subsets show a tail

on the peaks, this could be caused by the larger grain sizes found in SS316 which leads to a greater variation in the orientation spreads of the grains. This may also be caused by the DIC strain analysis causing noise in the strain data.

Figure 6.39 shows the E_{xx} strain for INVAR, this shows positive values of strain for all subsets, there is a large amount of spread in each subset, however, the peaks span the same ranges as one another. Figure 6.40 is the E_{yy} strain for the subsets of grains, this shows a slightly higher peak for the 220-orientation subset of grains than for the other grain orientation subsets, however, the spread of the peaks are very similar to one another. Figure 6.41 shows the histogram plot for the maximum principal strain for INVAR where all three orientation subsets have a maximum value of 0.035. These histograms show that the INVAR sample has a similar amount of spread as seen in the SS316 specimen, however, the subsets show less deviation in the peak location.

Figure 6.42 shows the strain data for the pure nickel sample in the loading direction, segmented into the 111, 220 and 200 orientation subsets. All strain values are shown to be positive in this direction indicating only extension is occurring. The number of occurrences varies for each orientation subset, with 220 having the highest amount but the spread of the peaks is the same for all subsets. As the relative proportion is the only way of indicating a higher strain in a given orientation, it can be observed at 0.035 that the 111 subset has nearly the same number of counts as the 220 and as the 220 is meant to have nearly double, this could imply that the 111 may have more deformation. Figure 6.43 shows the strain data for pure nickel perpendicular to the loading direction. All values are negative in this direction, indicating only contraction in this direction. The proportional height of the subsets remains constant for each strain value, implying that deformation is occurring uniformly for each subset. Figure 6.44 is the histogram plot showing the results of the maximum principal strain for the pure nickel specimen. As with the E_{xx} and E_{yy} histogram plots, there is no difference in spread between the orientation subsets. However, the 111 is proportionally higher at 0.035, and the 200 subset is proportionally higher at 0.04. This implies a slight difference in deformation between the subsets.

The histogram plots only show the strain values for the 111, 220 and 200 orientation subsets at 3% strain regional plots were selected from the DIC data to investigate the progression of strain throughout the tensile test. The regions needed to be at least 200 μm by 200 μm to include vector arrows from the DIC analysis. As this is larger than the grain sizes for INVAR and pure nickel, these regions contained grains with various orientations but were carefully selected to include the highest proportion of the given orientation.

The strain progression throughout the *in situ* HR-DIC tensile tests for the SS316 specimens is presented in Figure 6.45 for the loading direction and Figure 6.46 for the perpendicular direction. Due to the large grain sizes found in the SS316 specimen, the regions chosen for the strain progression plots were within a single grain with the chosen orientation. This showed there to be some correlation between the regions for each subset early in the test, however, once plastic deformation had occurred there was a wide spread of values for the 3 regions for each orientation subset. As the regions are predominately enclosing a single grain the spread in values cannot be linked to the orientation variation due to the regions containing multiple grains with varying orientations, like the INVAR and pure nickel samples. However, by looking at the histogram plots in Figure 6.36 and Figure 6.37 there is a large variation in strain values for each subset, so the grains showing different strain progression should be a reasonable result.

The INVAR showed three regions to behave largely differently from the others, this is seen for the 220-orientation for region 1 and region 3 and the 200-orientation for region 3. These regions of grains were selected solely from the EBSD map by selecting regions with the highest concentration of either the 111, 220 or 200 orientations. However, when looking at where the EBSD map is placed within the DIC image (Figure 6.19) the region is on the edge of the sample. Therefore, the change in the size of the edge is affecting the values, this makes a greater impact in the y direction (Figure 6.48 (a)) but is also seen in the loading direction above image number 80, although earlier in the test this seems to have less impact in this direction. This can be seen as all regions for the 220 subsets are in good agreement with one another up to image number 50. Considering this, when looking at the results for the INVAR sample in the loading direction in Figure 6.47 (b), the 220 regions show to be in good agreement with one another up to an image number of 50, after this, they start to deviate. The 111 orientation regions are all in good agreement up to an image number of 30, after this region 1 begins to show an increase in its values of strain. However, regions 2 and 3 are in good agreement up to image 100. The 200 subset shows a slight relationship between regions 2 and 3 up to image number ~50 but then region 3 shows the impact of being at the edge of the specimen. It is harder to see patterns in the perpendicular direction from Figure 6.48 due to the outlying regions, however, regions 2 and 3 for 111-orientation are in good agreement up to image 100 similar to the x direction. Therefore, despite the regions containing grains with orientations different from the desired orientation, relationships between the regions can be seen in the early stages of the test.

The regional strain plots for the loading direction of the pure nickel sample can be found in Figure 6.49. The comparative plot in Figure 6.49 (b) shows the magnitude and variation in the grain orientation subsets are much less drastic than seen in both the INVAR and SS316 specimens. For the 111 orientation subset, regions 1 and 2 show to be in reasonable agreement up to image 40,

whereas region 3 shows a large amount of deviation from the start of the test. For the 220 orientation subset, all regions are in good agreement up to image number ~70, after this region 3 shows an increase in strain values, however, regions 1 and 2 remain closely aligned up to the end of the test. For the 200 orientation subset, regions 2 and 3 are in reasonable agreement up to image number 60, but then a change in gradient can be seen, however, the shape of the curves are similar after this point. Region 1 shows a similar shape curve throughout the test but has more negative values. Figure 6.50 shows the regional strain results perpendicular to the loading direction show less correlation between the subsets with no regions correlating beyond image 10. The range of strain values is significantly less than both the INVAR and SS316. By looking at the comparative scale plots in Figure 6.49 (b) and Figure 6.50 (b) the difference in deformation for each subset region does not show as much variation as with the other specimens. This correlates to the segmented histogram plots and the strain maps showing that the pure nickel sample shows significantly less variation and deforms more universally than the SS316 and INVAR. It should be considered that these regions did contain numerous grains with different orientations, however, they were selected to have a high concentration of grains with the desired orientation. This may have led to some averaging of the strain values, however, looking at the histogram plots at 3% in the E_{xx} (Figure 6.42) and E_{yy} (Figure 6.43) there is little variation between the orientation subsets so it can be assumed that these values would be closely related.

The effects of SFE can be seen in the results from the *in situ* HR-DIC tensile tests. The alloys with the high SFE (INVAR and SS316) showed a large variation in strain values throughout their surfaces, however, the pure nickel sample with a high SFE shows near-uniform deformation during loading. The congruence DIC data was divided into the orientation subsets recorded in the neutron diffraction tests, however, this technique is not limited to these orientations.

7. Overall Discussion and Conclusions

7.1. Introduction

The results and discussion sections in chapters 4, 5, and 6 focussed solely on the techniques discussed in the relevant chapters. However, as this thesis is looking to compare the effectiveness of using three different strain measurement techniques, the following section will produce a comprehensive discussion of the results of the neutron diffraction tensile tests, the EBSD metrics, and the HR-DIC tensile tests. This is followed by a summary of the key conclusions of this research project.

7.2. Discussion

As discussed in Chapter 1, determining the lifetime of the constituent components within nuclear power reactors is essential as premature failure can have disastrous consequences. By studying the deformation mechanics of the component's materials, a better estimate can be derived as to the duration these materials can withstand these harsh environments. Typically, polycrystalline materials are used within nuclear reactors due to having a homogenous, isotropic mechanical response to loading. However, at the microscale, polycrystalline materials experience anisotropic deformation during loading, caused by the mismatch in mechanical performance between the orientations of neighbouring grains. This can lead to stress concentrations which can lead to macroscopic failure. Neutron diffraction is a well-researched method of measuring elastic strain at the grain scale and can quantify anisotropic deformation by measuring the average lattice strain for subsets of grains based on their crystallographic orientations (9). However, this technique is expensive and has limited accessibility, therefore, using HR-DIC to measure grain-scale deformation could provide a cheaper and more accessible alternative. Thus, this project looks to compare the strain results collected from in situ neutron diffraction to the strain in situ HR-DIC.

The results of the strain measurement techniques were compared by their abilities to identify the effect of SFE on deformation behaviour. The three materials investigated in this project were pure nickel, INVAR and SS316 (a detailed discussion on why these materials were selected can be found in sections 4.1 and 4.2.1). Both INVAR and SS316 have low SFE whereas pure nickel has a high stacking fault energy. This greatly influences the mechanisms of deformation that occur during loading. This project looked to see if the differences in the deformation behaviour could be identified in the strain measurement techniques.

Historically, comparisons between neutron diffraction and HR-DIC has focused on comparing the behaviour of individual grains using HR-DIC to the statistical results of neutron diffraction. For

example, Polatidis et al. (145) compared the results of in situ HR-DIC to in situ neutron diffraction for a low SFE steel alloy and a medium SFE alloy. This study used HR-DIC to verify the formation of martensite in individual grains that were seen in the in situ neutron diffraction in the low SFE alloy, which were not seen in the medium SFE alloy highlighting the differences in deformation behaviour of the two materials. However, this project compares statistical in situ HR-DIC data to in situ neutron diffraction. This allows a larger number of grains to be sampled, however, the development of subgrain features, such as the formation of martensite, is not visible at this length scale.

Neutron diffraction is limited to recording only elastic lattice strain data for grain subsets with orientations which diffract according to Bragg's law; the most useful of these subsets in the FCC system is the 111, 220 and 200 orientations. Thus, to compare the neutron diffraction results to HR-DIC, the HR-DIC strain data was divided into the same grain orientation subsets using EBSD mapping on the ROI before tensile testing. HR-DIC measures both elastic and plastic strains but is unable to distinguish between them, whereas neutron diffraction measures only elastic strains, therefore, post-mortem EBSD metric analysis was performed on the neutron diffraction samples to provide insight into the plastic strain. Several EBSD metrics have been shown to correlate well with plastic deformation (21) and these metrics can be calculated from the EBSD conducted after neutron diffraction. In Section 5.4, the three EBSD metrics KAM, GAM and GOS were compared, this showed that due to the noise caused by the large grain sizes in the SS316 sample for both the GAM and GOS results, the best comparison metric was KAM because it wasn't reduced to a single point per grain. Therefore, only the results of the KAM EBSD metrics will be discussed in this section. Both the KAM data and HR-DIC strain data were segmented to be within 7.5 degrees of the given crystallographic orientation, as this was the accuracy of the ENGIN-X neutron diffractometer, and this allowed the three techniques to be compared. Finally, as the pure nickel sample has been suggested as a replacement material for SS316 in modelling deformation behaviour, the EPSC model was included to show the difficulties of modelling two materials with vastly different SFE using the same hardening model.

Work hardening occurs in low SFE alloys because cross-slip is not energetically favourable and, therefore, dislocation pileups can occur (30). Dislocation pile-ups cause dislocation concentrations, therefore misorientation analysis can be used to show the effect of work hardening. In the KAM maps for SS316 (Figure 5.7 (a)) and INVAR (Figure 5.8 (c)), there is a large increase in misorientation between the undeformed region and the deformed region. This may indicate that dislocation pileups have formed causing misorientation. The pure nickel sample (Figure 5.9 (c)) does not show this same increase, however, the material has a large amount of misorientation in the undeformed region, so it is hard to determine the effects of deformation on this alone. Additionally, the effect of cross-slip

can be seen in the HR-DIC strain maps for the loading direction of the pure nickel sample (Figure 6.25), here the strain is seen to be constant throughout the region, whereas for the SS316 specimen (Figure 6.17) and the INVAR specimen (Figure 6.21) there is a large variation in strain values throughout the surface. Furthermore, the effect of work hardening can be seen in the macro stress-strain curves collected through the neutron diffraction tests seen in Figure 4.9 for the SS316 and INVAR specimens because following yield there is an increase in the stress required to increase the strain values. However, in Figure 4.9 the pure nickel does not show the same increase and instead plateaus, this indicates work hardening has happened at a lesser extent or not occurred. This is conclusive with other high SFE materials due to cross-slip being favourable. For example, Karaman et al. (29) showed that with the addition of nitrogen to a stainless steel alloy, the SFE energy was increased and led to cross-slip occurring in this alloy. Another example, of the difference in deformation behaviour of materials with varying SFE is shown by Kang et al. (31) where the lattice strain was measured using in situ neutron diffraction for the 111 and 222 orientation subsets are compared for two samples of Fe–Mn–C TWIP alloy, one with 0 wt.% and one with 2 wt.% Al (Figure 2.4 (b)). Here, it is shown that there is a greater difference in the lattice strain behaviour of the orientation subsets for the low SFE alloy (0 wt.%) than the higher SFE (2 wt.%). This is also observed in this thesis when comparing the results of lattice strain results from in situ neutron diffraction tests for the high SFE pure nickel sample in Figure 4.12 and the low SFE SS316 in Figure 4.10.

To directly compare the results of the in situ neutron diffraction, in situ HR-DIC and the KAM metric, the key figures from Chapters 4, 5 and 6 have been reproduced in Figure 7.1, Figure 7.2 and Figure 7.3 for the SS316, pure nickel and INVAR specimens respectively. The in situ neutron diffraction lattice strain data for the 111-, 220- and 200-orientation subsets to be distinctly different to one another, this is shown in Figure 7.1 (a). Specifically, the 220-orientation subset showed the onset of plastic deformation due to the lack of increase in strain with increasing stress at the end of the test. The 111-orientation subset showed elastic deformation throughout the test and the 200-orientation subset showed an increase in elastic strain towards the end of the test. This type of behaviour is comparable to similar studied of FCC materials (9,72). The *in situ* HR-DIC results showed the SS316 sample to have three distinct peaks for the 111, 220 and 200 orientation subsets in both the transverse and longitudinal direction, these results are presented again in Figure 7.1 (c) and (d) respectively. These results indicate that the 220 subset shows the largest amount of strain, this correlates with the neutron diffraction presented in Figure 7.1 (a) where the onset of plastic deformation is observed in the 220 subset by the halt in increasing elastic strain. This shows that the combination of HR-DIC and EBSD was able to accurately segment the strain data for the given orientations and yield results conclusive with *in situ* neutron diffraction tensile tests. However, as

DIC cannot distinguish between plastic and elastic deformation it is impossible to determine whether the grain subsets are deforming elastically or plastically. The KAM EBSD metric data for SS316 also verified the onset of plastic deformation observed in the neutron diffraction tests. The histogram plot showing the difference between KAM values for the deformed and undeformed regions is shown again in Figure 7.1 (b). This figure shows that the largest increase in KAM values is within the 220-orientation subset for the SS316 specimen. This indicates the largest accumulation of plastic strain is within this subset of grains, which reflects the results of the neutron diffraction tests where the 220-orientation subset shows the onset of plastic deformation.

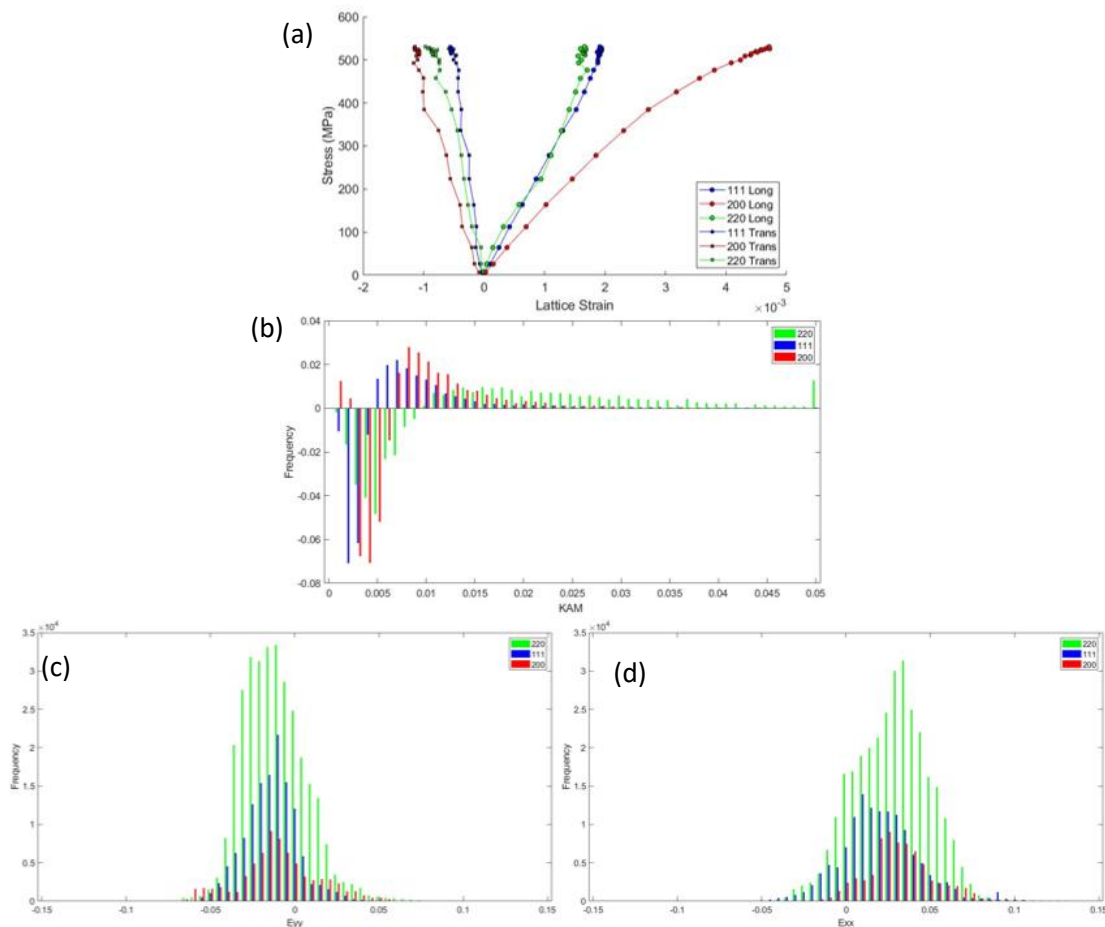


Figure 7.1: Strain data results collected for SS316 for the 111, 220 and 200 crystallographic orientation subsets. (a) Lattice strain data collected through *in situ* neutron diffraction for the longitudinal and transverse direction, (b) Difference in KAM values between the deformed and undeformed regions of the SS316 specimen, (c) and (d) the transverse and longitudinal (respectively) *in situ* HR-DIC strain data.

The lattice strain data recorded via *in situ* neutron diffraction for the pure nickel specimen are shown in Figure 7.2 (a). Like the SS316 sample (shown in Figure 7.1), this also shows the onset of plastic deformation in the 220-orientation subset and the elastic deformation to continue throughout loading in the 111-orientation. However, for the 200-orientation subset, the gradient remained constant throughout the loading process. This indicates less variation in the deformation

behaviour for the subsets of the nickel specimen. This same effect was seen for the nickel specimen *in situ* HR-DIC results, presented for reference again in this chapter in Figure 7.2 (c) for the transverse direction and Figure 7.2 (d) for the loading direction. Here, there is very little variation in the strain values for the subsets of grains, in contrast to the variation seen in the SS316 specimen (Figure 7.1). Additionally, the KAM histogram results, comparing the data between the deformed and undeformed regions (Figure 7.2 (b)), show the 220-orientation subset to have the highest values of KAM, indicating plastic deformation has occurred in this subset, this verifies the results for the neutron diffraction tests.

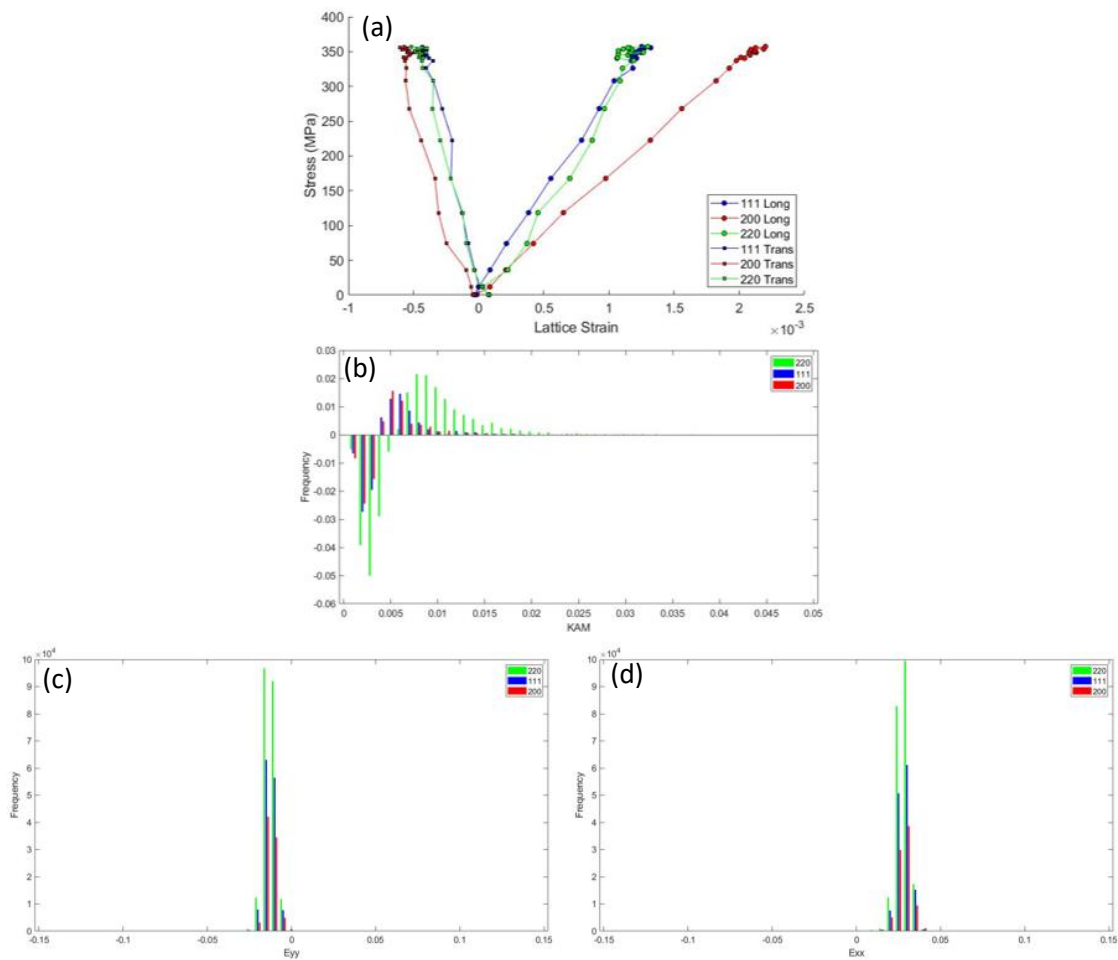


Figure 7.2: Strain data results collected for pure nickel for the 111, 220 and 200 crystallographic orientation subsets. (a) Lattice strain data collected through *in situ* neutron diffraction for the longitudinal and transverse direction, (b) Difference in KAM values between the deformed and undeformed regions of the pure nickel specimen, (c) and (d) the transverse and longitudinal (respectively) *in situ* HR-DIC strain data.

The neutron results for the INVAR (Figure 7.3 (a)) showed the material to behave somewhat in between the SS316 and the pure nickel sample. Here, the 220-orientation subset shows the onset of plastic deformation, and the 111-orientation subset shows elastic deformation, however, the 200-

orientation subset shows the same increase in elasticity but to a lesser degree than the SS316 sample. The *in situ* HR-DIC results for the INVAR specimen are shown in Figure 7.3 (c) and (d) for the transverse and longitudinal directions. These results show there is a larger spread in the strain values compared to the nickel sample, but less than compared to the SS316 sample. However, in this case, it is not possible to detect trends in the plasticity behaviour in the subsets. This may be expected considering the deviation from linear behaviour in the neutron results is less for invar compared to SS316, essentially there is less variation to detect. The KAM histogram plot showing the difference between the deformed and undeformed regions in Figure 7.3 (b) shows the 220-orientation subset to have the largest values of misorientation. The difference between the subsets is not as prominent as in the SS316 and pure nickel sample, it does still indicate that plastic deformation may be occurring in the 220-orientation subset. It should also be considered that the KAM values are an order of magnitude greater than seen in the SS316 and nickel samples and are likely oversaturated due to the undeformed material being well-annealed. These results show that when considering a replacement material to model a complex alloy, the influence of SFE on the deformation behaviour at the microscale should be considered, hence, despite there being significant differences between the behaviour of INVAR and SS316, INVAR would make a more suitable alternative to SS316 than the pure nickel specimen.

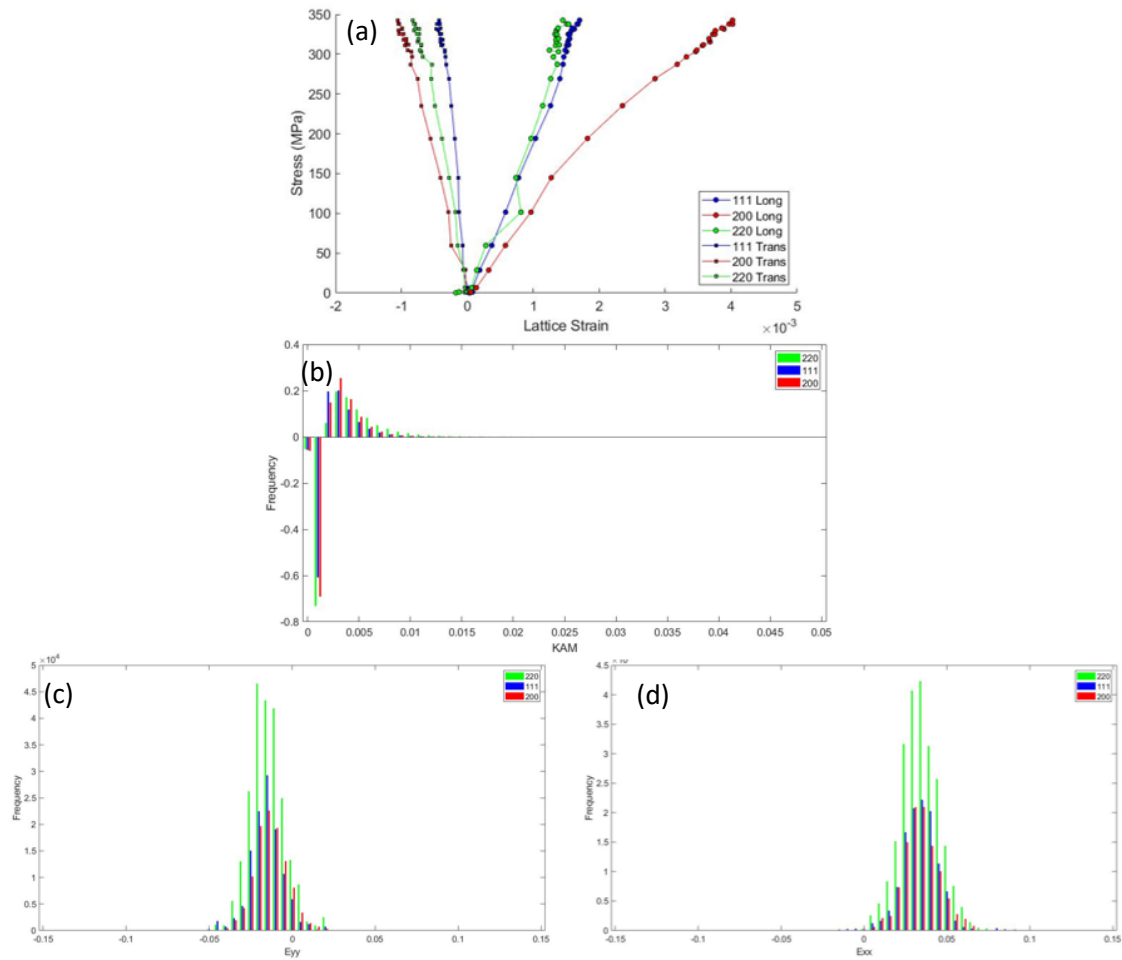


Figure 7.3: Strain data results collected for INVAR for the 111, 220 and 200 crystallographic orientation subsets. (a) Lattice strain data collected through in situ neutron diffraction for the longitudinal and transverse direction, (b) Difference in KAM values between the deformed and undeformed regions of the INVAR specimen, (c) and (d) the transverse and longitudinal (respectively) in situ HR-DIC strain data.

The results of the EPSC model showed the INVAR (Figure 4.17) and SS316 (Figure 4.16) specimens to have a good fit in the macro stress-strain curves, whereas the nickel specimen struggled to predict the deformation behaviour (Figure 4.17). This was because the model used the Voce hardening model which predicts work hardening to occur after yield, however as seen in the neutron diffraction results in Figure 4.9, pure nickel exhibits little work hardening due to being a material with a high SFE. Therefore, modelling the deformation of pure nickel is not a suitable proxy for modelling SS316 despite its apparent similarities. Instead, INVAR provides a better alternative as it is simplistic in chemical composition yet deforms similarly to SS316 as it also has a low SFE.

The correlation between the Taylor factor of grain subsets and the onset of plastic strain recorded by neutron diffraction was discussed in section 4.7. As neutron diffraction looks exclusively at elastic strain and the plastic strain is assumed due to the halt in increasing elastic strain, it seems to align better with the Taylor factor values of the orientation subsets. However, HR-DIC cannot distinguish

between elastic and plastic strains. Das et al. (15) found that Schmid factors were useful in predicting slip and phase transformations within grains. Although direct comparisons were not drawn between the HR-DIC results for the grain subsets and the Schmid factors it may be likely that HR-DIC aligns better with Schmid factor as it measures both plastic and elastic strains without distinguishing between them. By comparing the Schmid factors of the SS316 grain subsets (Figure 5.16), where the highest Schmid factors are found in the 200 and 220 subsets, to the strain in the loading direction for the SS316 by the HR-DIC (Figure 7.1 (d)), where the 220 and 200 subsets have peaks at higher strain values than the 111 subset, this may imply a correlation. Hence, Schmid factor could potentially be better suited in predicting HR-DIC strain data than the Taylor factor.

Due to limitations in the equipment and software used in this project, it was impossible to produce strain data during loading for the crystallographic orientation subsets similar to the graphs produced from the neutron diffraction analysis (shown in Figure 4.10, Figure 4.11, and Figure 4.12). The micro tensile tester used for the *in situ* neutron diffraction tensile tests was somewhat temperamental and inaccurately measured the stress throughout loading, making this data unusable. In future work, either an external stress measurement technique should be used to mitigate this or the use of a full-size tensile tester and therefore, a larger specimen size. Additionally, the DICE software was originally designed for use on a single image at a time, this was due to the previous image acquisition method being with an SEM, as this meant only a few images could be taken throughout loading. However, by using the high-resolution camera and telecentric lens, images can be taken every second, providing more stress states during loading. For example, Table 6.3 shows the number of images analysed in this project for each sample (as these were the images where the specimens reached 3% strain) with the average being around 150, whereas over 500 images were taken for each specimen during the entirety of the tensile tests. Due to the vast amount of data collected through HR-DIC and the accompanying EBSD analysis, it is possible to produce progression strain maps similar to those of neutron diffraction, but to accommodate this, a complete rewrite would be required of the DICE software to expand the number of images it can handle. Nevertheless, a technique was devised using the EBSD map coordinates, the calibration file used to align the EBSD map and the strain map and the DaVis software to produce progression strain data for regions enclosing grains with 111, 220 and 200- orientations. It was found that interrogation windows in the HR-DIC data analysis were too large to select a singular grain in the INVAR and pure nickel samples so a region with a high concentration of either the 111, 220 or 200 crystallographic orientations was selected. For the low SFE material, SS316 (Figure 6.45 and Figure 6.46) and INVAR (Figure 6.47 and Figure 6.48), there is a large spread in the strain values between the regions for each orientation, even considering the outliers in the INVAR specimen. For the high SFE pure nickel specimen, there is

much less variation in the strain values, between the regions and between the orientations themselves. This does draw some correlations to the neutron diffraction lattice strain results, shown in Figure 4.12, for the neutron diffraction tests where less variation was seen in the strain behaviour compared to both SS316 (Figure 4.10) and INVAR (Figure 4.11). Additionally, in the histogram plot for the nickel specimen results in situ HR-DIC tensile test at 3% strain (Figure 6.42 and Figure 6.43), there is little spread in values, whereas INVAR (Figure 6.39 and Figure 6.40) shows some spread in strain values and SS316 (Figure 6.36 and Figure 6.37) shows a large amount of spread.

The results show that the HR-DIC and neutron diffraction results were conclusive in their ability to predict the influence of SFE on deformation. In both the neutron diffraction and HR-DIC analysis it could be seen that the low SFE materials behaved more similarly to one another than to pure nickel specimens with a high SFE. This verification between the two techniques shows the potential of using congregate HR-DIC data as an alternative to neutron diffraction. However, the HR-DIC technique still requires further tuning to produce results to be used as an alternative to neutron diffraction, with a complete rewrite of the DICE software to enable multiple images to be run at once. Furthermore, due to its inability to separate elastic and plastic strains, HR-DIC will not act as a complete replacement for neutron diffraction studies, but these results do show the potential capabilities of aggregate HR-DIC strain measurements at the grain scale. Therefore, using multiple strain measurement techniques allows for a clearer understanding of the deformation behaviour as all techniques have strengths and weaknesses.

7.3. Conclusions

This project has shown the potential capabilities of using *in situ* HR-DIC tensile tests to obtain congregate strain data, by studying the effect of SFE on the deformation behaviour of SS316, INVAR and pure nickel. To corroborate the strain data from HR-DIC, the results were compared to data collected via *in situ* neutron diffraction tensile tests and post-mortem EBSD analysis. The key conclusions drawn from this work are as follows:

- The *in situ* neutron diffraction tensile tests yielded lattice strain data for subsets of grains, which were within 7.5 degrees of 111, 220 and 200 orientations. All three materials showed the onset of plastic deformation in the 220-orientated subset of grains. However, the low SFE metals, SS316 and INVAR showed the largest variation in lattice strain response of the grain subsets compared to the high SFE, pure nickel specimen. Additionally, load sharing was observed in both SS316 and INVAR, where the 200-orientation subset showed an increase in elastic behaviour once plastic deformation occurred. This effect was not seen in the pure nickel sample as the strain continued to increase linearly with increasing stress.

- The EPSC model was in reasonable agreement with the experimental neutron diffraction data for the SS316 and INVAR specimens. However, due to the lack of work hardening in the pure nickel specimen, it struggled to fit the macro-stress strain curve. This resulted in lattice strain data predictions that did not accurately reflect the overall shape of the experimental data.
- Post-mortem EBSD analysis was performed on the neutron specimens to verify the onset of plastic deformation. To study this, EBSD metrics were used to measure the misorientations within the specimens. It was found that the large grain size of the SS316 specimen resulted in noisy data for the GAM and GOS metrics, therefore, KAM provided the most accurate comparison between the three materials within this project. The KAM results showed the largest accumulation of misorientation to be within the 220-orientation subset for all materials, this indicates plastic deformation had occurred within this subset before the 111 and 200 subsets.
- The *in situ* HR-DIC tensile test results showed that the 220-orientation subset in the SS316 specimen has the highest strain values compared to the other orientation subsets. This corroborated the results of the neutron diffraction tests and the post-mortem EBSD metric analysis. Moreover, the HR-DIC results showed a spread in the strain values for all orientation subsets in both the SS316 and INVAR specimens, whereas the nickel specimen did not show the same spread in strain values. This was conclusive with the neutron diffraction lattice strain data which showed a greater variation in strain response between the orientation subsets within the low SFE materials compared to the pure nickel sample.

Further tuning of the HR-DIC method would be required for this technique to produce comparative strain data to that collected through *in situ* neutron diffraction tensile tests. Although, it should be noted that the HR-DIC strain measurement technique cannot fully replace neutron diffraction as HR-DIC is unable to distinguish between elastic and plastic strains. But using neutron diffraction alone cannot give plastic strain values, and instead only indicates the onset of plastic deformation. Therefore, combining the neutron diffraction data with post-mortem EBSD analysis provided more insight into plastic deformation. This highlights the importance of using multiple strain measurement techniques for material characterisation to produce an in-depth evaluation of a material's deformation behaviour as all techniques yield some limitations.

7.4. Limitations Imposed on this Work

During the completion of this project, the COVID-19 pandemic and subsequent lab closures restricted the number of experiments that could be completed. This ultimately resulted in being

unable to investigate the Hall-Petch effect, in addition to the SFE, as had been planned. To mitigate the impact on the overall project, the EPSC model was used on completed neutron diffraction experiments to continue working during this time. This provided an additional method of verification for the HR-DIC tests.

7.5. Future work

This project has shown the potential for HR-DIC as an aggregate strain measurement, and as this method of strain measurement yields a large amount of data, there is further analysis in which work could be performed to extract more insights. This section will discuss potential ways in which the work in this project can be expanded and developed further.

- Additional modelling such as using the CPFEM models could be used to highlight the difficulty in modelling two materials with vastly different SFEs using the same model parameters.
- To accurately record the SFE values for each material, TEM analysis should be performed on the specimens. Additionally, this would allow a comparative observation between the formation partial dislocation and stacking faults generation between materials with high and low SFEs.
- The post-mortem neutron diffraction data could be further analysed by using the MTEX Toolbox to calculate the GND values in the deformed and undeformed regions. These results could then be compared directly to the KAM values as well as the implications for the neutron diffraction tests.
- Verify DIC using an independent material, such as using a known phenomenon like the Hall-Petch effect. This would allow for a method of verifying the technique further with an additional, independently well-established phenomenon.
- To distinguish between the elastic and plastic deformation in the HR-DIC tests, post-mortem EBSD analysis could be performed on the same region as the initial EBSD map. This could be used to measure the changes in dislocation concentrations.
- Further analysis of the DIC images could be performed to access strain data throughout loading for the selected orientation subsets.
- To better understand the impact grain size had in the ability to compare the materials and the strain measurement techniques, the tensile tests should be performed again on three materials of similar grain sizes.

8. References

1. Mamun AA. Origin of creep-fatigue back stress and its effect on deformation and damage. The Open University; 2016.
2. Withers PJ. Residual stress and its role in failure. *Reports Prog Phys*. 2007;70(12):2211–64.
3. Chen B, Flewitt PEJ, Cocks ACF, Smith DJ. A review of the changes of internal state related to high temperature creep of polycrystalline metals and alloys. Vol. 60, *International Materials Reviews*. 2015. p. 1–29.
4. Moturu SR. Characterization of Residual Stress and Plastic Strain in Austenitic Stainless Steel 316L(N) Weldments. The Open University; 2015.
5. Ojima M, Adachi Y, Suzuki S, Tomota Y. Stress partitioning behavior in an fcc alloy evaluated by the in situ/ex situ EBSD-Wilkinson method. *Acta Mater*. 2011;59(10):4177–85.
6. Petkov MP, Chevalier M, Dean D, Cocks ACF. Creep-fatigue interactions in a polycrystalline structural material under typical high-temperature power plant operating conditions.
7. Wang YD, Tian H, Stoica AD, Wang XL, Liaw PK, Richardson JW. The development of grain-orientation-dependent residual stress in a cyclically deformed alloy. *Nat Mater*. 2003;
8. Schajer GS. *Practical Residual Stress Measurement Methods*. 1st ed. John Wiley & Sons, Incorporated; 2013.
9. Daymond MR, Bouchard PJ. Elastoplastic deformation of 316 stainless steel under tensile loading at elevated temperatures. *Metall Mater Trans A*. 2006 Jun;37(6):1863–73.
10. Clausen B, Lorentzen T, Leffers T. Self-consistent modelling of the plastic deformation of F.C.C. polycrystals and its implications for diffraction measurements of internal stresses. *Acta Mater*. 1998;46(9):3087–98.
11. Hu J, Cocks ACF. A multi-scale self-consistent model describing the lattice deformation in austenitic stainless steels. *Int J Solids Struct*. 2016 Jan 1;78–79:21–37.
12. Clausen B. Characterisation of polycrystal deformation by numerical modelling and neutron diffraction measurements. *Riso-Reports-Riso R*. 1997;985(September):1–86.
13. Neil CJ, Wollmershauser JA, Clausen B, Tomé CN, Agnew SR. Modeling lattice strain evolution at finite strains and experimental verification for copper and stainless steel using in situ neutron diffraction. *Int J Plast*. 2010;26(12):1772–91.
14. Forsey AN, Das YB, Simm TH, Clarke D, Boswell J, Gungor S, et al. Mechanical property heterogeneity in additively manufactured nickel superalloy. *Mater Sci Eng A*. 2018;712:681–4.
15. Das YB, Forsey AN, Simm TH, Perkins KM, Fitzpatrick ME, Gungor S, et al. In situ observation of strain and phase transformation in plastically deformed 301 austenitic stainless steel. *Mater Des*. 2016;112:107–16.
16. Jiang J, Zhang T, Dunne FPE, Britton T Ben. Deformation compatibility in a single crystalline Ni superalloy. *Proc R Soc A Math Phys Eng Sci*. 2016 Jan 1;472(2185).
17. Lim H, Carroll JD, Battaile CC, Buchheit TE, Boyce BL, Weinberger CR. Grain-scale experimental validation of crystal plasticity finite element simulations of tantalum oligocrystals. *Int J Plast*. 2014;60:1–18.
18. Guery A, Hild F, Latourte F, Roux S. Slip activities in polycrystals determined by coupling DIC

- measurements with crystal plasticity calculations. *Int J Plast.* 2016;81:249–66.
19. Borovikov V, Mendeleev MI, King AH, Lesar R. Effect of stacking fault energy on mechanism of plastic deformation in nanotwinned FCC metals. *Model Simul Mater Sci Eng.* 2015;23(5).
 20. Orozco-Caballero A, Lunt D, Robson JD, Quinta da Fonseca J, Ao J, Da Fonseca Q, et al. How magnesium accommodates local deformation incompatibility: A high-resolution digital image correlation study. *Acta Mater.* 2017 Jul;133:367–79.
 21. Harte A, Atkinson M, Preuss M, Quinta da Fonseca J. A statistical study of the relationship between plastic strain and lattice misorientation on the surface of a deformed Ni-based superalloy. *Acta Mater.* 2020 Aug 15;195:555–70.
 22. Guan Y, Chen B, Zou J, Britton T Ben, Jiang J, Dunne FPE. Crystal plasticity modelling and HR-DIC measurement of slip activation and strain localization in single and oligo-crystal Ni alloys under fatigue. *Int J Plast.* 2017 Jan 1;88:70–88.
 23. Friedrich W, Knipping P, Laue M. In *Sitzungsberichte der Math. Phys. Klasse (Kgl.) Bayerische Akademie der Wissenschaften.* 1912;303–322.
 24. Thomas JM. The birth of X-ray crystallography. *Nat* 2012 4917423. 2012 Nov 7;491(7423):186–7.
 25. Bragg WL. The Diffraction of Short Electromagnetic Waves by a Crystal. In: *Proceedings of the Cambridge Philosophical Society.* 1913. p. 43–57.
 26. Collister Jr WD, Rethwisch DG. *Materials Science and Engineering.* Eighth. John Wiley and Sons; 2011.
 27. Hull D, Bacon DJ. *Introduction of Dislocations.* Fifth. *Introduction to Micromechanics and Nanomechanics.* Oxford: Butterworth-Heinemann; 2011.
 28. Hull D, Bacon DJ. *Introduction to Dislocations.* Introduction to Dislocations. Butterworth-Heinemann; 2011.
 29. Karaman I, Sehitoglu H, Chumlyakov YI, Maier HJ. The Deformation of Low-Stacking- Fault-Energy Austenitic Steels. *JOM.* 2002;(54):31–7.
 30. Tian YZ, Zhao LJ, Chen S, Shibata A, Zhang ZF, Tsuji N. Significant contribution of stacking faults to the strain hardening behavior of Cu-15%Al alloy with different grain sizes. *Sci Reports* 2015 51. 2015 Nov 19;5(1):1–9.
 31. Kang M, Woo W, Lee Y-K, Seong B-S. Neutron diffraction analysis of stacking fault energy in Fe-18Mn-2Al-0.6C twinning-induced plasticity steels. *Mater Lett.* 2012;76:93–5.
 32. Karaman I, Sehitoglu H, Chumlyakov YI, Maier HJ. The deformation of low-stacking-fault-energy austenitic steels. *JOM.* 2002;54(7):31–7.
 33. W. Hertzberg R. *Deformation and Fracture Mechanics of Engineering Materials.* Fourth. John Wiley & Sons, Ltd; 1996.
 34. Dong Z, Li W, Schönecker S, Jiang B, Vitos L. Invariant plastic deformation mechanism in paramagnetic nickel-iron alloys. *Proc Natl Acad Sci U S A.* 2021 Apr 6;118(14).
 35. Schmid E, Boas W. *Plasticity of Crystals.* London: Hughes & Co; 1950.
 36. Nye JF. *Physical Properties of Crystals .* Oxford University Press. 1985. 1–352 p.
 37. Oliver EC. *THE GENERATION OF INTERNAL STRESSES IN SINGLE AND TWO PHASE.* 2002;

38. Peierls R. The size of a dislocation. *Proc Phys Soc.* 1940;52(1):34–7.
39. Kocks UF, Tome CN, Wenk H-R. *Texture and anisotropy : preferred orientations in polycrystals and their effect on materials properties.* Cambridge University Press. 2000.
40. Vinogradov A. A phenomenological model of deformation twinning kinetics Inspired by the classical Olson and Cohen model for martensitic phase transformations, a simple phenomeno-logical model of the deformation twinning kinetics is proposed with account for twin-twin. 2020;
41. Dye D, Stone HJ, Reed RC. Intergranular and interphase microstresses. *Curr Opin Solid State Mater Sci.* 2001;5(1):31–7.
42. Poshadel AC, Dawson PR. Role of Anisotropic Strength and Stiffness in Governing the Initiation and Propagation of Yielding in Polycrystalline Solids. *Metall Mater Trans A Phys Metall Mater Sci.* 2019;50(3):1185–201.
43. Taylor GI. Plastic Strain in Metals. *J Inst Met.* 1938;62(307).
44. Bunge HJ. *Texture Analysis in Materials Science – Mathematical Methods.* 1st ed. Butterworth-Heinemann; 1982.
45. Cui C, Dong J, Epp J, Schulz A, Steinbacher M, Acar S, et al. In Situ X-Ray Diffraction Analysis of Microstructure Evolution during Deep Cryogenic Treatment and Tempering of Tool Steels. *Steel Res Int.* 2021 Dec 1;92(12):2100076.
46. Peng Z, Tian G, Jiang J, Li M, Chen Y, Zou J, et al. Mechanistic behaviour and modelling of creep in powder metallurgy FGH96 nickel superalloy. 2016;
47. Clark M, Clare A, Dryburgh P, Li W, Patel R, Pieris D, et al. Spatially resolved acoustic spectroscopy (SRAS) microstructural imaging. In: *AIP Conference Proceedings.* 2019. p. 20001.
48. Schwartz AJ, Kumar K, Adams BL, Field DP, Kumar M, Adams BL, et al. *Electron Backscatter Diffraction in Materials Science.* Schwartz AJ, Kumar M, Adams BL, Field DP, editors. Paper Knowledge . Toward a Media History of Documents. Boston, MA: Springer US; 2009.
49. Unnikrishnan R. Characterization of inelastic strain in type 316H austenitic stainless steel using electron backscatter diffraction. 2019.
50. Engler O, Randle V. *Introduction to Texture Analysis : Macrotexture, Microtexture, and Orientation Mapping, Second Edition.* 2nd Editio. *Handbook of Texture Analysis.* Boca Raton: Taylor & Francis Group; 2009. 488 p.
51. Wright SI, Nowell MM, Field DP. A review of strain analysis using electron backscatter diffraction. *Microsc Microanal.* 2011;17(3):316–29.
52. Randle V (Valerie). *Microtexture determination and its applications.* Second. Maney for the Institute of Materials, Minerals and Mining; 2003. 138 p.
53. Kikuchi S. -. In: *J Appl Phys.* 1928. p. 83.
54. Wynick GL, Boehlert CJ. Use of electropolishing for enhanced metallic specimen preparation for electron backscatter diffraction analysis. *Mater Charact.* 2005;55(3):190–202.
55. Das Y. *Characterization of Stresses and Strains Involved in the Martensitic Phase Transformations.* 2017.
56. Katrakova D, Mücklich F. *Probenpräparation für die Rückstreuungselektronen-Kikuchi-Beugung*

- (Electron Backscatter Diffraction, EBSD) / Specimen Preparation for Electron Backscatter Diffraction — Part I: Metals. *Pract Metallogr.* 2001 Oct 1;38(10):547–65.
57. Sachs G. Zur Ableitung einer Fließbedingung. *Z Ver Deu Ing.* 1928;72–22(734).
 58. Bishop JFW. VI. A theoretical examination of the plastic deformation of crystals by glide. London, Edinburgh, Dublin *Philos Mag J Sci.* 1953 Jan;44(348):51–64.
 59. Bishop JFW, Hill R. CXXVIII. A theoretical derivation of the plastic properties of a polycrystalline face-centred metal. London, Edinburgh, Dublin *Philos Mag J Sci.* 1951 Nov;42(334):1298–307.
 60. Bishop JFW, Hill R. XLVI. A theory of the plastic distortion of a polycrystalline aggregate under combined stresses. London, Edinburgh, Dublin *Philos Mag J Sci.* 1951 Apr;42(327):414–27.
 61. Dawson P, Boyce D, MacEwen S, Rogge R. Residual strains in HY100 polycrystals: comparisons of experiments and simulations. *Metall Mater Trans A Phys Metall Mater Sci.* 2000;31(6):1543–55.
 62. Dawson P, Boyce D, MacEwen S, Rogge R. On the influence of crystal elastic moduli on computed lattice strains in AA-5182 following plastic straining. Vol. 313, *Materials Science and Engineering.* 2001.
 63. Quinta Da Fonseca J, Oliver EC, Bate PS, Withers PJ. Evolution of intergranular stresses during in situ straining of IF steel with different grain sizes. *Mater Sci Eng A.* 2006;437:26–32.
 64. Eshelby JD. The determination of the elastic field of an ellipsoidal inclusion, and related problems. Vol. 241, *Proceedings of the Royal Society of London. Series A. Mathematical and Physical Sciences.* 1957.
 65. Tomé CN, Oliver EC. Code ELASTO-PLASTIC SELF-CONSISTENT (EPSC).
 66. Hill R. Continuum micro-mechanics of elastoplastic polycrystals. *J Mech Phys Solids.* 1965 Apr 1;13(2):89–101.
 67. Hill RJ. The essential structure of constitutive laws for metal composites and polycrystals. *Mech Phys Solids.* 1967;15(2):79–95.
 68. Hutchinson JW. Elastic-Plastic Behaviour of Polycrystalline Metals and Composites. Vol. 319, *Source: Proceedings of the Royal Society of London. Series A, Mathematical and Physical Sciences.* 1970.
 69. Pang JWL, Holden TM, Wright JS, Mason TE. Generation of intergranular strains in 309H stainless steel under uniaxial loading. *Acta Mater.* 2000;48(5):1131–40.
 70. Pang JWL, Holden TM, Mason TE. In situ generation of intergranular strains in an A17050 alloy. *Acta Mater.* 1998;46(5):1503–18.
 71. Korsunsky AM, James KE, Daymond MR. Intergranular stresses in polycrystalline fatigue: Diffraction measurement and self-consistent modelling. *Eng Fract Mech.* 2004;71(4–6):805–12.
 72. Francis EM, Grant BMB, Fonseca JQ Da, Phillips PJ, Mills MJ, Daymond MR, et al. High-temperature deformation mechanisms in a polycrystalline nickel-base superalloy studied by neutron diffraction and electron microscopy. *Acta Mater.* 2014 Aug 1;74:18–29.
 73. Tome CN, Lebensohn RA. Manual for Code: VISCO-PLASTIC SELF-CONSISTENT (VPSC). Los Alamos Natl Lab. 2009;

74. Anglin BS, Gockel BT, Rollett AD. Developing constitutive model parameters via a multi-scale approach. *Integr Mater Manuf Innov.* 2016 Dec 1;5(1):212–31.
75. Jeong Y, Tomé CN. Extension of the visco-plastic self-consistent model to account for elasto-visco-plastic behavior using a perturbed visco-plastic approach Recent citations Elastic-viscoplastic self-consistent modeling for finite deformation of polycrystalline materials H. 2019;
76. Li DF, Odowd NP. On the evolution of lattice deformation in austenitic stainless steels - The role of work hardening at finite strains. *J Mech Phys Solids.* 2011;59(12):2421–41.
77. Turner PA, Christodoulou N, Tomé CN. Modeling the mechanical response of rolled Zircaloy-2. *Int J Plast.* 1995;11(3):251–65.
78. Sarma GB, Dawson PR. Effects of interactions among crystals on the inhomogeneous deformations of polycrystals. *Acta Mater.* 1996;44(5):1937–53.
79. Van Houtte P, Li S, Seefeldt M, Delannay L. Deformation texture prediction: From the Taylor model to the advanced Lamel model. *Int J Plast.* 2005;21(3):589–624.
80. Mukherji D, Wahi RP. On the measurement of lattice mismatch between γ and γ' phases in nickel-base superalloys by CBED technique. *Scripta Materialia Elsevier Ltd*; Jul 1, 1996 p. 117–22.
81. Withers PJ, Bhadeshia HKDH. Residual stress. Part 1-Measurement techniques. *Mater Sci Technol.* 2001;17(4):355–65.
82. Morris MA, Martin JL. Microstructural dependence of effective stresses and activation volumes during creep. *Acta Metall.* 1984;32(10):1609–23.
83. Morris MA, Martin JL. Evolution of internal stresses and substructure during creep at intermediate temperatures. *Acta Metall.* 1984;32:1909–1623.
84. Buchheit TE, Carroll JD, Clark BG, Boyce BL. Evaluating Deformation-Induced Grain Orientation Change in a Polycrystal during in Situ Tensile Deformation using EBSD. *Microsc Microanal.* 2015;21(4):969–84.
85. Kamaya M. Measurement of local plastic strain distribution of stainless steel by electron backscatter diffraction. *Mater Charact.* 2009;60(2):125–32.
86. Rollett A. Recrystallization and Texture Development in Hot Rolled 1050 Aluminum. *Mater Sci Forum.* 2004 Jan 1;
87. Barton NR, Dawson PR. A methodology for determining average lattice orientation and its application to the characterization of grain substructure. *Metall Mater Trans A* 2001 328. 2001;32(8):1967–75.
88. Cheong SW, Weiland H. Understanding a Microstructure Using GOS (Grain Orientation Spread) and Its Application to Recrystallization Study of Hot Deformed Al-Cu-Mg Alloys. *Mater Sci Forum.* 2007 Oct;558–559:153–8.
89. ICOTOM, Canadian Institute of Mining M and P. Proceedings of the Twelfth International Conference on Textures of Materials / ICOTOM-12, McGill University, Montreal, Canada, August 9 - 13, 1999. [List of sponsors: Canadian Institute of Mining, Metallurgy and Petroleum ...] Ed. by Jerzy A. Szipunar ; Vo. In Ottawa: National Research Press; 1999. p. 1791.
90. Harshavardhana N, Sundar SP, Sivam S, Kumar G, Saxena AK. A Comparative Study on Misorientations to Determine the Extent of Recrystallization in Pure ETP Copper. *Phys Met*

- Metallogr. 2021;122(13):1279–87.
91. Githinji DN. Characterisation of Plastic and Creep Strains From Lattice Orientation Measurements. 2014.
 92. Biroscas S. The deformation behaviour of hard and soft grains in RR1000 nickel-based superalloy. In: IOP Conference Series: Materials Science and Engineering. 2015.
 93. Yvell K, Grehk TM, Hedström P, Borgenstam A, Engberg G. Microstructure development in a high-nickel austenitic stainless steel using EBSD during in situ tensile deformation. Mater Charact. 2018;135:228–37.
 94. Whittle K. Nuclear Materials Science. Bristol: IOP Publishing; 2016. 1–198 p. (2053-2563).
 95. Mansur LK, Rowcliffe AF, Nanstad RK, Zinkle SJ, Corwin WR, Stoller RE. Materials needs for fusion, Generation IV fission reactors and spallation neutron sources - Similarities and differences. J Nucl Mater. 2004;329–333:166–72.
 96. Oliver E, Santisteban J. ENGIN-X user manual. 2004;
 97. Santisteban JR, Daymond MR, James JA, Edwards L. ENGIN-X: A third-generation neutron strain scanner. J Appl Crystallogr. 2006 Dec 1;39(6):812–25.
 98. Windsor C. Pulsed neutron scattering. 1981;237–400.
 99. Mamun AA, Moat RJ, Kelleher J, Bouchard PJ. Generation of intergranular strains during high temperature creep fatigue loading of 316H stainless steel. Mater High Temp. 2014;31(4):378–82.
 100. De Broglie L. Recherches sur la théorie des Quanta. [Paris]; 1924.
 101. Simm T. THE USE OF DIFFRACTION PEAK PROFILE ANALYSIS IN STUDYING THE THE USE OF DIFFRACTION PEAK PROFILE ANALYSIS IN STUDYING THE PLASTIC DEFORMATION OF METALS. University of Manchester; 2012.
 102. Peters WH, Ranson WF, Sutton MA, Chu TC, Anderson J. Application Of Digital Correlation Methods To Rigid Body Mechanics. Opt Eng. 1983 Dec 1;22(6):226738.
 103. Sutton M, Mingqi C, Peters W, Chao Y, McNeill S. Application of an optimized digital correlation method to planar deformation analysis. Image Vis Comput. 1986 Aug 1;4(3):143–50.
 104. Lee C, Peters WH, Sutton MA, Chao YJ. A study of plastic zone formation by digital image processing. Int J Plast. 1987 Jan 1;3(2):129–42.
 105. Schreier HW, Sutton MA. Investigation of two and three-dimensional image correlation techniques with applications in experimental mechanics. Vol. 3115135. University of South Carolina; 2003.
 106. Pan B, Xie H, Wang Z. Equivalence of digital image correlation criteria for pattern matching. Appl Opt. 2010;49(28):5501–9.
 107. Sutton MA, Ortu JJ, Schreier HW, Ortu JJ, Sutton MA. Image Correlation for Shape, Motion and Deformation Measurements Basic. Acta chirurgica Belgica. New York: Springer Science+Business Media; 2009. 748–752 p.
 108. Pan B, Qian K, Xie H, Asundi A. Two-dimensional digital image correlation for in-plane displacement and strain measurement: A review. Meas Sci Technol. 2009;20(6).

109. Pan B, Yu L, Wu D. High-Accuracy 2D Digital Image Correlation Measurements with Bilateral Telecentric Lenses: Error Analysis and Experimental Verification. *Exp Mech.* 2013;53:1719–1733.
110. Sutton MA, McNeill SR, Helm JD, Chao YJ. Advances in Two-Dimensional and Three-Dimensional Computer Vision. In: *Photomechanics*. Springer Berlin Heidelberg; 2000. p. 323–72.
111. Bruck HA, McNeill SR, Sutton MA, Peters WH. Digital image correlation using Newton-Raphson method of partial differential correction. *Exp Mech.* 1989 Sep;29(3):261–7.
112. Pan B, Xie HM, Xu BQ, Dai FL. Performance of sub-pixel registration algorithms in digital image correlation. In: *Measurement Science and Technology*. 2006. p. 1615–21.
113. Peng B. Modified correlation criterion for digital image correlation considering the effect of lighting variations in deformation measurements. *Opt Eng.* 2012 Feb 13;51(1):017004.
114. Hagara M, Hunady R, Stamborska M. Using of digital image correlation in experimental modal analysis of a horizontal stabilizer of the airplane model phoenix Trainer60. In: *Mod Mech Mechatr Sys.* 2011. p. 151–159.
115. Sun Z, Lyons JS, McNeill SR. Measuring Microscopic Deformations with Digital Image Correlation. *Opt Lasers Eng.* 1997;27(4):409–28.
116. Pitter MC, See CW, L Goh JY, Somekh MG, Bruck HA, McNeill SR, et al. Focus errors and their correction in microscopic deformation analysis using correlation References and links. 2002 Optical Society of America OCIS codes. 2002.
117. Berfield TA, Patel JK, Shimmin RG, Braun P V, Lambros J, Sottos NR. Fluorescent image correlation for nanoscale deformation measurements. *Small.* 2006;2(5):631–5.
118. Di Gioacchino F, Quinta da Fonseca J. Plastic Strain Mapping with Sub-micron Resolution Using Digital Image Correlation. *Exp Mech.* 2013;53(5):743–54.
119. Sutton MA, Li N, Joy DC, Reynolds AP, Li X. Scanning Electron Microscopy for Quantitative Small and Large Deformation Measurements Part I: SEM Imaging at Magnifications from 200 to 10,000. *Exp Mech.* 2007 Dec 3;47(6):775–87.
120. Sutton MA, Li N, Garcia D, Cornille N, Orteu JJ, McNeill SR, et al. Scanning Electron Microscopy for Quantitative Small and Large Deformation Measurements Part II: Experimental Validation for Magnifications from 200 to 10,000. *Exp Mech.* 2007 Dec 3;47(6):789–804.
121. Chasiotis I, Knauss WG. A new microtensile tester for the study of MEMS materials with the aid of atomic force microscopy. *Exp Mech.* 2002 Mar 1;42(1):51–7.
122. Vendroux G, Knauss WG. Submicron deformation field measurements: Part 1. Developing a digital scanning tunneling microscope. *Exp Mech.* 1998;38(1):18–23.
123. Vendroux G, Knauss WG. Submicron deformation field measurements: Part 2. Improved digital image correlation. *Exp Mech.* 1998;38(2):86–92.
124. Vendroux G, Schmidt N, Knauss WG. Submicron deformation field measurements: Part 3. Demonstration of deformation determinations. *Exp Mech.* 1998;38(3):154–60.
125. Di Gioacchino F, Quinta Da Fonseca J. An experimental study of the polycrystalline plasticity of austenitic stainless steel. *Int J Plast.* 2015;74:92–109.

126. McMurtrey MD, Was GS, Cui B, Robertson I, Smith L, Farkas D. Strain localization at dislocation channel-grain boundary intersections in irradiated stainless steel. *Int J Plast.* 2014;56:219–31.
127. Rao A, John Bouchard P, Northover SM, Fitzpatrick ME. Anelasticity in austenitic stainless steel. *Acta Mater.* 2012 Nov 1;60(19):6851–61.
128. Bhadeshia HKDH, Honeycombe SR. *Steels: Microstructure and Properties. Steels: Microstructure and Properties.* Elsevier, Butterworth-Heinemann; 2006. 1–344 p.
129. Mijangos D, Mejia I, Cabrera JM. Influence of Microalloying Additions (Nb, Ti, Ti/B, V and Mo) on the Microstructure of TWIP Steels. *Metallogr Microstruct Anal.* 2022;11(3):524–36.
130. Akeroyd FA, Ashworth RL, Johnston SD, Martin JM, Moreton-Smith CM, Sivia DS. *Open GENIE User Manual.* 2000.
131. Kocks UF, Tomé CN, Wenk HR. *Texture and anisotropy: preferred orientations in polycrystals and their effect on materials properties.* Cambridge University Press. 2000.
132. G. P. *Metallographic Etching, 2nd Edition: Techniques for Metallography, Ceramography, Plastography.* ASM International; 1999. 240 p.
133. INTERNATIONAL A. *Standard Test Methods for Determining Average Grain Size.* Astm E112-10. 2010;1–27.
134. Rasband WS. *ImageJ.* U. S. National Institutes of Health. Bethesda, Maryland, USA.: U. S. National Institutes of Health;
135. Schneider CA, Rasband WS, Eliceiri KW. NIH Image to ImageJ: 25 years of image analysis. *Nat Methods* 2012 97. 2012 Jun 28;9(7):671–5.
136. Lord, J D, Morrell R. Elastic modulus measurement. *Measurement Good Practice Guide No. 98.* Vol. 98. 2007. p. 1–100.
137. Muyupa E. *Measurement of Deformation in Varying Stress Fields.* 2020;
138. Spinner S, Reichard TW, Tefft WE. A comparison of experimental and theoretical relations between Young's modulus and the flexural and longitudinal resonance frequencies of uniform bars. *J Res Natl Bur Stand Sect A Phys Chem.* 1960;64A(2):147.
139. ASTM. *Standard Test Method for Dynamic Young's Modulus, Shear Modulus, and Poisson's Ratio by Impulse Excitation of Vibration 1.* Annual Book of ASTM Standards 15. 2005. p. 19.
140. Bachmann F, Hielscher R, Schaeben H. Texture analysis with MTEX- Free and open source software toolbox. In: *Solid State Phenomena.* 2010. p. 63–8.
141. Hielscher R, Schaeben H. A novel pole figure inversion method: specification of the MTEX algorithm. *J Appl Cryst.* 2008;41:1024–37.
142. Edwards TEJ, Maeder X, Ast J, Berger L, Michler J. Mapping pure plastic strains against locally applied stress: Revealing toughening plasticity. *Sci Adv.* 2022;8(30):1–12.
143. LaVision. *StrainMaster8.3.* In Goettingen; 2016.
144. Forsey AN. *DICEbsd.* 2022.
145. Polatidis E, Sofinowski K, Hsu WN, Swygenhoven H Van. Following Microstructures during Deformation: In situ X-ray/Neutron Diffraction and HRDIC. In: *IOP Conference Series: Materials Science and Engineering.* 2019.

